HEAT AND MOISTURE TRANSFER IN ENERGY WHEELS

A Thesis Submitted to the College of

Graduate Studies and Research

in Partial Fulfillment of the Requirements

for the Degree of Doctor of Philosophy

in the Department of Mechanical Engineering

University of Saskatchewan

Saskatoon

By

Carey James Simonson

Spring 1998

PERMISSION TO USE

The author grants permission to the University of Saskatchewan Libraries to make this thesis available for inspection. Copying of this thesis, in whole or in part, for scholarly purposes may be granted by my supervisor (Robert W. Besant), the Head of the Department of Mechanical Engineering, or the Dean of the College of Engineering. It is understood that any copying or publication or use of this thesis or parts thereof for financial gain shall not be allowed without my written permission. It is also understood that due recognition to me and the University of Saskatchewan must be granted in any scholarly use which may be made of any material in this thesis.

Requests for permission to copy or to make other use of material in this thesis in whole or in part should be addressed to:

Head of Department of Mechanical Engineering

University of Saskatchewan

57 Campus Drive

Saskatoon, Saskatchewan

S7N 5A9

ABSTRACT

In this thesis, a numerical model for heat and moisture transfer in energy wheels is developed and validated. The numerical model is based on physics with only wheel and desiccant property data and inlet flow properties needed as input. The simultaneous heat and moisture transfer model includes moisture transfer due to sorption, condensation and frosting and considers a unique boundary condition for phase change at the interface between the air and matrix. The total uncertainty in the numerically predicted effectiveness (including the accuracy of the numerical algorithm and the uncertainty of the input properties for the model) is less than ±3% for sensible effectiveness and ±5% for latent effectiveness; whereas, the uncertainty of reliable laboratory measurements are generally in the order of ±5% for sensible and ±6% to ±8% for latent effectiveness. Validation of the numerical model with laboratory and field measurements is presented for a significant range of operating conditions which include condensation and frosting.

Effectiveness correlations and governing dimensionless groups for energy wheels are developed from physical principles. These new developments include an operating condition factor which is used to explain the sensitivity of effectiveness to operating conditions and the link between sensible, latent and total effectivenesses. The effectiveness correlations are accurate within ± 2.5% of simulation data for a large range of operating conditions and wheel designs.

The numerical model is also used to study several sensitivity issues such as: the importance of the energy of phase change, energy rate control, conduction in the matrix, extrapolation of experimental test data and the effect of operating conditions. Condensation and frosting in energy wheels are also studied.

ACKNOWLEDGMENTS

A sincere thanks is firstly extended to Professor Robert W. Besant. Thank you for generously giving your thoughtful insights, support and guidance throughout this project. I especially thank you for so willing taking the time to discuss the many and varied aspects of this project as well as many other research projects and aspirations. Thanks to Dustin Ciepliski and Allan Johnson for undertaking the experimental studies that were necessary to validate my numerical model. A special thank you to those who helped in so many ways with love and words of encouragement, especially: Dad, Mom, Timo, Rauha and many brothers and sisters and their spouses. Erityinen kiitos niille jotka auttoivat niin monin tavoin, rakkaudesta ja kannatuksen sanoista, erityisesti: Isä, Äiti, Timo, Rauha ja monet siskot ja veljet ja heidän aviopuolisot.

Financial assistance is also acknowledged and appreciated from: the Natural Science and Engineering Research Council of Canada (NSERC), the American Society of Heating, Refrigerating and Air Conditioning Engineers (ASHRAE), Petro-Canada, the Solar Energy Society of Canada (SESCI), the donors of the Fredeen Scholarship in Engineering and the U of S Alumni.

DEDICATION

I dedicate this thesis to my wife, Virpi, and children, Jonathan and Nicholas. Thank you very much for your love and support throughout my Ph. D. studies.

Minä omistan tämän väitöksen vaimolleni Virpille, ja lapsilleni Jonathanille ja Nicholakselle. Oikein paljon kiitoksia teidän rakkaudestanne ja kannatuksestanne tohtoriksi opiskellessani.

TABLE OF CONTENTS

LIST OF TABLES

LIST OF FIGURES

NOMENCLATURE

ACRONYMS

COP Coefficient of performance

DEAC Desiccant Enhanced Air Conditioner

HVAC Heating, Ventilating and Air Conditioning

R.H. relative humidity

ENGLISH SYMBOLS

A cross-sectional area of each tube [m^2]

A_m cross-sectional area of one tube of the matrix [m^2]

$A_{m,t}$ total cross-sectional area of the matrix [m^2]

A_s heat and mass transfer surface area on the supply or exhaust side [m^2]

A'_s heat and mass transfer surface area of one tube [m^2]

a coefficient in the discretized equations or general constant

a* height to base ratio of a sine duct

B Bias uncertainty

b constant term in the discretized equations or general constant

C a general constant or a constant describing the shape of the sorption curve

C* ratio of the minimum to maximum heat capacity rate of the air streams

C_I constant representing the shape of a Type I sorption curve

C_κ axial conduction correction factor

Cp specific heat capacity [J/(kg·K)]

Cr* matrix heat (or moisture) capacity ratio on the supply or exhaust side

Cr^*_o overall matrix heat (or moisture) capacity ratio

Crm* matrix moisture capacity ratio on the supply or exhaust side

Crm^*_o	overall matrix moisture capacity ratio
c_ϕ	magnitude of non-uniformity in inlet relative humidity [%]
c_T	magnitude of non-uniformity in inlet temperature [K or C]
D	diameter of the energy wheel [m]
D_h	hydraulic diameter of one tube in the energy exchanger [m]
F	function used in the saturation pressure equation
f	general function
f^{-1}	inverse of function f
H	total enthalpy per mass of dry air [J/ kg_a or kJ/ kg_a]
H*	operating condition factor that represents the ratio of latent to sensible enthalpy differences between the inlets of the energy wheel
h	convective heat transfer coefficient [W/(m^2·K)]
h*	ratio of the heat of sorption to the heat of vaporization
h_{ad}	heat of sorption (adsorption and desorption) [J/kg]
$(hA_s)^*$	convective conductance ratio $(hA_s)_s/(hA_s)_e$
h_{fg}	heat of vaporization [J/kg]
h_m	convective mass transfer coefficient [m/s]
i	integer
j	iteration number
k	thermal conductivity [W/(m·K)]
L	length of the energy wheel or heat exchanger [m]
Le	Lewis number
M	total mass of the energy wheel or heat exchanger [kg]
m	constant
m*	ratio of supply to exhaust mass flow rate ($\dot{m}_s$ / $\dot{m}_e$)

$\dot{m}$	mass flow rate of dry air (unless specified by a specific subscript) [kg/s] or $\dot{m}Cp$ when $\chi = T$ in equations (2.44) and (2.45)
$\dot{m}'$	rate of phase change per unit length [kg/(s·m)]
N	angular speed of the wheel [cycles/s]
NTU	number of transfer units on the supply or exhaust side
NTU_o	overall number of transfer units
Nu	Nusselt number
n	integer
P	pressure [Pa] or precision uncertainty
p	period of exposure per cycle for the supply or exhaust gas [s/cycle]
R	specific gas constant [J/(kg·K)]
Re	Reynolds number
r	radial coordinate [m]
S	sensitivity coefficient in uncertainty analysis
T	bulk temperature [K or C]
t	time [s]
t*	dimensionless time
U	mean air flow velocity in the tube [m/s] or uncertainty
u	mass fraction of water in the desiccant [kg_w/kg_d]
W	humidity ratio (mass of water vapor per mass of dry air) [kg_w/kg_a]
Wm	empirical coefficient used in the sorption isotherm describing the maximum moisture capacity of the desiccant [kg_w/kg_d]
x	axial coordinate [m]
x*	dimensionless axial coordinate

GREEK SYMBOLS

α	thermal diffusivity [m^2/s]

β	surface area density [m^2/m^3]
χ	general variable, property or measurement
Δ	difference
ΔH_l	latent energy difference between supply and exhaust inlets conditions (kJ/kg_a)
ΔH_s	sensible energy difference between supply and exhaust inlet conditions (kJ/kg_a)
ΔT_g	temperature difference between supply and exhaust inlet conditions (C)
ΔW	humidity ratio difference between supply and exhaust inlet conditions (kg_w/kg_a)
ε_{cf}	effectiveness of a counter flow recuperator
ε_l	latent heat transfer (or moisture transfer) effectiveness
ε_s	sensible heat transfer effectiveness
ε_t	total energy (enthalpy) effectiveness
Φ	parameter used in the axial conduction correction (Shah, 1988)
ϕ	relative humidity
η	fraction of the phase change energy that is delivered directly to the air
κ	dimensionless axial conduction through the matrix
λ	coefficient which describes how, as a function of moisture content (u) the heat of sorption approaches the heat of vaporization
θ	rotational angle [°]
ρ	density [kg/m^3]
σ	volume fraction
ξ	dummy variable

SUBSCRIPTS

Al	aluminum
a	air
ave	average

c	critical moisture level representing saturation conditions
d	desiccant
dry	dry properties
e	exhaust side
e,i	average exhaust air stream inlet conditions
e,o	average exhaust air stream outlet conditions
g	total gas phase (air and water vapor)
ht	dimensionless heat transfer group for energy wheels
i	average inlet conditions
m	matrix (including support material, desiccant and moisture)
max	maximum
min	minimum
mt	dimensionless moisture transfer group for energy wheels
o	average outlet conditions or overall dimensionless group applying to the entire wheel
s	supply side
s,i	average supply air stream inlet conditions
s,o	average supply air stream outlet conditions
sat	saturation properties
v	water vapor
w	liquid water or frost

SUPERSCRIPTS

o	old value (value of a variable at the previous time step or the previous cycle)

CHAPTER 1

INTRODUCTION

Ventilation of buildings, to provide fresh air and remove contaminants, has been of considerable interest to people since the first fire was brought indoors. By cutting a hole in the roof, smoke and other contaminants were able to escape and fresh air for combustion and respiration was provided by infiltration of outside air. Throughout the ages, the adverse effects of poor ventilation have been recognized to varying degrees and it is interesting to note that in 1600, King Charles I of England decreed that new houses must have a ceiling height greater than 3 m and that windows, which were always openable, were to be higher than wide to improve the removal of smoke and odors by natural ventilation (Woods, 1988). It is believed that the first estimate of a minimum standard for ventilation air flow rates was published in England by Tredgold (1836) (Klauss et al., 1970). Since then, numerous reports and standards have been written specifying minimum outdoor ventilation air flow rates for buildings. After the development of electrical power stations at the turn of the century and electrical motor driven fans, ventilation requirements in North America were at their highest from 1890 to 1930 and, not surprisingly, were at their lowest after the oil based energy crisis of the 1970's (Janssen, 1994). These historical events exemplify the tradeoff between indoor air

quality and energy conservation that has troubled building owners and engineers for more than a century.

After standard ventilation rates for buildings were sharply decreased to reduce energy use in buildings in 1975 (ASHRAE Standard 90-1975), the number of buildings with air quality problems because of high indoor air concentrations of contaminants such as volatile organic compounds (VOC's), smoke, odors, dust and bacteria increased significantly in many buildings (Sundell, 1996 and Heiselberg, 1996). Inadequate mechanical ventilation for new air-tight buildings, built in the 1970's and 1980's, led to many new and unforeseen indoor air quality problems. As a result, most industrial countries revised their ventilation standards to include higher outdoor ventilation air flow rates. For example, ANSI/ASHRAE Standard 62-1989 specifies required ventilation air flow rates, which are about three times larger than those in ASHRAE Standard 90-1975, to maintain acceptable indoor air quality for a wide range of building types and building spaces. Wyon (1996) estimates that the annual benefit in terms of improved productivity is $55 billion if all buildings in the U.S. were upgraded to meet ANSI/ASHRAE Standard 62-1989. The average economic payback time is expected to be 1.6 years.

An important part of indoor air quality is humidity control and ANSI/ASHRAE Standard 62-1989 recommends indoor relative humidities below 60% to prevent the growth of mold and mildew that may occur on surfaces where the local humidity exceeds 70% (ASTM, 1994). Buildings in cold climates such as Canada often require much lower relative humidities in winter if condensation on windows is to be avoided. If the indoor

humidity is not controlled, usually between 20% and 60%, increasing outdoor ventilation may actually decrease occupant comfort because excessively low or high humidities may result in evaporation rates from exposed skin and lungs that is either too low or too high (ASHRAE, 1997 and Downing and Bayer, 1993).

Energy must be expended to condition outdoor ventilation air so that building space conditions remain within a "comfort" zone (ANSI/ASHRAE Standard 55-1992). As illustrated by Shirey and Rengarajan (1996), comfort conditions and the outdoor ventilation rates specified by ANSI/ASHRAE Standards 55 and 62 are not always satisfied by conventional air conditioning systems for buildings in hot humid climates. High equipment and operating costs for adequate HVAC systems has lead to interest in energy wheels (also known as enthalpy wheels or desiccant coated rotary energy exchangers) because they can transfer both heat and moisture and thereby increase comfort while reducing HVAC system capital and operating costs. The energy required to condition ventilation air typically constitutes 20 to 40% of the thermal load for commercial buildings (ASHRAE, 1997) and can be even higher in universities, schools, day cares, laboratories, hospitals and recreational facilities that require 100% fresh air to meet ventilation standards. Energy recovery devices, such as energy wheels, could satisfy a large fraction of the heating and cooling load for ventilation supply air in new and existing buildings.

1.1 ENERGY RECOVERY IN BUILDINGS

Figure 1.1 shows an energy wheel exchanging energy between the supply and exhaust air streams of a building. When the outdoor conditions are warm and humid, warm moist air passes through the wheel on the supply side, transferring heat and moisture to the matrix. This heat and moisture is then transferred from the matrix to the air on the exhaust side. In this manner, the storage of heat and moisture in the wheel is utilized to transfer heat and moisture between the two air streams.

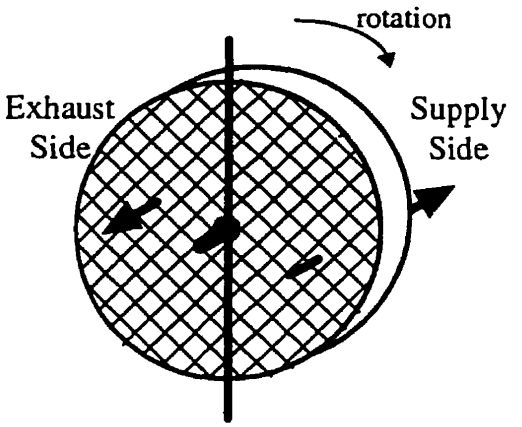

Figure 1.1. *Schematic of an energy wheel transferring energy between the supply and exhaust air streams of a building.*

In the past, energy recovery systems in buildings have been designed with the main focus on sensible heat transfer and with little emphasis on latent heat transfer (or moisture transfer) (Carnes, 1984 and Sauer and Howell, 1981). Typically, fixed plate, sensible heat transfer wheel, heat pipe and coil run-around loop heat exchangers have been used. If correctly designed, these heat exchangers can provide significant savings (Johnson et al., 1995), but they cannot directly control the indoor humidity which is costly and difficult to perform using auxiliary cooling and heating equipment. Sensible

heat exchangers, such as heat pipes, can be used to reduce indoor humidity by precooling the air entering conventional air conditioners thereby increasing condensation on the cooling coil (McFarland et al., 1996). However, as shown by Shirey and Rengarajan (1996), moisture evaporation from the wet cooling coil and drain pan can increase the indoor humidity when the compressor is operating at part load. On the other hand, an energy wheel that is coated with a desiccant can save energy and control humidity because it transfers both heat and moisture between the supply and exhaust air streams. This has been shown to be the case in both new and renovated buildings which employ energy wheels (Schaefer et al., 1996, Tamblyn, 1994 and Downing and Bayer, 1993). In each case, the energy wheel improved indoor humidity and comfort without increasing energy costs and, in some cases, the capital cost of the project was also decreased. Irwin et al. (1998) showed that energy wheels greatly reduce the cooling load and needed chiller capacity for rooms with high ventilation rates (i.e., smoking lounges).

Rengarajan et al. (1996) and Shirey and Rengarajan (1996) calculated the energy saving and operational benefits of energy wheels for large and small office buildings in Florida. In hot and humid climates, an energy wheel can transfer 2 to 3 times as much energy (or enthalpy) as a sensible heat exchanger of similar size as shown in Figure 1.2. Figure 1.2 shows that the energy required to dehumidify outdoor air can be several times greater than the sensible energy required to cool the air. As a result, the current trend in warm humid climates of North America is to use energy wheels (or enthalpy wheels), which transfer both sensible and latent energy, to reduce the energy needed to condition ventilation air for buildings.

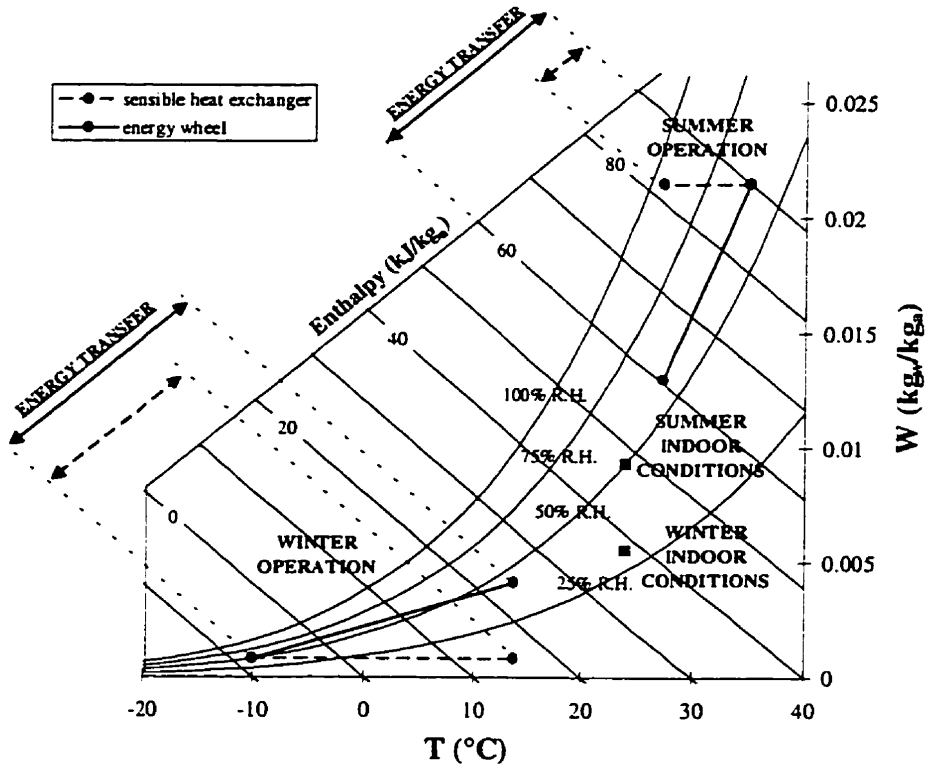

Figure 1.2. Psychrometric chart showing that for the same temperature difference an energy wheel can transfer more energy than a similar sensible heat exchanger, especially during hot and humid summer operation.

1.2 LITERATURE REVIEW

1.2.1 Sensible Rotary Heat Exchangers

The pertinent literature relevant to energy recovery by energy wheels begins with rotary heat exchangers that transfer sensible energy. These wheels have been used for several decades in gas turbine plants and electrical power generating stations to recover thermal energy from the exhaust gases and preheat inlet combustion air thus increasing the overall plant thermal efficiency (Harper and Rohsenow, 1953 and Shah, 1981). The subject of heat transfer in rotary heat exchangers has been studied extensively over a period of many years. Lambertson (1958) numerically solved the temperature distributions in the matrix and air streams using a finite difference method. His results are

for an idealized case of no fluid carryover and no axial conduction in the matrix. As an extension to Lambertson's work, Bahnke and Howard (1964) included the effect of axial conduction in the matrix for a range of matrix thermal conductivity and operating conditions. To enable a thermal stress analysis, Mondt (1964) presented the effect of axial conduction on the temperature distribution in the matrix and fluid. Harper (1957) developed a theory to predict and account for carryover and pressure leakage in rotary heat exchangers for gas turbines; while, the transient response of sensible rotary heat exchangers was studied by London et al. (1964).

These papers, summarized by Shah (1981) and Kays and London (1984), form the basis of analyzing sensible heat transfer in rotary heat exchangers. These summaries contain many design charts and design equations that allow a designer to predict the performance of sensible rotary heat exchangers under various operating conditions. Shah (1988) has combined these charts and equations into a structured design methodology for sensible rotary heat exchangers. This design methodology is important because it applies to energy wheels even though general design charts and effectiveness correlations for energy wheels are not readily available. Therefore, a significant contribution of this thesis is to present effectiveness correlations for energy wheels operating in a wide range of operating conditions and to show why energy wheel performance is a function of the operating conditions.

1.2.2 Analogy Between Heat and Mass Transfer

The studies in the previous section include only sensible heat transfer and therefore cannot be directly applied to energy wheels which transfer both heat and moisture. Attempts to apply these heat transfer solutions to the coupled heat and mass transfer problem have had limited success.

Maclaine-cross and Banks (1972) present a method to solve the coupled heat and mass transfer problem by analogy with heat transfer for any number of components. The method involves transforming the coupled equations into a number of sets of equations where each set describes only one of the characteristic potentials for heat and mass transfer and is of the same form as the equation for heat transfer alone. This allows the solution for sensible rotary heat exchangers to be used to solve each characteristic potential and hence the temperature and moisture content in the air. Banks (1972) and Close and Banks (1972) used the method of Maclaine-cross and Banks (1972) for heat and mass transfer in fluid flow through a porous medium, assuming thermodynamic equilibrium. They were able to predict the main features of an experiment with a silica-gel dryer. However, as pointed out by Banks (1985a), this method contains two significant errors which fortuitously cancel and give acceptable results for the special case of silica gel as a desiccant. This cancelling of errors cannot be guaranteed for other desiccants and operating conditions. Banks (1985b) presented a nonlinear analogy that was deemed to be more accurate for other desiccants than the linear analogy of Maclaine-cross and Banks (1972), but this nonlinear model reduced only one of the two significant errors and had, in fact, higher errors for a silica gel dehumidifier than the linear model.

The main advantage of using the analogy between heat and mass transfer is that it reduces the computation time necessary to obtain a solution. With further developments of computers and numerical techniques, this advantage has become less important. As a result, more recent studies have usually solved the coupled heat and mass transfer equations numerically. This is the approach used in this thesis.

1.2.3 Desiccant Dehumidifiers

The heat and mass transfer processes in desiccant dehumidifiers and energy wheels are similar and the only significant difference is the operating conditions. The emphasis in desiccant dehumidifiers is air drying and desiccant dehumidifiers use external heat sources to regenerate the desiccant. Energy wheels, on the other hand, exchange energy (i.e., sensible and latent energy) between air streams and use no external heat source for regeneration of the desiccant. Zheng and Worek (1993) presented an implicit numerical model which solved heat and mass transfer in adiabatic rotary dehumidifiers. Some results obtained with their numerical model are compared with results from other models but not with experimental measurements. In a subsequent paper, Zheng et al. (1993) used this numerical model to show the effect of wheel speed, type and amount of desiccant and size of the dehumidifier on the performance of adiabatic dehumidifiers.

Charoensupaya and Worek (1988) parametrically studied an open-cycle adiabatic desiccant cooling system using an explicit finite difference method. They report that maximizing the amount of moisture removed from the air does not optimize the dehumidifier-air conditioning system thermal coefficient of performance (COP). COP is

the ratio of the cooling provided by the system to the energy added by external sources. They also showed that for an optimal COP, the optimal mass fraction of desiccant is relatively low (20%) and the optimal isotherm is that of a weakly sorbing Type I desiccant. Van den Bulk et al. (1988) used a second law analysis to study solid desiccant dehumidifiers. They concluded that parameters which optimize second law efficiency (based on availability (i.e. enthalpy, entropy and absolute temperature)) also guarantee nearly optimal first law performance (COP).

The above-mentioned studies have developed the theory of desiccant dehumidifiers to the point where this theory has been applied to predict the performance of air conditioning systems. For example, Nimmo et al. (1993) and Rengarajan and Nimmo (1993) used the desiccant wheel numerical model developed by Collier (1988) to show the advantage of using a desiccant wheel together with conventional air conditioning systems. They compared DEAC (Desiccant Enhanced Air Conditioner) to other air conditioning options and found that for a warm and humid climate (e.g., Miami) the DEAC had the best performance considering energy use, comfort and capital cost. The DEAC system provided the same comfort while using 10% less energy than a current high efficiency air conditioner.

Meckler (1995) introduced a desiccant preconditioning module that can supply dry air to two or more conventional air conditioning units. Simulation results, presented in the paper, show that preconditioning ventilation air using desiccant dryers can reduce the required installed air chilling capacity by 30% in the United States. This new system

results in improved indoor air quality at a lower cost because of independent temperature and humidity control.

A collection of works by ASHRAE (1992), shows that the inclusion of desiccant dehumidifiers in HVAC systems for large and small office buildings and special applications such as supermarkets, ice rinks, and storage rooms has proven to be effective. The benefits include reduced capital and operating costs together with improved building performance. Many researchers state that similar benefits can be realized with the integration of energy wheels into HVAC systems (e.g., Rengarajan et al., 1996, Stiesch et al., 1995, and Tamblyn, 1994, to name a few). However, in spite of the high performance characteristics of energy wheels and the interest of building owners and HVAC engineers, there is little published research concerning their practical application in the literature, indicating a need for more research. In the past, detailed numerical models, together with experimental measurements, have been used to optimize HVAC technology for use in buildings (e.g., desiccant dehumidifiers (ASHRAE, 1992) and run-around heat exchangers (Johnson et al., 1995)). This is the method pursued in this thesis.

1.2.4 Modeling Energy Wheels

A few simultaneous heat and moisture transfer models of energy wheels, other than the one developed in this thesis, exist in the literature. Holmberg (1979) was the first to numerically solve the coupled governing equations for energy wheels. His model is quite complete, but it neglects the storage of energy and moisture in the air within the

energy wheel and the increased heat and moisture transfer in the entrance region of the energy wheel. Furthermore, detailed validation of the model is not presented.

Stiesch et al. (1995) simulated energy wheels using the desiccant drying model of Maclaine-cross (1974). Their numerical results agree with the manufacturer's performance data at a certain operating condition, but the effect of individual simplifying assumptions on the predicted performance was not analyzed. Although the fundamental physics and surface chemistry of desiccant drying and energy exchange are similar, according to Banks (1985a) the appropriate methods for modeling a desiccant dehumidifier and an energy wheel may not be the same because the operating conditions are significantly different. Since all models include simplifying assumptions, it is necessary to study the importance of these assumptions for the specific application of the model and to validate the model under the new operating conditions. These investigations are performed for the numerical model developed in this thesis.

A major difference between desiccant dehumidifiers and energy wheels is that the heat and moisture transfer are of similar importance in energy exchange applications while heat transfer is typically of secondary importance in dehumidifying applications. Therefore, whether the energy of phase change is transferred to the air or to the matrix can greatly affect the performance of an energy wheel. The literature has not discussed this point and, in fact, models in the literature have used different assumptions concerning this energy of phase change. Typically the energy of phase change is assumed to be delivered to the matrix (e.g., Stiesch et al., 1995, Zheng and Worek, 1993 and Holmberg,

1979); however, the model of Collier et al. (1986) assumes that the energy of phase change is delivered to the air. The correctness and significance of these assumptions needs to be investigated.

The rotational wheel speed of desiccant dehumidifiers is generally an order of magnitude lower than the wheel speed of energy wheels. This significant change in the wheel speed will likely change the analysis, design and optimization of energy wheels compared to desiccant dehumidifiers. For example, the storage of water vapor and energy in the air and axial conduction through the matrix are expected to be more important in the analysis of energy wheels. In addition, desiccant dryers, which use high temperatures to desorb moisture from the wheel, are expected to require somewhat different sorption characteristics than energy wheels which operate over a small temperature range.

1.2.5 Validation of Numerical Models

Detailed validation with accurate experimental data is necessary, but not always completed, for all numerical models of HVAC systems and components (Lebrun, 1996). ANSI/ASHRAE Standard 84-1991 is often the starting point for measuring the performance of air-to-air heat exchangers. It specifies the facilities, instrumentation and procedure to calculate the sensible, latent and total effectivenesses using measured data. This standard, however, does not explicitly specify an uncertainty analysis which is critical to understanding the significance of the results. ANSI/ASME Standard PTC 19.1-1985 provides a methodology of uncertainty analysis which is discussed in detail by

Moffat (1988) and Coleman and Steele (1989). This methodology has been used to describe the uncertainty in experimental measurements of heat exchangers (e.g., Sunden and Karlsson (1991) and Wang et al. (1996)).

ANSI/ASME PTC 30-1991 addresses the application of Standard PTC 19.1 uncertainty analysis for heat exchangers, but is limited to liquid-to-air heat exchangers which only transfer sensible energy; i.e., when sorption, condensation and frosting effects do not occur. Uncertainty analysis is particularly important for energy wheels because mass balances for dry air and water vapor and an energy balance should be satisfied at steady state. Also, the measurement of relative humidity, which is important in determining the latent and total effectiveness of energy wheels, is often difficult to perform without large uncertainties (Lafarie, 1985). Therefore, the experimental data that is used to validate the numerical model in this thesis has undergone a rigorous uncertainty analysis to ensure proper validation. The experimental measurements were performed by Dustin Ciepliski, a recent M.Sc. graduate from the University of Saskatchewan (Ciepliski, 1997) and Allan Johnson, an engineer at KS Engineering Inc., Saskatoon (Johnson et al., 1998).

1.2.6 Effectiveness Correlations for Energy Wheels

Validated numerical models of energy wheels, although detailed and accurate, do not lend themselves to simple application design methods or optimization. Despite the lack of accepted design methods or effectiveness correlations, energy wheels are rapidly being introduced into HVAC designs because they can reduce cooling and heating loads,

increase thermal comfort, while decreasing HVAC system life cycle costs. Because the economics of energy wheels strongly depend on their performance, correlations are needed to help HVAC engineers optimize designs for different climates and operating conditions.

Effectiveness is widely accepted as the best means to characterize and design most types of heat exchangers operating under a wide range of operating conditions where only the inlet properties are known. For sensible energy exchange, effectiveness (ε) is defined as the ratio of the actual heat transfer to the thermodynamic maximum heat transfer and therefore is restricted to values between 0 and 1. The ε-NTU method is a favored design method because ε typically depends on two dimensionless groups for sensible recuperative heat exchangers (NTU & C*) and four dimensionless groups for sensible rotary heat exchangers (NTU_o, C*, Cr^*_o and $(hA_s)^*$) (Kays and London, 1984, Shah, 1981 and Coppage and London, 1953). These dimensionless groups are functions of the size and shape of the heat exchanger and the flow rate through the heat exchanger; but, for most designs, they are only weak functions of the operating temperatures of the heat exchanger when condensation and frosting are not significant. That is, for a given heat exchanger design with known flow rates, the effectiveness is essentially constant regardless of small changes in inlet fluid temperatures. This important characteristic of heat exchangers transferring sensible energy allows the designer to estimate energy savings over a wide range of operating temperatures without iterative calculation procedures.

By analogy with sensible heat exchangers, one might expect the effectiveness of energy wheels to be nearly constant for a range of inlet temperatures and humidities. However, several energy wheel manufacturers and researchers have noticed that the effectiveness of energy wheels is a function of the operating temperature and humidity. The effectiveness of energy wheels seems to be particularly affected by changes in the inlet humidities, but recent effectiveness correlations for energy wheels by Stiesch et al. (1995) and Klein et al. (1990) do not account for humidity effects nor do the authors give physical insight into why effectiveness varies as a function of the inlet operating conditions. This needs physical explanation. Furthermore, Stiesch et. al. (1995) and Klein et al. (1990) assume that the sensible and latent (or moisture) effectivenesses are equal because the Lewis number for the heat and moisture transfer problem is unity. This is different than the findings in this thesis which indicates that the practical effectiveness relations for energy wheels are more complex than those given by Stiesch et. al. (1995) and Klein et al. (1990). In this thesis, the dimensionless groups derived from the governing equations are used to explain the link between operating conditions and effectiveness. These dimensionless groups are then used to develop correlations for the sensible, latent and total energy transfer effectiveness of energy wheels.

Frequently engineering correlations are based on measured data; however, in some cases, due to the lack of a large range of accurate experimental data for all operating parameters, numerical models are used to simulate data that is then correlated into functional relationships for convenient engineering design. This can be done when the numerical model has been validated with an adequate range of experimental data and

with sensitivity studies. This approach has been adopted in the past for regenerative heat (and mass) exchangers (e.g., Stiesch et al., 1995, Shah, 1981 and Lambertson, 1958) and is the method used in this thesis.

1.2.7 Condensation and Frosting in Energy Wheels

Condensation and frosting is a practical problem that is currently limiting the application of energy wheels. Often energy wheels are selected and operated to avoid any condensation or frosting within the wheel. However, during hot and humid operating conditions, water may condense in the energy wheel, saturate the desiccant and finally run off. It is known that this type of uncontrolled condensation in energy wheels will damage the desiccant coating. This will result in poorer performance of the energy wheel and, in extreme cases, can ruin the energy wheel. A similar problem exists during cold weather operation where frost may build up in the energy wheel, restrict the air flow and reduce the effectiveness of the wheel. The frosting problem has been the subject of numerical and experimental studies for both hygroscopic and nonhygroscopic regenerators (Holmberg, 1989, Leersum and Banks, 1977 and Ruth et al., 1975). Heavy frosting in energy wheels will make a defrost cycle necessary and may even result in physical degradation of the desiccant by spalling. During defrost, the large amounts of water that run off the energy wheel may also remove the desiccant. Therefore, it is important to know under what operating conditions condensation and frosting occur in energy wheels and under what conditions condensation and frosting will alter the effectiveness and lead to uncontrolled accumulation. To increase the understanding of this complex problem, this thesis includes results concerning condensation and frosting in energy wheels.

1.3 SCOPE AND OVERVIEW

The purpose of this Ph.D. research is to rectify some of the shortcomings in the literature concerning energy wheels as cited in Section 1.2. As a result, most of the research presented in this thesis has been published, is pending publication or has been submitted for publication in scientific journals. Each chapter in this thesis covers specific topics from these research papers. The main objectives of this thesis are to:

1. develop a numerical model for simultaneous heat and moisture transfer in energy wheels;
2. validate the numerical model with experimental data from laboratory and field tests;
3. use the validated numerical model to develop effectiveness correlations for energy wheels; and
4. numerically study condensation and frosting conditions in energy wheels.

A physical/numerical model of energy wheels (objective 1) is developed in detail in Chapter 2. This numerical model is one dimensional and transient and is formulated using the finite volume method with an implicit time discretization. The model is developed from physical principles and the effect of several simplifying assumptions on the predicted performance of energy wheels is studied. In particular, diffusion of the energy of phase change is treated in a unique manner and is shown to have a significant effect on the performance of energy wheels with thin desiccant coatings. This research has been published recently by Simonson and Besant (1997a and b) and Simonson et al. (1997).

In Chapter 3, experimental validation of the numerical model is presented for an energy wheel operating with a wide range of inlet conditions for mass flux, temperature and humidity. Typically, the agreement between simulated and measured (laboratory and field) results is well within the numerical and experimental uncertainties. Chapter 3 also includes extrapolation of experimental test data and recommendations for improvements to performance standards for energy wheels. The research work covered in Chapter 3 is from research papers by Simonson et al. (1998a and b), Johnson et al. (1998) and Ciepliski et al. (1998).

The fundamental dimensionless groups and effectiveness correlations for energy wheels (objective 3) are derived in Chapter 4. The dimensionless groups for simultaneous heat and moisture transfer are found to be functions of the operating temperature and humidity of the energy wheel. The physical meaning of the dimensionless groups and the importance of a new operating condition factor are explained. Simonson and Besant (1998a and b) have recently submitted this work for publication.

The final objective of this thesis is to study condensation and frosting in energy wheels. In Chapter 5, it is shown that condensation/frosting increases with humidity and at some humidity level, water/frost will continually accumulate in the wheel. The sensitivity of condensation and frosting to wheel speed and desiccant type are studied. In addition, the energy wheel performance is presented during both sorption and saturation conditions for an energy wheel that is coated with a molecular sieve desiccant and a silica

gel desiccant. Simulation results show that a silica gel desiccant is favorable for ventilation air energy recovery because it has better performance characteristics and smaller amounts of condensation/frosting for extreme operating conditions. This has significant implications for energy wheel manufacturers because many manufacturers are presently using molecular sieve desiccants. The research in this chapter has been published by Simonson et al. (1997) and, in more detail, in a recently accepted submission by Simonson and Besant (1998c).

Air-to-air energy recovery is receiving renewed attention in the HVAC industry. Within the last few years, several companies have started manufacturing, designing, marketing, selling and installing energy wheels in buildings. Therefore, the research in this thesis has potential for significant impact on energy recovery in commercial, industrial and residential buildings. The examples, test conditions and constraints used in this thesis reflect this, yet the methods are general and could be applied to energy wheels for application in other industries such as the transportation and power generation industries.

CHAPTER 2

NUMERICAL MODEL

The purpose of this chapter is to develop a numerical model for heat and moisture transfer in energy wheels. This model is intended to be used to design or optimize energy wheels and therefore it must include all important parameters that affect their performance. The model must be complete and accurate, without being overly complex, to facilitate design and optimization. In this chapter, the governing equations and assumptions used to develop the numerical model are presented in detail. As well, the effect of certain assumptions are investigated for sensitivity of the predicted performance of energy wheels.

2.1 ASSUMPTIONS

Figure 2.1(a) shows an energy wheel operating in a counter flow arrangement and Figure 2.1(b) and Figure 2.1(c) show the details of the flow tubes in the wheel and the coordinate system used in the model. The support material shown here is aluminum, but it could be any rigid material. The geometry selected for the core material (Figure 2.1(b)) changes the details of the model but not the conclusions. The numerical model solves the simultaneous heat and moisture transfer in one tube as it rotates around the axis of the wheel. Under typical operating conditions, warm moist air enters the tube during the supply part of the cycle and transfers energy and moisture to the matrix. This energy and

moisture is then transferred from the matrix to the air during the exhaust part of the cycle. The half plane of the matrix tube is assumed impermeable and adiabatic and the bulk mean temperatures and moisture concentrations in the air are used in the model. The formulation is therefore one dimensional and transient with space (x) and time (t) as the independent variables. The model inherently includes the carryover flow and its effects on performance of the energy wheel. Energy and moisture storage in the air, a variable heat of sorption and the entry length are included in the model.

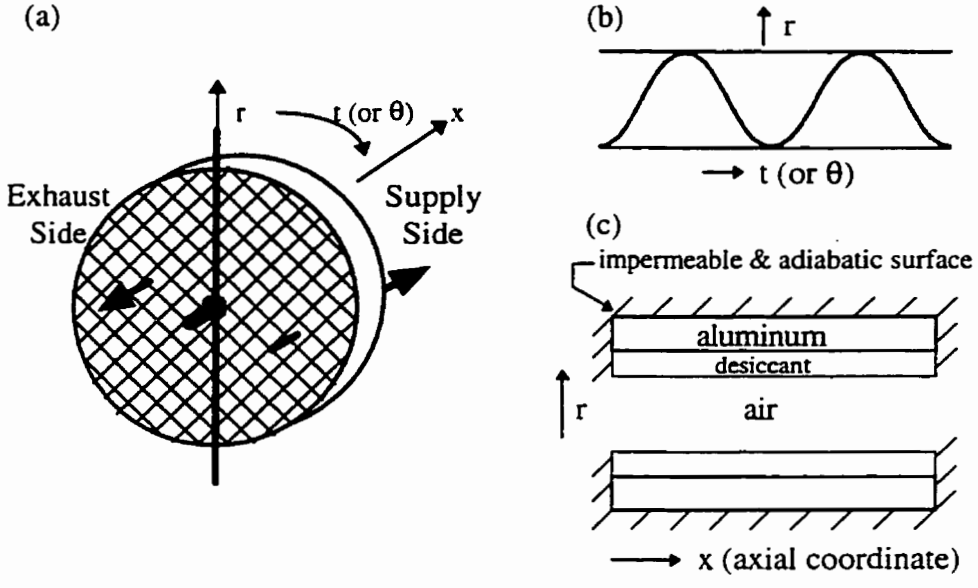

Figure 2.1. *Schematic of the energy wheel showing (a) the entire wheel, (b) the tube geometry cross-section and (c) a side view of one of the tubes.*

The assumptions used in the analysis are:

1. the heat and mass transfer process can be modeled using the bulk mean temperatures and moisture concentrations of the air within each tube shown in Figure 2.1(b) and Figure 2.1(c);
2. the axial (x direction) heat conduction and water vapor molecular diffusion in the air are negligible;
3. the axial molecular diffusion and capillary motion of moisture within the desiccant coating are negligible;

4. there are no radial (r direction) temperature or moisture content gradients in the matrix;
5. the heat conduction through the matrix in the x direction is dominated by conduction through the aluminum;
6. the half plane and ends of the matrix tubes are impermeable and adiabatic as shown in Figure 2.1(c);
7. hysteresis in the sorption isotherm and the heats of sorption for the desiccant coating are assumed negligible;
8. the temperature, velocity and concentration profiles develop simultaneously within each tube;
9. the pressure drop across the energy wheel does not result in a significant change in the absolute pressure or air density;
10. the inlet air conditions are uniform radially (r direction), but may vary with time (or rotational angle);
11. the tubes that make up the energy wheel are identical;
12. the properties of the aluminum, desiccant and adsorbed water are constant;
13. the dependent variables and properties vary periodically with time with each rotation of the wheel (i.e., within one cycle the dependent variables and properties vary in a cyclic transient manner); and
14. other assumptions concerning boundary conditions will be discussed in conjunction with the development of the theoretical model.

The first two assumptions simplify the analysis in the air. Assumption 1 avoids the problem of determining the radial temperature and moisture concentration distributions in each tube and simplifies the problem to one-dimensional in space for each bulk fluid variable. The second assumption is valid because the flux, or advection of heat and water vapor in air, is much larger than the axial conduction and molecular diffusion for a wheel under normal operating conditions. The Peclet number for typical operating conditions is in the order of 100; whereas, fluid axial heat conduction is generally neglected for $Pe > 50$ and can be neglected for $Pe > 10$ in this specific application (Shah and London, 1978).

The third assumption is typically valid because water molecules form strong physical bonds with the desiccant and therefore the molecular diffusion within the matrix will be negligible in the axial direction, yet sufficient in the direction normal to the desiccant surfaces to exchange water molecules cyclically. Furthermore, the capillary movement of water in the matrix could only occur for large accumulations of water, which is an operating condition that should be avoided in desiccant coated wheels. Assumption 4 is valid if the heat and mass transfer Biot numbers are less than 0.1 (see, for example, Incropera and Dewitt, 1996). Both the heat and mass transfer Biot numbers are less than 0.1 for this problem because the extremely thin walled tubes of aluminum (typically 0.04 mm) are coated with a thin layer of desiccant (typically 0.045 mm). This means that the matrix behaves like a heat exchanger fin with negligible temperature (and moisture content) differences in the r and θ directions but with significant temperature (and moisture content) differences in the x direction.

Assumption 5 arises because the thermal conductivity of typical desiccants (and water) is much lower than the thermal conductivity of aluminum. This coupled with the manufacturing process where the desiccant is placed in a thin layer on the aluminum and the operating process where water is adsorbed by the desiccant in a thin layer (often monolayers), results in the desiccant having little effect on the axial (x direction) thermal conduction through the wheel. For non-metallic support materials in place of aluminum foil, such as plastic or paper, with lower thermal conductivity, this assumption will not always be valid. In such cases, the thermal conductivity of the matrix can be easily modified to include conduction through the desiccant.

The ends of the matrix tubes are assumed impermeable and adiabatic because they constitute less than 0.1% of the total heat and moisture transfer surface area of the energy wheel. In addition, the temperature and moisture content of adjacent tubes in the wheel are nearly equal, permitting the assumption of an impermeable and adiabatic half plane (assumption 6).

Simplifying assumption 7 is used because molecular sieve desiccants are expected to have a type I isotherm with little or no hysteresis (Gregg and Sing, 1982). Similarly, the heats of adsorption and desorption are expected to be equal. Assumption 8 arises because the Prandtl and Lewis numbers for the problem are nearly unity. The pressure drop across the energy wheel due to skin friction is in the order of 50 Pa. This pressure drop is negligible compared to atmospheric pressure and thus changes in air pressures due to skin friction within the wheel will not influence the other properties. Assumptions 10 and 11 mean that only one of the tubes in the matrix needs to be analyzed and assumption 12 simplifies the analysis with little loss in accuracy. Assumption 10 also implies that air leakage from the supply side to the exhaust side, or vice versa, is negligible or zero. On the other hand, carry over, due to rotation of the air mass within the wheel matrix, is included in the analysis.

2.2 GOVERNING EQUATIONS

The governing equations for coupled heat and moisture transfer in energy wheels based on the above assumptions are now presented for one flow tube (see Figure 2.1(b) and Figure 2.1(c)). The energy equations for the air and matrix include energy storage,

convection, conduction and energy associated with phase change and are respectively (where all the symbols used in this thesis are defined in the nomenclature on page xv):

$$\rho_g Cp_g A_g \frac{\partial T_g}{\partial t} + U\rho_g Cp_g A_g \frac{\partial T_g}{\partial x} - \dot{m}' h_{ad} \eta + h \frac{A'_s}{L}(T_g - T_m) = 0, \text{ and} \qquad (2.1)$$

$$\rho_m Cp_m A_m \frac{\partial T_m}{\partial t} - \dot{m}' h_{ad}(1-\eta) - \dot{m}' Cp_w (T_g - T_m) - h \frac{A'_s}{L}(T_g - T_m) = \frac{\partial}{\partial x}(k_{Al} A_{Al} \frac{\partial T_m}{\partial x}). \qquad (2.2)$$

A significant difference between equations (2.1) and (2.2) and those in the literature is the term η, where η accounts for the distribution of phase change energy between the desiccant and the air. This new term in the energy equations is discussed in more detail below and in Appendix A.

In equations (2.1) and (2.2), η is the fraction of the phase change energy that enters the air directly and is shown schematically in Figure 2.2.

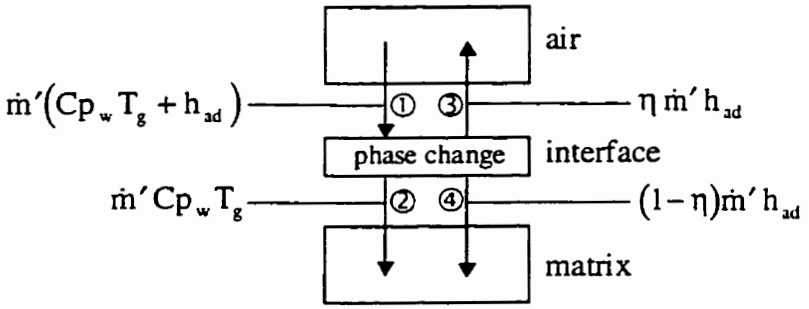

Figure 2.2. *Flow of energy between the air and the matrix due to phase change at the interface.*

Figure 2.2 shows that the term η arises from an energy balance at the phase change interface. If the local two or three dimensional temperature and moisture concentrations were obtained in the air and matrix, η would be intrinsically included in

the energy balance at this interface. However, in this case, the bulk mean properties are used for transient fluid flow with heat and mass transfer in the duct and therefore it is important to define how the energy source terms are distributed between the fluid and solid.

In Figure 2.2, energy flow ① represents the flow of energy associated with the water vapor that is leaving the air due to lateral diffusion. This water vapor undergoes a phase change at the interface as it attaches to the matrix (i.e., desiccant) as a sorbed liquid with the energy represented by ②. The water is assumed to be at the bulk mean temperature of the air which has negligible effect on the results because the energy of phase change is over 100 times greater than the sensible cooling energy. This is further explained by Christianson and Newhouse (1985) for heat and mass transfer in wet-bulb thermometers. Energy flows ③ and ④ represent the fraction of the energy of phase change that is transferred to the air and matrix respectively. To approximate η, the analytical solution for temperatures in two infinite solids with a constant heat source initiated at time t = 0 at the interface is used (Carslaw and Jaeger, 1959). The analysis is in Appendix A and the result is,

$$\eta = \frac{k_g/\sqrt{\alpha_g}}{k_g/\sqrt{\alpha_g} + k_d/\sqrt{\alpha_d}} \ , \tag{2.3}$$

where, for convection, k_g is taken to be,

$$k_g = h\, D_h \ , \tag{2.4}$$

and the thermal diffusivity of the air is modified to reflect this increased conduction. Using equation (2.3), the calculated value of η for the energy wheel modeled in this thesis

is $\eta = 0.07$; whereas, the actual value of η is probably slightly smaller because the interface between the desiccant and air is not a smooth surface (see Appendix A for further discussion). A value of $\eta = 0.05$ is estimated for the molecular sieve coating investigated here. This means that 5% of the energy of phase change is assumed to be delivered directly to the air. In Appendix A, the value of η for various applications of heat and mass transfer theory is discussed, the development of equation (2.3) is presented and it is suggested that more research is necessary to obtain a more accurate value of η.

The conservation of mass in the air results in two continuity equations, one for the water vapor and one for the dry air. These equations include storage, convection and phase change. The equations are:

$$A_g \frac{\partial \rho_v}{\partial t} + \frac{\partial}{\partial x}(\rho_v U A_g) + \dot{m}' = 0 \text{ , and} \tag{2.5}$$

$$\frac{\partial \rho_a}{\partial t} + \frac{\partial}{\partial x}(\rho_a U) = 0 \text{ .} \tag{2.6}$$

The conservation of mass for the matrix is,

$$\dot{m}' = \rho_{d,dry} A_d \frac{\partial u}{\partial t} \text{ ,} \tag{2.7}$$

where u is the mass fraction of water (vapor or liquid) in the desiccant (i.e. mass of water per mass of dry desiccant). To complete the formulation of the problem, several thermodynamic relations are needed. They are as follows:

$$P_g = P_a + P_v \text{ ,} \tag{2.8}$$

$$P_a = \rho_a R_a T_a \text{ ,} \tag{2.9}$$

$$P_v = \rho_v R_v T_v \text{ ,} \tag{2.10}$$

$$\rho_g = \rho_a + \rho_v \ , \tag{2.11}$$

$$h_{fg} = 2\,500\,800 - 2\,307(T - 273.15) \ , \tag{2.12}$$

$$h_{ad} = h^* h_{fg} = \left[1 + (h^*_{max} - 1)\left(1 - \frac{u}{Wm}\right)^{\lambda}\right] h_{fg} \ , \text{ and} \tag{2.13}$$

$$P_{v,sat} = f(T) = e^F \ , \tag{2.14}$$

where Wm is the maximum moisture capacity of the desiccant, λ describes the shape of heat of sorption as a function of moisture content and

$$F = \begin{cases} \frac{C_1}{T} + C_2 + C_3 T + C_4 T^2 + C_5 T^3 + C_6 T^4 + C_7 \ln T & ; \ 173 < T < 273K \\ \\ \frac{C_8}{T} + C_9 + C_{10} T + C_{11} T^2 + C_{12} T^3 + C_{13} \ln T & ; \ 273 < T < 473K \end{cases} . \tag{2.15}$$

The constants in equation (2.15) are (ASHRAE, 1997): $C_1 = -5674.5359$, $C_2 = 6.3925247$, $C_3 = -9.677843 \times 10^{-3}$, $C_4 = 6.22115701 \times 10^{-7}$, $C_5 = 2.0747825 \times 10^{-9}$, $C_6 = -9.484024 \times 10^{-13}$, $C_7 = 4.1635019$, $C_8 = -5800.2206$, $C_9 = 1.3914993$, $C_{10} = -4.8640239 \times 10^{-2}$, $C_{11} = 4.1764768 \times 10^{-5}$, $C_{12} = -1.4452093 \times 10^{-8}$, and $C_{13} = 6.5459673$.

The geometry and property relations for the air (g), desiccant (d) and matrix (m) are:

$$Cp_g = \frac{\rho_a Cp_a + \rho_v Cp_v}{\rho_g} \ , \tag{2.16}$$

$$\rho_d = \rho_{d.dry}(u + 1) \ , \tag{2.17}$$

$$Cp_d = \frac{\rho_{d.dry}\left(uCp_w + Cp_{d.dry}\right)}{\rho_d} \ , \tag{2.18}$$

$$\rho_m = \sigma_d \rho_d + \sigma_{Al} \rho_{Al} \ , \tag{2.19}$$

$$Cp_m = \frac{\sigma_d \rho_d Cp_d + \sigma_{Al} \rho_{Al} Cp_{Al}}{\rho_m} \ , \text{ and} \tag{2.20}$$

$$\sigma_d + \sigma_{Al} = 1 \ . \tag{2.21}$$

For the fully developed flow region within the matrix tubes, the convective heat transfer coefficient is taken for laminar flow through a tube with constant heat flux boundary conditions. The geometric shape of each tube in the matrix is assumed to be sinusoidal as shown in Figure 2.1(b). The hydrodynamic and thermal entry region in the tubes, which is typically less than 10% of the total matrix length, may be important because the temperature, concentration and velocity profiles are developing. To account for this, the convective heat and mass transfer coefficients are a function of x in the entry region. These heat transfer coefficients are obtained from numerical simulations of simultaneously (thermal and hydrodynamic) developing flow in an equilateral triangular duct (Shah and London, 1978).

2.2.1 Moisture Transfer

Modeling the moisture transfer is one of the most important parts of the model. During adsorption and desorption, the moisture transfer can be simply calculated knowing the convective mass transfer coefficient and the difference between the water vapor density in air (ρ_v) and the water vapor density on the surface of the desiccant ($\rho_{v,m}$). That is,

$$\dot{m}' = h_m \frac{A'_s}{L} (\rho_v - \rho_{v,m}) \ . \tag{2.22}$$

The surface area (A'_s) and the length (L) of each tube can be found from geometry and the convective mass transfer coefficient (h_m) can be determined directly or using the analogy between heat and mass transfer. The latter is used in this thesis. The only unknown is the water vapor density on the desiccant surface. It is known that the water vapor density on the surface of a desiccant increases as (ASHRAE, 1997):

- the amount of adsorbed water increases, and
- the temperature of the desiccant increases.

Therefore, it is logical to propose that the water vapor density on the surface of the desiccant is some function of mass fraction of water in the desiccant (u) and temperature of the desiccant. Assuming that the temperature of the desiccant is the same as the temperature of the matrix (assumption 4) gives,

$$\rho_{v,m} = f(u, T_m) \ . \tag{2.23}$$

If the function in equation (2.23) is known, equation (2.23) can be used together with equation (2.22) to calculate the rate of phase change if the kinetics of sorption are negligible (Pesaran and Mills, 1992). It is proposed to use the sorption isotherms to obtain the function that accurately describes the water vapor density on the desiccant surface as a function of moisture content and temperature.

There are six basic types of isotherms which describe the amount of gas adsorbed or desorbed as a function of the relative pressure of the gas (Gregg and Sing, 1982 and Kaviany, 1991). For a particular desiccant at a given temperature, the sorption isotherm for water vapor is,

$$u = f(\phi) , \tag{2.24}$$

where ϕ is the relative water vapor pressure (or density). By taking the inverse of equation (2.24) and knowing the saturation density of the water vapor, the density of the water vapor in the air can be determined as a function of the amount of moisture adsorbed. That is,

$$\rho_v = \rho_{v,sat} f^{-1}(u) . \tag{2.25}$$

When taking the inverse of equation (2.24) the issues of existence and uniqueness of the solution together with stability of the inverse process must be considered (Beck et. al., 1985), especially for desiccants that have complicated sorption isotherms with hysteresis.

The sorption isotherm describes the equilibrium mass fraction of water in the desiccant (i.e. when the net flux of water vapor to the desiccant is zero). That is, at equilibrium, there is no net driving potential for further adsorption or desorption. Since the difference between the partial pressure (or density) of the water vapor on the surface of the desiccant and the partial pressure (or density) of the water vapor in the air is the driving potential for sorption (equation (2.22)), it can be assumed that the partial pressure (or density) of water vapor on the surface of the desiccant will be equal to the partial pressure (or density) of the water vapor in the air at equilibrium. Therefore, equation (2.25) also gives the density of water vapor on the desiccant surface as a function of the amount of moisture in the desiccant when equilibrium sorption is assumed.

Although the analysis presented in this chapter concentrates on water vapor sorption on a molecular sieve desiccant, the procedure is applicable to any adsorptive and

adsorbent. The energy wheel, modeled in this chapter and studied experimentally in the next, is coated with a molecular sieve desiccant which has a pore size in the order of the diameter of the water molecule (3Å). The surface chemistry of water vapor sorption on these coatings is not fully understood, suggesting the need for more research. This desiccant, however, is expected to have a Type I isotherm with little or no hysteresis (Gregg and Sing, 1982). The isotherm can be described by the Langmuir equation,

$$\frac{u}{Wm} = \frac{C_l \phi}{1 + C_l \phi} \quad , \tag{2.26}$$

where: u is the mass of water vapor adsorbed per mass of dry desiccant, ϕ is the relative humidity (as a fraction) and C_l and Wm are constants which are typically determined experimentally. The dimensionless constant C_l is a function of the heat of sorption and temperature (see Appendix B) and C_l at one temperature is related to C_l at another temperature by the following relationship,

$$C_{l@T_2} = C_{l@T_1} \frac{P_{sat,2}}{P_{sat,1}} \left(\frac{T_2}{T_1} \right)^{\frac{h^* 2\,307}{R_v}} e^{\frac{h^* 3\,130\,960}{R_v}\left(\frac{T_1 - T_2}{T_1 T_2} \right)} \quad , \tag{2.27}$$

where the reference temperature (T_1) is 293.15 K (20°C) in this thesis. Taking the inverse of equation (2.26) gives,

$$\phi = \frac{\rho_v}{\rho_{v,sat}} = \frac{u}{(Wm - u)C_l} \quad , \tag{2.28}$$

which is graphed in Figure 2.3.

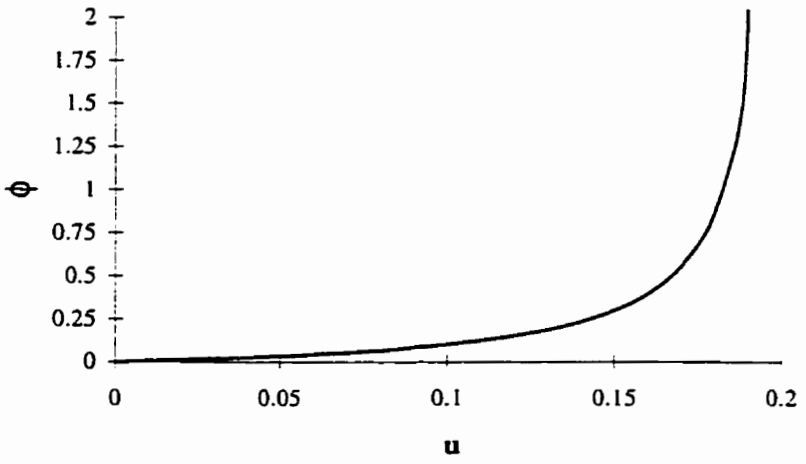

Figure 2.3. *The inverse of a Type I sorption curve. Relative humidity (fraction) as a function of the mass fraction of water (equation (2.28)).*

Equation (2.28) and Figure 2.3 point out two issues that must be considered because of the inversion. One is that the relative humidity cannot be greater than 1 and the other is the inverted solution is undefined if the denominator in equation (2.28) is zero. Therefore, we need to restrict the solution of equation (2.28) to include only the range where ϕ is between 0 and 1. By definition u is greater than or equal to zero therefore it is required that,

$$u \le (Wm - u)C_I \quad \text{and} \quad (Wm - u)\, C_I \ge 0 \tag{2.29}$$

which simplify to,

$$u \le \frac{WmC_I}{1+C_I} \quad \text{and} \quad u \le Wm \ . \tag{2.30}$$

The second condition in equation (2.30) is always satisfied if the first condition is satisfied because Wm and C_I are positive constants, which means that the ratio $C_I/(1+C_I)$ is always less than 1. It should also be noted that the constraints in equation (2.30) also ensure that the inversion solution exists by ensuring that the denominator of equation (2.28) is never

equal to zero. At u=0, $\frac{d\phi}{du} = \frac{1}{WmC_1}$, suggesting a finite slope at u=0 in the plot of ϕ versus u in Figure 2.3.

Returning to equation (2.28) and using the fact that the water vapor density on the surface of the matrix will be equal to the water vapor density in the air at equilibrium, gives the following,

$$\rho_{v,m} = \begin{cases} \frac{P_{v,sat}(T_m)}{R_v T_m} \frac{u}{(Wm-u)C_1} & ; 0 \le u \le Wm\frac{C_1}{1+C_1} \\ \frac{P_{v,sat}(T_m)}{R_v T_m} & ; u > Wm\frac{C_1}{1+C_1} \end{cases} . \qquad (2.31)$$

Equation (2.31), is used to give the needed function in equation (2.22) and completes the formulation of the governing equations during adsorption and desorption.

Although the analysis in this thesis will often concentrate on energy wheels that are coated with molecular sieve desiccant, other desiccants are sometimes used. In this case, the general sorption curve is applicable (Zheng et al., 1993),

$$u = \frac{Wm}{1 - C + C/\phi} , \qquad (2.32)$$

where Wm represents the maximum moisture content of the desiccant and C determines the type of desiccant. Several desiccant coatings, such as molecular sieve, silica gel, activated alumina and activated carbon, have sorption characteristics that can be modeled using equation (2.32). The density at the surface of the matrix derived from the general sorption curve is,

$$\rho_{v,m} = \begin{cases} \dfrac{P_{v,sat}(T_m)}{R_v T_m} \dfrac{C}{\left(\dfrac{Wm}{u} - 1 + C\right)} & ; \; 0 \le u \le Wm \\ \dfrac{P_{v,sat}(T_m)}{R_v T_m} & ; \; u > Wm \end{cases} \quad . \tag{2.33}$$

When the air becomes saturated ($\phi = 1.0$ or 100%), moisture transfer will be in the form of condensation or evaporation (ablimation or sublimation at temperatures below the triple point). This operating condition, although possible, is uncommon because uncontrolled condensation or ablimation will damage the desiccant coating on the wheel. Mathematically and physically, the problem becomes more complex when condensation and frosting are included. These conditions require a different numerical solution strategy because equation (2.22) cannot be used to calculate $\dot{m}'$. Physically, the rate of phase change at saturation, limits the relative humidity of the air to 100% and yet conserves mass (i.e., water vapor). Therefore, the conservation of water vapor in the air (equation (2.5)) is used to calculate $\dot{m}'$ during saturation and ρ_v is calculated with

$$\rho_v = \rho_{v,sat} = \frac{P_{v,sat}}{R_v T_g} \; , \tag{2.34}$$

where $P_{v,sat}$ is the saturation vapor pressure which is a function only of temperature (see equation (2.14)). This treatment is physically correct because the relative humidity of the air cannot exceed 100%. Therefore, during saturation, the axial gradient of temperature in the air will determine the amount of phase change that will occur. It is noted that the properties of water and the heat of phase change are assumed to be independent of whether the moisture accumulation is in the form of liquid water or ice. Simulation

results show that these assumptions affect the predicted effectiveness of the energy wheel by less than 0.5%. The energy of phase change during melting and freezing is neglected in this analysis because the heat of fusion is an order of magnitude lower than the heat of vaporization and the period or time for phase change to occur is small (1.5s to 6 s at wheel speeds of 20 rpm to 5 rpm). This will be discussed further in Chapter 5.

2.3 BOUNDARY CONDITIONS

The required boundary conditions for the problem are the supply and exhaust air stream inlet conditions. These conditions can generally vary with time on both the supply and exhaust sides of the energy wheel and are for any integer (n):

supply side [$n(p_s+p_e) \leq t \leq n(p_s+p_e)+p_s$]:

$$T_g(t,0) = T_{g_{s,i}}(t), \tag{2.35}$$

$$\rho_v(t,0) = \rho_{v_{s,i}}(t), \tag{2.36}$$

$$U(t,0) = U_{s,i}(t); \text{ and} \tag{2.37}$$

exhaust side [$n(p_s+p_e) + p_s \leq t \leq (n+1)(p_s+p_e)$]:

$$T_g(t,L) = T_{g_{e,i}}(t)\,, \tag{2.38}$$

$$\rho_v(t,L) = \rho_{v_{e,i}}(t), \tag{2.39}$$

$$U(t,L) = U_{e,i}(t). \tag{2.40}$$

Because time is a continuous variable from t=0 to $t=(p_s+p_e)$ to $t=n(p_s+p_e)$, the periodic boundary conditions are inherently included in the formulation.

The end surfaces of the matrix at the air flow entrance and exit from the wheel make up less than 0.1% of the total heat and moisture transfer area of the matrix. The

heat and moisture transfer through the ends will therefore be negligible compared to the heat and moisture transfer within the tube. Hence, the boundary conditions for the matrix are chosen to be adiabatic and impermeable. Mathematically this is,

$$\left.\frac{\partial T_m}{\partial x}\right|_{x=0} = \left.\frac{\partial T_m}{\partial x}\right|_{x=L} = 0 \text{ , and} \tag{2.41}$$

$$\left.\frac{\partial u}{\partial x}\right|_{x=0} = \left.\frac{\partial u}{\partial x}\right|_{x=L} = 0 \text{ .} \tag{2.42}$$

It should be noted that the initial conditions for the problem are not critical because the desired solution is the quasi-steady-state solution for an energy wheel rotating at constant speed with constant inlet conditions for both the supply and exhaust air flows.

2.4 PERFORMANCE CRITERIA

To assess the overall performance of an energy wheel, the average inlet and outlet conditions are needed for both the supply and exhaust air flows. The average inlet and outlet conditions, for any variable or property (χ), are defined as:

$$\chi_{s,i} = \frac{\int_0^{\theta_s} \dot{m}\chi(x=0)d\theta}{\int_0^{\theta_s} \dot{m}(x=0)d\theta} \text{ , } \chi_{e,i} = \frac{\int_{\theta_s}^{\theta_s+\theta_e} \dot{m}\chi(x=L)d\theta}{\int_{\theta_s}^{\theta_s+\theta_e} \dot{m}(x=L)d\theta} \text{ ; and} \tag{2.43}$$

$$\chi_{s,o} = \frac{\int_0^{\theta_s} \dot{m}\chi(x=L)d\theta}{\int_0^{\theta_s} \dot{m}(x=L)d\theta} \text{ , } \chi_{e,o} = \frac{\int_{\theta_s}^{\theta_s+\theta_e} \dot{m}\chi(x=0)d\theta}{\int_{\theta_s}^{\theta_s+\theta_e} \dot{m}(x=0)d\theta} \text{ ,} \tag{2.44}$$

where $\dot{m}$ represents $\dot{m}(Cp_a + WCp_v)$ when $\chi = T$. For uniform inlet conditions, as used in this thesis (except for Section 3.3.3), only the average outlet conditions (equation (2.44)) are required and they are calculated using numerical integration. The humidity ratio and total enthalpy are given by:

$$W = \frac{\rho_v}{\rho_a} \text{ , and} \tag{2.45}$$

$$H = Cp_a(T - 273.15) + W\left(h_{fg} + Cp_w(T - 273.15)\right) . \tag{2.46}$$

Using these definitions, the most important performance criteria of energy wheels (and any air-to-air heat exchanger), effectiveness, can be calculated. The classical definition of effectiveness (ε), as defined in many heat transfer and heat exchanger books (e.g., Incropera and Dewitt, 1996 and Kays and London, 1984), applies to sensible energy transfer with no moisture transfer. Interest in energy wheels, which transfer heat and moisture simultaneously, has resulted in an extension of the classical definition of heat exchanger effectiveness to exchangers that transfer sensible, latent and total energy. The definition of sensible, latent (or moisture) and total (or enthalpy) effectiveness can be found in several testing standards (ENV Standard 308-1996, ANSI/ASHRAE Standard 84-1991 and CSA Standard C439-M1988) and research papers (Klein et al., 1990 and Gawley and Fisher, 1975). These are defined for steady-state conditions as follows:

- sensible heat transfer effectiveness assuming a constant specific heat:

$$\varepsilon_s = \frac{\dot{m}_s(T_{s,i} - T_{s,o}) + \dot{m}_e(T_{e,o} - T_{e,i})}{2\dot{m}_{min}(T_{s,i} - T_{e,i})} , \tag{2.47}$$

- latent heat transfer effectiveness assuming the enthalpy of phase change is constant (moisture transfer effectiveness):

$$\varepsilon_l = \frac{\dot{m}_s(W_{s,i} - W_{s,o}) + \dot{m}_e(W_{e,o} - W_{e,i})}{2\,\dot{m}_{min}(W_{s,i} - W_{e,i})} \quad , \text{ and} \tag{2.48}$$

- total energy (enthalpy) transfer effectiveness:

$$\varepsilon_t = \frac{\dot{m}_s(H_{s,i} - H_{s,o}) + \dot{m}_e(H_{e,o} - H_{e,i})}{2\,\dot{m}_{min}(H_{s,i} - H_{e,i})} \quad . \tag{2.49}$$

The effectiveness relations in equations (2.47) to (2.49) differ slightly from those in the literature and are the average of the supply and exhaust side effectivenesses which correspond to the lowest uncertainty in the effectiveness value (Ciepliski et al., 1998 and Johnson et al., 1998). The effectiveness of an energy wheel typically depends on the overall number of transfer units (NTU_o) and the overall dimensionless wheel capacitance (Cr^*_o). These dimensionless groups are defined for sensible heat transfer as (Shah, 1981):

$$NTU_o = \frac{1}{(\dot{m}Cp_a)_{min}}\left[\frac{1}{\frac{1}{(hA_s)_s} + \frac{1}{(hA_s)_e}}\right] \quad , \text{ and} \tag{2.50}$$

$$Cr^*_o = \frac{MCp_m N}{(\dot{m}Cp_a)_{min}} \quad . \tag{2.51}$$

2.5 NUMERICAL ALGORITHM

The governing equations are discretized using an implicit finite volume method with a staggered grid (Patankar, 1980). Velocity is solved at the faces and all the

remaining dependent variables and properties are solved at the nodes. The upwind differencing scheme is used for the air and the central differencing scheme is used for the matrix. The algebraic equations are solved using a Gauss-Seidel iteration technique with under relaxation and, to speed up convergence, the energy equation in the matrix (equation (2.2)) is solved using the Tridiagonal Matrix Algorithm (Patankar, 1980). The algebraic equations and numerical code are in Appendix C. The algorithm used during sorption conditions is not the same as the algorithm used during saturation conditions as can be seen in Table 2.1.

Table 2.1. *Algorithm used to solve the governing equations.*

Sorption ($\phi < 100\%$)	Common	Saturation ($\phi = 100\%$)
	1. Estimate the rate of phase change and the properties needed in the governing equations.	
2. Solve the T_m, ρ_v, U, u and T_g fields in order with equations (2.2), (2.5), (2.6), (2.7) and (2.1) respectively.		2. Solve the T_m, $\dot{m}'$, U, u and T_g fields in order with equations (2.2), (2.5), (2.6), (2.7) and (2.1) respectively.
	3. Update properties.	
4. Update the rate of phase change ($\dot{m}'$).		4. Update the water vapor density (ρ_v).
	5. Return to step 2 and iterate until a converged solution is reached.	
	6. Adjust, as necessary, the algorithm used in each grid for the next time step.	
	7. Increment time, return to step 2 and iterate until a quasi-steady solution is obtained.	

The local air relative humidity is used to determine which algorithm should be used. If the relative humidity of the air, at any grid point, is less than 100%, the sorption algorithm is used to solve the governing equations for that grid point. If the relative humidity of the air is greater than 100%, the relative humidity is set to 100% and the saturation algorithm is used. Each grid point can be saturated or unsaturated independent of the rest of the grid points in the solution domain. This allows some regions of the wheel to be under saturation conditions while other regions are under sorption conditions. The algorithm uses a fixed grid and therefore the saturation and sorption zones will change by finite steps equal to the grid size. To prevent unstable numerical oscillations between sorption and saturation, the algorithm is changed in an explicit manner. This means that the algorithm will be changed only after a converged solution is reached and will be updated for the next time step (see step 6 in Table 2.1).

The order of solution in step 2 seems to give the most rapid convergence of the equations and was chosen by trial and error. This trial and error analysis showed that the most important feature in step 2 is that T_g be solved very last. This reduced the solution time by approximately a factor of two compared to the case where T_g is solved first.

The transient solution is solved until quasi-steady state is reached. Even though the most important result is the quasi-steady solution, the model must be time accurate because the quasi-steady solution is a transient solution that varies periodically. The numerical solution is time accurate because time is incremented only when a converged solution is reached. The normalized residuals of the governing equations are low ($\sim 10^{-16}$)

because upwinding and the tridiagonal matrix algorithm are used. As a result, the convergence criteria is based on the amount the dependent variables change from iteration to iteration. Time is incremented when the following is satisfied for each dependent variable and the rate of phase change:

$$\frac{\sum_{i=1}^{n}\left|\chi(i)^{j+1}-\chi(i)^{j}\right|}{n(\chi_{max}-\chi_{min})} \leq 1\times10^{-4} \ . \tag{2.52}$$

Decreasing the convergence limit from 10^{-4} to 10^{-5} nearly doubles the solution time but changes the predicted effectiveness by less than 0.05%. This justifies the selected convergence limit in equation (2.52).

Quasi-steady state can be determined using the periodicity of the energy wheel or by conservation of energy and moisture across the wheel. Bahnke and Howard (1964), found that using an energy and mass balance to determine quasi-steady conditions is more stringent than the periodicity conditions at typical operating conditions. Based on energy and mass balances, quasi-steady state is defined as the time when all the energy and moisture that is lost by one air stream is taken up by the other air stream. This means that the cyclic energy or moisture storage in the matrix over one revolution of the energy wheel is zero (or, negligible). The quasi-steady conditions for energy and mass balances are defined when:

$$\left|\frac{\dot{m}_s(W_{s,i}-W_{s,o})-\dot{m}_e(W_{e,o}-W_{e,i})}{\dot{m}_{min}(W_{s,i}-W_{e,i})}\right| \leq 1\times10^{-2} \text{ , and} \tag{2.53}$$

$$\left|\frac{\dot{m}_s(H_{s,i}-H_{s,o})-\dot{m}_e(H_{e,o}-H_{e,i})}{\dot{m}_{min}(H_{s,i}-H_{e,i})}\right| \leq 1\times10^{-2} \ . \tag{2.54}$$

If the quasi-steady-convergence criteria is set to 1 x 10^{-3}, the effectiveness changes by 0.1% from that predicted with a convergence criteria of 1 x 10^{-2}, showing that the convergence limits in equations (2.53) and (2.54) are acceptable. When condensation and frosting occur within the energy wheel, it is desirable to reduce the quasi-steady-convergence limit to distinguish between accumulation due to uncontrolled condensation/frosting and that due to the convergence limit. In all chapters of this thesis, except Chapter 2, the operating conditions are such that condensation and frosting may occur in the energy wheel; in these cases, the converge limit in equations (2.53) and (2.54) is decreased to 2 x 10^{-3}. To ensure that equations (2.53) and (2.54) give the quasi-steady solution, the periodicity of the energy wheel is checked by calculating the effectiveness after each revolution of the wheel. Periodicity is reached when the change in effectiveness is small or negligible, i.e.,

$$\left|\frac{\partial \varepsilon}{\partial t}\right| \approx \frac{\left|\varepsilon - \varepsilon^{o}\right|}{p_s + p_e} \leq 1 \times 10^{-4} \ , \tag{2.55}$$

where ε^{o} is the effectiveness of the previous wheel rotation. Again, decreasing the convergence level in equation (2.55) by a factor of 10 has a negligible effect on the calculated effectiveness. Therefore, if equations (2.53) to (2.55) are satisfied, the solution is deemed to be the quasi-steady solution.

2.5.1 Switching Between Saturation and Sorption

The algorithm used in the numerical model is different for saturation conditions than for sorption conditions. For this reason, it is important that the numerical switching be stable and, of course, physically correct. As a first attempt, the algorithm was changed

implicitly and updated in the current time step. Although this method is physically accurate, it tended to result in numerical oscillation for fine grid meshes and small time steps. Therefore, to increase numerical stability, the algorithm is changed explicitly as indicated in Table 2.1. This means that the relative humidity of the air can now go slightly above 100% for one time step before the algorithm will be switched, but the change from implicit to explicit switching changed the simulated effectiveness of the energy wheel by less than 0.5%.

A numerical switch from the sorption algorithm to the saturation algorithm is clear because the calculated relative humidity will exceed 100% when this switch is to be made. However, a numerical switch from the saturation algorithm to the sorption algorithm cannot be based on the air relative humidity falling below 100% because the saturation algorithm sets the air relative humidity to 100%. To determine a realistic strategy for the numerical switching from the saturation algorithm to the sorption algorithm, the physics of this transition must be understood. Figure 2.4 shows the physical transition from saturation conditions to sorption conditions.

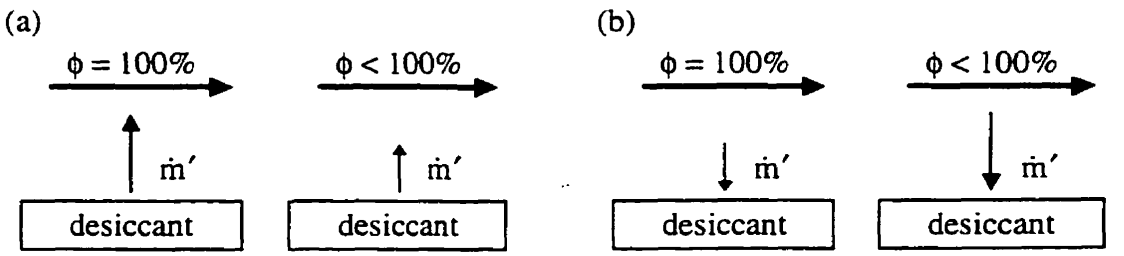

Figure 2.4. *Transition from saturation to sorption occurs as (a) the evaporation rate decreases or (b) the condensation rate increases.*

If moisture is being removed from the desiccant and the air flowing above the desiccant is saturated (Figure 2.4(a)), the rate of evaporation phase change is such that the air relative humidity remains 100%. If the evaporation rate reduces, the air relative humidity will fall below 100% and sorption conditions will result. Similarly, as the condensation rate increases, the relative humidity of the air will fall below 100% as can be seen in Figure 2.4(b). Clearly, the rate of phase change calculated with the saturation algorithm will be the maximum amount of evaporation that can occur and the minimum amount of condensation that can occur. If the physics of the convective mass transfer and the sorption properties of the desiccant cause the evaporation rate to be less than this maximum or cause the condensation rate to be greater than this minimum, the relative humidity of the air will fall below 100%. These cases are physically possible and mark the transition from saturation to sorption. Therefore, when a converged solution is reached, the calculated phase change rate at each saturation node is compared with the phase change rate that would occur due to convection mass transfer under sorption conditions (i.e. equation (2.22)), to determine if the numerical algorithm should be changed for that node. The numerical algorithm is changed from saturation to sorption when,

$$\dot{m}'\Big|_{\substack{\text{saturation}\\ \text{algorithm}}} < h_m \frac{A'_s}{L}(\rho_v - \rho_{v,m}), \tag{2.56}$$

where $\dot{m}'$ is positive for moisture accumulation in the desiccant (i.e., adsorption/condensation/ablimation) and $\dot{m}'$ is negative for moisture removal from the desiccant (i.e., desorption/evaporation/ sublimation).

There are other possible methods to determine when a numerical switch must be made between saturation and sorption conditions. One approach would be to use the moisture content of the desiccant. It may be possible to determine a critical moisture content (u_c), such that if $u < u_c$, sorption conditions exist and if $u > u_c$, saturation conditions exist. One problem with this method is the difficulty in determining u_c. Also, the physical meaning of this approach is not as clear as the physical meaning of the method used in this thesis (i.e., equation (2.56)). Simulation results show that the predicted effectiveness of the energy wheel is nearly the same (~0.5% different) for the two different methods. However, Figure 2.5 shows that the predicted moisture content distribution in the desiccant is not the same for both methods. The moisture content predicted with the proposed approach based on the rate of phase change is clearly more physically realistic than the approach based on the moisture content of the desiccant. For the results in Figure 2.5, the critical moisture content in the molecular sieve desiccant coating has been defined as,

$$u_c = \frac{Wm}{1 - C + C/\phi_c}, \quad \phi_c = 1.0 \text{ (or } 100\% \text{ R.H.)} \; . \tag{2.57}$$

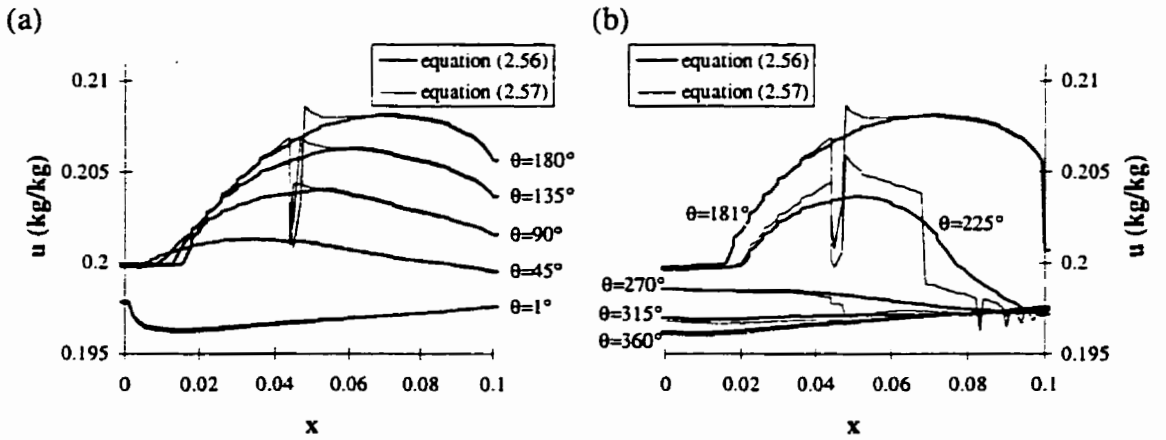

Figure 2.5. *Moisture content profiles in the desiccant during (a) supply air flow (40°C & 80% R.H.) and (b) exhaust air flow (24°C & 50% R.H.) through the wheel comparing two methods of numerical switching between saturation and sorption conditions. The dark lines use the approach of this thesis (i.e., equation (2.56)) and the light lines use the approach based on the critical moisture content in the desiccant (i.e., equation (2.57)).*

Figure 2.5 shows that the moisture content in the desiccant has a significant dip between x = 0.04 and 0.05 m when equation (2.57) is used to determine when to switch from saturation to sorption conditions but not when equation (2.56) is used. This figure suggests that equation (2.56) is a more accurate model for the transition from saturation to sorption conditions than equation (2.57). Therefore, equation (2.56) is used throughout the rest of this thesis.

2.6 STEP SIZE AND NUMERICAL ACCURACY

To determine an acceptable grid size and time step for the numerical solution, the number of spatial and time steps are varied for supply side inlet conditions of 5°C and 20% relative humidity and exhaust side inlet conditions of 20°C and 40% relative humidity. The wheel parameters are given in Table 2.2 and the results are in Figure 2.6.

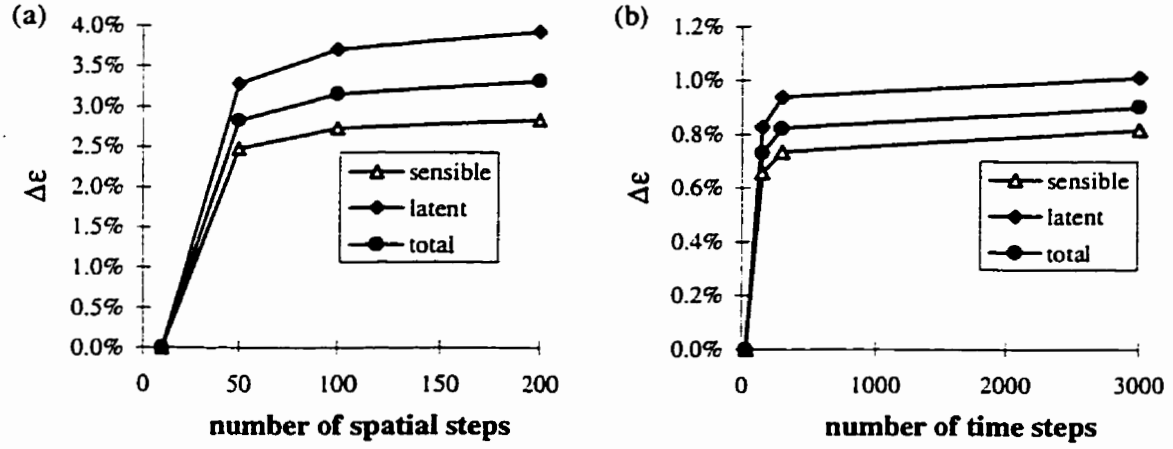

Figure 2.6. *Effect of the number of (a) spatial steps and (b) time steps on the predicted effectiveness of an energy wheel* ($\Delta\varepsilon = \varepsilon - \varepsilon_{\text{smallest number of steps}}$).

The results in Figure 2.6(a) are calculated with 300 time steps and the results in Figure 2.6(b) are calculated with 100 spatial steps. Figure 2.6 shows that increasing the number of spatial steps above 100 and time steps above 300 has little effect on the predicted performance. Therefore, 100 spatial steps ($\Delta x = 0.001$m) and 300 time steps ($\Delta t = 0.01$s) are used throughout the rest of this thesis. The selection of an acceptable time step and grid size is a balance between speed and accuracy. For example, increasing the number of spatial steps from 100 to 200 and increasing the number of time steps from 300 to 3000, changes the predicted effectivenesses by only 0.2%, but increases the solution time by a factor of 20.

The accuracy of the numerical solution that results from the numerical model is related to the accuracy of the energy and mass balances across the energy wheel. The quasi-steady-convergence criteria based on energy and mass balances is set to 1%. Reducing the quasi-steady convergence criteria to 0.1%, changes the effectiveness by

only 0.1% from that predicted with a convergence criteria of 1% (see equations (2.53) and (2.54)). Also, increasing the convergence criteria by a factor of 10 changes the calculated effectiveness by less than 0.05%. These tests, together with the results in Figure 2.6, indicate that the effectivenesses that are calculated from the numerical model are accurate within at least ±0.5% effectiveness and likely ±0.2% effectiveness.

The total uncertainty in predicted effectiveness, when simulating an existing energy wheel, will be a function of both the accuracy of the numerical model and the uncertainty in the measured input property data. Following ANSI/ASME Standard PTC 19.1-1985, the uncertainty in the predicted effectiveness can be estimated as,

$$U_{\varepsilon,\text{predicted}} = \left[(\text{bias})^2 + (\text{precision})^2\right]^{1/2}, \tag{2.58}$$

where, in this case, bias represents the bias uncertainty in the input data and precision represents the uncertainty in the numerical algorithm or numerical noise. The sensitivity coefficients for each individual input property can be determined by Monte Carlo simulations (Uddin and Bell, 1988) or estimated from sensitivity studies (Section 2.7). The input properties that have the greatest effect on the uncertainty of the predicted sensible effectiveness are the Nusselt number (Nu), heat transfer surface area (A'_s), thermal conductance of the matrix ($k_m \cdot A_m/L$) and the fraction of phase change energy that is delivered directly to the air (η). Considering that the uncertainty in these property data is likely less than ±5%, the uncertainty in the predicted value of ε_s is likely less than ±3%. The uncertainty in the predicted latent effectiveness will be slightly higher because of uncertainties in the sorption properties of the desiccant (Wm and C_l). The uncertainty in

the predicted value of ε_l is expected to be less than ±5%. The uncertainty in the predicted total effectiveness will lie between the uncertainty in the sensible and latent effectivenesses. The total uncertainty of the numerical model simulated results (including numerical accuracy and input data uncertainty) is further displayed by comparison with experiments in Chapter 3 and sensitivity studies in the next section.

2.7 SENSITIVITY STUDIES

The purpose of the simulations presented in this section is to show the effect of certain assumptions and parameters on the predicted performance of an energy wheel. The boundary conditions, properties and wheel parameters used in these simulations are given in Table 2.2. It should be noted that in all the simulations in this section $\eta = 0$ and $h^* = 1$ except in Sections 2.7.1 and 2.7.2 as specified.

Since the purpose of this section is to highlight the sensitivity of various assumptions and property data on the numerically predicted effectiveness of an energy wheel, most of the results are presented as changes in effectiveness. For completeness the predicted effectivenesses for the base parameters shown in Table 2.2 and 100 spatial steps and 300 time steps are:

- cold test: ε_s=71%, ε_l=76% and ε_t=73% ($T_{e,i}$=20°C, $\phi_{e,i}$=40%, $T_{s,i}$=5°C, $\phi_{s,i}$=20%); and
- hot test: ε_s=66%, ε_l=65% and ε_t=65% ($T_{s,i}$=35°C, $\phi_{s,i}$=70%, $T_{e,i}$=24°C, $\phi_{e,i}$=40%).

An effectiveness of 71.5% can be expected for a sensible wheel with the same characteristics as the one in Table 2.2 (Shah, 1988). This is nearly equal to the value of 71% calculated for the cold test, but quite different from the value of 66% calculated for

the hot test. This indicates that the relations in Shah (1988 and 1981) can be used to calculate the performance of energy wheels only when the latent energy transfer is relatively small. This is further explained in Chapter 4.

Table 2.2. Boundary conditions and wheel properties used in the sensitivity studies.

AIR	$T_{e,i}$ = 20°C (cold test) $T_{s,i}$ = 5°C (cold test)	$\phi_{e,i}$ = 40% (cold test) $\phi_{s,i}$ = 20% (cold test)	$\dot{m}_s = \dot{m}_e$ = 0.5 kg/s = 1.6 kg/(s·m^2)
	$T_{s,i}$ = 35°C (hot test) $T_{e,i}$ = 24°C (hot test)	$\phi_{s,i}$ = 70% (hot test) $\phi_{e,i}$ = 40% (hot test)	
WHEEL	M = 11 kg	L = 0.1 m	D = 0.9 m
speed = 20 rpm	D_h = 1.47 x 10^{-3} m	Re_{D_h} = 149	porosity = 85%
Nu = 2.48 *	Le = 1	h = 44.6 W/(m^2·K) *	h_m = 0.036 m/s *
NTU_o = 3.6	Cr^*_o = 6.1	U = 1.5 m/s	
DESICCANT	ρ = 350 kg/m^3	Cp = 600 J/(kg·K)	mass fraction = 20%
σ_d = 0.66	Wm = 0.2	C_l = 20 (@ 20°C)	

* Fully developed laminar flow

2.7.1 Phase Change Interface Term

In the development of the numerical model, the fraction of the energy associated with phase change that is delivered to the air was defined as,

$$\eta = \frac{k_g/\sqrt{\alpha_g}}{k_g/\sqrt{\alpha_g} + k_d/\sqrt{\alpha_d}} \quad . \tag{2.59}$$

The effect of η on the predicted performance of an energy wheel is presented in Figure 2.7.

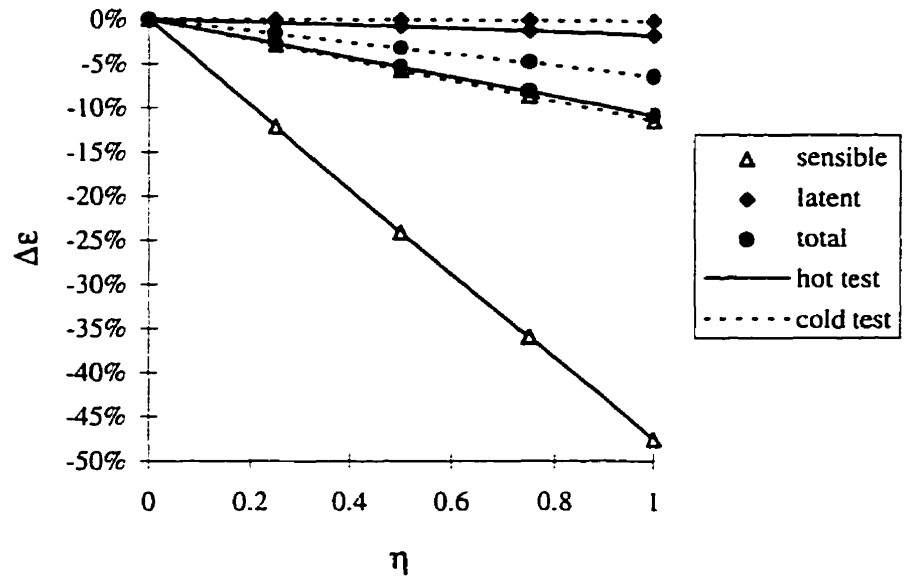

Figure 2.7. *Change in the predicted effectiveness for various values of* η *(the fraction of the energy of phase change that is delivered directly to the air) (* $\Delta\varepsilon = \varepsilon - \varepsilon_{\eta=0}$ *).*

The results in Figure 2.7 show that the predicted effectiveness is very sensitive to η and that the effectiveness changes nearly linearly with η. Whether the energy of phase change remains entirely in the air ($\eta = 1$) as assumed by Collier et. al. (1986) or whether it remains entirely in the matrix ($\eta = 0$) as assumed by Stiesch et al. (1995), Zheng and Worek (1993) and Holmberg (1979) has a large impact on the performance of an energy wheel. The largest effect is for the sensible effectiveness. This may explain why these assumptions were not emphasized in the analysis of adiabatic dehumidifiers where sensible heat transfer is of secondary importance to moisture transfer. If the phase change energy is assumed to remain entirely in the air ($\eta = 1$), the predicted sensible effectiveness is decreased by 12% for the cold test and 48% for the hot test. Therefore, for the hot test, η must be determined within ± 0.01 to ensure that the predicted sensible effectiveness is accurate to within $\pm 0.5\%$. Even with the small value of η for the energy

wheel modeled in this thesis ($\eta = 0.05$), a difference of 2.5% in the predicted sensible effectiveness may result compared to $\eta = 0$. Clearly much larger errors will result if η is assumed to be equal to 1.

The large decrease in effectiveness that results when η is varied from $\eta = 0$ to $\eta = 1$ can be explained by noting that when the warm and moist air passes through the energy wheel, moisture is deposited on the wheel and energy is released. If this energy goes directly into the matrix ($\eta = 0$), the matrix will contain more energy which can be transferred to the cold side air stream resulting in a high sensible effectiveness. On the other hand, if the energy remains in the air ($\eta = 1$), the hot air outlet temperature will increase, causing a decrease in sensible effectiveness. Similar arguments can be made for the cold side where energy is needed to desorb moisture from the desiccant. The change in effectiveness is so large because the energy transfer due to phase change is nearly equal to the energy transfer due to the advection of energy through the energy wheel for the cold test and nearly four times greater for the hot test.

2.7.2 Heat of Sorption and Sorption Isotherm

The heat of adsorption and desorption can be as much as two to three times the heat of vaporization for low moisture accumulations on a molecular sieve desiccant (Collier et. al., 1986). This high heat of phase change not only affects the heat released during phase change, but it also affects the isotherm dependence on temperature. These effects are included in the numerical model as follows:

$$h_{fg} = 2\,500\,800 - 2\,307(T - 273.15) \ , \qquad (2.60)$$

$$h_{ad} = h^* h_{fg} = \left[1 + (h^*_{max} - 1)\left(1 - \frac{u}{Wm}\right)^{\lambda}\right] h_{fg} \text{ , and} \tag{2.61}$$

$$C_{1@T_2} = C_{1@T_1} \frac{P_{sat,2}}{P_{sat,1}} \left(\frac{T_2}{T_1}\right)^{\frac{h^* 2307}{R_v}} e^{\left[\frac{h^* 3\,130\,960}{R_v}\left(\frac{T_1 - T_2}{T_1 T_2}\right)\right]} . \tag{2.62}$$

In this section, the effect of various heats of sorption on the predicted effectiveness is presented. Figure 2.8(a) contains the ratio of the heat of sorption to the heat of vaporization (h*) for $h^*_{max} = 3$ (the maximum heat of sorption to heat of vaporization ratio) and various values of λ (the rate at which the heat of sorption approaches the heat of vaporization as a function of u). Figure 2.8(a) shows that h* is greater for $\lambda = 2$ than for $\lambda = 5$. When $\lambda = 2$, the increase in the heat of sorption is quite large and is expected to be a maximum. When $h^*_{max} = 3$ and $\lambda = 2$, the sorption isotherm is most affected by a change in temperature. This is shown in Figure 2.8(b).

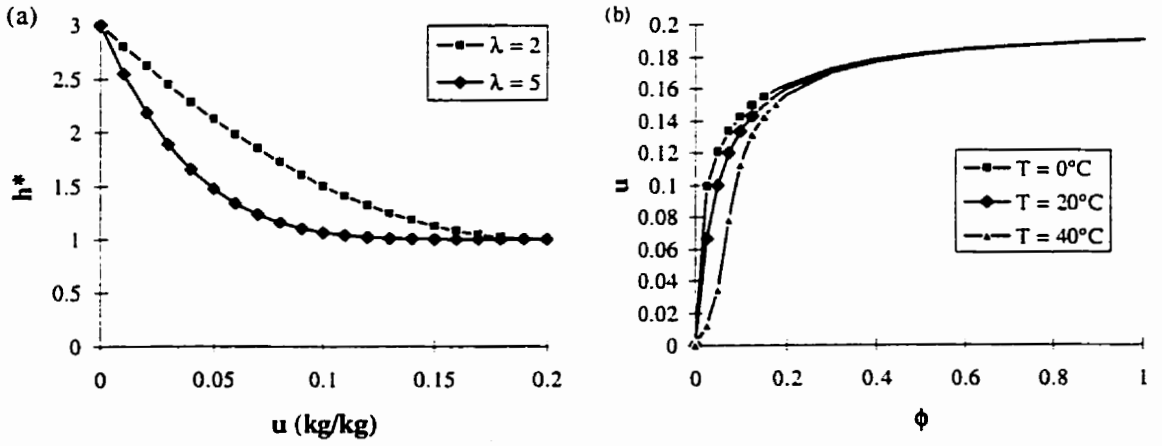

Figure 2.8. *(a) Ratio of the heat of sorption to the heat of vaporization as a function of moisture content for $h^*_{max} = 3$ and (b) effect of temperature on the sorption isotherm when $h^*_{max} = 3$ and $\lambda = 2$.*

Figure 2.9 shows how the sensible, latent and total effectivenesses change, when a variable heat of sorption and a temperature dependent isotherm are included in the model, compared to the case where the sorption isotherm is constant and the heat of sorption is equal to a constant value. The value chosen is $h_{ad} = h_{fg} = 2\,445\,000$ J/kg which corresponds to the heat of vaporization at 24°C.

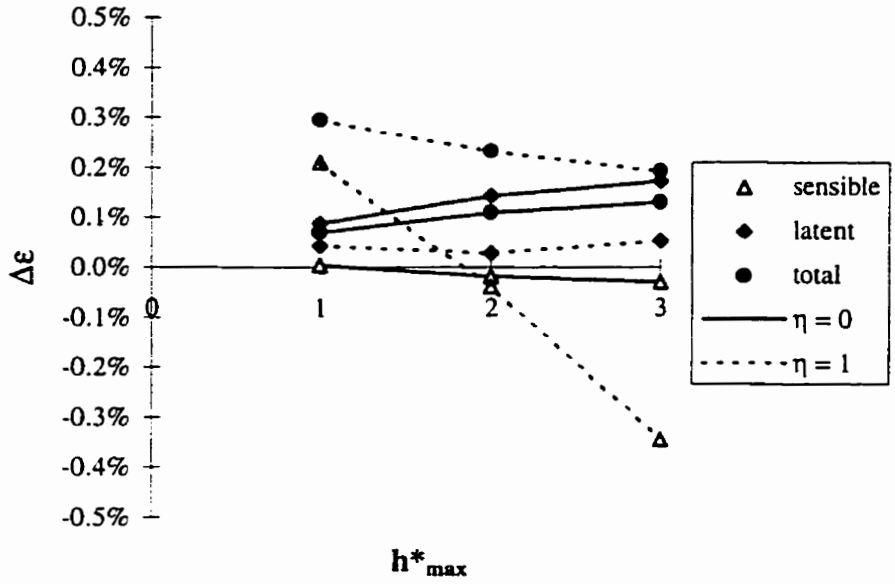

Figure 2.9. *Change in effectiveness that results when the heat of sorption and the sorption isotherm are allowed to change as a function of moisture content and temperature respectively for* $\lambda = 2$ *and the hot test conditions* ($\Delta\varepsilon = \varepsilon_{\text{including changing sorption}} - \varepsilon_{\text{neglecting changing sorption}}$).

From Figure 2.9, it can be seen that including the heat of sorption and the temperature dependent isotherm in the model has a small effect on the predicted effectiveness. For the hot test results in Figure 2.9, the change in effectiveness is less than 0.5% in all cases. The effect of the heat of sorption for the cold tests and for $\lambda = 5$ are even smaller and not presented in Figure 2.9. These results show that the effect of

the magnitude of the heat of sorption and the resulting temperature effect of the sorption isotherm are not very important for energy wheels. The reason for this is mainly because the temperature difference between the supply and exhaust air streams is usually small (~ 20°C) and the mean matrix temperatures on the supply and exhaust sides are nearly the same. This indicates that a constant heat of condensation can be used in the model in place of equation (2.60) (or equation (2.12)) with little loss in accuracy.

To assess the importance of uncertainties in the measured sorption isotherm, the sorption isotherm coefficients are varied (Wm = 0.1 to 0.3 and C_l = 10 to 30). The sorption isotherms that result from these different assumptions for Wm and C_l cover a wide range of Type I sorption isotherms as is evident in Figure 2.10. The effect of the assumed sorption isotherms on the predicted effectiveness of the energy wheel is presented in Figure 2.11.

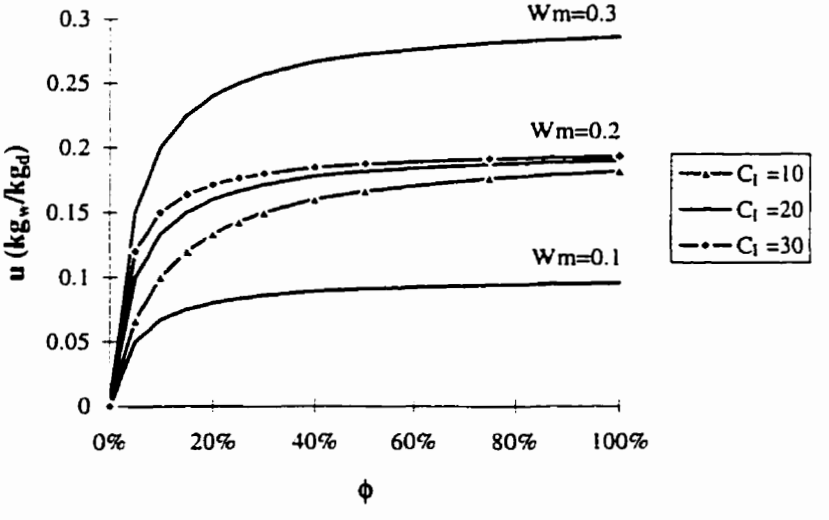

Figure 2.10. *Type I sorption isotherm with various assumptions for Wm and C_l.*

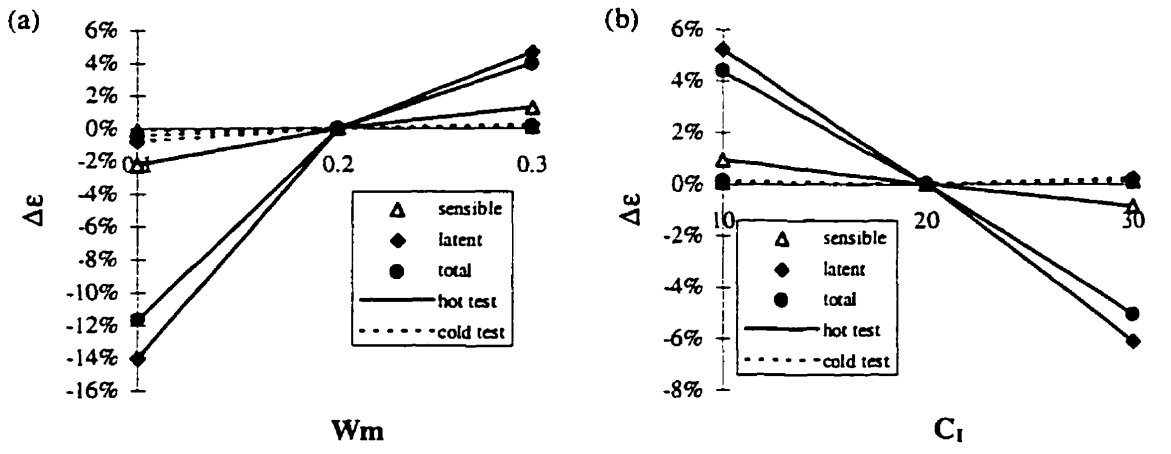

Figure 2.11. Change in effectiveness that results when (a) the maximum moisture content of the desiccant (Wm) is changed with C_l = 20 and (b) the shape of the sorption isotherm (C_l) is changed with Wm = 0.2 ($\Delta\varepsilon = \varepsilon_{\text{various Wm \& } C_l} - \varepsilon_{\text{Wm=0.2 \& } C_l=20}$).

The results in Figure 2.11 show that the effectiveness of an energy wheel is very sensitive to the sorption isotherm of the desiccant at hot and humid operating conditions but insensitive at cold and dry operating conditions. As expected, the latent (or moisture) effectiveness is the most significantly affected. Changing Wm has a larger impact on the latent effectivenesses (14%) than changing C (6%) for the range studied here. These results suggest that each climate may have a unique desiccant (sorption isotherm) that will provide optimal performance of the energy wheel.

2.7.3 Energy Rate Control Using Wheel Speed

It is known that decreasing the rotational wheel speed of energy wheels will decrease their effectiveness. Wheel speed control is, therefore, a potential method of energy (or heat) rate control and is investigated for a range of wheel speeds. The results of this study are presented in Figure 2.12.

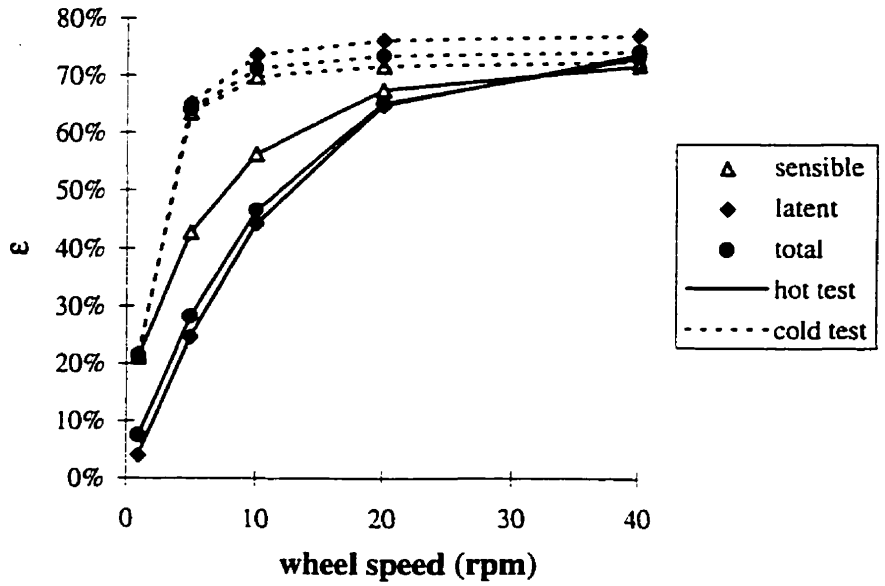

Figure 2.12. Sensible, latent and total effectivenesses as a function of wheel speed.

The trend of decreasing effectiveness with decreasing wheel speed, in Figure 2.12, is somewhat similar to regenerative wheels without desiccant coatings. However, the significant difference between the sensitivity in effectiveness to wheel speed for the hot and cold tests could make speed control difficult to use as a energy rate control method in practice. In the cold test, the sensible, latent and total effectivenesses are equally sensitive to changes in wheel speed and show a large change in effectiveness for speeds in the range of 1 to 5 rpm. On the other hand, the sensible, latent and total effectivenesses each have a different sensitivity for the hot test and show a more gradual change as the wheel speed changes over the full range of tested wheel speeds. These results show that an accurate numerical model is important to study the energy rate control of energy wheels. If the sensitivity of effectiveness to wheel speed is determined during cold test conditions, the results could not be applied to hot test conditions without significant errors. For example, reducing the wheel speed from 20 rpm to 10 rpm reduces the heat

and moisture transfer rates by 17% and 32% respectively for the hot test, but has little effect on the heat and moisture transfer rates (3%) for the cold test. Furthermore, Figure 2.12 implies that decreasing the wheel speed to control heat and moisture transfer may, under high ambient air humidity conditions, allow the supply air humidity downstream of the energy wheel to be high when the desired supply air temperature has been met. Means, other than speed control, will likely be required to control both heat and moisture transfer under part load conditions when energy wheels are used in HVAC applications.

Figure 2.12 shows that the effectiveness of an energy wheel is not solely a function of the number of transfer units for sensible energy transfer (NTU_o) and wheel speed (N) because the sensitivity of effectiveness is very different for the hot and cold tests even though NTU_o is essentially constant in all tests. The effectiveness is nearly constant for $N > 5$ rpm (0.083 cycles/s) for cold temperature conditions and $N > 20$ rpm (0.33 cycles/s) for warm conditions of ambient air. This shows that the dimensionless matrix capacity (Cr^*_o) is not the same for heat and moisture transfer and is a function of the operating conditions. This functional relationship is clarified in Chapter 4.

2.7.4 Axial Heat Conduction in the Matrix

Bahnke and Howard (1964) studied the effects of matrix axial heat conduction on the performance of rotary sensible heat exchangers and their results can be correlated as shown by Shah (1988). The effect of axial conduction in the matrix of the desiccant coated energy wheel is shown in Figure 2.13 together with the results of Bahnke and Howard (1964).

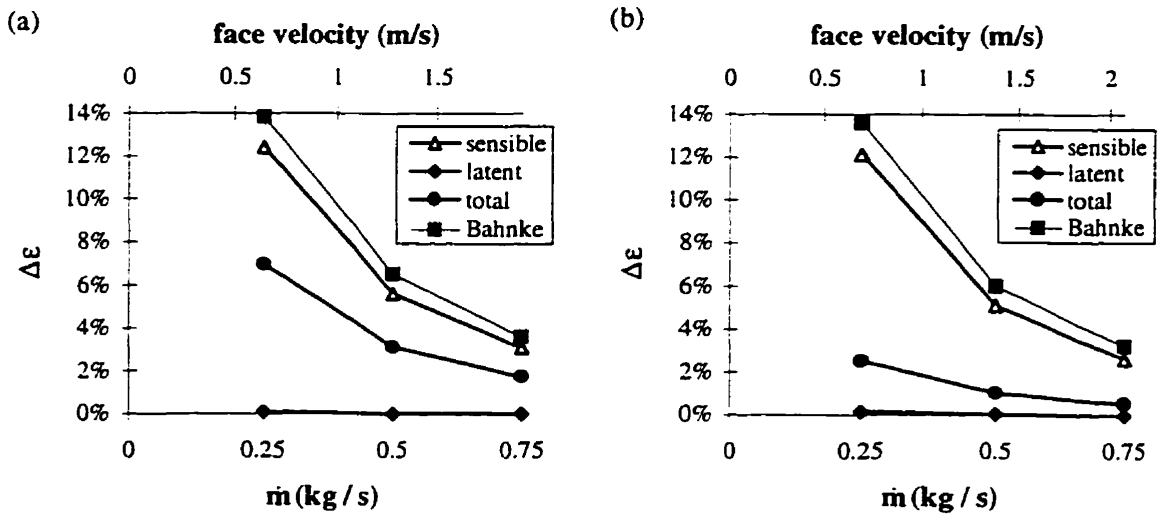

Figure 2.13. *Effect of axial conduction in an energy wheel ($\Delta\varepsilon = \varepsilon_{k=0} - \varepsilon_{k=237\,W/(m\cdot K)}$) compared to the results of Bahnke and Howard (1964) for the (a) cold and (b) hot tests.*

The results in Figure 2.13 show that the axial heat conduction through the wheel matrix is important for the energy wheel described in Table 2.2. Neglecting axial conduction will overestimate the sensible effectiveness by 6% at a flow rate of 0.5 kg/s and 12% at a flow rate of 0.25 kg/s for both the hot and cold tests. The latent effectiveness is unaffected by the axial conduction and the change in the total effectiveness lies between the changes in sensible and latent effectivenesses. In the cold test, the total effectiveness is more sensitive to axial conduction because the moisture transfer is smaller in this case. The effect of axial conduction on the sensible effectiveness is very close to the numerical results of Bahnke and Howard (1964) which indicates that their results, for sensible energy transfer, and the correlations in Shah (1988 and 1981) can be applied to desiccant coated energy wheels. Sensible effectivenesses that are calculated neglecting matrix axial conduction can be corrected to account for axial conduction using their results. On the other hand, the effect of matrix axial heat

conduction on total effectiveness is not as easily correlated because it will be a function of both the heat and moisture transfer. These results imply that models for energy wheels need to include axial heat conduction corrections, especially when the face velocity or mass flux is low.

2.7.5 Storage in the Air

The transient storage of energy and moisture in the air is often neglected in the analysis of rotary sensible heat exchangers and rotary dehumidifiers because it is deemed negligible compared to the storage of energy and moisture in the matrix. To study the effect of this assumption for energy wheels, the governing equations, which include storage in the air, are altered slightly. The transient terms in the energy equation for the air (i.e., equation (2.1)) and the conservation of mass equations for the air (i.e., equations (2.5) and (2.6)) are removed from the model when energy and moisture storage in the air are neglected. The results of this sensitivity study are presented in Figure 2.14 where the difference between the effectiveness calculated when storage is included and effectiveness calculated when storage is neglected is presented for a range of wheel speeds.

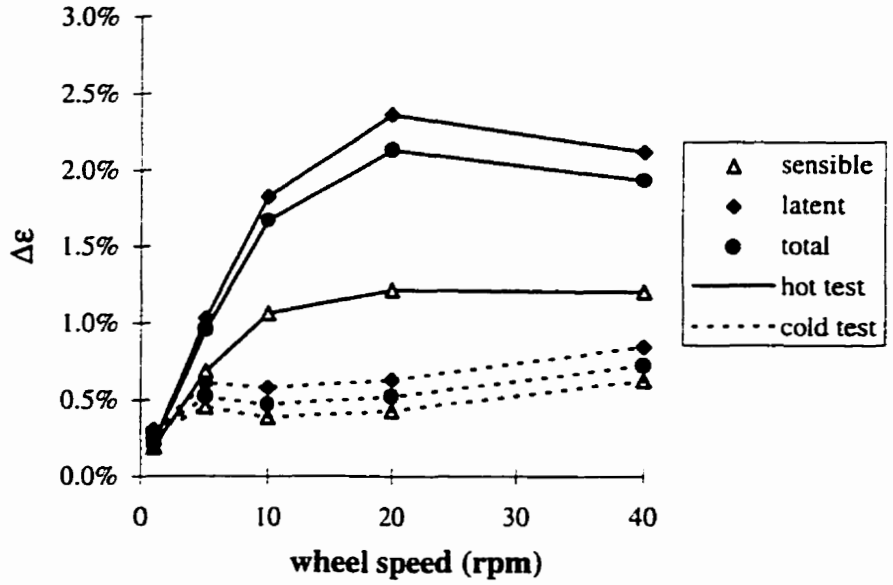

Figure 2.14. *Change in the predicted effectiveness of an energy wheel when energy and moisture storage in the air are neglected at various wheel speeds* ($\Delta\varepsilon = \varepsilon_{\text{including storage}} - \varepsilon_{\text{neglecting storage}}$).

Figure 2.14 shows that the errors in the predicted effectiveness that result from neglecting the storage of energy and moisture in the air stream are larger for the hot test than for the cold test. At a typical operating speed of 20 rpm, the errors in the predicted effectiveness that result from neglecting the storage of energy and moisture in the air stream are 1.2% for ε_s, 2.4% for ε_l, and 2.1% for ε_t. In all cases, the change in ε_t lies between the changes in ε_s and ε_l. The importance of storage in the air generally increases as the wheel speed increases because, as the wheel speed increases, the cyclic period decreases and the transients become more important. Furthermore, including the transient term in the governing equations is similar to including the effect of carry-over leakage which generally increases with rotational speed (but not proportionally because the effect of carry-over leakage is a function of both the wheel speed and the effectiveness of the energy wheel). At wheel speeds typically used in rotary dehumidifiers

(~0.2 rpm), neglecting storage in the air stream will have a very small effect on the predicted effectiveness (< 0.3%). This is not the case for energy wheels, which have wheel speeds of about 20 rpm.

2.7.6 Entry Length

All of the previous results include the increased heat and mass transfer in the hydrodynamic and thermal entry length region for the air entering each pore of the matrix. In order to assess the importance of including the entry length, simulations are performed where the increased heat and mass transfer coefficients in the thermal entry length region are neglected. Figure 2.15 shows the effect of neglecting the entry length on the predicted effectiveness as a function of the flow rate of air.

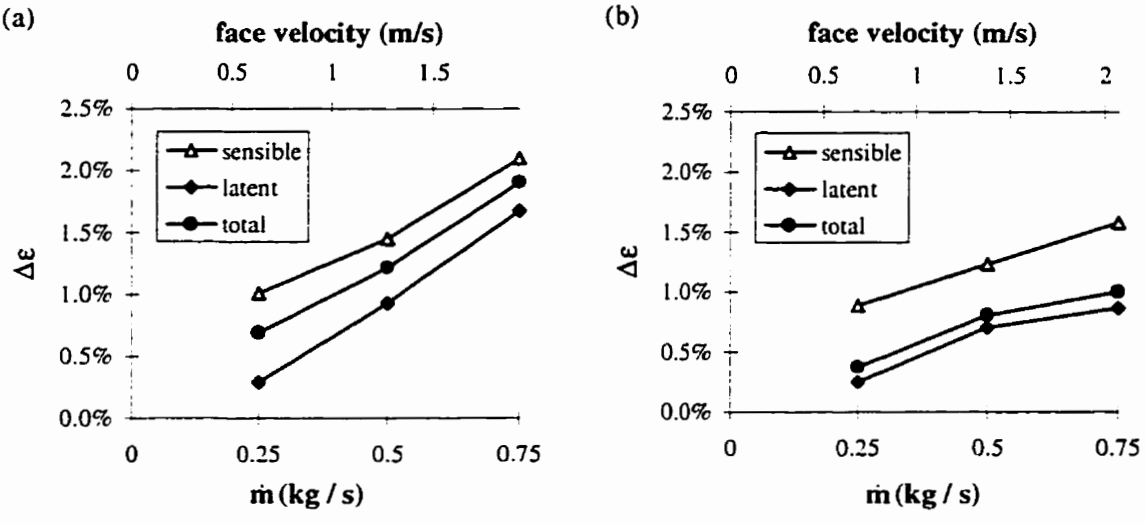

Figure 2.15. *Effect of neglecting the entry region as a function of the flow rate of air through the energy wheel ($\Delta\varepsilon = \varepsilon_{\text{including entry length}} - \varepsilon_{\text{neglecting entry length}}$) for (a) the cold test and (b) the hot test.*

It can be seen in Figure 2.15 that neglecting the entry length reduces the predicted sensible effectiveness by as much as 2% for a mass flow rate of 0.75 kg/s for the cold test

and slightly lower for the hot test. As mass flow rate decreases, the importance of the entry length also decreases because, for laminar flow, the size of the entry region decreases as mass flow rate decreases. At the design mass flow rate of 0.5 kg/s (1.3 m/s face velocity), the errors that result from neglecting the entry length can be as high as 1.5%.

Neglecting the entry length will result in an under prediction of the effectiveness because the convective heat and mass transfer coefficients are higher in the entry region. The question arises as to whether the predicted effectiveness will be the same as that predicted when the entry length is correctly accounted for in the analysis, if the heat and mass transfer coefficients are increased to reflect this increase but kept constant throughout the energy wheel. To study this, the average convective heat (and similarly mass) transfer coefficient is defined as,

$$h_{ave} = \frac{1}{L}\int_0^L h(x)dx \quad . \tag{2.63}$$

Figure 2.16 shows how increasing the average heat and mass transfer coefficients, to account for the entry region, changes the predicted effectiveness as a function of the flow rate of air.

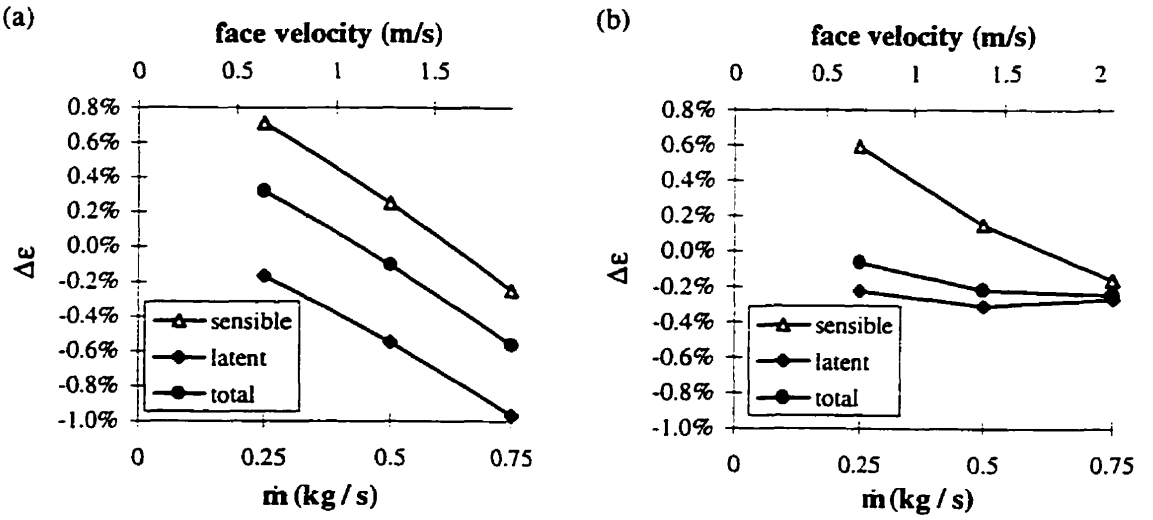

Figure 2.16. *The effect of increasing the average heat and mass transfer coefficient to approximate the entry length* ($\Delta\varepsilon = \varepsilon_{\text{using } h(x)} - \varepsilon_{\text{using } h_{ave}}$) *for the (a) cold and (b) hot tests.*

The results in Figure 2.16 show that the error in effectiveness is reduced when the entry length is approximated by increased (but constant) heat and mass transfer coefficients. The errors, however, can still be as large as 1%. It is expected that using h_{ave} in place of h(x) would result in a higher effectiveness because the convective heat and mass transfer coefficients will be higher at the airflow outlet of each pore in the wheel which tends to affect the outlet conditions and thus the effectiveness. This is the case for the latent effectiveness, however, the sensible effectiveness is sometimes greater when using h_{ave} and sometimes greater when using h(x). The reason for this is likely axial conduction in the matrix which affects the sensible effectiveness but not the latent effectiveness. To show that this is the case, the simulations of Figure 2.16 are repeated with the matrix thermal conductivity set equal to zero and the results are presented in Figure 2.17.

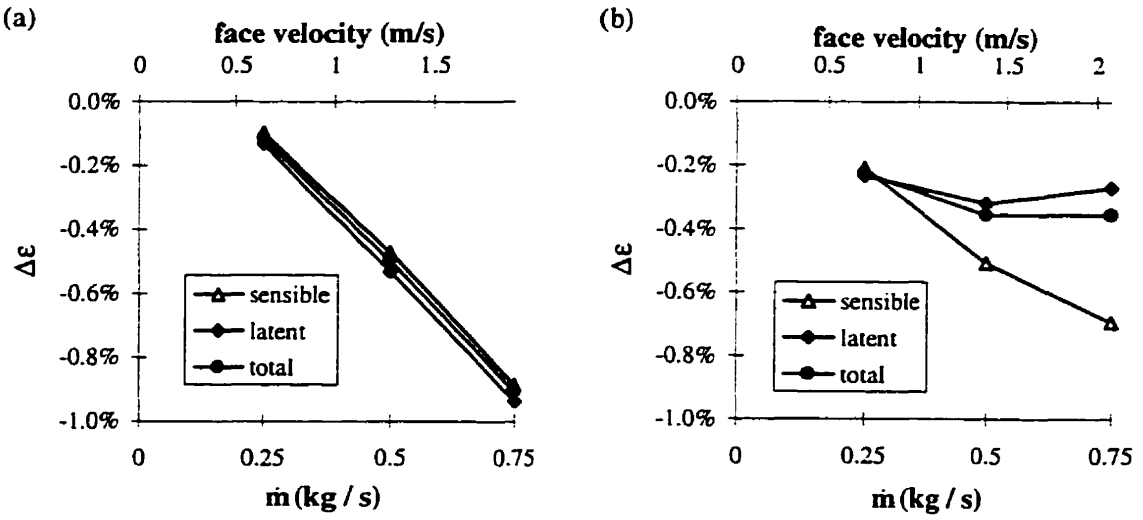

Figure 2.17. *The effect of increasing the average heat and mass transfer coefficient to approximate the entry length when the matrix thermal conductivity is set equal to 0 for (a) the cold test and (b) the hot test* ($\Delta\varepsilon = \varepsilon_{\text{using h(x)}} - \varepsilon_{\text{using h}_{ave}}$).

The results in Figure 2.17 show that the predicted effectiveness is greater when using h_{ave} than when using h(x) for all three effectivenesses as expected. The change in all three effectivenesses in the cold test and the sensible effectiveness in the hot test are nearly all equal. This indicates that the dimensionless matrix capacity (Cr^*_o) is essentially the same for these cases because changes in the assumptions concerning the entry region are similar to changes in the number of transfer units (NTU_o) of the energy wheel. The change in the latent and total effectivenesses for the hot test are significantly lower, indicating that Cr^*_o is lower as well. This shows that the operating conditions of the energy wheel affect the dimensionless groups that are widely used for sensible heat exchangers and that the dimensionless group for heat transfer may not be the same as the dimensionless groups for moisture transfer. These effects are further investigated in Chapter 4 where the governing dimensionless groups for energy wheels are developed from the governing equations.

To summarize, approximating the entry length by simply increasing the average convective heat and mass transfer coefficients to reflect the entry length as in equation (2.63) will result in errors in the order of 1%, while neglecting the entry length will result in errors in the order of 2%.

2.8 SUMMARY

In this chapter, a numerical model that predicts the heat and moisture transfer during sorption, condensation and frosting processes in energy wheels has been developed from physical principles. All the assumptions are explained and justified. The model is one dimensional and transient and is developed in a general manner to help determine the importance of certain assumptions on the predicted performance of energy wheels. This model of energy wheels can been used to predict the sensible, latent and total energy effectivenesses for different wheel designs and operating conditions. The uncertainty in the numerically predicted effectiveness (including only the numerical accuracy) is less than ±0.5%. The total uncertainty, which also includes the input data uncertainties, is expected to be less than ±3% for ε_s, ±5% for ε_l, and ±3% to ±5% for ε_t. These numerical uncertainties are verified in Chapter 3 by comparison with experiments.

The governing energy equations used in the model are developed in a distinct way to include the fact that the energy released during moisture transfer processes can be delivered to the air, matrix or both. This has a significant effect on the performance of energy wheels with thin desiccant coatings because the energy transfer due to phase change in energy wheels can be up to six times greater than the energy transfer due to

advection through the energy wheel for hot and humid operating conditions. The latent effectiveness is nearly unaffected by assumptions concerning the energy of phase change, but the sensible effectiveness is affected by 12% for the cold test conditions and 48% for hot test conditions selected for investigation. As a result of this large effect, the governing equations that describe the energy transfer in the air and matrix must accurately include these effects. The method used to estimate the fraction of phase change energy that enters the air is based on a boundary condition derived from the analytical solution to heat generation between two solids. This boundary condition needs further research.

Including a variable heat of sorption and the resulting temperature dependent isotherm in the model has a small effect (less than 0.5%) on the predicted performance. As a result, a constant heat of vaporization and a temperature independent sorption isotherm will be used throughout the rest of this thesis. However, the maximum moisture content of the desiccant and the shape of the sorption isotherm have a significant influence on the latent effectiveness and must be modeled accurately.

Simulation results show that the sensible, latent and total effectivenesses all decrease as wheel speed decreases. The results suggest that wheel speed control may not be a practical means of controlling both the heat and moisture transfer in energy wheels because the change in each effectiveness is a non-linear and different function of the operating conditions and wheel speed. For example, reducing the wheel speed from 20 rpm to 10 rpm, reduces the energy rate by 30% for hot test conditions, but reduces the energy rate by only 3% for the cold test conditions examined in this chapter.

Axial conduction through the matrix is very important for the energy wheel studied in this chapter. At design operating conditions, neglecting axial conduction will lead to errors of 6% and 3% in the predicted sensible and total effectivenesses respectively. Close agreement between the numerical results and those of Bahnke and Howard (1964), shows that the effect of axial conduction on the sensible effectiveness can be calculated using the correlations given by Shah (1988 and 1981). This fact will be further exploited in Chapter 4 to correlate energy wheel effectiveness.

The simulations presented in this chapter show that the storage of energy and moisture in the air is moderately important at the typical wheel speeds of energy wheels. Neglecting transient storage in the air can lead to errors in the predicted effectivenesses of 0.8% and 2.4% for the investigated cold-dry and hot-humid test conditions respectively. The storage of energy and moisture in the air will be included in all simulation results in this thesis except for those presented in Chapter 4 to develop effectiveness correlations.

The entry region in an energy wheel is also found to affect the predicted performance only slightly. For the test conditions in this chapter, neglecting the entry region underpredicts the effectiveness by 2% while increasing the average heat and mass transfer coefficients to reflect the entry region overpredicts the effectiveness by 1%. Therefore, the entry region will be neglected in the simulation results of Chapter 4 to facilitate the correlating of effectiveness, but will be included throughout the rest of the thesis.

CHAPTER 3

EXPERIMENTAL VALIDATION AND EXTRAPOLATION

The purpose of this chapter is to validate the numerical model, presented in Chapter 2, with measured data for a commercial energy wheel and to extrapolate these results to other operating conditions. The experimental and numerical results, combined with uncertainty analysis, quantify the performance of energy wheels for a wide range of operating temperatures, humidities and flow rates. Both balanced and unbalanced supply and exhaust flow rates are investigated in the laboratory experiments while the field experiments include only balanced flow rates. The model is validated for cold (-10°C and -20°C) and hot (40°C) supply air temperatures with both high and low humidities.

3.1 LABORATORY EXPERIMENTS

The laboratory experiments were conducted by Dustin Ciepliski and are reported in detail by Ciepliski (1997) and Simonson et al. (1998a). The energy wheel used in the laboratory experiments (Table 3.1) was divided into quadrants and the air flowed through opposite quadrants (Figure 3.1). This reduced the cross-over leakage between the two air streams and also reduced the required flow rate of air and consequently the size of the heating and cooling equipment and fans. Four fans were used in the tests to keep the pressure at the wheel near atmospheric pressure and thus minimize the leakage between the air streams and between the air streams and the surroundings (Figure 3.2). Leakage

was measured by tracer gas tests to be usually less than 2% and always less than 4% of the flow rate for the complete range of flow rates.

Table 3.1. Properties of the energy wheel used in the laboratory and field experiments.

WHEEL	M = 13.5 kg	L = 0.102 m	D = 0.92 m
speed = 20 rpm	$D_h = 1.20 \times 10^{-3}$ m	porosity = 82%	Nu = 2.39 (fully developed)
DESICCANT	ρ = 350 kg/m3	Cp = 615 J/(kg·K)	mass fraction = 22%
$\sigma_d = 0.69$	Wm = 0.13	$C_l = 40$	$\eta = 0.05$

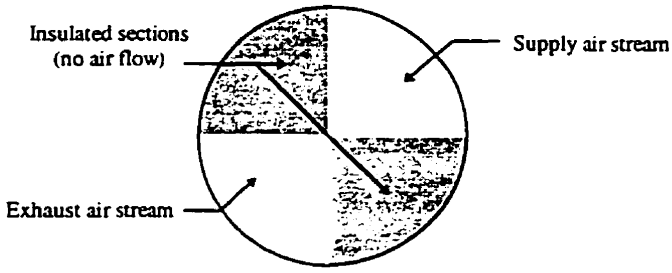

***Figure 3.1.** Schematic diagram of the energy wheel showing the dividing of the flow.*

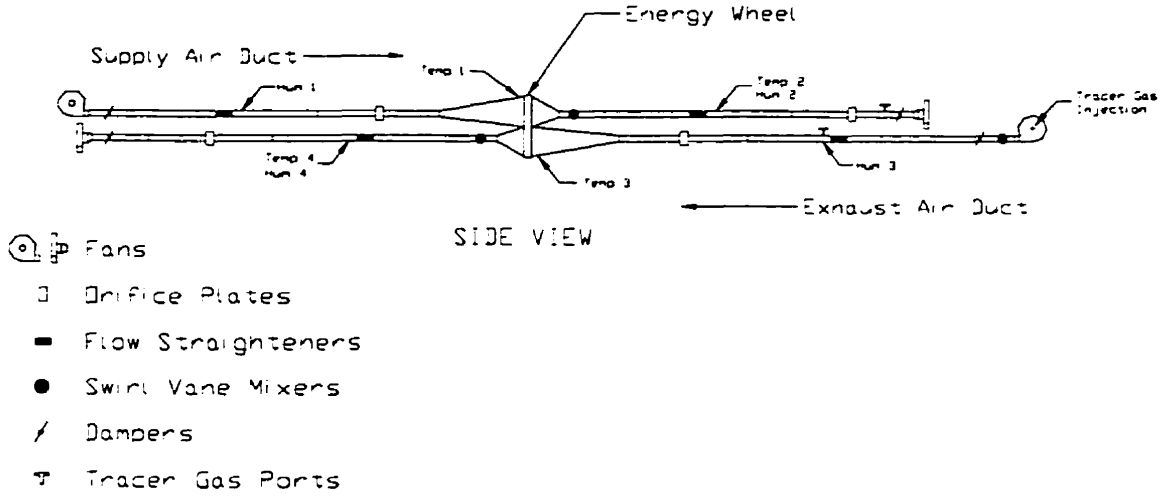

***Figure 3.2.** The laboratory-test facility.*

The measurements were performed in accordance with ANSI/ASHRAE Standard 84-1991 but with slight modifications. These modifications did not increase the

uncertainty in the calculation of each effectiveness (sensible, latent and total energy) (Ciepliski et al., 1998). Air flow rate measurements were done with orifice plates designed according to ISO Standard 5167-1 (1991) and humidity measurements were done with capacitance and resistance relative humidity sensors that were calibrated against a chilled mirror dew point sensor and aqueous salt solutions (ASTM Standard E 104-85). Temperature was measured with type T thermocouples calibrated with a thermocouple simulator to ±0.1°C. To improve accuracy, the average of three thermocouple readings were used at each station. The bias and precision uncertainties of each measurement is shown in Table 3.2. Experimental tests were run until steady state conditions were achieved and then more than 30 time averaged data points were recorded to disk. During any test, inlet temperatures, humidities and flow rate variations were less than ±0.5°C, ±1% R.H. and ±0.5% respectively.

Table 3.2. *Bias and precision uncertainties for each measurement in the laboratory test.*

Measurement	Bias Uncertainty	Precision Uncertainty
barometric pressure	35 Pa	35 Pa
temperature	0.2 K	0.1 K
relative humidity	2% R.H.	1% R.H.
mass flow rate of air	2 - 5%	1%

The uncertainty of the measured effectiveness depends on the bias and precision uncertainties of the sensors for flow, temperature, humidity and barometric pressure and the difference between the supply and exhaust temperatures, humidity ratios and enthalpies. The uncertainty in the measured effectiveness was determined with the

method outlined in ANSI/ASME Standard PTC 19.1-1985 using the 95% uncertainty limits with the added requirement that all the data must satisfy mass (dry air and water vapor) and energy balances within the experimental uncertainty limits as determined using the on-line data acquisition and analysis system.

3.1.1 Cold Tests

The cold tests represent typical operating conditions in cold climates during winter. The dry indoor conditions are representative of dry indoor air within office buildings, apartment buildings or houses and the humid indoor conditions are representative of hospitals, museums and possibly leisure complexes. For all tests, the supply and exhaust inlet dry air mass flow rates are equal unless specified. The test conditions for the cold tests are given in Table 3.3 and shown on a psychrometric chart in Figure 3.3. It should be noted that the values in Table 3.3 and Figure 3.3 are averages for the six different flow rates tested. Individual tests may have conditions that vary by ±1°C and ±5% R.H. from the average. The exact experimental supply and exhaust inlet temperature and humidity conditions are used in all calculations of experimentally determined effectivenesses and in the numerical model. An atmospheric pressure of 96 kPa is used in the numerical model to represent that measured in the experiments. Flow through half of the energy wheel is also taken into account in the model.

Table 3.3. *Temperature and humidity inlet conditions for the cold tests.*

Test	supply air conditions		exhaust air conditions	
	T (°C)	ϕ	T (°C)	ϕ
-10°C (dry)	-10	50%	23	10%
-10°C (humid)	-10	50%	26	45%
-20°C (dry)	-20	50%	24	12%
-20°C (humid)	-20	50%	26	40%

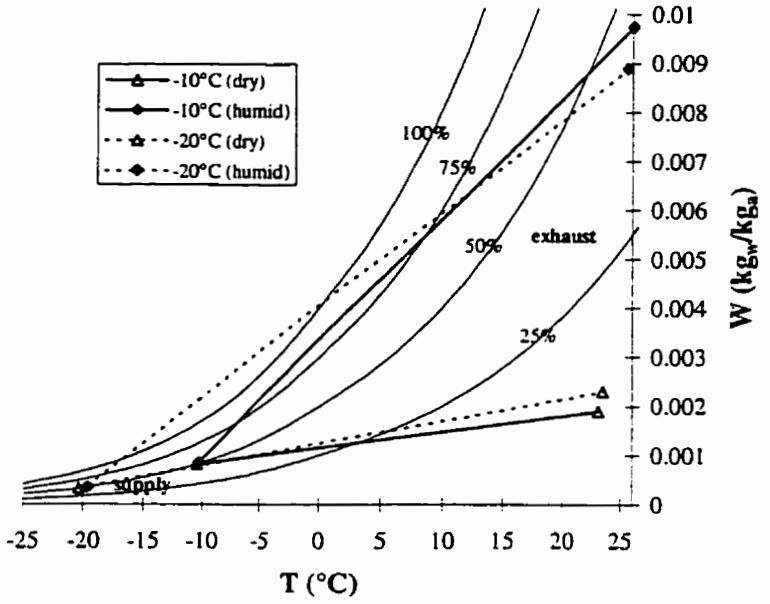

Figure 3.3. *Supply and exhaust inlet conditions for the energy wheel in the cold tests.*

Figure 3.4 contains a comparison between the measured and simulated effectivenesses when the supply temperature is -10°C. The 95% uncertainty limits are shown for effectiveness because it is the prime variable of this research. Experimental uncertainties are calculated according to ANSI/ASME Standard PTC 19.1-1985 as,

$$U_\varepsilon = \left[B_\varepsilon^{\,2} + P_\varepsilon^{\,2}\right]^{1/2}, \tag{3.1}$$

where B_ε and P_ε represent the bias and precision uncertainties for 95% coverage. The bias in effectiveness (B_ε), for example, is calculated from the bias in each individual measurement (B_i) as,

$$B_\varepsilon = \left[\sum_{i=1}^{n} (S_i B_i)^2 \right]^{1/2} \tag{3.2}$$

and the precision uncertainty (P_ε) is calculated similarly. The sensitivity coefficient (S_i) in equation (3.2) indicates the sensitivity of B_ε to the bias in measurement (χ_i) and is determined by,

$$S_i = \frac{\partial \varepsilon}{\partial \chi_i} . \tag{3.3}$$

The detailed calculations and experimental uncertainties for the laboratory tests are reported by Ciepliski (1997). The numerical uncertainties in Figure 3.4 are determined using equation (3.1) as well. In this case, B represents the uncertainty in the input property data and P represents the uncertainty in the numerical algorithm. The sensitivity coefficients for the numerical model are determined from the sensitivity studies in Section 2.7. As discussed in Chapter 2, the uncertainty in the simulated effectiveness for an existing energy wheel is ±3% for ε_s, ±5% for ε_l and between ±3% and ±5% for ε_t.

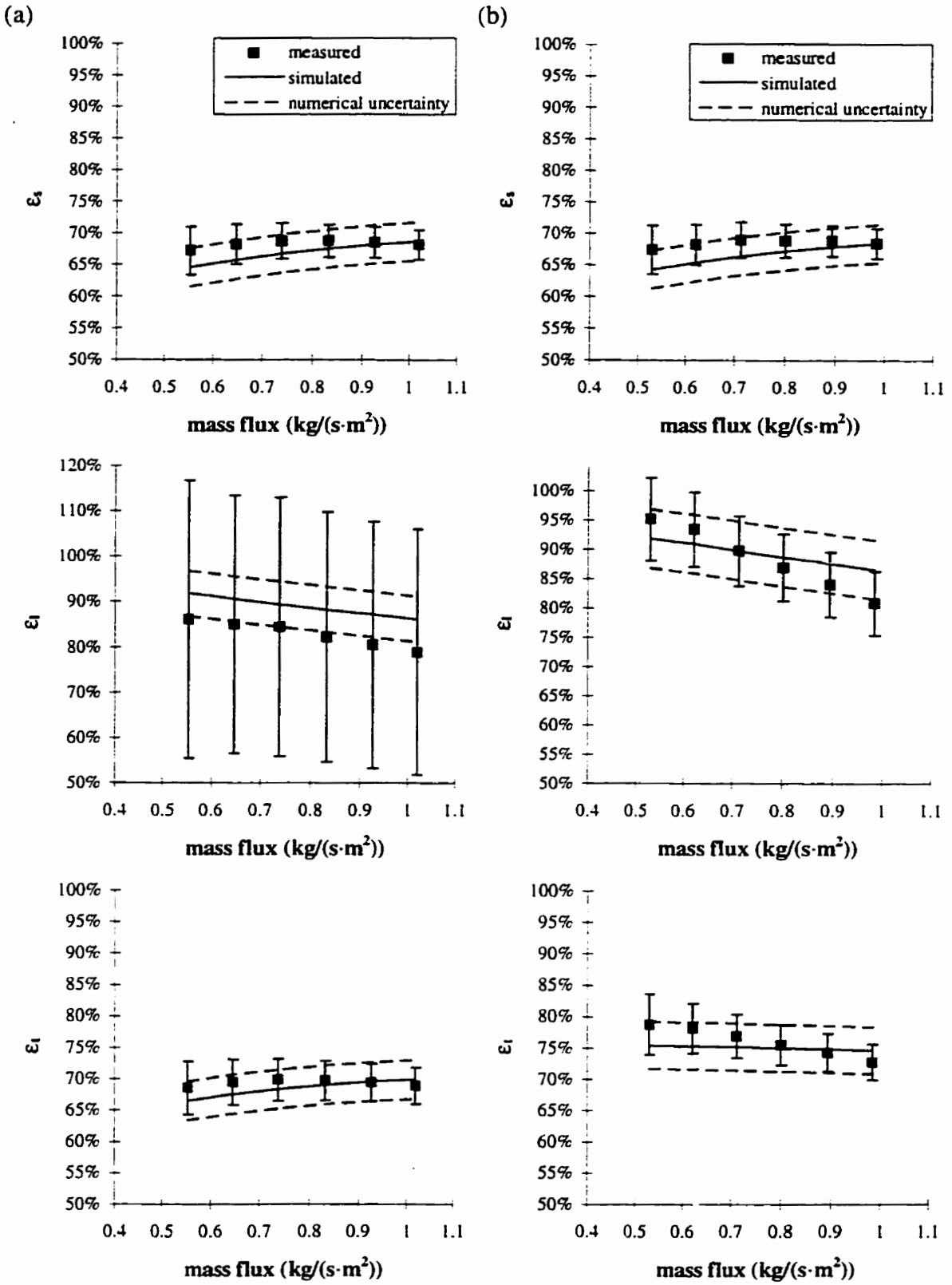

Figure 3.4. *Comparison of simulated and measured effectivenesses for a supply inlet temperature of -10°C and exhaust inlet conditions that are (a) dry and (b) humid. (Error bars indicate the 95% uncertainty in measured data.)*

The results in Figure 3.4 show good agreement between measured and simulated effectivenesses for both the dry and humid exhaust conditions. The simulated effectivenesses are well within the 95% uncertainty limits of the experiment and show the same trends as the measured data. Similarly, the experimental data points are within the uncertainty limits of the numerically predicted effectiveness. In Figure 3.4, the average difference between the measured and simulated effectivenesses is 1.5% for sensible effectiveness, 3.5% for latent effectiveness and 0.9% for total effectiveness. The maximum difference between the measured and simulated effectivenesses is also small for each of the three effectivenesses (3% for ε_s, 7% for ε_l and 3.5% for ε_t).

Figure 3.4 shows large experimental uncertainties in the latent effectiveness for the dry test because the difference between the supply and exhaust humidity is small. Despite the large measurement uncertainty, the measured and simulated latent effectivenesses are quite close for this case and within the expected uncertainty of the numerical model. This shows that the uncertainty in the numerically predicted effectiveness for an existing energy wheel is often smaller than the uncertainty in experimental data. Furthermore, the estimated numerical uncertainties are nearly constant for each test condition (i.e., $\pm 3\%$ for ε_s, $\pm 5\%$ for ε_l and $\pm 3\%$ to $\pm 5\%$ for ε_t) and therefore only the experimental uncertainty limits will be included in the remaining figures in this chapter.

Increasing the mass flux through the wheel tends to increase the sensible effectiveness in Figure 3.4 which is different than that expected for sensible counter flow

heat exchangers with constant overall heat transfer coefficients. The sensible effectiveness increases with mass flow rate because axial heat conduction through the wheel matrix is important for the energy wheel tested (see Section 2.7.4). The latent effectiveness decreases with increased flow rate for all cases; whereas, the total effectiveness increases for the dry test, but decreases for the humid test. The reason for this contrary response for dry and humid conditions is that the moisture transfer has a larger effect on the total effectiveness in the humid test than in the dry test.

Comparison of the dry and humid tests shows that the sensible effectiveness is almost the same for both tests. The latent effectiveness is higher in the humid test because the air in the energy wheel becomes saturated for a small time during the wheel rotation. Saturation conditions tend to increase the latent effectiveness as will be shown in Chapter 5. Total effectiveness values are between the sensible and latent effectiveness values. The total effectiveness is nearly equal to the sensible effectiveness for the dry case because there is little moisture transfer, but is 5 to 10% greater for the humid case because there is significant moisture transfer.

The agreement between the measured and simulated average outlet conditions for the -10°C tests can be seen in Figure 3.5. Figure 3.5 contains results for dry and humid inlet conditions with a balanced mass flux of 1.0 kg/(s·m^2) and clearly displays good agreement between the simulated and measured outlet properties. It is noted that the outlet conditions are nearly on a line connecting the supply inlet and exhaust inlet for the

dry test conditions in Figure 3.5(a) but not for the humid test conditions in Figure 3.5(b) where large rates of moisture transfer occur.

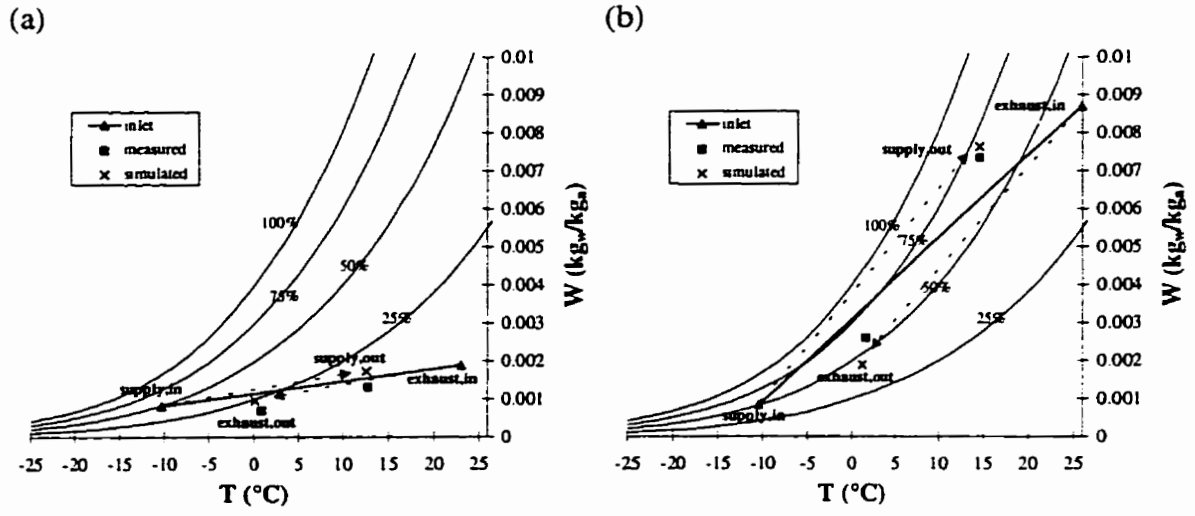

Figure 3.5. *Average supply and exhaust inlet and outlet conditions for the -10°C tests with (a) dry and (b) humid indoor conditions. The mass flux is 1 kg/(s·m^2).*

A comparison between the measured and simulated results for the -20°C tests are contained in Figures 3.6 and 3.7. The agreement is acceptable in all cases, especially when the uncertainties in the simulated effectivenesses are considered.

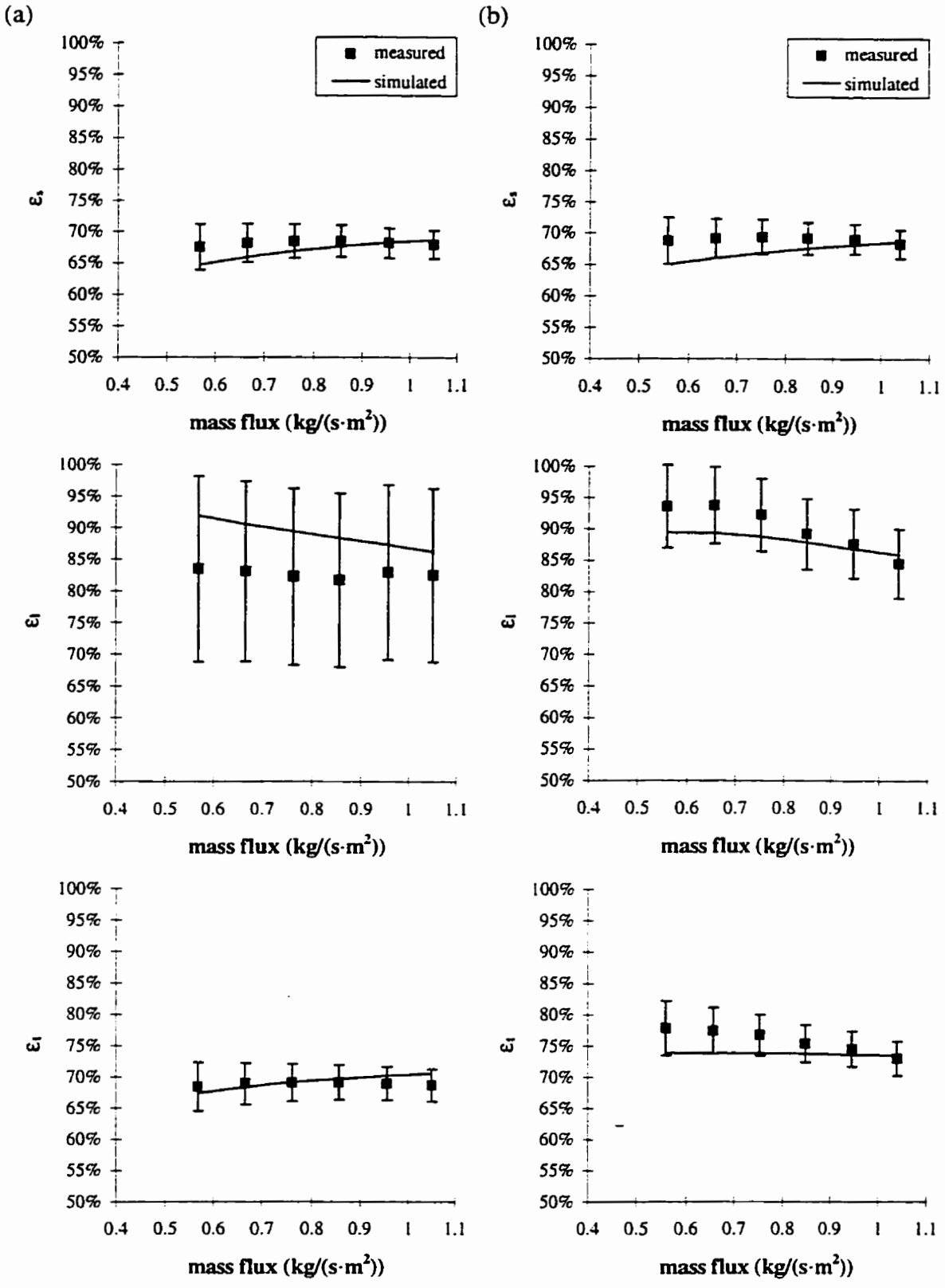

Figure 3.6. Comparison of simulated and measured effectivenesses for a supply inlet temperature of -20°C and exhaust inlet conditions that are (a) dry and (b) humid. (Error bars indicate the 95% uncertainty in measured data.)

The agreement between the measured and simulated effectiveness in Figure 3.6 is quite good. The simulated effectivenesses fall within the 95% uncertainty limits for all but a few test cases and are well within the 99% uncertainty limits (not shown). Again the measured latent effectiveness for the dry test has large uncertainties because the difference between the humidity of the supply and exhaust air streams is small. The sensitivity of effectiveness to the mass flow rate is the same as in the -10°C tests. Differences between the dry and humid tests are also similar to those shown in Figure 3.4. The simulated outlet temperature and humidity ratios, shown in Figure 3.7, correspond well with the measured values.

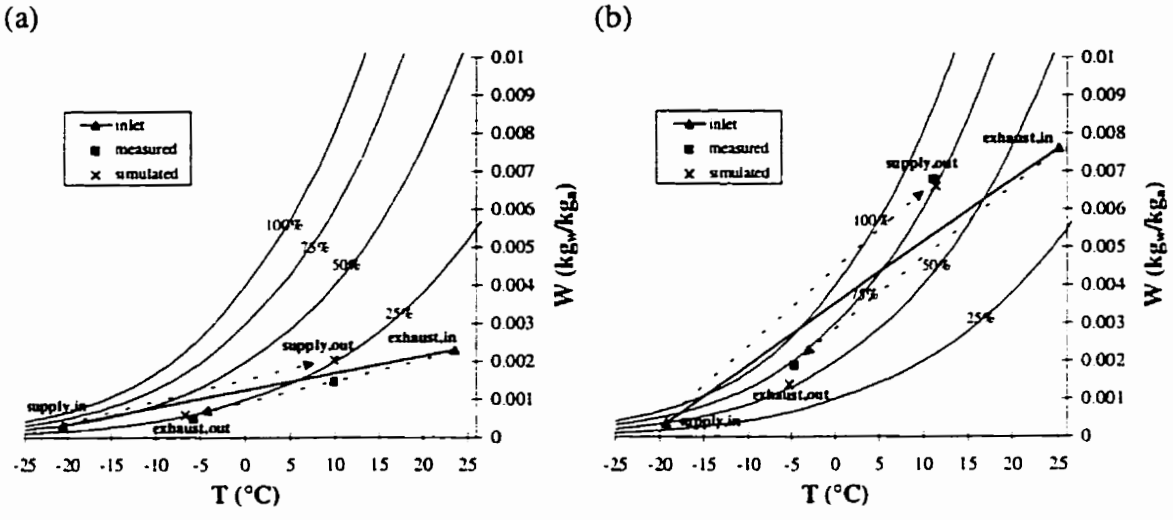

Figure 3.7. Average supply and exhaust inlet and outlet conditions for the -20°C tests with (a) dry and (b) humid indoor conditions. The mass flux is 1 kg/(s·m²).

It is noted that the supply air inlet and outlet properties in Figure 3.7(b) suggest that this air may be going through a super saturation process from inlet to outlet. This is most unlikely; however, the surfaces of the matrix and the air within the wheel experience condensation and evaporation as the supply air flows from one side of the wheel to the

other. On the exhaust side there is no condensation effects. The numerical model includes these physical processes and predicts uncontrolled frosting for these operating conditions at frost blockage rates of 0 to 12% per hour depending on the flow rate. The blockage rate of the wheel was not measured in the experiments but seemed to be small because the flow rate was constant during the four hours of cold testing. These results also help to confirm the numerical model.

3.1.2 Hot Tests

Hot operating conditions are important for energy wheels because the potential savings are the greatest during these conditions. For the hot tests studied here, the average supply and exhaust inlet conditions for the six flow rates (balanced) are given in Table 3.4 and shown on a psychrometric chart in Figure 3.8. These test conditions represent a range of outdoor conditions from hot and very humid to hot and very dry. A test is also run with hot and dry outdoor conditions in conjunction with humid indoor conditions that may be typical for office buildings in hot dry climates where evaporative cooling can be used because the indoor and outdoor air have nearly the same enthalpy.

Table 3.4. Temperature and humidity inlet conditions for the hot tests.

Test	supply air conditions		exhaust air conditions	
	T (°C)	ϕ	T (°C)	ϕ
dry	40	4%	23	15%
humid	40	86%	22	14%
dry-humid	40	4%	26	40%

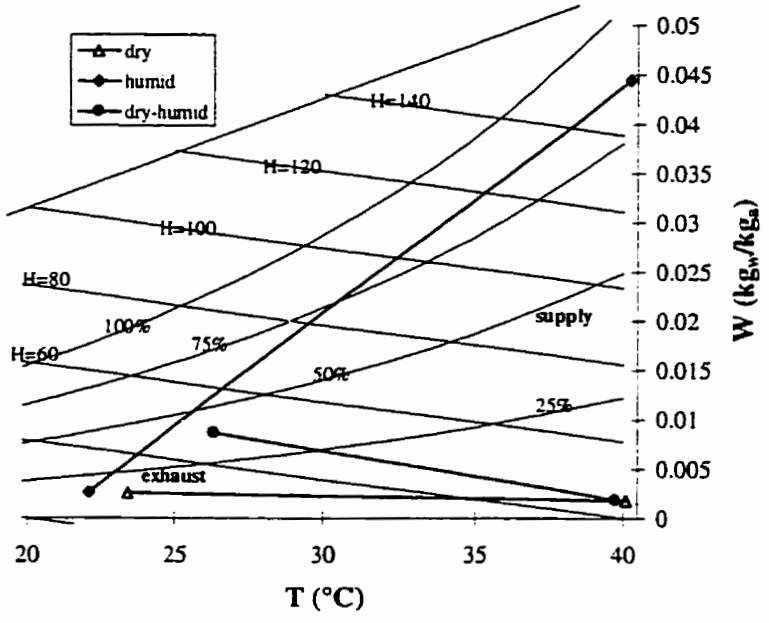

Figure 3.8. *Supply and exhaust inlet conditions for the energy wheel in the hot tests.*

Figures 3.9 and 3.10 compare the measured and simulated results for the dry and humid tests. The agreement is good and generally within the experimental uncertainty for both the dry and humid test conditions.

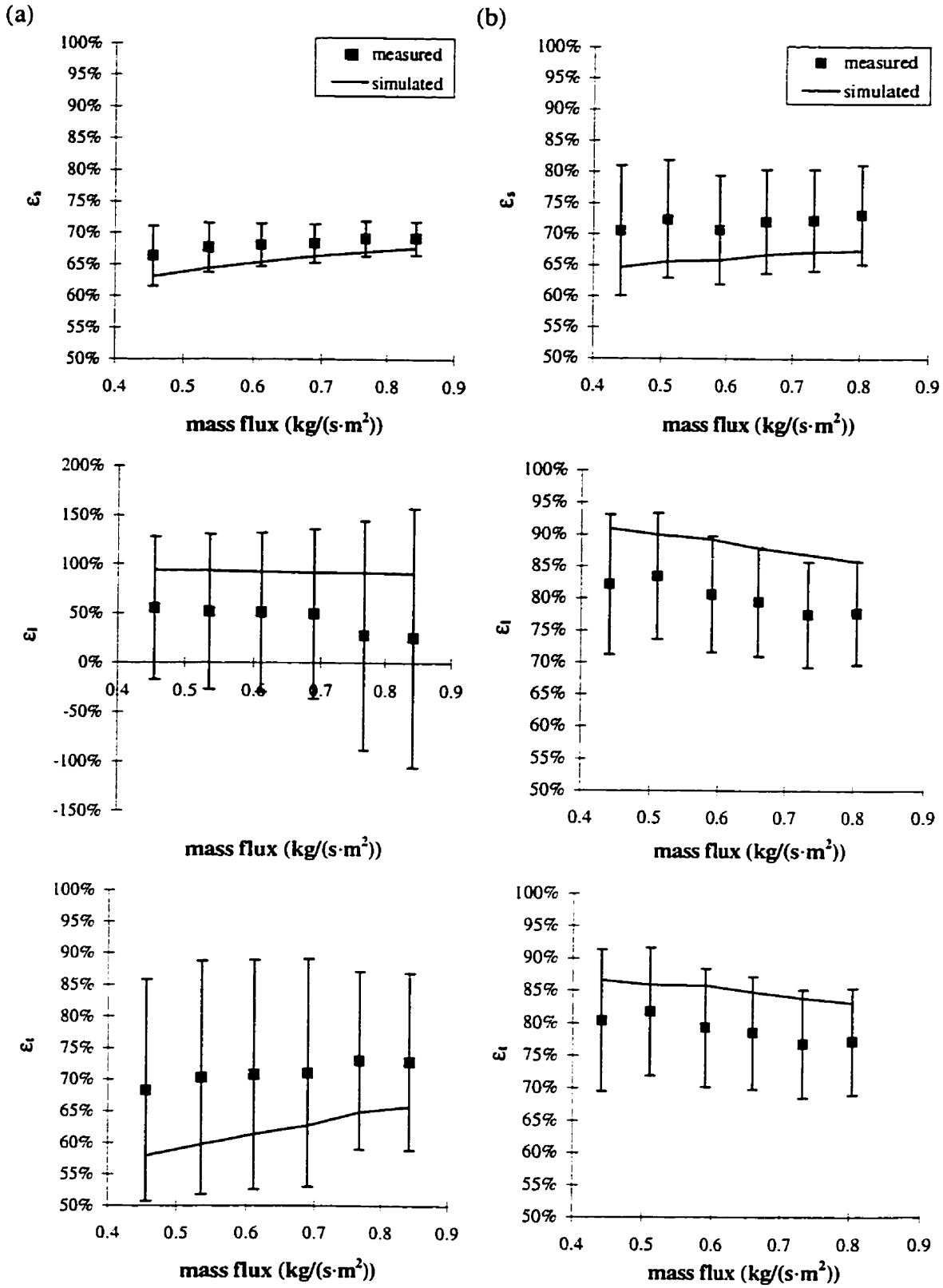

Figure 3.9. Comparison of simulated and measured effectivenesses for the hot tests with (a) dry and (b) humid operating conditions.
(Error bars indicate the 95% uncertainty in measured data.)

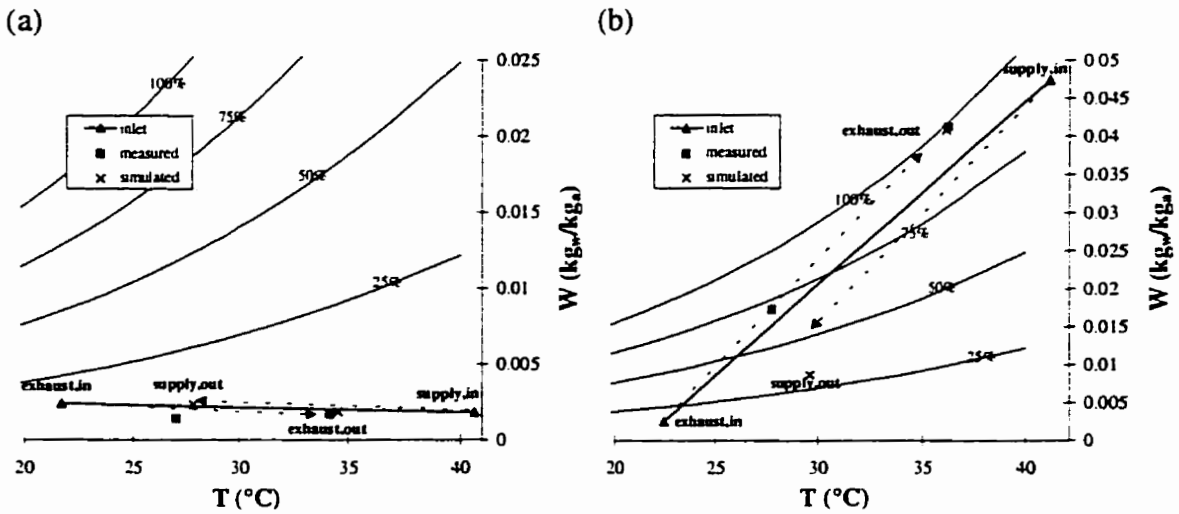

Figure 3.10. *Average supply and exhaust inlet and outlet conditions for the (a) dry and (b) humid hot tests with supply and exhaust mass fluxes of 0.8 kg/(s·m^2).*

The measured and simulated outlet temperature and humidity ratios for the tests in Figure 3.10 compare well for the dry test and satisfactorily for the humid test. Since the humid tests have inlet relative humidities generated by hot steam in the order of 90% R.H., condensation in the energy wheel and on the pipes of the experiment is possible. Condensation in the connecting pipes of the experiment would result in additional systematic errors. In fact, when the experiment was dismantled after the hot tests, condensation was clearly evident in the piping system. The uncertainty limits in Figure 3.9(b) reflect this.

In the humid tests, saturation conditions existed in the energy wheel and water was observed running off the wheel after about 3 hours of testing. The numerical model predicts run-off after about 8 hours if the moisture content in the desiccant remains uniform due to capillary and drag forces and the maximum moisture content before run-off is 1 kg/kg. Axial movement of water in the desiccant is neglected in the model and

therefore excess moisture accumulation is predicted very near the supply inlet. Comparing the numerical and experimental results shows that capillary and drag forces may cause the condensed water to move axially in the energy wheel. The excess moisture is likely distributed over about 1/3 of the energy wheel before water begins to run off the wheel with increasing amounts towards the end of the supply cycle (i.e., near $\theta = 180°$).

Comparing the hot and cold test shows that in the hot and dry tests, the effectivenesses values are similar to those in the cold and dry tests because the moisture transfer is small in both cases. The variation of effectiveness as a function of mass flux is also the same; the sensible and total effectivenesses increase slightly with increasing flow rate, but the latent effectiveness decreases with increasing flow rate. In the hot and humid tests, only ε_s increases with flow rate, while ε_l and ε_t decrease with increasing flow rate as was found in the cold and humid tests.

The enthalpy of the supply and exhaust inlet air streams are nearly the same in the dry-humid tests. Measured and simulated effectivenesses for this unique test case are in Figure 3.11.

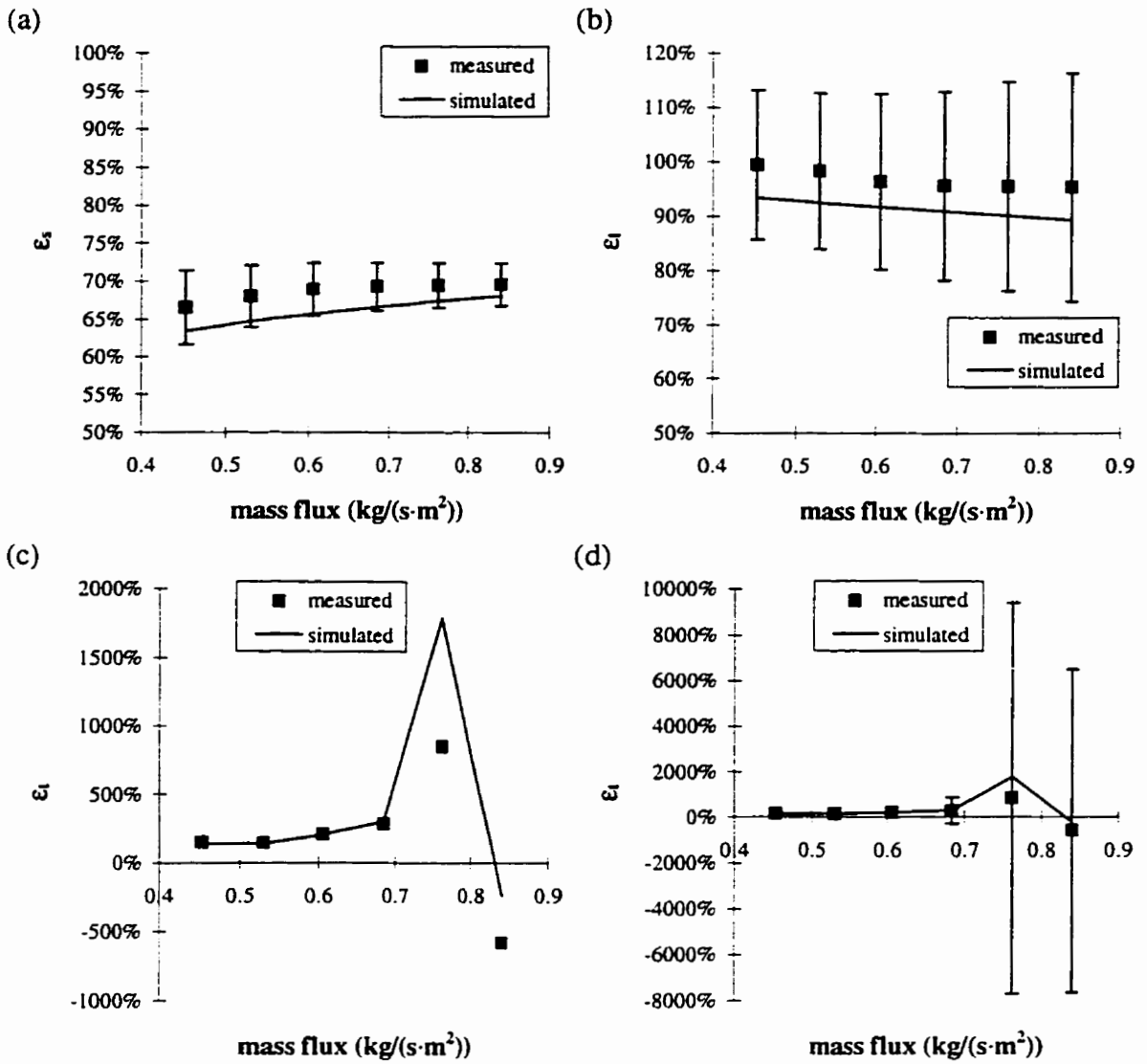

Figure 3.11. *Simulated and measured (a) sensible, (b) latent, (c) total (without error bars) and (d) total effectiveness (with error bars) for the hot tests with dry-humid operating conditions. (Error bars indicate the 95% uncertainty in measured data.)*

Figure 3.11 shows that the numerical model predicts the performance of energy wheels operating under dry-humid test conditions very well. The predicted values for sensible, latent and total effectivenesses conform well with the measured values. It can be seen in Figure 3.11(c), that the dry-humid hot test conditions can give rise to measurements of ε_t that are greater than 100% and less than 0%. The numerical model

also predicts similar results even though the measurement uncertainty in the total effectiveness is high because the difference between supply and exhaust inlet air enthalpies is small (see Figure 3.8). This suggests that the total effectiveness as defined by ANSI/ASHRAE Standard 84-1991 and Klein et al. (1990) is not a good performance criteria for this operating condition. It also means that the difference in enthalpies between the supply and exhaust air streams is not the thermodynamic maximum energy transfer between the two air streams.

To show that the effectivenesses in Figure 3.11 are possible, the operating conditions are shown on a psychrometric chart in Figure 3.12 for balanced dry air mass fluxes of 0.75 kg/(s·m^2) and 0.85 kg/(s·m^2). The former mass flux and operating conditions give rise to ε_t greater than 100% and the latter give rise to ε_t less than 0%. Clearly the inlet and outlet points on the psychrometric chart in Figure 3.12 are thermodynamically possible. The hot and dry supply air has been cooled and humidified and the cooler and humid exhaust air has been warmed and dried. This operation is as expected and the measured and simulated results show close agreement. The enthalpy of the supply air increases and the enthalpy of the exhaust air decreases, as shown in Figure 3.12, for both tests because the latent effectiveness is greater than the sensible effectiveness.

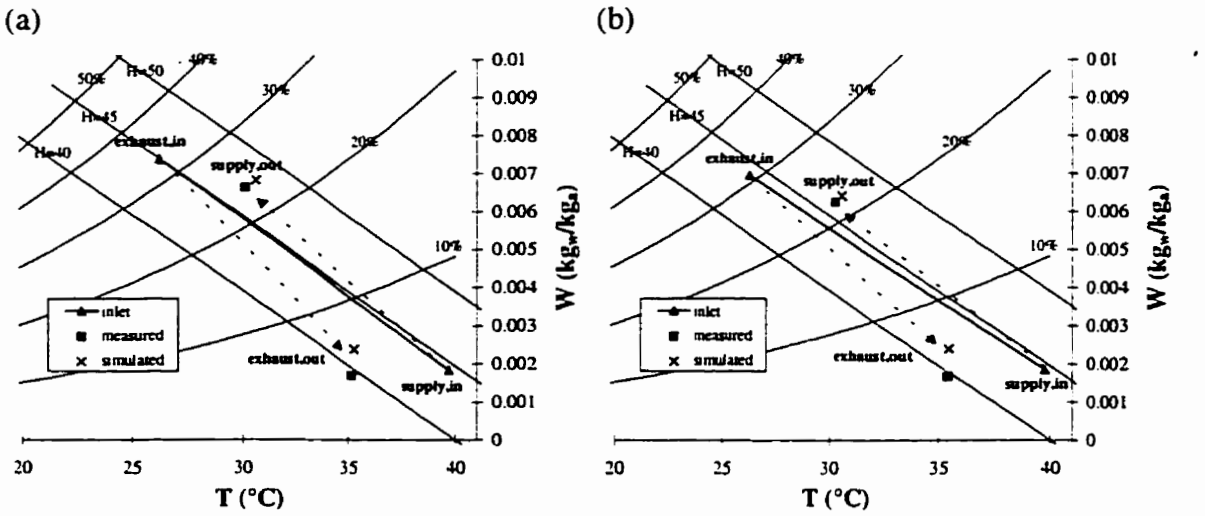

Figure 3.12. *Average supply and exhaust inlet and outlet conditions for the dry-humid hot tests with supply and exhaust mass fluxes of (a) 0.75 kg/(s·m^2) and (b) 0.85 kg/(s·m^2).*

A detailed look at Figure 3.12 shows why the total effectiveness is not limited between 0 and 100% as might be believed from classical heat exchanger theory. In Figure 3.12(a), the supply inlet condition has a lower enthalpy than the exhaust inlet condition which means that the effectiveness will be positive because the enthalpy of the air with the lowest inlet enthalpy increases as it flows through the energy wheel and the enthalpy of the air with the highest inlet enthalpy decreases as it flows through the wheel. The value of the total effectiveness will be greater than 100% because the enthalpy of the supply air leaving the energy wheel exceeds the enthalpy of the exhaust air entering the energy wheel. Similarly, the enthalpy of the exhaust outlet is lower than the enthalpy of the supply inlet. In Figure 3.12(b), the supply inlet air has a slightly higher enthalpy than the exhaust inlet air, but the enthalpy of the supply air stream increases and the enthalpy of the exhaust air stream decreases as they flow through the energy wheel. Because the enthalpy of the air stream with the highest enthalpy is further increased as it flows

through the wheel, the total effectiveness will be negative. This can be seen more clearly in Table 3.5 where the effectivenesses are calculated for the test cases in Figure 3.12.

Table 3.5. *Sensible, latent, total effectivenesses for the dry-humid hot tests.*

	mass flux	T (°C)	W (kg/kg)	H (kJ/kg)	ε_s	ε_l	ε_t
supply inlet	0.75 kg/(s·m^2)	39.7	1.8E-03	44.6	67%	90%	1790%
supply outlet		30.6	6.8E-03	47.9			
exhaust inlet		26.2	7.4E-03	44.8			
exhaust outlet		35.3	2.4E-03	41.5			
supply inlet	0.85 kg/(s·m^2)	39.7	1.8E-03	44.7	68%	89%	-240%
supply outlet		30.6	6.4E-03	46.8			
exhaust inlet		26.3	6.9E-03	43.8			
exhaust outlet		35.4	2.4E-03	41.7			

The classic definition of enthalpy effectiveness begins to break down for heat and moisture transfer in opposite directions (i.e., when one inlet condition is warmer and dryer than the other inlet condition). Therefore, it is recommended to only consider ε_s and ε_l as performance criteria for this operating condition. Yearly energy use simulations with energy wheels will be affected by this finding for climates where there are many hours when the outdoor and indoor enthalpies are nearly equal or when the outdoor conditions are warmer and dryer or cooler and more humid than the indoor conditions. It is important to know that ε_t is not limited between 0% and 100% for these operating conditions when calculating yearly energy and life cycle cost savings.

3.1.3 Unbalanced Flow Rates

It is important to validate the numerical model for unbalanced supply and exhaust flows because these operating conditions frequently occur in HVAC applications. In the tests presented in this section, the supply and exhaust inlet dry air mass flow rates are unequal but the inlet and outlet flows for each stream, supply and exhaust, are always balanced. The test conditions are given in Table 3.6 and Figure 3.13. A range of supply and exhaust flow rates are tested with outdoor temperatures near -20°C and indoor humidities that are dry and humid. The dry air mass flow rate ratio (m*) is defined as,

$$m^* = \frac{\dot{m}_s}{\dot{m}_e} \quad . \tag{3.4}$$

Table 3.6. *Temperature and humidity conditions for the unbalanced flow rate tests.*

Test	$T_{s,i}$ (°C)	$\phi_{s,i}$	$T_{e,i}$ (°C)	$\phi_{e,i}$
dry	-20	50%	24	14%
humid	-19	50%	26	40%

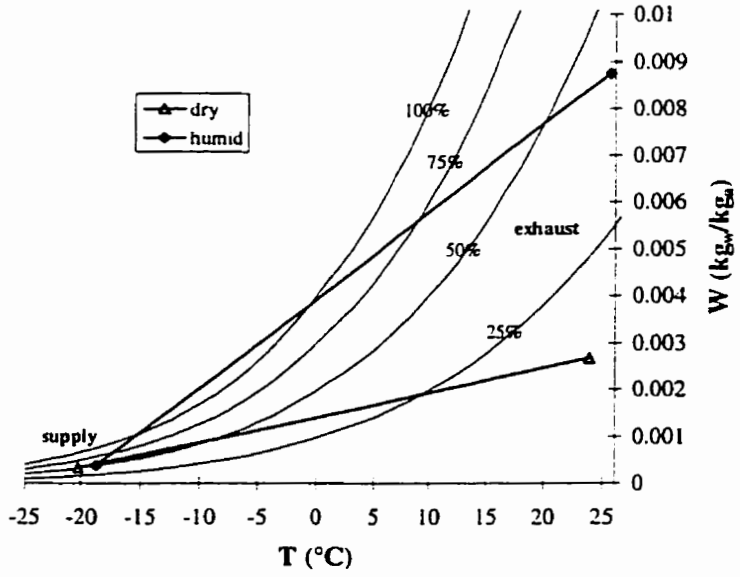

Figure 3.13. *Inlet conditions for the energy wheel in the unbalanced flow rate tests.*

The measured and simulated effectivenesses as a function of m*, presented in Figure 3.14, show good agreement and the average difference between all the measured and simulated effectiveness values is less than 1%. Each graph contains tests with four different supply mass fluxes and three different exhaust mass fluxes in the range of (0.55 to 1.15 kg/(s·m^2)). The individual effectiveness values are a function of the value of the mass flux as well as the value of m* and therefore the simulation results corresponding to the measured data show some scatter for the same value of m*. The effect of the mass flux (or scatter in the data) is small for ε_s and ε_t, but is significant for ε_l. The v-shaped curves for ε_s and ε_t as a function of m* are similar to that for a sensible counterflow heat exchanger with a constant overall heat transfer coefficient (Guo et al., 1998). On the other hand, the shape of the ε_l versus m* curve is slightly different than that which is expected for a sensible counterflow heat exchanger with a constant overall heat transfer coefficient. This can be more clearly seen in Figure 3.15 for the dry test conditions and in Figure 3.16 for the humid test conditions.

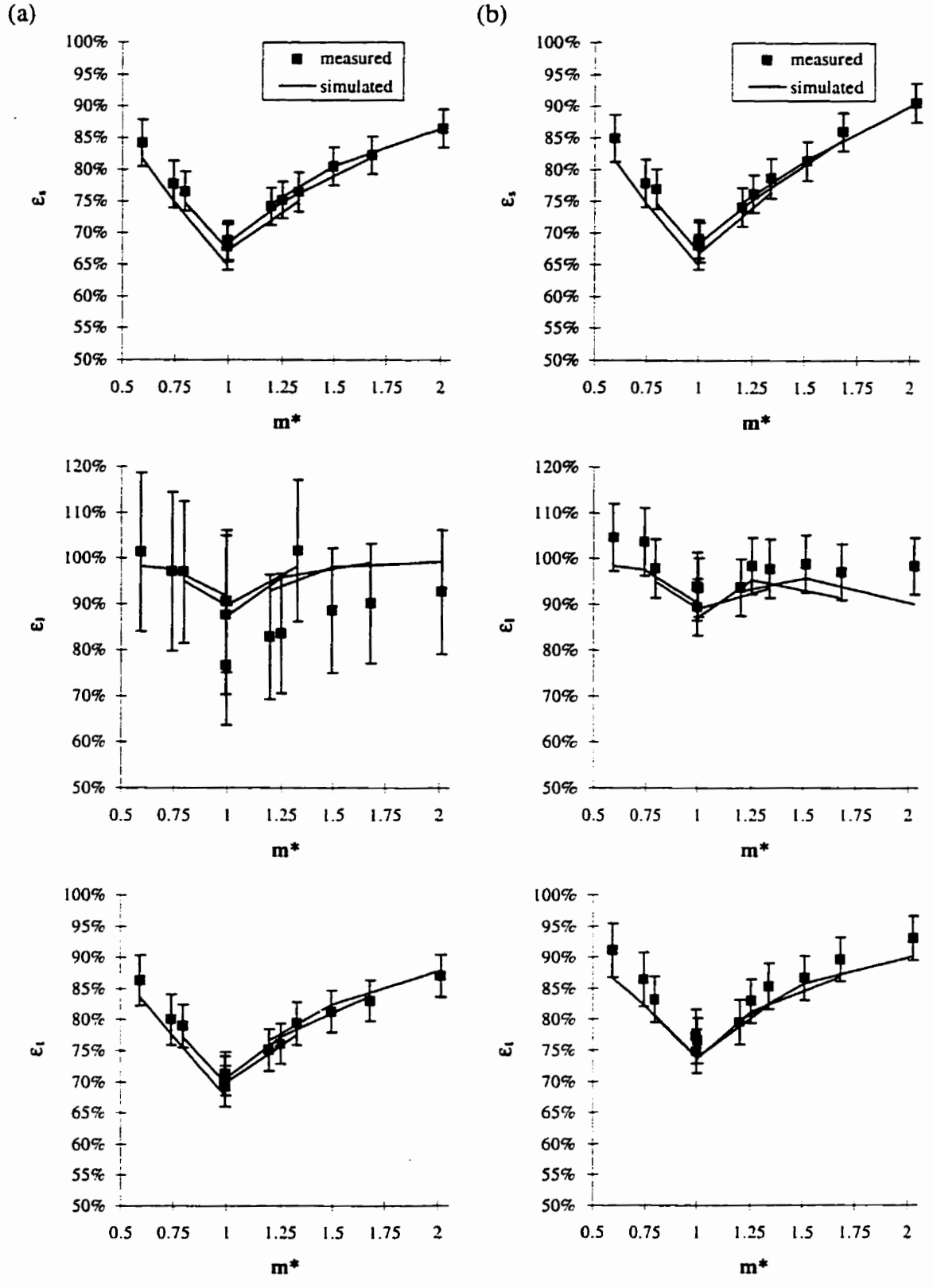

Figure 3.14. Comparison of simulated and measured effectivenesses for the unbalanced flow rate tests with (a) dry and (b) humid indoor conditions. (Error bars indicate the 95% uncertainty in measured data.)

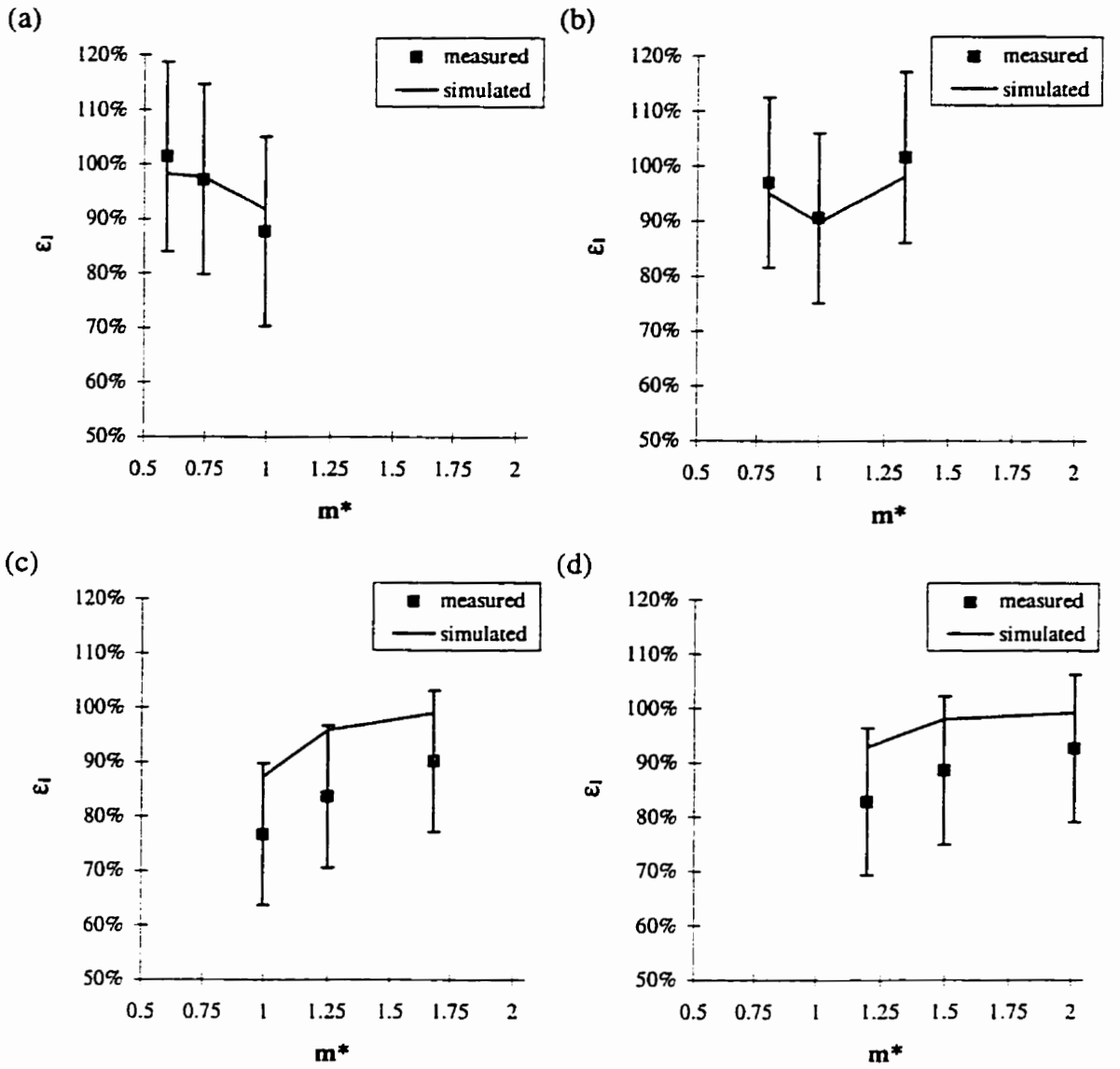

Figure 3.15. *Simulated and measured latent effectiveness for the unbalanced tests and dry indoor conditions. The supply mass fluxes are: (a) 0.55, (b) 0.75, (c) 0.95 and (d) 1.15 kg/(s·m^2). (Error bars indicate the 95% uncertainty in measured data.)*

In Figure 3.15, all the points in each graph have the same supply mass flux which eliminates the scatter due to mass flux seen in Figure 3.14. Figure 3.15 clearly shows the influence of m* on the latent effectiveness. The simulated and measured results have the same trends and agree well within the experimental uncertainty. The results show that ε_l is minimum for m* = 1 and increases as m* increases or decreases from this point. This

is similar to the v-shaped curves in Figure 3.14 for ε_s and ε_t as a function of m*, except the ε_l versus m* curve flattens for m* > 1.5 in Figure 3.15. This is more evident in Figure 3.16 which shows results for the humid test conditions.

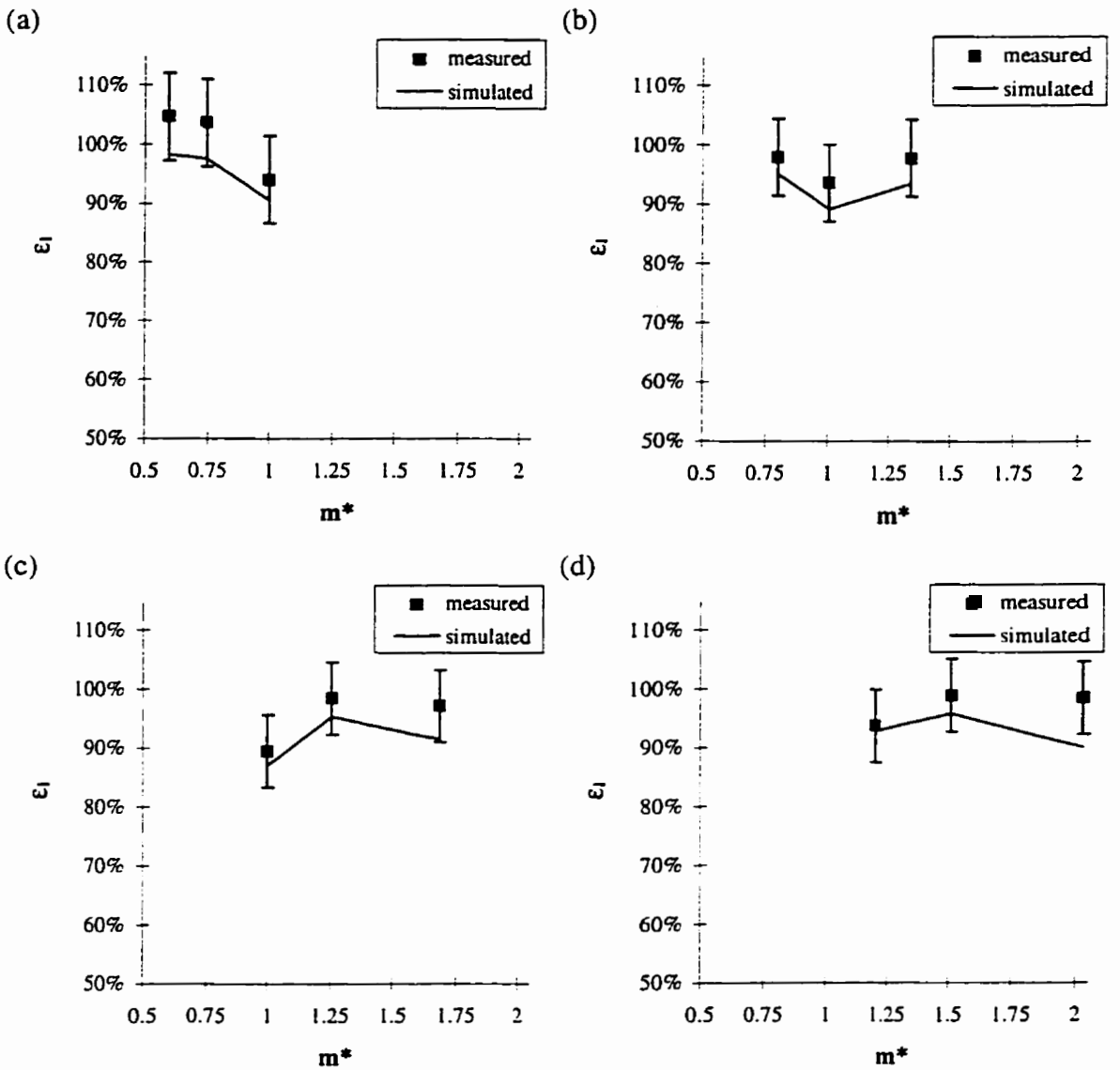

Figure 3.16. *Simulated and measured latent effectiveness for the unbalanced tests and humid indoor conditions. The supply mass fluxes are: (a) 0.55, (b) 0.75, (c) 0.95 and (d) 1.15 kg/(s·m²). (Error bars indicate the 95% uncertainty in measured data.)*

Figure 3.16 displays the same trends for ε_t as a function m* for both the simulated and measured results and the actual values are almost always contained within the experimental uncertainty bounds. In all cases, ε_t is a minimum for m* = 1 and increases as m* decreases which is expected based on the results for counter flow sensible heat exchangers. However, as shown in Figure 3.16(c) and Figure 3.16(d), ε_t increases initially for m* > 1 but levels off and begins to decrease slightly as m* approaches 2. This leveling can be explained by the fact that the duration of time that the wheel is exposed to saturation conditions in the air is lower as m* approaches 2 because of the increased flow rate of dry supply air. A decrease in ε_t with decreasing saturation conditions will be shown in Chapter 5.

As further evidence of the agreement between the measured and simulated results, the average temperature and humidity ratios are shown on psychrometric charts in Figure 3.17. Figure 3.17(a) contains results for m* = 0.6 and Figure 3.17(b) contains results for m* = 2.0.

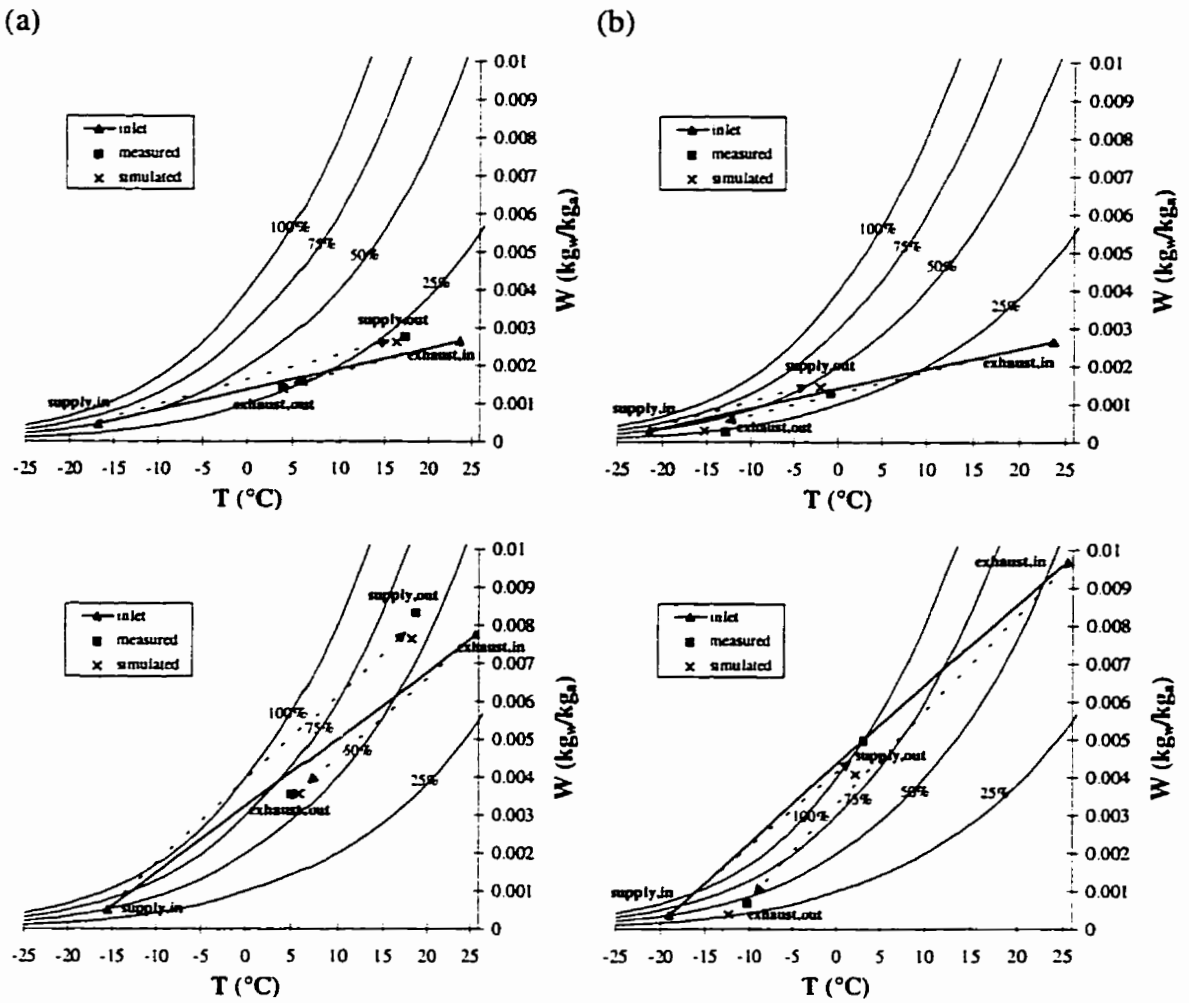

Figure 3.17. *Average supply and exhaust inlet and outlet conditions for the unbalanced tests and (a) $m^* = 0.6$ ($\dot{m}_s < \dot{m}_e$) and (b) $m^* = 2.0$ ($\dot{m}_s > \dot{m}_e$).*

The average outlet conditions are clearly different in Figure 3.17(a) than in Figure 3.17(b). The air with the lowest mass flow rate undergoes the greatest change in temperature and humidity as it flows from the inlet to the outlet of the wheel. This is as expected because energy and mass must be conserved and gives further confidence in the measured and simulated data. The simulated and measured results in Figure 3.17 are in close agreement.

3.2 FIELD EXPERIMENT

The field measurements were performed by Allan Johnson on an energy wheel that was installed in a small newspaper printing building located in Weyburn, Saskatchewan. The property data of the energy wheel are given in Table 3.1. Measurements were taken between October 21, 1995 and November 4, 1995 giving 14 days of data. The bias and precision uncertainties for the field test are given in Table 3.7 and are higher than those in the laboratory experiments (Table 3.2). Details concerning the field experiment can be found in Johnson et al. (1998).

Table 3.7. *Bias and precision uncertainties for each measurement in the field test.*

Measurement	Bias Uncertainty	Precision Uncertainty
velocity traverse	7%	2%
supply inlet temperature	1.18°C	0.2°C
supply outlet temperature	0.20°C	0.1°C
exhaust inlet temperature	0.21°C	0.1°C
exhaust outlet temperature	0.21°C	0.1°C

The supply and exhaust air flow rates were determined with a hot film sensor traverse (6 point) and a fixed pitot tube array (9 point) in regions of the ducting where the flow was expected to be the most uniform. The difference between the average flow rate measured by the hot film sensor traverse and the pitot tube array was less than ±7%. Temperature measurements were performed with type T thermocouples. The measured air temperature at each measuring station was averaged using a straight string of three thermocouples in parallel and assumed to be somewhat non-uniform by using two strings

of thermocouples evenly spaced in the duct. Spatial variations in temperature and velocity across the duct were observed at some of the measuring stations. These spatial variations increase the bias uncertainty in the bulk mean temperature and air flow rate for each air stream. The bias uncertainty due to these spatial variations is accounted for in the values reported in Table 3.7 (Johnson et al., 1998). Humidity was measured using a calibrated sensor in each airflow stream. The relative humidity measurements indicated very small changes in absolute humidity from supply to exhaust. Consequently, no humidity data are presented and validation is performed using sensible effectiveness only. Calibration for each sensor was done prior to the in-situ field monitoring in the laboratory using traceable transfer standards.

The cross leakage between the supply and exhaust air streams was not measured with tracer gas tests because this is a very difficult measurement to perform in the field. Comparison between the field measurements and numerical results will tend to indicate the magnitude of cross leakage and other problems.

The supply inlet temperature (outdoor temperature) ranged from -14°C to +15°C during the test period and the exhaust inlet temperature was nearly constant at 22°C as shown in Figure 3.18. The measured flow rates were 494 L/s and 481 L/s on the supply and exhaust sides respectively. The difference between these flow rates is less than 3% and thus the supply and exhaust mass flow rates are assumed constant and equal during the testing period.

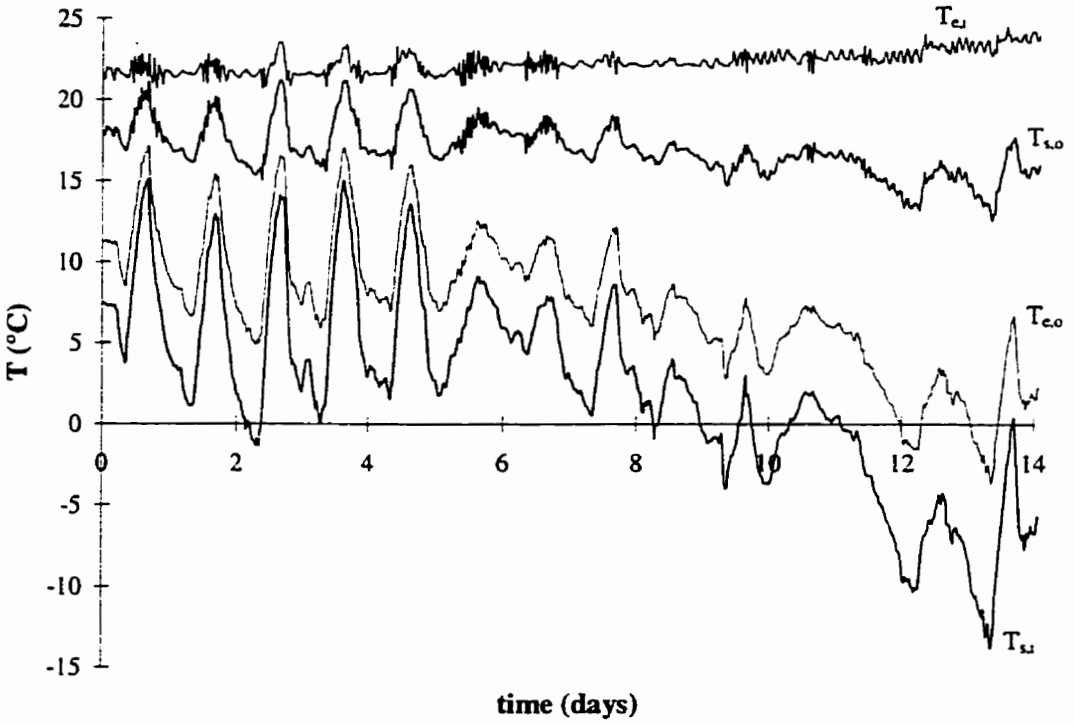

Figure 3.18. *Average measured temperatures during the field test.*

Figure 3.19 contains the measured sensible effectiveness and the 95% certainty range compared with simulation results obtained using the actual temperatures and humidities measured in the field. The measured and simulated results agree well within the experimental uncertainty. The measured and simulated effectivenesses of the energy wheel are quite constant over the test time and have average values of 73.5% and 73.7% respectively. This close agreement indicates that cross leakage between the supply and exhaust air streams in the field test is small. Carry-over leakage, which is less than 4%, is included in the numerical model and increases the apparent effectiveness of the energy wheel by less than 0.5%. In the simulations, the supply and exhaust mass flow rates are assumed constant and equal during the test ($\dot{m}_s = \dot{m}_e = 0.57$ kg/s). If the supply and exhaust volume flow rates are assumed constant and equal, the simulated effectiveness

increases by an average of 2.6%. This slight increase in effectiveness is due to the unbalanced supply and exhaust mass flow rates that result when the supply and exhaust volume flow rates are assumed constant and equal.

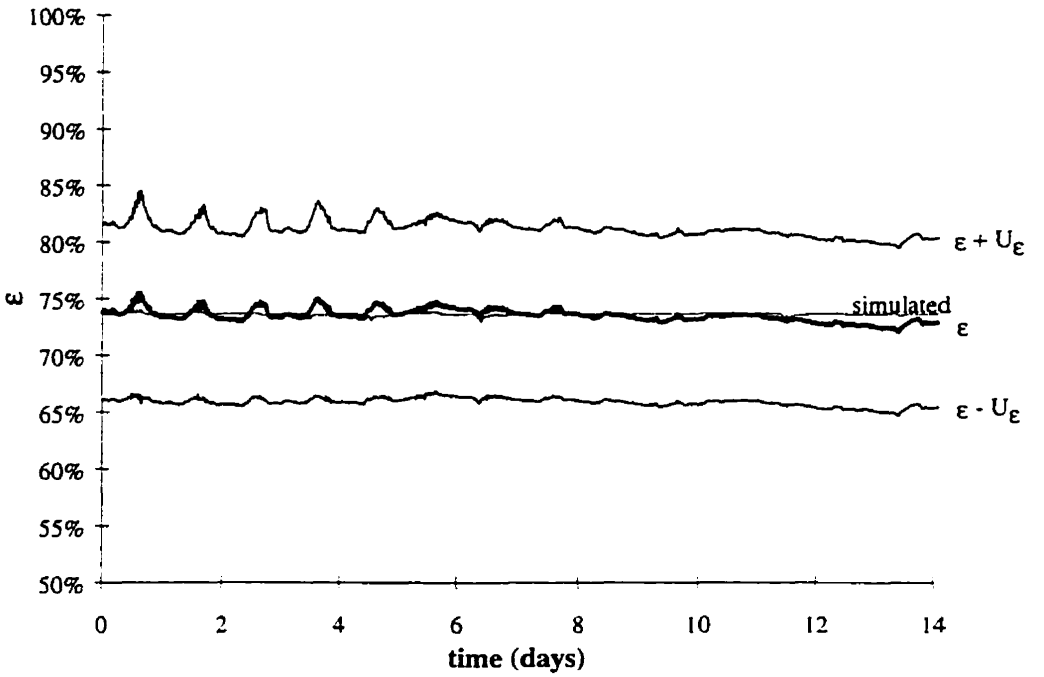

Figure 3.19. *Measured sensible effectiveness of the energy wheel and the 95% certainty range for the field data compared to simulation results.*

3.3 EXTRAPOLATION OF TEST DATA

After the numerical model has been validated with experimental data, the model can be used to extrapolate test data and predict energy wheel performance under different operating conditions. This could be done for many practical operating conditions and wheel designs, but the tests examined here focus on extrapolation of the half wheel experimental tests to full wheel tests and extrapolation of non-uniform inlet condition field tests to uniform inlet condition tests. That is, the operation of the energy wheel

under manufacturer's design condition is desired because only half of the wheel is used in the laboratory experiments due to capacity limitations in the laboratory. The effect of non-uniform inlet conditions as found in the field tests is important to quantify in-situ performance where non-uniformities in temperature, humidity and flow rate often exist.

3.3.1 Effect of Using Half of the Wheel in the Laboratory Experiments

Simulated results using half of the wheel, as in the laboratory experiments, are compared with results for the full wheel for the -10°C and dry and -10°C and humid test conditions in Figure 3.20. The test conditions are given in Table 3.3.

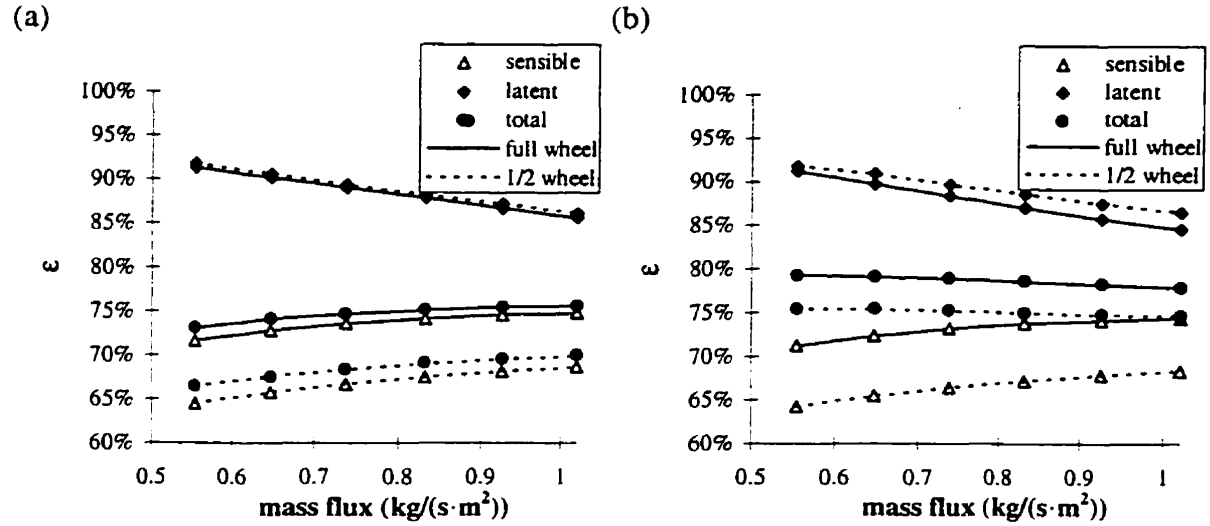

Figure 3.20. *Comparison of simulated effectivenesses when using the entire wheel as compared to using half of the wheel for -10°C and (a) dry and (b) humid test conditions.*

The results in Figure 3.20 show that using half of the wheel decreases the sensible effectiveness in all cases, particularly at low mass fluxes where the maximum decrease is 7%. The decrease in sensible effectiveness is due to axial heat conduction through the matrix during the no flow section which tends to flatten the temperature distribution as a

function of x (Figure 3.21). The latent effectiveness is unaffected by using half of the wheel for the dry tests because the adsorbed moisture in the matrix does not move in the axial direction within the no flow section. In the humid tests, the latent effectiveness increases slightly when half of the wheel is used. The reason for this is that saturation conditions exist in part of the wheel for these conditions and changes in the matrix and air temperatures (or sensible effectiveness) affect the amount of saturation and therefore the latent effectiveness.

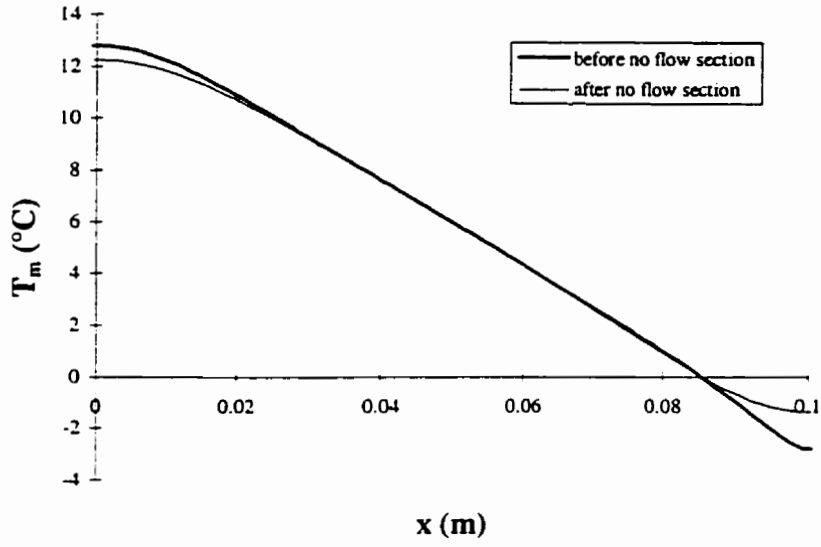

Figure 3.21. *Temperature distribution in the matrix before and after the no flow section for -10°C and dry test conditions. The mass flux is 1.0 kg/(s·m^2).*

Figures 3.20 and 3.21 show that using half of the wheel will affect the measured performance of an energy wheel. The effectiveness values change by up to 7% which may create problems when extrapolating measured results if a numerical model is not available. If a numerical model has been validated with the experimental data using half

of the wheel, the model can then accurately predict performance when the entire wheel is used.

3.3.2 Effectiveness for a Full Wheel at Design Conditions

The design dry air mass flux for the wheel tested in this chapter is 1.5 kg/(s·m^2) while the laboratory test data was measured using half of the wheel with mass flux in the range of 0.4 to 1.1 kg/(s·m^2). In this section, the numerical model is used to determine the performance of the entire energy wheel operating over the range of 50% to 150% of the design mass flux. The average temperature and humidity conditions for these tests are summarized in Table 3.8 and Figure 3.22. The atmospheric pressure in these tests is chosen to be 101.325 kPa. These test conditions span nearly the entire range of expected operating conditions in the highly populated regions of North America.

Table 3.8. *Temperature and humidity conditions for the full wheel performance tests.*

Test	supply air conditions		exhaust air conditions	
	T (°C)	ϕ	T (°C)	ϕ
cold and dry	-20	50%	22	20%
cold and humid	-20	50%	22	50%
hot and humid	35	50%	24	50%
hot and very humid	35	90%	26	50%

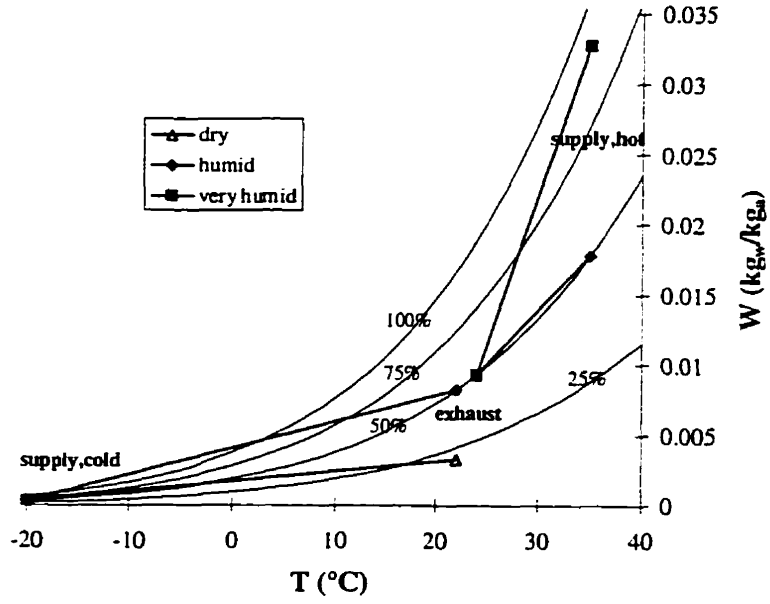

Figure 3.22. *Supply and exhaust inlet conditions for the full wheel performance tests.*

The results in Figure 3.23 that show $\varepsilon_s > \varepsilon_t > \varepsilon_l$ for the hot tests differ significantly from the validation model simulations and test data presented previously where generally $\varepsilon_s < \varepsilon_t < \varepsilon_l$. Also, the values of effectiveness are lower in Figure 3.23 than those presented previously. There are two important operational differences between these simulations: the mass flux is significantly higher in Figure 3.23 and the whole wheel is employed with half the area devoted to supply air and the other half to exhaust air. Only two quadrants were used for these flows in the laboratory tests as described in Section 3.1. These operational differences affect ε_s little but affect ε_l significantly, especially in the hot tests. In nearly all cases, the effectiveness of the energy wheel decreases with increasing mass flux with the decrease in ε_l (and sometimes ε_t) being larger than the decrease in ε_s. This shows that the moisture storage capacity of the matrix is limiting the latent effectiveness for operating conditions where the moisture transfer is significant.

Also, for the hot supply air conditions (35°C) in Figure 3.23, the air in the energy wheel is approaching or experiencing saturation conditions for a short part of the cycle; whereas, in the validation tests for hot and humid conditions (40°C and 86% R.H.), saturation conditions are quite dominant. Saturation conditions, although possibly detrimental to the integrity of desiccant coated energy wheels, increase the latent effectiveness as will be shown in Chapter 5.

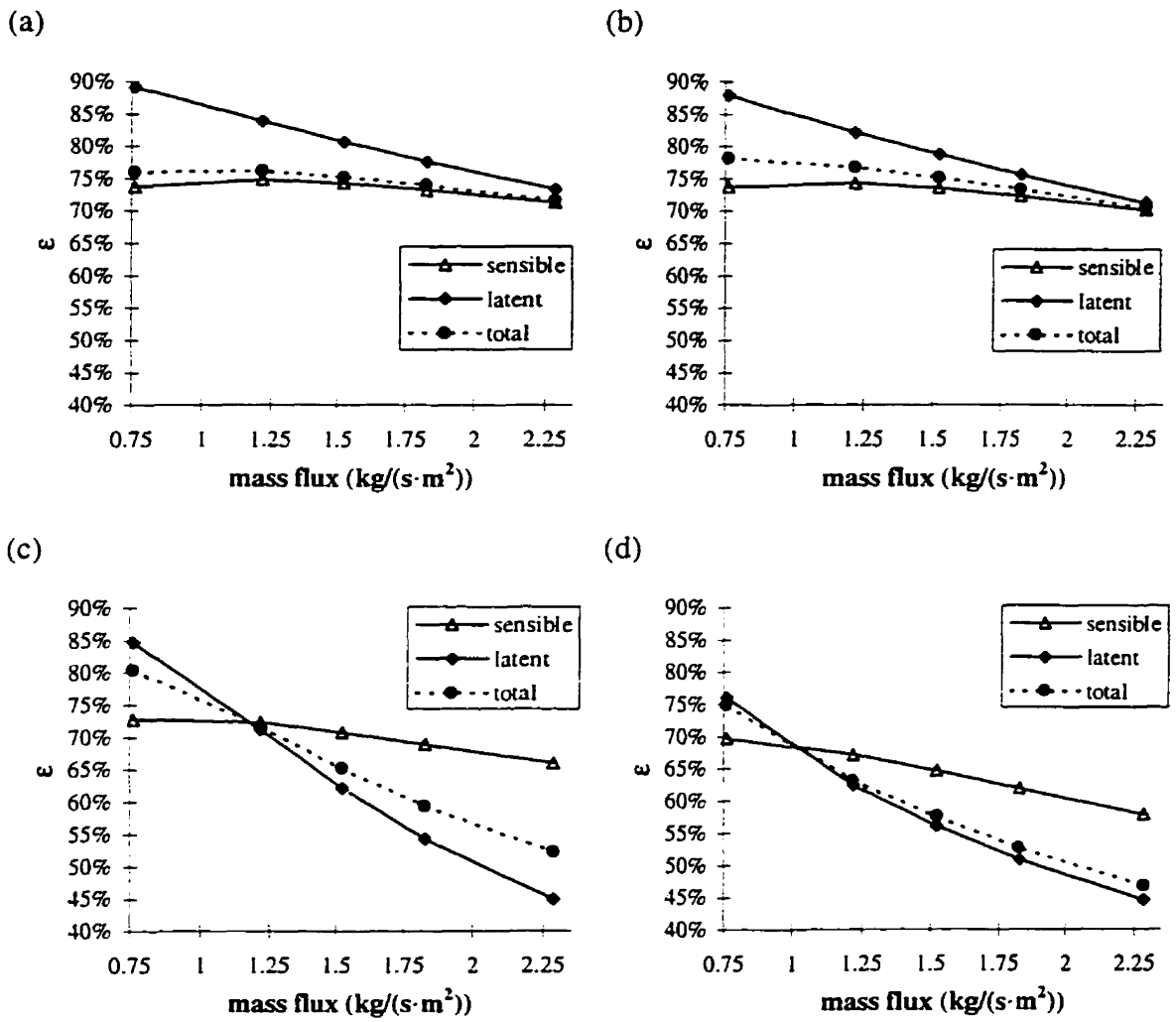

Figure 3.23. *Effectiveness of the energy wheel for the following test conditions: (a) -20°C and dry, (b) -20°C and humid, (c) 35°C and humid and (d) 35°C and very humid.*

The performance of the energy wheel at different mass fluxes, temperatures and humidities can be directly compared in Figure 3.23. These results imply that the design of energy wheels and the selection of operating conditions that will be most cost effective in HVAC applications will be very complicated because very large changes in effectiveness can occur with changes in humidity and air flow rates.

Energy wheel performance with unbalanced flow rates are presented in Figure 3.24 for the entire wheel operating near design operating conditions for the test conditions given in Table 3.8 and Figure 3.22. In all cases the exhaust mass flux is kept constant at 1.5 kg/(s·m^2) and the supply mass flow rate is changed. This simulates the bypass of supply air for the case of $m^* < 1$.

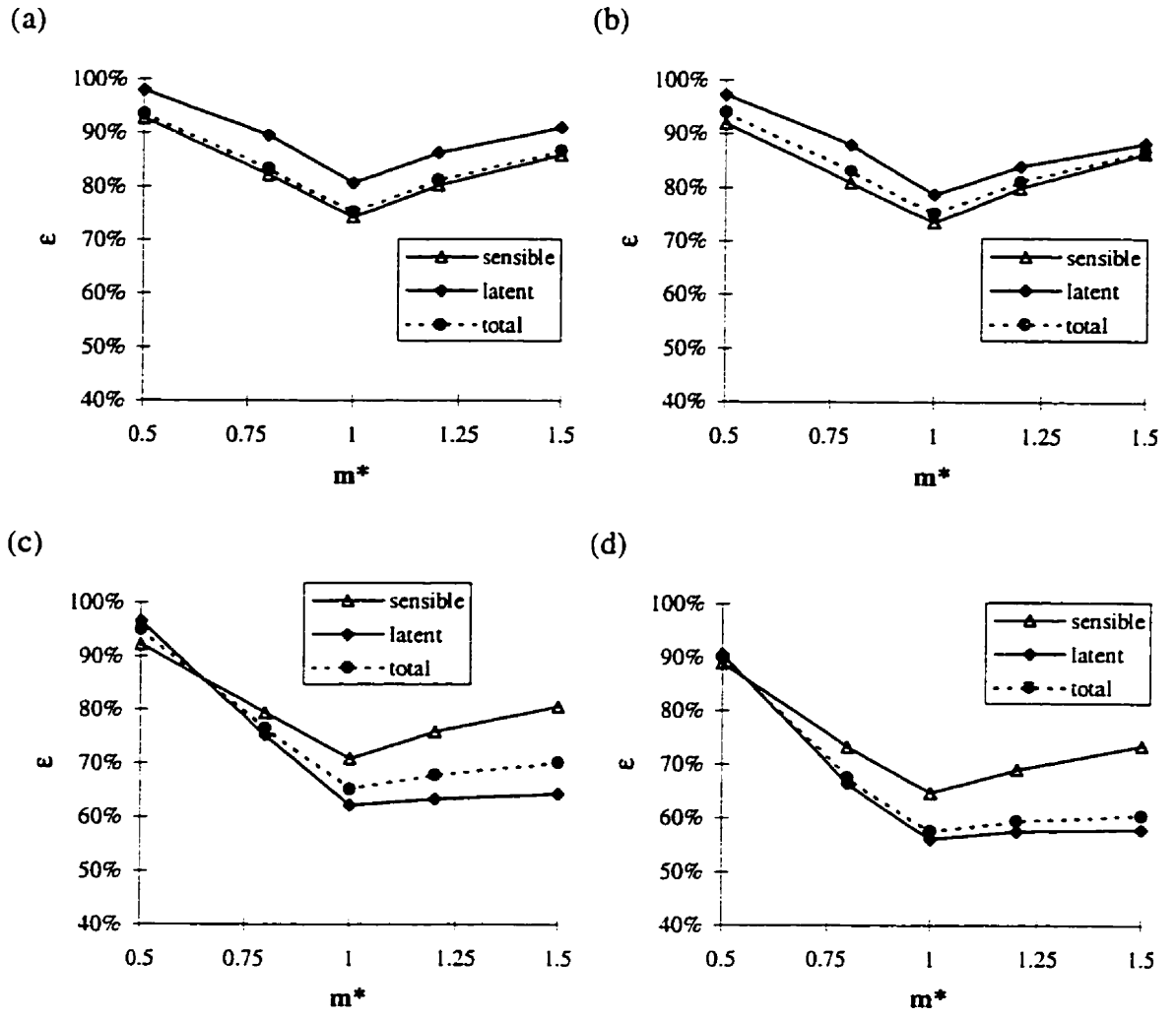

Figure 3.24. *Effectiveness of the energy wheel for unbalanced flow rates and (a) -20°C (dry), (b) -20°C (humid), (c) 35°C (humid) and (d) 35°C (very humid) test conditions.*

The v-shaped curves in Figure 3.24 show that, in most cases, the effectiveness (especially ε_s) as a function of m* is similar to that for sensible heat transfer only in a counter flow heat exchanger with constant overall heat transfer coefficients (Guo et al., 1998). This means that the sensible effectiveness as a function of m* could likely be correlated with results from the literature on sensible heat exchangers. However, for humid operating conditions, the latent and, sometimes, the total effectivenesses have a trend that differs with the sensible effectiveness. This further shows that an accurate

numerical model is necessary to extrapolate the measured performance data of energy wheels to other flow rate, temperature and humidity operating conditions.

The results in Figure 3.24 for $m^* < 1$ represent operating conditions where the supply air is bypassed for energy rate control. In the cold tests, the three effectivenesses (ε_s, ε_l and ε_t) all change by similar magnitudes as a function of m^*; however, in the hot tests, the effectivenesses change by different magnitudes as function of m^*. This shows that energy rate control by bypassing supply air around the energy wheel may result in new control problems in practice.

3.3.3 Effect of Non-uniform Inlet Conditions

The effect of non-uniform inlet conditions on the performance of energy wheels is important. If performance is measured with uniform inlet conditions in a laboratory test, the results must be extrapolated to represent the non-uniform inlet conditions that often exist in the field. Non-uniform velocity distributions in the duct are not likely to cause flow maldistributions through heat exchangers with constant pore sizes because the velocity head is much lower than the friction pressure loss through the heat exchanger. In the field test reported in this chapter, the pressure drop due to friction was in the order of 50 to 250 Pa, while the dynamic velocity pressure was below 5 Pa.

Non-uniform temperature and humidity inlet conditions, on the other hand, may affect the performance of heat/energy exchangers. Guo et al. (1998) show that the effectiveness of a heat pipe heat exchanger is constant over a fairly large range of operating conditions which indicates that a non-uniform inlet temperature will not have a

significant effect on the performance of sensible heat exchangers. However, Brandemuehl and Banks (1981) show that a large spatial temperature variation of 50% from the average can change the effectiveness of sensible rotary heat exchangers by as much as 10%. The effectiveness increases when the temperature is highest near the end of the hot cycle and decreases when the temperature is lowest at the end of the hot cycle. The purpose of this section is to quantify the effect of non-uniform temperature and humidity supply inlet conditions on the performance of energy wheels. The equations used to generate the Type 1 and Type 2 distributions, shown in Figure 3.25, are respectively:

$$\chi = \chi_{ave} + c_{\chi} \sin(\theta - 90°) \quad \text{and} \tag{3.5}$$

$$\chi = \chi_{ave} + c_{\chi} \sin(2\theta - 90°) \ , \tag{3.6}$$

where χ represents temperature (T) or relative humidity (ϕ).

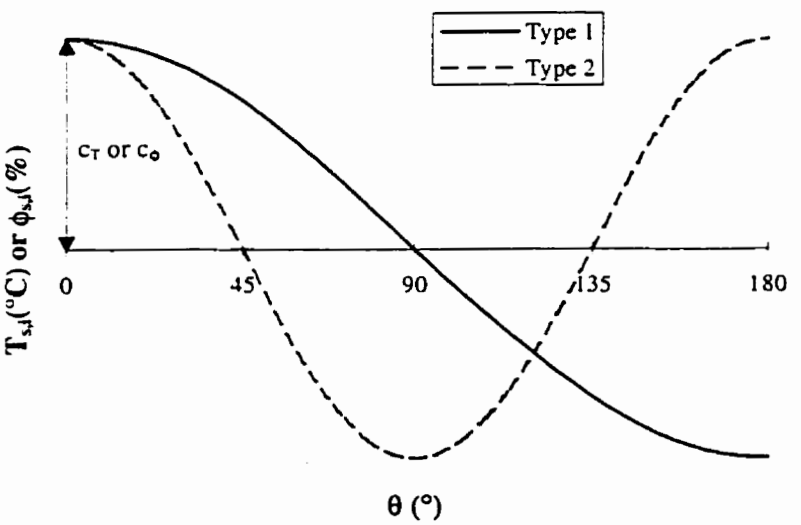

Figure 3.25. *Non-uniform temperature and humidity distributions in the supply inlet.*

The largest difference between the maximum and minimum temperatures measured in the supply inlet duct of the field tests were 4°C. To simulate a larger range, c_T is allowed to vary from -5°C to +5°C and the results are presented in Figure 3.26(a). Humidity distributions were not measured in the field tests so c_ϕ is estimated to be 10% R.H. for an extreme case of non-uniform humidity and the results are presented in Figure 3.26(b). In Figure 3.26, the hot and very humid test conditions in Table 3.8 are used to represent χ_{ave}. Although Figure 3.26 shows only hot and humid operating conditions, cold and dry operating conditions were also simulated but the effect of non-uniform temperature and humidity supply inlet conditions were less than 0.3% for these conditions and are not presented. The flow rates in Figure 3.26 are representative of those in the field tests (i.e., $\dot{m}_s = \dot{m}_e = 0.57$ kg/s).

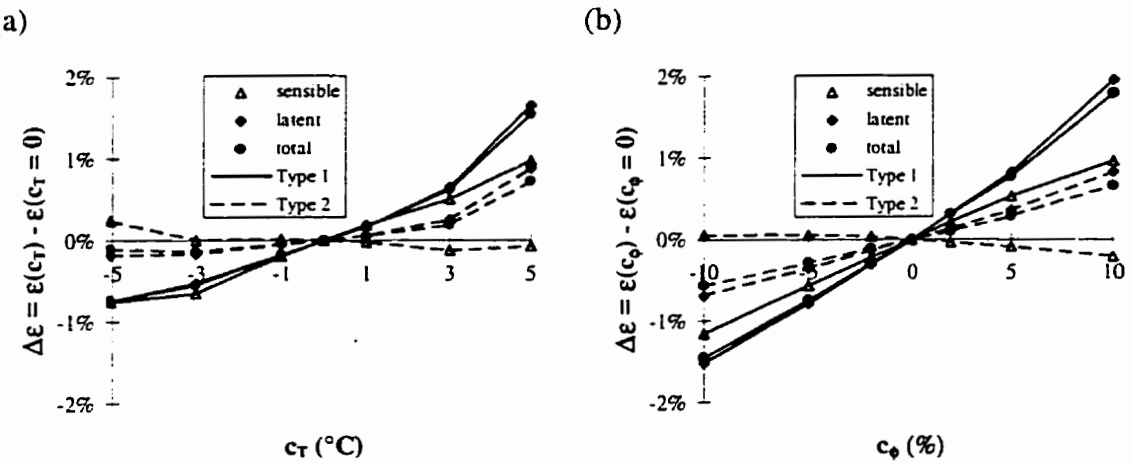

Figure 3.26. *Effect of non-uniform (a) temperature and (b) relative humidity distribution in the supply inlet duct for the hot and very humid test conditions.*

The results in Figure 3.26 show that the magnitude of temperature and humidity variations studied here do not have a large effect on the performance of an energy wheel.

Type 1 distributions affect the effectiveness more than Type 2 distributions, but the predicted effectiveness changes by less than 2% in all cases. This is as expected from Brandemuehl and Banks (1981) for a sensible heat exchanger with a high value of Cr^*_o ($Cr^*_o = 6.5$ in this case). This confirms the belief that moderate non-uniform distributions in the temperature and humidity levels entering a heat/energy exchanger, as would be typical in field experiments, will have only a small effect on the performance. This means that controlled laboratory test data represents field performance as well. However, as pointed out Johnson et al. (1998), the bias uncertainty in the bulk mean temperature or humidity that results from non-uniform temperature or humidity distributions must be included in the uncertainty analysis of effectiveness.

3.4 PERFORMANCE STANDARDS

Several standards are available (i.e., ANSI/ASHRAE Standard 84-1991, CSA Standard C439-M1988 and ENV Standard 308-1996) for developing experimental testing procedures to determine the performance of air-to-air heat exchangers. An implication of these standards is that the denominator used in the effectiveness equations (i.e., equations (2.47) to (2.49)) represents the maximum possible energy transfer rate. This is not always true for the total effectiveness as was shown in Figure 3.11. Similarly, Figure 3.27 shows that an energy wheel may have sensible and latent effectiveness values greater than 100% or less than 0% when the operating conditions are such that the difference between the supply air and exhaust air inlet temperatures or humidity ratios are small but not zero.

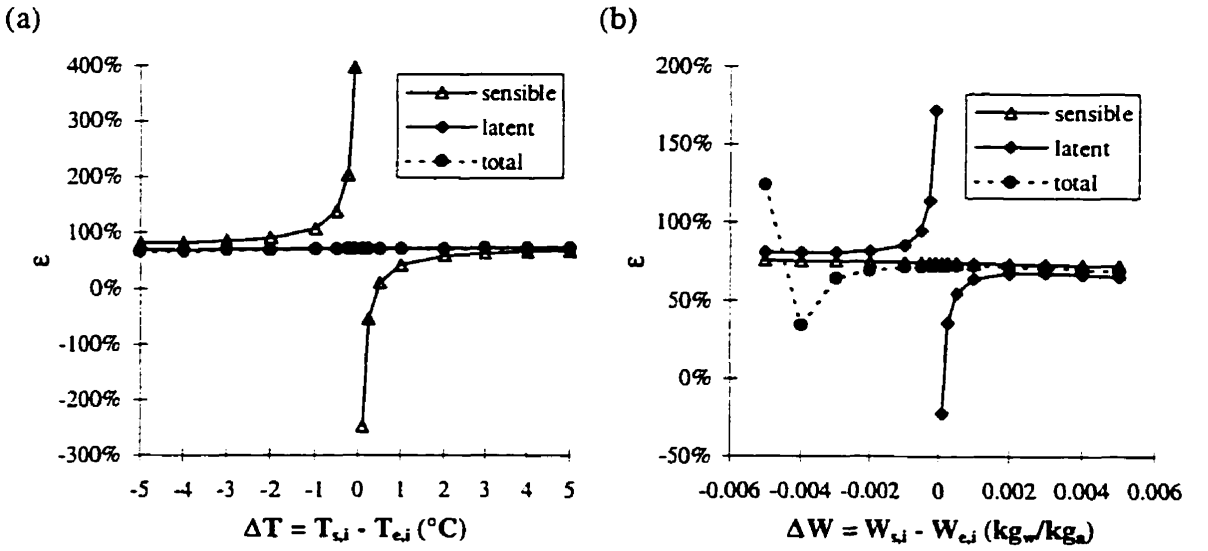

Figure 3.27. *Effectiveness of an energy wheel versus (a) temperature difference when $T_{e,i}$ = 24°C, $\phi_{e,i}$ = 30% R.H. and $W_{s,i}$ = 0.014 kg/kg and (b) humidity ratio difference when $T_{e,i}$ = 24°C, $W_{e,i}$ = 0.01 kg/kg and $T_{s,i}$ = 35°C.*

The finding that effectiveness values are not limited between 0% and 100% is in agreement with research on desiccant dehumidifiers where a negative value for latent (or moisture) effectiveness has long been accepted (e.g., Stiesch et al., 1995 and Zheng et al., 1993). Figure 3.27 also shows that the total energy effectiveness exceeds 100% when ΔW = -0.005, which corresponds to a small enthalpy difference between the exhaust and supply inlets. These results, together with those presented in Figure 3.11, show that the denominators in the effectiveness equations do not represent the maximum possible sensible, latent, or total energy transfer for energy wheels. Anyone using performance standards must be aware of the fact that effectiveness values need not lie between 0 and 100%. Designers of HVAC systems should also be aware of this possibility if they are using numerical models of energy wheels and not test data.

A question could be raised - should energy wheel effectiveness equations be modified so that the denominator will be the thermodynamic maximum energy transfer rate for latent and total effectiveness? Since the problems with the definition of effectiveness tend to occur only when the operating conditions result in effectiveness uncertainties that are very high, such a change would add complications which could confuse the user of these standards and the designer of HVAC air-to-air heat/energy recovery systems. Furthermore, more research will be required to establish the correct equation for the maximum energy rate in these cases. Without further evidence to the contrary, a change to the definition does not seem to be warranted at this time because the performance uncertainty levels at these conditions should disqualify any of these test results.

Performance uncertainty is the most crucial component of any test standard. The performance uncertainty quantifies the experimental results and determines the confidence limits and quality of a test. In most cases, the uncertainty of an experimental result is pre-determined once the instruments, apparatus and procedure have been selected for a specific test. Therefore, the testing engineer must perform a pre-test analysis of uncertainty to ensure that the final results will have acceptable uncertainty bounds. Pre-test uncertainty analyses for air-to-air energy recovery devices are complicated by the large number of independent variables (i.e., in addition to the atmospheric pressure three sensors per air stream). The uncertainty for each sensor reading depends on both its calibration uncertainty (bias) and random uncertainty (precision). Furthermore, equations couple the sensor reading values for both the mass flow rate and effectiveness.

Nonetheless, the experimenter must select not only the instrumentation but also the operating conditions for testing. To facilitate this pre-test uncertainty analysis a graphical method of selecting the operating conditions is considered where, given the instrumentation uncertainty characteristics, contours of equal effectiveness uncertainty can be plotted on the psychrometric chart.

The psychrometric chart in Figure 3.28 allows a pre-test estimation of the uncertainty levels $U(\varepsilon_s)$, $U(\varepsilon_l)$ and $U(\varepsilon_t)$ associated with the combination of any supply condition and an exhaust condition of 24°C and 50% R.H.. Figure 3.28(a) is for typical lower effectiveness values while Figure 3.28(b) is for higher effectiveness values. Figure 3.28 shows that the uncertainty in effectiveness depends on the value of effectiveness, the bias and precision uncertainties and the operating conditions. The uncertainty bounds for sensible effectiveness are straight lines and depend on the difference between the supply and exhaust inlet dry-bulb temperatures. The latent and total effectiveness uncertainty bounds are curved lines, suggesting that the latent and total effectiveness uncertainties are dependent on both the difference in dry-bulb temperature and humidity ratio, which is known to be true (Ciepliski, 1997). These results suggest that the uncertainties in latent and total effectivenesses will be significantly higher than the uncertainties in sensible effectiveness for most laboratory test conditions. Also, for equal uncertainty levels, wheels with high effectiveness values (i.e., Figure 3.28(b)) require more extreme test conditions than wheels with low effectiveness values (i.e., Figure 3.28(a)).

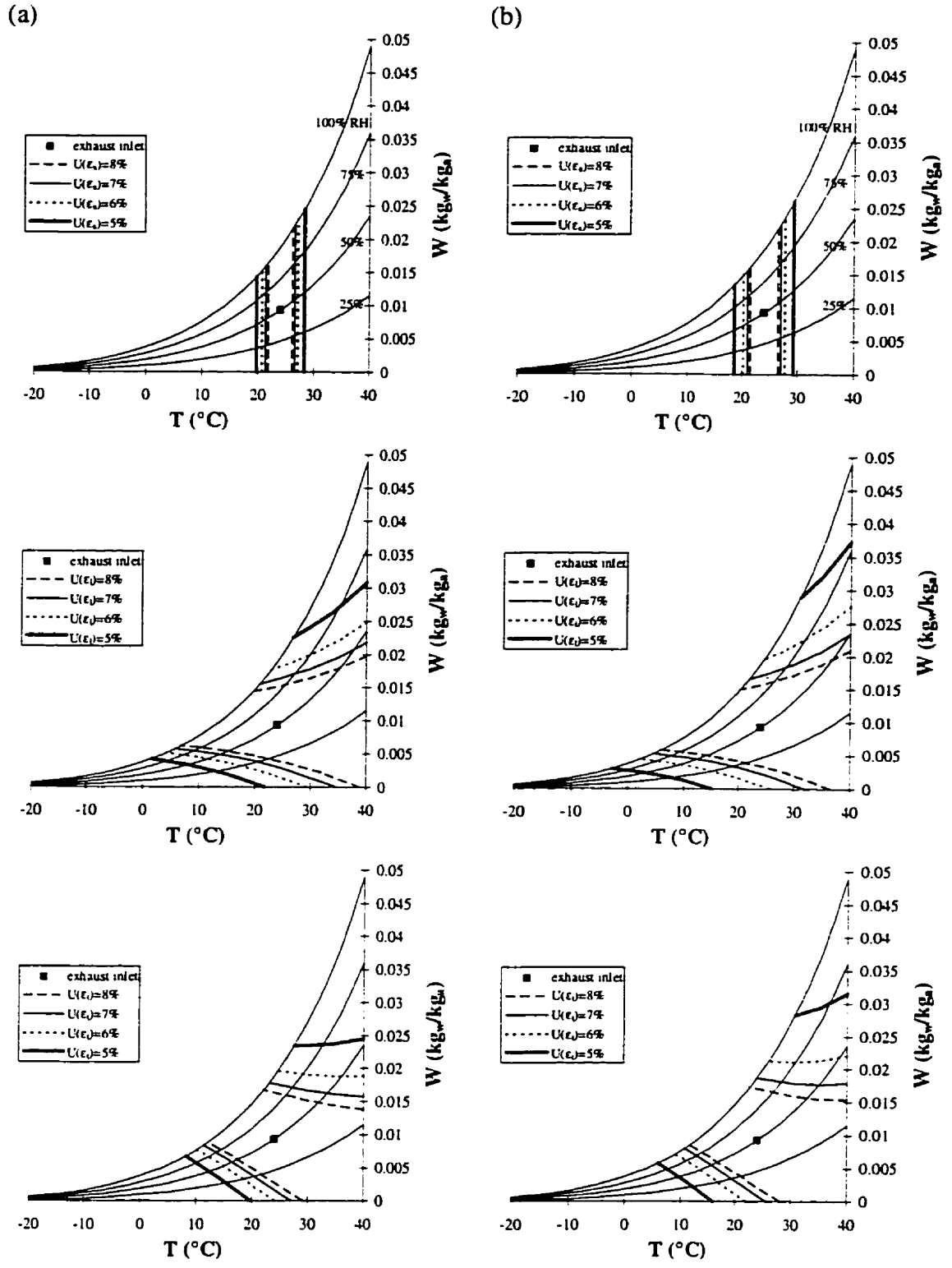

Figure 3.28. *Lines of constant uncertainty in measured effectiveness values for different supply inlet conditions. The assumed bias and precision in mass flow rate, temperature and humidity are: ±4% & ±1%, ±0.2 K & ±0.1 K and ±2% R.H & ±1% R.H. respectively. In (a)* $\varepsilon_s = \varepsilon_l = \varepsilon_t = 60\%$ *and in (b)* $\varepsilon_s = \varepsilon_l = \varepsilon_t = 70\%$.

Figure 3.29 presents similar results to those in Figure 3.28 except the assumed bias and precision uncertainties for flow rate, temperature, and humidity are increased to represent conditions that are likely to occur during in-situ field testing. These results suggest that finding field operating conditions with uncertainties less than 8% may be practical for ε_s, but not likely for ε_l or ε_t. These figures should not be used when condensation or frosting effects are significant.

Based on laboratory experimental results presented in Section 3.1, an uncertainty of less than ±5% would appear to be a reasonable limit for sensible effectiveness, but it appears to be too strict for latent and often total effectiveness. The results for ε_l, and often ε_t, imply that the corresponding uncertainty limits should be higher than for ε_s as shown in Figures 3.28 and 3.29. That is,

$$U(\varepsilon_s) < U(\varepsilon_t) < U(\varepsilon_l) \tag{3.7}$$

provided the operating conditions are such that the sensor measurement uncertainties, not the operating condition uncertainties, dominate. The results for uncertainty presented in Figures 3.28 and 3.28 assume constant performance and uncertainty values for temperature, humidity and mass flow rate. The pre-test uncertainty analysis for the case where these can vary with operating conditions is addressed by Ciepliski et al. (1998).

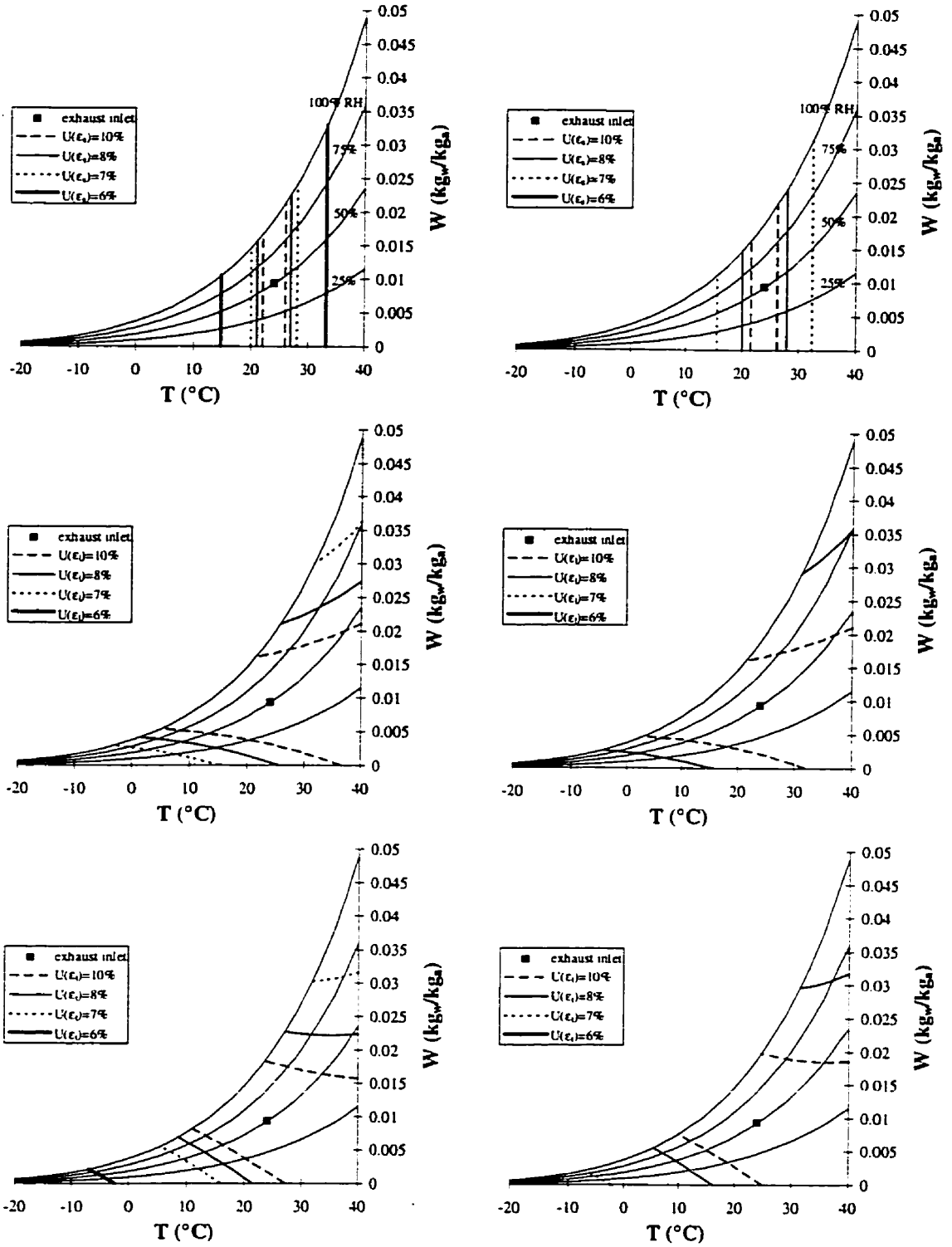

Figure 3.29. Lines of constant uncertainty in measured effectiveness values for different supply inlet conditions. The assumed bias and precision in mass flow rate, temperature and humidity are: ±5% & ±3%, ±0.5 K & ±0.1 K and ±3% R.H & ±1% R.H. respectively. In (a) $\varepsilon_s = \varepsilon_l = \varepsilon_t = 60\%$ and in (b) $\varepsilon_s = \varepsilon_l = \varepsilon_t = 70\%$.

3.5 SUMMARY

The numerical model presented in Chapter 2 has been validated with laboratory and field experimental data that cover a range of mass fluxes, temperatures and humidities. The numerical and experimental effectiveness values agree within the experimental and numerical uncertainties and the trends in the experimental data are the same as the trends in the simulated results. Both the experimental and numerical results show that the three effectiveness values (i.e., sensible, latent and total) are unequal and each has its own unique sensitivity to operating conditions.

Extrapolation of measured energy wheel performance to other test conditions is quite complex and requires a validated numerical model. Simulated results show that experimental results measured using half of the energy wheel, to reduce equipment sizes, do not directly apply to full wheel performance. Non-uniformities in the inlet temperature and humidity, on the other hand, can typically be neglected when extrapolating between field and laboratory tests.

The results in this chapter show that the sensible, latent and total energy effectivenesses are not limited to values between 0 and 100% because, for certain test conditions, the denominator used in the effectiveness equations is not the thermodynamic maximum energy transfer rate when both heat and moisture are transferred. These test conditions are usually accompanied by large uncertainties and therefore, despite their inherent weakness, it is recommended that the standard effectiveness equations be used to quantify energy wheel performance because they are functional, familiar and simple to apply. A simple graphical method is presented that will aid test engineers in performing pre-test uncertainty analyses and selecting operating conditions to minimize uncertainty.

CHAPTER 4

EFFECTIVENESS CORRELATIONS FOR ENERGY WHEELS

In this chapter, the fundamental dimensionless groups for energy wheels are derived from the governing, non-linear and coupled heat and moisture transfer equations presented in Chapter 2. These new dimensionless groups give insight into why the effectiveness of energy wheels is dependent on the operating temperature and humidity. The physical meaning of the dimensionless groups and the importance of the operating condition factor (H*) are explained and illustrated. Using these parameters, new effectiveness correlations are developed that accurately predict the sensible, latent and total effectiveness of energy wheels. These effectiveness correlations can be used by manufacturers and HVAC engineers to accurately predict the performance and life cycle cost savings of energy wheels in HVAC systems without time dependent simulations.

4.1 DIMENSIONLESS GROUPS FOR ROTARY SENSIBLE HEAT WHEELS

The method of deriving the governing dimensionless groups for rotary sensible heat wheels from the governing equations is presented by Shah (1981). Shah shows that a set of simplified governing equations that govern the transfer and storage of sensible energy on the supply or exhaust side of a counterflow sensible regenerative heat exchanger can be approximated by,

$$\frac{\partial T_g}{\partial x^*} = NTU\left(T_m - T_g\right), \text{ and} \tag{4.1}$$

$$\frac{\partial T_m}{\partial t^*} = \frac{NTU}{Cr^*}\left(T_g - T_m\right) . \tag{4.2}$$

The form of equations (4.1) and (4.2) will be referred to as the standard dimensionless form. The dimensionless number of heat transfer units and matrix heat capacity on the supply and exhaust side are:

$$NTU = \frac{hA'_s}{(\rho AUCp)_g} = \frac{hA_s}{(\dot{m}Cp)_g}, \text{ and} \tag{4.3}$$

$$Cr^* = \frac{(\rho ACp)_m L}{(\rho AUCp)_g p} = \frac{(MCp)_m N}{(\dot{m}Cp)_g} . \tag{4.4}$$

Recognizing that the supply and exhaust sides of the heat exchanger may have different heat transfer coefficients or surface areas, dimensionless groups that parallel those of a recuperator (Kay and London, 1984) can be defined as:

$$NTU_o = \frac{1}{(\dot{m}Cp)_{g.min}}\left[\frac{1}{(hA_s)_s} + \frac{1}{(hA_s)_e}\right]^{-1} \quad \text{and} \quad Cr^*_o = \frac{(MCp)_m N}{(\dot{m}Cp)_{g.min}} . \tag{4.5}$$

In the case of equal flow areas, heat transfer coefficients and mass flow rates on the hot and cold side, NTU_o and Cr^*_o become simply,

$$NTU_o = \frac{hA_s}{2(\dot{m}Cp)_{g.min}} = \frac{NTU}{2} \quad \text{and} \quad Cr^*_o = Cr^* . \tag{4.6}$$

Kays and London (1984) and Shah (1981 and 1988) present the following empirical correlation, which demonstrates the effect of Cr^*_o and NTU_o on the effectiveness of a sensible heat regenerator:

$$\varepsilon = \varepsilon_{cf}\left[1 - \frac{1}{9(Cr^*_o)^{1.93}}\right], \qquad (4.7\ a)$$

where:
$$\varepsilon_{cf} = \frac{1-\exp[-NTU_o(1-C^*)]}{1-C^*\exp[-NTU_o(1-C^*)]}, \text{ and} \qquad (4.7\ b)$$

C^* is the ratio of minimum to maximum heat capacity rate of the air streams. Equation (4.7) was obtained by correlating the numerical results of Lambertson (1958) and Bahnke and Howard (1964) and is recommended for $\varepsilon \leq 90\%$. Equation (4.7) agrees with the numerical data compiled in Kays and London (1984) within 1% for $C^* = 1$ and the following parameter ranges: $2 < NTU_o < 14$ for $Cr^*_o \geq 1.5$; $NTU_o \leq 20$ for $Cr^*_o \geq 2$; and a complete range of NTU_o for $Cr^*_o \geq 5$. As C^* decreases, the error in equation (4.7) increases with lower values of Cr^*_o. As Cr^*_o becomes large, the effectiveness approaches the effectiveness of a counterflow heat recuperator (ε_{cf}). Increasing NTU_o and Cr^*_o increases the effectiveness of a sensible rotary heat exchanger as is shown in Figure 4.1.

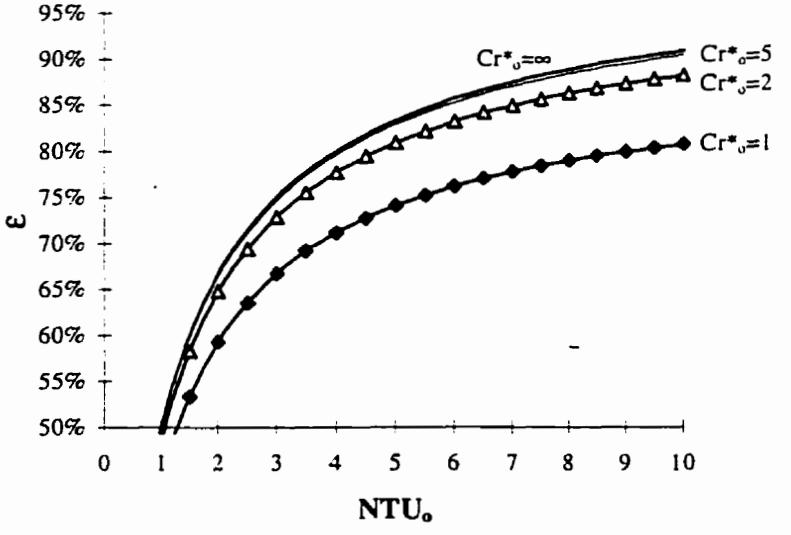

Figure 4.1. *Effectiveness of a counterflow rotary heat exchanger as a function of NTU_o and Cr^*_o for $C^* = 1$ (equation (4.7)).*

4.2 DIMENSIONLESS GROUPS FOR ENERGY WHEELS

The method of deriving the governing dimensionless heat and moisture transfer groups for energy wheels from the governing equations follows the method of Shah (1981) described in Section 4.1. The governing equations for simultaneous heat and moisture transfer in energy wheels are presented in Chapter 2 and are summarized below:

$$\rho_g Cp_g A_g \frac{\partial T_g}{\partial t} + U\rho_g Cp_g A_g \frac{\partial T_g}{\partial x} - \dot{m}' h_{fg} \eta + h \frac{A'_s}{L}(T_g - T_m) = 0 \ , \qquad (4.8)$$

$$\rho_m Cp_m A_m \frac{\partial T_m}{\partial t} - \dot{m}' h_{fg}(1-\eta) - \dot{m}' Cp_w (T_g - T_m) - h \frac{A'_s}{L}(T_g - T_m) = \frac{\partial}{\partial x}(k_m A_m \frac{\partial T_m}{\partial x}), \qquad (4.9)$$

$$A_g \frac{\partial \rho_v}{\partial t} + \frac{\partial}{\partial x}(\rho_v U A_g) + \dot{m}' = 0 \ , \qquad (4.10)$$

$$\frac{\partial \rho_a}{\partial t} + \frac{\partial}{\partial x}(\rho_a U) = 0 \ , \text{ and} \qquad (4.11)$$

$$\dot{m}' = \rho_{d.dry} A_d \frac{\partial u}{\partial t} \ , \qquad (4.12)$$

where during adsorption and desorption, the moisture transfer ($\dot{m}'$) can be calculated by,

$$\dot{m}' = h_m \frac{A'_s}{L}(\rho_v - \rho_{v.m}) \ . \qquad (4.13)$$

During saturation conditions, the density of the water vapor is calculated using,

$$\rho_v = \rho_{v,sat} = \frac{P_{v,sat}}{R_v T_g} \ , \qquad (4.14)$$

where $P_{v,sat}$ is the saturation vapor pressure and is a function of temperature only.

4.2.1 Moisture Transfer

Starting with the equations that govern the transfer (equation (4.10)) and storage (equation (4.12)) of moisture, the dimensionless groups that govern the moisture transfer process (i.e. NTU_{mt} and Cr^*_{mt}) can be developed for balanced mass flow rates (i.e., $\dot{m}_s = \dot{m}_c$). The effect of $(hA_s)^*$ on effectiveness is negligible for the range of $0.25 \leq (hA_s)^* \leq 4$ (Shah, 1981) and is neglected in this thesis.

4.2.1.1 NTU_{mt}

Combining the equation for moisture transfer (equation (4.10)) with the rate of sorption phase change (equation (4.13)) gives,

$$A_g \frac{\partial \rho_v}{\partial t} + \frac{\partial}{\partial x}\left(\rho_v U A_g\right) + h_m \frac{A'_s}{L}\left(\rho_v - \rho_{v,m}\right) = 0 \quad . \tag{4.15}$$

Introducing dimensionless variables for t and x as,

$$x^* = \frac{x}{L} \text{ , and} \tag{4.16 a}$$

$$t^* = \frac{1}{p}\left(t - \frac{x}{U}\right) , \tag{4.16 b}$$

where the second term in t^* is small for small dwell times or carry over rates. The time and spatial derivatives can be written for any dependent variable, χ, as follows,

$$\frac{\partial \chi}{\partial t} = \frac{\partial \chi}{\partial t^*}\frac{\partial t^*}{\partial t} = \frac{1}{p}\frac{\partial \chi}{\partial t^*} \text{ , and} \tag{4.17 a}$$

$$\frac{\partial \chi}{\partial x} = \frac{\partial \chi}{\partial x^*}\frac{\partial x^*}{\partial x} + \frac{\partial \chi}{\partial t^*}\frac{\partial t^*}{\partial x} = \frac{1}{L}\frac{\partial \chi}{\partial x^*} - \frac{1}{p\,U}\frac{\partial \chi}{\partial t^*} \quad . \tag{4.17 b}$$

It should be noted that the above equations apply to the supply or exhaust side of the energy wheel so that each variable could have a subscript s or e. The subscripts have been left out for clarity for the above transformations. Substituting equations (4.17) into equation (4.15) and rearranging yields,

$$\frac{\partial \rho_v}{\partial x^*} = \frac{h_m A'_s}{A_g U}\left(\rho_{v.m} - \rho_v\right) + \frac{\rho_v}{U}\left(\frac{L}{\rho U}\frac{\partial U}{\partial t^*} - \frac{\partial U}{\partial x^*}\right) . \tag{4.18}$$

If it is assumed that the density of dry air is constant or changes little within the energy wheel, the velocity gradient and time derivative can be neglected and equation (4.18) can be approximated by writing it in the standard dimensionless form similar to (4.1),

$$\frac{\partial \rho_v}{\partial x^*} = NTU_{mt}\left(\rho_{v.m} - \rho_v\right) . \tag{4.19}$$

NTU_{mt} is the number of moisture transfer units on the supply or exhaust side of the energy wheel defined as,

$$NTU_{mt} = \frac{h_m A'_s}{A_g U} . \tag{4.20}$$

If the Lewis number $(h/(h_m \rho_g Cp_g)$ is unity, which is a good approximation for simultaneous heat and water vapor transfer in air, NTU_{mt} can be rewritten as,

$$NTU_{mt} = \frac{h}{\rho_g Cp_g}\frac{A'_s}{A_g U} = \frac{hA_s}{(\dot{m}Cp)_g} = NTU . \tag{4.21}$$

Equation (4.21) shows that for Le = 1, the number of moisture transfer units for an energy wheel is equal to the number of heat transfer units for a sensible rotary heat

exchanger. This means that the number of moisture transfer units is independent of the operating humidity and temperature. If, however, the density of the air was not considered constant, NTU_{mt} would be slightly dependent on the operating conditions. Finally it should be noted that, NTU_{mt} on the supply side of the energy wheel will not always be equal to NTU_{mt} on the exhaust side, but these values will be nearly equal for most practical operating conditions.

4.2.1.2 Cr^*_{mt}

Equation (4.12) describes the storage of moisture in the desiccant coated matrix. Introducing the dimensionless independent variables (4.16), and substituting equation (4.13) into equation (4.12) gives,

$$\frac{h_m A'_s}{L}\left(\rho_v - \rho_{v,m}\right) = \frac{\rho_{d,dry} A_d}{p}\frac{\partial u}{\partial t^*} = \frac{\rho_{d,dry} A_d}{p}\frac{\partial u}{\partial \rho_{v,m}}\frac{\partial \rho_{v,m}}{\partial t^*} \quad . \tag{4.22}$$

Rearranging equation (4.22) gives an equation in the standard dimensionless form similar to equation (4.2),

$$\frac{\partial \rho_{v,m}}{\partial t^*} = \frac{NTU_{mt}}{Cr^*_{mt}}\left(\rho_v - \rho_{v,m}\right) , \tag{4.23}$$

where:

$$Cr^*_{mt} = \frac{\rho_{d,dry} A_d L}{A_g U p}\frac{\partial u}{\partial \rho_{v,m}} \quad . \tag{4.24}$$

Using the general sorption curve (i.e., equation (2.32)),

$$u = \frac{Wm}{1 - C + C/\phi} = \frac{Wm}{1 - C + C/\phi_m} , \tag{4.25}$$

Cr^*_{mt} becomes,

$$Cr^*_{mt} = Crm^* \frac{\partial u}{\partial \phi} \frac{\phi}{W} , \tag{4.26}$$

where: $\phi_m \approx \phi$, $\rho_{v,m} \approx \rho_v$ and

$$Crm^* = \frac{\rho_{d,dry} A_d L}{\rho_a A_g U p} = \frac{M_{d,dry} N}{\dot{m}} . \tag{4.27}$$

Further simplification of equation (4.26) to include those parameters most familiar to an HVAC engineer (T and ϕ) by using the Clapeyron equation to represent the saturation vapor pressure and assuming standard atmospheric pressure (101.325 kPa) gives,

$$Cr^*_{mt} = (Crm^*) \frac{\partial u}{\partial \phi} \left(\frac{e^{\left(\frac{5294}{T}\right)}}{10^6} - 1.61\phi \right) , \tag{4.28}$$

where T is in K. The second term in the brackets in equation (4.28) is typically less than 5% of the first term; thus, Cr^*_{mt} is a function of the slope of the sorption curve and the operating temperature and to a lesser extent the relative humidity.

4.2.2 Heat Transfer

By performing a similar analysis as in section 4.2.1, the governing dimensionless groups for heat transfer can be obtained.

4.2.2.1 NTU_{ht}

Starting with the equation that describes the transfer of heat between the air and the matrix (i.e., equation (4.8)) and introducing the dimensionless independent variables and equation (4.13) (which applies to sorption only) gives,

$$\frac{\rho_g Cp_g A_g}{p}\frac{\partial T_g}{\partial t^*} + U\rho_g Cp_g A_g\left(\frac{1}{L}\frac{\partial T_g}{\partial x^*} - \frac{1}{p\,U}\frac{\partial T_g}{\partial t^*}\right) - h_m\frac{A'_s}{L}(\rho_v - \rho_{v,m})h_{fg}\eta + h\frac{A'_s}{L}(T_g - T_m) = 0 \cdot \quad (4.29)$$

Rearranging equation (4.29) yields,

$$\frac{\partial T_g}{\partial x^*} = \frac{hA'_s}{U\rho_g Cp_g A_g}(T_m - T_g) - \frac{h_m A'_s}{U\rho_g Cp_g A_g}(\rho_{v,m} - \rho_v)h_{fg}\eta \ . \quad (4.30)$$

Putting equation (4.30) in the standard dimensionless form of equation (4.1) gives,

$$\frac{\partial T_g}{\partial x^*} = NTU_{ht}(T_m - T_g) \ . \quad (4.31)$$

where:

$$NTU_{ht} = NTU\left[1 - \frac{h_{fg}\eta}{\rho_g Cp_g}\frac{(\rho_{v,m} - \rho_v)}{T_m - T_g}\right] , \quad (4.32)$$

because $Le = 1 = h/(h_m\rho_g Cp_g)$. For NTU_{ht} to be a useful as a design tool, it needs to be calculated from known or determinable quantities. Clearly the ratio $\frac{(\rho_{v,m} - \rho_v)}{T_m - T_g}$ is not directly known to the designer, but can be related to the number of heat and moisture transfer units. Using equations (4.19) and (4.31) this unknown ratio can be expressed as,

$$\frac{(\rho_{v,m} - \rho_v)}{T_m - T_g} = \frac{NTU_{ht}}{NTU_{mt}}\frac{\frac{\partial \rho_v}{\partial x^*}}{\frac{\partial T_g}{\partial x^*}} \approx \frac{NTU_{ht}}{NTU_{mt}}\frac{\varepsilon_l \Delta W}{\varepsilon_s \Delta T_g}\rho_a \ , \quad (4.33)$$

where: $\varepsilon_l = \frac{(W_i - W_o)_l}{(W_{s,i} - W_{e,i})}$, $\varepsilon_s = \frac{(T_i - T_o)_s}{(T_{s,i} - T_{e,i})}$, $\Delta W = W_{s,i} - W_{e,i}$, $\Delta T_g = T_{g_{s,i}} - T_{g_{e,i}}$ and ρ_v and T_g are assumed to be linear functions of x*. Equation (4.33) can be inserted in equation (4.32) to give,

$$NTU_{ht} = NTU\left[1 - \frac{h_{fg}\eta}{\rho_g Cp_g}\frac{NTU_{ht}}{NTU_{mt}}\frac{\varepsilon_l}{\varepsilon_s}\frac{\Delta W}{\Delta T_g}\rho_a\right] . \tag{4.34}$$

Equation (4.34) can be further simplified by defining an operating condition factor as,

$$H^* = \frac{h_{fg}}{\rho_g Cp_g}\rho_a \frac{\Delta W}{\Delta T_g} \approx 2500\frac{\Delta W}{\Delta T_g} , \tag{4.35}$$

and using the fact that NTU = NTU_{mt} for Le = 1. The resulting dimensionless number of heat transfer units is,

$$NTU_{ht} = \frac{NTU}{1 + \eta\frac{\varepsilon_l}{\varepsilon_s}H^*} . \tag{4.36}$$

The number of heat transfer units for an energy wheel is a function of NTU (with no moisture transfer), the ratio of latent to sensible effectiveness and the operating conditions such that, as the fraction of phase change energy entering the air (η) goes to zero, only NTU is a factor. The operating condition factor (H*) can in theory vary from $-\infty$ to $+\infty$, but varies typically from -6 to + 6 for energy wheels used in HVAC applications.

The operating condition factor (H*) is essentially a ratio of latent to sensible energy differences across the energy wheel. This enthalpy ratio can also be expressed in

terms of the sensible heat ratio between two operating points which is familiar to HVAC engineers. The relationship is,

$$H^* = \frac{\Delta H_l}{\Delta H_s} = \left(\frac{\Delta H_s}{\Delta H_t} \right)^{-1} - 1 \ . \tag{4.37}$$

Therefore, H* can be determined graphically by joining the inlet conditions on the psychrometric chart and determining the value of the sensible heat ratio ($\Delta H_s/\Delta H_t$) from the protractor and then calculating H* from equation (4.37). For numerical calculations, H* can be calculated from equation (4.35).

Figure 4.2 shows lines of constant H* for exhaust conditions of 24°C and 50% R.H. and various supply conditions on the psychrometric chart. The value of η is typically less than 0.1 for energy wheels and the ratio of $\varepsilon_l/\varepsilon_s$ will tend to be near unity for practical applications. Therefore the value of NTU_{ht} will tend to be between 0.5 to 3 times the value of NTU for a wheel where no moisture transfer occurs.

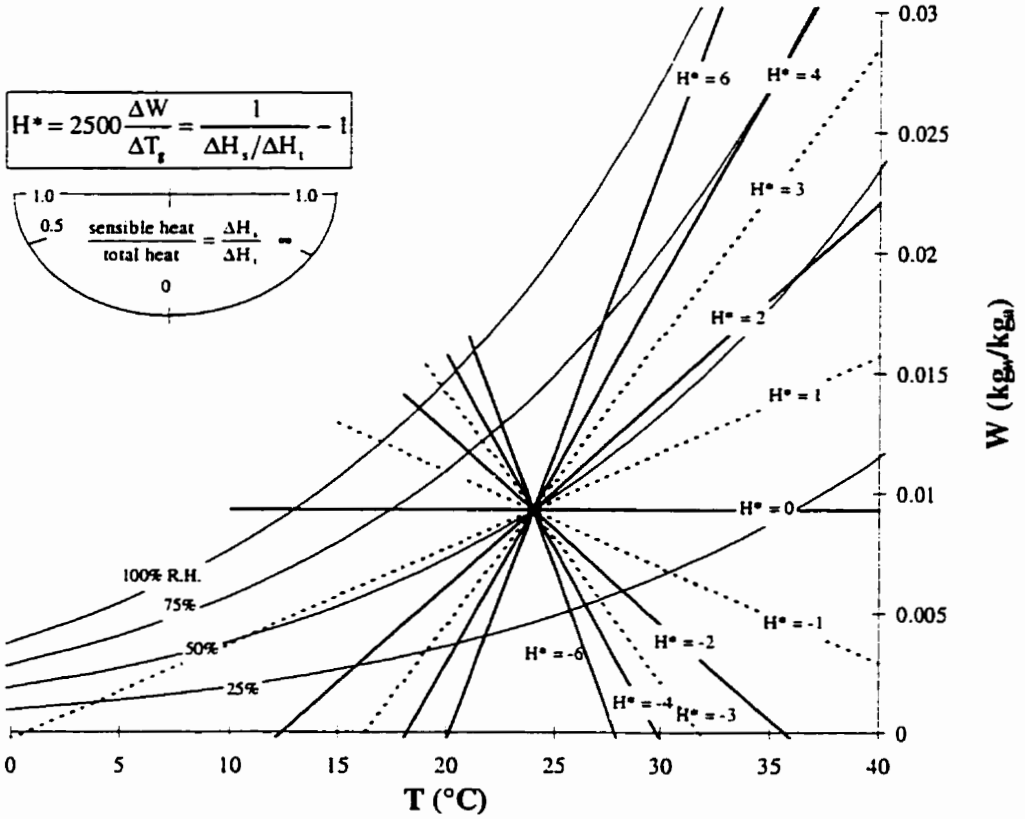

Figure 4.2. *Psychrometric chart showing the operating condition factor (H*) for exhaust conditions of 24°C and 50% R.H. and different supply conditions.*

If H* is positive (i.e. heat and moisture transfer in the same direction between the supply and exhaust air), the moisture transfer will decrease NTU_{ht} and the sensible effectiveness. On the other hand, if H* is negative, the moisture transfer will increase NTU_{ht}. This can be explained by the fact that adsorption is exothermic. When moisture is adsorbed on the matrix, heat is released which (when $\eta > 0$) is partly taken up by the air. This will tend to increase the local temperature of the air and consequently the temperature of the air leaving the energy wheel. If H* is positive, the warmer of the two inlet air steams is simultaneously cooled and dried and the cooler air stream is heated and humidified. When moisture is removed from the warm air by adsorption onto the matrix,

energy is released and the air temperature will increase and consequently the ability for the energy wheel to cool the warm air will be reduced. The net result will be that the sensible effectiveness will decrease. On the other hand, if H* is negative, the warm air is simultaneously cooled and humidified. In this case, when moisture is added to the warm air by desorption, the temperature of the warm air will decrease (desorption is endothermic) which will increase the sensible effectiveness of the energy wheel.

4.2.2.2 Cr^*_{ht}

To develop the equation for Cr^*_{ht}, the starting point is the energy equation for the matrix (equation (4.9)) which, upon introduction of the dimensionless independent variable for time, is

$$\frac{\rho_m Cp_m A_m}{p}\frac{\partial T_m}{\partial t^*} - h_m \frac{A'_s}{L}(\rho_v - \rho_{v,m})h_{fg}(1-\eta) - h\frac{A'_s}{L}(T_g - T_m) = 0 \ , \qquad (4.38)$$

where the term $\dot{m}' Cp_w (T_g - T_m)$ (which is several orders of magnitude smaller than the other terms) and axial heat conduction in the matrix have been neglected. It should be noted that axial conduction can alter the effectiveness of energy wheels and will need to be accounted for with methods described in Shah (1988 and 1981). Rearranging equation (4.38) shows that the standard dimensionless form is,

$$\frac{\partial T_m}{\partial t^*} = \frac{NTU_{ht}}{Cr^*_{ht}}(T_g - T_m) \ , \qquad (4.39)$$

where,

$$\frac{NTU_{ht}}{Cr^*_{ht}} = \frac{NTU}{Cr^*}\left[1 + \frac{h_{fg}(1-\eta)}{\rho_g Cp_g}\frac{\rho_v - \rho_{v,m}}{T_g - T_m}\right] . \qquad (4.40)$$

Using equations (4.33) and (4.35), equation (4.40) can be simplified to,

$$\frac{NTU_{ht}}{Cr^*_{ht}} = \frac{NTU}{Cr^*}\left[1 + (1-\eta)\frac{NTU_{ht}}{NTU_{mt}}\frac{\varepsilon_l}{\varepsilon_s}H^*\right] . \tag{4.41}$$

Rearranging equation (4.41) to solve for Cr^*_{ht} and using the definition of NTU_{ht} from equation (4.36) and Le = 1 gives,

$$Cr^*_{ht} = \frac{Cr^*}{1 + \frac{\varepsilon_l}{\varepsilon_s}H^*} . \tag{4.42}$$

Examining equation (4.42) shows that Cr^*_{ht} is independent of η, but dependent on the ratio of latent to sensible effectiveness ($\varepsilon_l/\varepsilon_s$) and the operating condition factor (H*). Since H* varies from -6 to +6, in typical HVAC applications, the value of Cr^*_{ht} can be positive or negative.

4.2.3 Energy Transfer

There are only two independent effectiveness values for energy wheels. In this thesis, the latent and sensible effectivenesses have been chosen and the total effectiveness can be derived from these. Starting with the definition of total effectiveness,

$$\varepsilon_t = \frac{\dot{m}_s\left(H_{s,i} - H_{s,o}\right)}{\dot{m}_{min}\left(H_{s,i} - H_{e,i}\right)} = \frac{\dot{m}_e\left(H_{e,o} - H_{e,i}\right)}{\dot{m}_{min}\left(H_{s,i} - H_{e,i}\right)} , \tag{4.43}$$

and introducing the definition of enthalpy as,

$$H = Cp_a T_g + W\left(h_{fg} + Cp_v T_g\right) , \tag{4.44}$$

where T is in °C, the total effectiveness can be shown to be,

$$\varepsilon_t \approx \frac{\varepsilon_s + \varepsilon_l H^*}{1 + H^*} . \tag{4.45}$$

Equation (4.45) shows that ε_t is essentially a weighted average of ε_s and ε_l. As $H^* \rightarrow \infty$ (i.e., dominant moisture transfer), $\varepsilon_t \rightarrow \varepsilon_l$ and as $H^* \rightarrow 0$ (i.e., negligible moisture transfer), $\varepsilon_t \rightarrow \varepsilon_s$. Also as $H^* \rightarrow -1$ (i.e., supply and exhaust enthalpies nearly equal), $\varepsilon_t \rightarrow \pm\infty$ if $\varepsilon_s \neq \varepsilon_l$ which was discovered in both measured and simulated results in Chapter 3. Equation (4.45) gives values of ε_t that are in close agreement with those obtained from simulations.

4.2.4 Saturation Conditions

Saturation operating conditions will be addressed in Chapter 5 and are not discussed here except to note why the effectiveness and governing dimensionless groups are more difficult to define under these conditions. When the energy wheel is operating under condensation and evaporation conditions, the amount of moisture that the matrix can store is much larger than it can store during sorption conditions. This is expected to increase Cr^*_{mt} and similarly increase ε_l. Furthermore, when condensation occurs, the moisture transfer to the matrix is controlled by the mass flow rate of water vapor and the axial gradient of temperature. Condensation will occur at a rate that will keep the air, that is flowing through the wheel, saturated. This may result in a greater phase change rate than that governed by convection mass transfer with only sorption. In a sense, this is like increasing the convective mass transfer coefficient h_m. If h_m is increased, NTU_{mt} will also increase, resulting in an increase in ε_l. The value of ε_l calculated with the correlations in this chapter will be a conservative estimate during condensation and frosting conditions. On the other hand, the value of ε_s calculated with the correlations

will be quite accurate because ε_s is less affected by saturation conditions than ε_l as will be seen in Chapter 5. It is expected that the total effectiveness can still be calculated with equation (4.45) during saturation conditions.

4.2.5 Summary

The governing dimensionless groups for simultaneous heat and moisture transfer in energy wheels have been developed. These dimensionless groups parallel the dimensionless groups for rotary sensible heat exchangers which can be found in many heat exchanger books. For the case of C* = 1, the dimensionless groups for coupled heat and mass transfer are NTU_{mt}, Cr^*_{mt}, NTU_{ht} and Cr^*_{ht} which are related to NTU and Cr* for rotary sensible heat exchangers. These dimensionless groups are functions of the operating temperature and humidity of the wheel and the sorption characteristics of the desiccant as well as functions of NTU, Cr* and Crm*. Crm* is a moisture capacitance ratio that is analogous to Cr*. The importance of the operating conditions are evident in the new dimensionless groups and an operating condition factor (H*) has been defined which depends on the ratio of the latent to sensible energy change across the energy wheel.

To summarize the findings of this section, the simplified governing equations for heat and moisture transfer with the dimensionless independent variables are listed below. The equations for moisture transfer are:

$$\frac{\partial \rho_v}{\partial x^*} = NTU_{mt}\left(\rho_{v,m} - \rho_v\right), \text{ and} \tag{4.46}$$

$$\frac{\partial \rho_{v,m}}{\partial t^*} = \frac{NTU_{mt}}{Cr^*_{mt}}\left(\rho_v - \rho_{v,m}\right), \tag{4.47}$$

where:

$$NTU_{mt} = NTU = \frac{hA_s}{\dot{m}Cp_a}, \tag{4.48}$$

$$Cr^*_{mt} = (Crm^*)\frac{\partial u}{\partial \phi}\left(\frac{e^{\left(\frac{5294}{T}\right)}}{10^6} - 1.61\phi\right), \text{ and} \tag{4.49}$$

$$Crm^* = \frac{M_{d,dry}N}{\dot{m}}. \tag{4.50}$$

Equation (4.46) shows that NTU_{mt} is the proportionality constant that relates the axial gradient of water vapor density in the air to the driving potential for moisture transfer, which is the difference between the water vapor density on the surface of the desiccant to the water vapor density in the air. Similarly, equation (4.47) shows that NTU_{mt} / Cr^*_{mt} is the proportionality constant which relates the storage of water vapor in the desiccant to the potential for moisture transfer. These proportionality constants are clearly dependent on the physical size, shape and rotational speed of the energy wheel as well as the mass flow rate of air. Cr^*_{mt} also depends on the operating temperature and humidity. It should be noted that the definition of NTU presented in equation (4.48) uses the approximation that $(\dot{m}Cp)_g \approx \dot{m}Cp_a$ for typical operating conditions for energy wheels.

The simplified equations for heat transfer are:

$$\frac{\partial T_g}{\partial x^*} = NTU_{ht}(T_m - T_g), \text{ and} \tag{4.51}$$

$$\frac{\partial T_m}{\partial t^*} = \frac{NTU_{ht}}{Cr^*_{ht}}(T_g - T_m) \ , \tag{4.52}$$

where:

$$NTU_{ht} = \frac{NTU}{1 + \eta \frac{\varepsilon_l}{\varepsilon_s} H^*} \ , \tag{4.53}$$

$$Cr^*_{ht} = \frac{Cr^*}{1 + \frac{\varepsilon_l}{\varepsilon_s} H^*} \text{ , and} \tag{4.54}$$

$$Cr^* = \frac{(MCp)_m N}{\dot{m} Cp_a} \ . \tag{4.55}$$

Equations (4.51) and (4.52) are analogous to equations (4.46) and (4.47) except that Cr^*_{ht} (and NTU_{ht}, if η is large) can have negative values. This may seem physically impossible, but negative values for NTU_{ht} and Cr^*_{ht} can be explained in light of the governing equations shown above. For example, equation (4.51) shows that the axial gradient of the temperature in the air will be proportional to the temperature difference between the air and the matrix. The proportionality constant, NTU_{ht}, will typically be positive. However, if the moisture transfer is dominant and in the opposite direction of the heat transfer (i.e., H^* is a large negative value), NTU_{ht} can have a negative value. According to equation (4.51), this means that the axial temperature gradient in the air will be negative when $T_m > T_g$ and NTU_{ht} is negative. This is an important observation because it means that even though the matrix is warmer than the air, the air temperature can decrease as it flows through the wheel if the heat released due to phase change is large.

Similarly in equation (4.52), the change in temperature of the matrix with time is proportional to the temperature difference between the gas and matrix. Under normal conditions, the temperature of the matrix will increase when the temperature of the air is warmer than the temperature of the matrix. However, in the case of $NTU_{ht}/Cr^*_{ht} < 0$, the change in the temperature of the matrix will be opposite to the convection heat transfer. That is, when the moisture transfer is large and in the opposite direction of the heat transfer, the temperature of the matrix can increase with time even though the temperature of the matrix is greater than the temperature of the air. In this case, the heat transfer due to moisture transfer is larger than the heat transfer due to radial heat convection and the resulting net heat transfer will be in the opposite direction of the radial convection. These observations are very important because they explain the strong coupling between heat and moisture transfer.

Finally it is important to note that the assumption of Le = 1 is used in this analysis. As shown previously, this means that $NTU_{mt} = NTU$ but does not guarantee that $\varepsilon_s = \varepsilon_l$ because NTU_{ht}, Cr^*_{ht} and Cr^*_{mt} can all have different values depending on the wheel design and operating conditions.

Summarizing, the effectivenesses of energy wheels for $C^* = 1$, $0.25 \le (hA_s)^* \le 4$ and $k_m = 0$ are expected to be functions of the overall dimensionless groups as follows:

$$\varepsilon_s = f_1\left(NTU_{ht,o}, Cr^*_{ht,o}\right), \tag{4.56}$$

$$\varepsilon_l = f_2\left(NTU_{mt,o}, Cr^*_{mt,o}\right), \text{ and} \tag{4.57}$$

$$\varepsilon_t = f_3(\varepsilon_s, \varepsilon_l, H^*) \; ; \tag{4.58}$$

where the overall dimensionless groups are defined as:

$$NTU_{mt,o} = NTU_o \; , \tag{4.59}$$

$$Cr^*_{mt,o} = (Crm^*_o)\frac{\partial u}{\partial \phi}\left(\frac{e^{\left(\frac{5294}{T}\right)}}{10^6} - 1.61\phi\right) \; , \tag{4.60}$$

$$NTU_{ht,o} = \frac{NTU_o}{1+\eta\dfrac{\varepsilon_l}{\varepsilon_s}H^*} \; , \text{ and} \tag{4.61}$$

$$Cr^*_{ht,o} = \frac{Cr^*_o}{1+\dfrac{\varepsilon_l}{\varepsilon_s}H^*} \; ; \tag{4.62}$$

with:

$$NTU_o = \frac{1}{(\dot{m}Cp_a)_{min}}\left[\frac{1}{(hA_s)_s} + \frac{1}{(hA_s)_e}\right]^{-1} \; , \tag{4.63}$$

$$Cr^*_o = \frac{(MCp)_m N}{(\dot{m}Cp_a)_{min}} \; , \tag{4.64}$$

$$Crm^*_o = \frac{M_{d,dry} N}{\dot{m}_{min}} \; , \text{ and} \tag{4.65}$$

$$H^* = \frac{\Delta H_l}{\Delta H_s} = \left(\frac{\Delta H_s}{\Delta H_t}\right)^{-1} - 1 = 2500\frac{\Delta W}{\Delta T_g} \; . \tag{4.66}$$

4.3 SENSITIVITY OF DIMENSIONLESS GROUPS

In this section, the importance of the dimensionless groups for heat and moisture transfer are shown through sensitivity studies. The effect of the sorption curve and the operating condition factor (H*) as well as the operating temperature and relative

humidity will be studied for the wheel parameters given in Table 4.1. The effect of individual dimensional parameters such as mass flow rate, surface area, wheel mass and wheel speed will also be examined. The sorption curve used in the simulations is the general sorption curve of equation (4.25) which can model several desiccant coatings, such as molecular sieve, silica gel, activated alumina and activated carbon.

The general governing equations and numerical model, developed in Chapter 2, are used to generate the numerical data presented in this chapter rather than the simplified governing equations, developed in Section 4.2, so that the numerical results are unaffected by simplifications made in developing the dimensionless groups. In addition to the approximations listed in Section 2.1, storage in the air (or carry over) is assumed negligible and constant convective heat and moisture transfer coefficients are used. These approximations are expected to change the effectiveness by typically less than 2% (see Section 2.7). Axial heat conduction in the wheel is neglected (i.e., $k_m = 0$) but can be treated by methods presented in Shah (1988 and 1981). All the simulations are performed with a grid size of 0.001 m and a time step of 0.01 s. The numerical inaccuracy for these grid and time step sizes is expected to be less than ±0.5% for effectiveness (see Section 2.6). Also, all simulations use balanced mass flow rates (i.e., $\dot{m}_s = \dot{m}_e$).

Table 4.1. Energy wheel parameters used in the dimensionless group sensitivity studies.

Wheel number	NTU_o	Cr^*_o	Crm^*_o
1	10	10	10
2	5	5	5
3	3	3	3

4.3.1 Effect of Sorption Curve on Latent Effectiveness

The storage of moisture in the desiccant ($Cr^*_{mt,o}$) depends on the slope of the sorption curve as can be seen in the following equation,

$$Cr^*_{mt,o} = (Crm^*_o)\left.\frac{\partial u}{\partial \phi}\right|_{\phi_{ave}} \left(\frac{e^{\left(\frac{5294}{T_{ave}}\right)}}{10^6} - 1.61\,\phi_{ave} \right), \tag{4.67}$$

where:

$$Crm^*_o = \frac{M_{d,dry}\,N}{\dot{m}_{min}}, \text{ and} \tag{4.68}$$

T_{ave} is $(T_{s,i} + T_{e,i})/2$ in K and ϕ_{ave} is $(\phi_{s,i} + \phi_{e,i})/2$. It is expected that $Cr^*_{mt,o}$ will be proportional to the slope of the sorption curve at the average operating humidity. Therefore, to see if the latent effectiveness changes as expected with changes in the slope of the sorption curve, simulations with constant exhaust conditions (24°C and 50% R.H.) and various supply relative humidities and a constant supply temperature of 35°C are given in Figure 4.3 for the three wheels listed in Table 4.1 with various sorption curve constants (C). Wm is also varied in Figure 4.3.

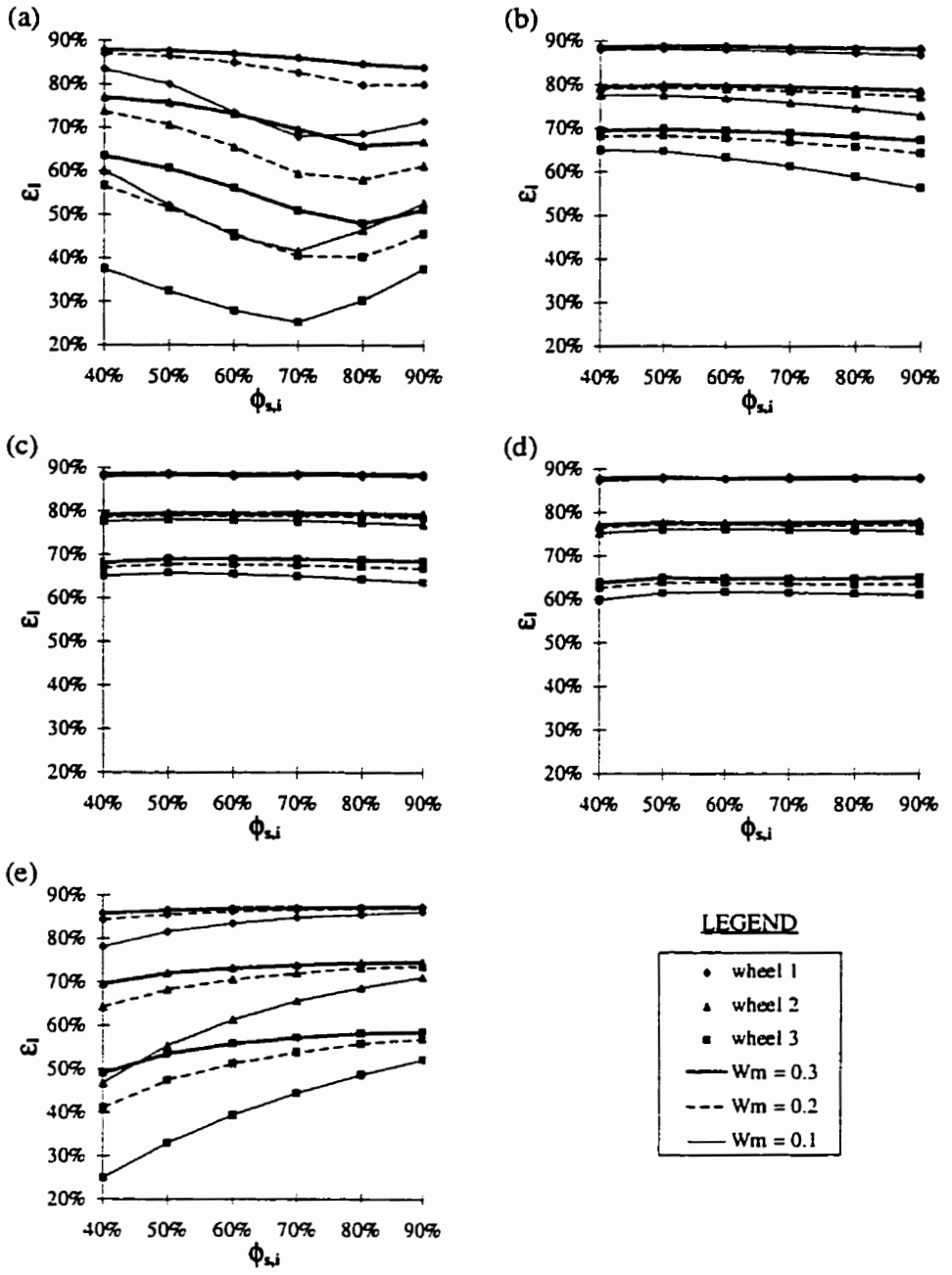

Figure 4.3. *Variation in latent effectiveness with supply inlet humidity for different energy wheels and sorption curve constants: (a) C = 0.01, (b) C = 0.1, (c) C = 1, (d) C = 10 and (e) C = 100 with* $T_{e,i}$ *= 24°C,* $\phi_{e,i}$ *= 50% and* $T_{s,i}$ *= 35°C.*

The results in Figure 4.3 show a wide range of effectiveness values for the different wheels with different sorption curves and supply inlet humidities. To help

explain the results in Figure 4.3, the sorption curves and slope of the sorption curve are presented in Figure 4.4.

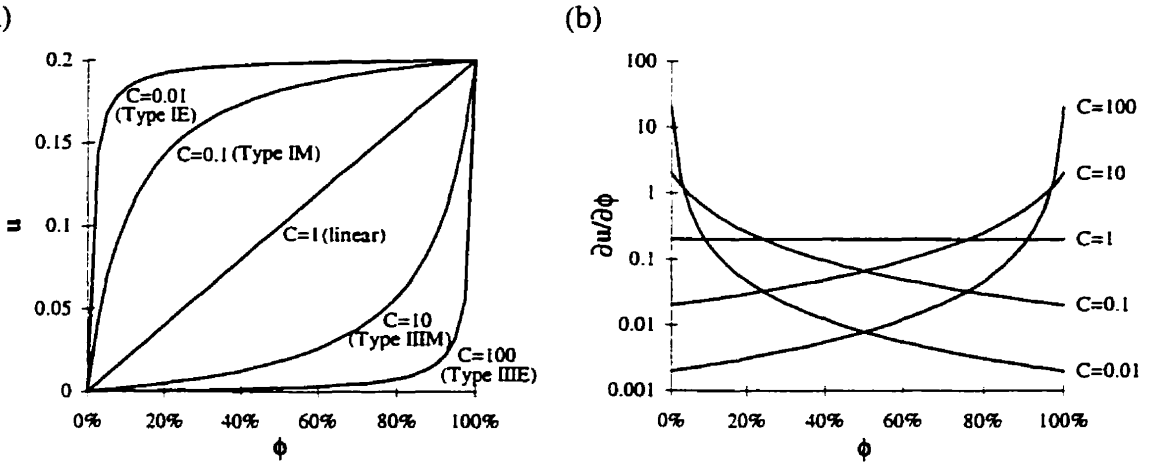

Figure 4.4. *The (a) sorption curve and (b) slope of the sorption curve for Wm = 0.2.*

The results in Figure 4.3 clearly show that the slope of the sorption curve influences the latent effectiveness, particularly for wheel 3 which has low values of NTU_o, Cr^*_o and Crm^*_o. The effectiveness values for a linear sorption curve (C = 1) are the highest and are nearly constant with changing humidity because the slope of a linear sorption curve is constant as a function of ϕ.

Figure 4.3(a) shows that a wheel coated with a Type I extreme (Type IE) desiccant (i.e., C = 0.01) will have a high effectiveness at low supply inlet relative humidities but ε_l decreases as ϕ increases. This result can be explained from equation (4.67) and Figure 4.4 because the slope of a Type I extreme sorption curve is high for low values of ϕ and decreases as ϕ increases. At about 70% relative humidity, ε_l begins to increase with increasing ϕ for a Type IE sorption curve (i.e., a molecular sieve

desiccant coating) because saturation conditions begin at this humidity as will be shown in Chapter 5. The change in effectiveness is particularly large for wheel 3 which has a low value of Crm^*_o. This trend of increasing sensitivity of $Cr^*_{mL,o}$ for lower value of $Cr^*_{mL,o}$ is the same as for regenerative sensible heat exchangers shown in Figure 4.1.

The variation of effectiveness as a function of relative humidity for a wheel with a Type III extreme (Type IIIE) desiccant (i.e., C = 100) is opposite to that for a wheel with a Type IE desiccant. As ϕ increases, ε_t increases for the Type IIIE desiccant because the slope of the sorption curve increases with increasing ϕ. The results predicted with Type I and III moderate sorption curves are similar to those for their respective extreme sorption curves except that the change in ε_t is much smaller because the slope of the sorption curve changes less dramatically with ϕ.

The results in Figure 4.3 show that a linear sorption curve has the highest effectiveness over a typical range of operating conditions. Figure 4.4(b) shows that this is due to the steep slope of the linear sorption curve over the range $25\% < \phi < 75\%$. This type of desiccant (e.g., silica gel) is therefore recommended for most air conditioning energy recovery applications where both sensible and latent energy transfer occur. As a result, the linear sorption curve will be used for simulations in the rest of this chapter unless specified otherwise. An additional advantage of silica gels is that they have high moisture capacities, typically 40% by mass (i.e., Wm = 0.4). This will further increase ε_t as can be seen in Figure 4.3.

Desiccant dryers, which are intended to transfer water vapor, are very different than energy wheels. The reason why a Type 1M desiccant has been recommended for desiccant dryers by several researchers (e.g., Zheng et al., 1993 and Charoensupaya and Worek, 1988 and Collier et al., 1986) is now apparent when Figures 4.3 and 4.4 are examined together with equation (4.67). The inlet conditions to a desiccant dryer are typically 90°C & 3-5% R.H. for regeneration and 35°C & 40-45% R.H. for air drying, giving an average operating humidity in the desiccant dryer wheel of 20 to 25%. At this humidity, the Type 1M sorption curve has the largest slope (see Figure 4.4(b)) and therefore would be expected to perform the best for these operating conditions. Clearly, $Cr^*_{mt,o}$ is essential to understand changes in ε_l caused by changes in the sorption curve and inlet humidity for both desiccant dryers and energy wheels.

4.3.2 Effect of Temperature on Latent Effectiveness

The storage of moisture in the desiccant ($Cr^*_{mt,o}$) depends on the operating temperature of the energy wheel as indicated in equation (4.67). Equation (4.67) shows that $Cr^*_{mt,o}$ and consequently ε_l is expected to decrease as the average operating temperature increases. Figure 4.5 shows simulations of the variation in latent effectiveness due to changes in the operating temperature with constant exhaust conditions (24°C and 50% R.H.) and different supply temperatures and a constant supply humidity of 60%.

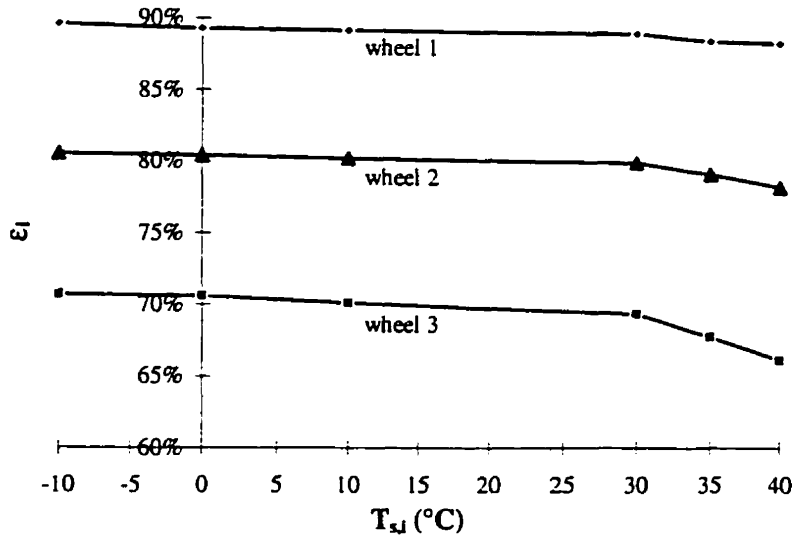

Figure 4.5. *Latent effectiveness versus supply inlet temperature for the energy wheels in Table 4.1 with $T_{e,i}$ = 24°C, $\phi_{e,i}$ = 50% and $\phi_{s,i}$ = 60%.*

The results in Figure 4.5 suggest that the operating temperature affects the latent energy performance of energy wheels, especially at high values of inlet temperature. The decrease in ε_l for $T_{s,i} > 30°C$ is expected from the dimensionless group $Cr^*_{mt,o}$. The decrease in effectiveness is particularly large for wheel 3 which has low values of NTU_o, Cr^*_o and Crm^*_o. Wheels 1 and 2 are less affected by changes in operating temperature because they have higher values of NTU_o, Cr^*_o and Crm^*_o.

4.3.3 Effect of H* and η on Sensible Effectiveness

According to the developed dimensionless groups for heat transfer,

$$NTU_{ht,o} = \frac{NTU_o}{1+\eta\frac{\varepsilon_l}{\varepsilon_s}H^*} \quad \text{and} \tag{4.69}$$

$$Cr^*_{ht,o} = \frac{Cr^*_o}{1+\frac{\varepsilon_l}{\varepsilon_s}H^*}, \tag{4.70}$$

where:
$$NTU_o = \frac{hA_s}{(\dot{m}Cp_a)_{min}} \quad \text{and} \tag{4.71}$$

$$Cr^*_o = \frac{(MCp)_m N}{(\dot{m}Cp_a)_{min}} \quad . \tag{4.72}$$

Equations (4.69) to (4.72) show that the effectiveness of an energy wheel should depend on the operating condition factor (H*) and the fraction of phase change energy that is delivered directly to the air (η). This is the case as can be seen in Figure 4.6 which shows the sensible effectiveness as a function of H* for the three wheels listed in Table 4.1 when $\eta = 0$ and $\eta = 0.1$. The simulation results in Figure 4.6 have exhaust inlet conditions of 24°C and 50% R.H. and a supply inlet temperature of 27°C.

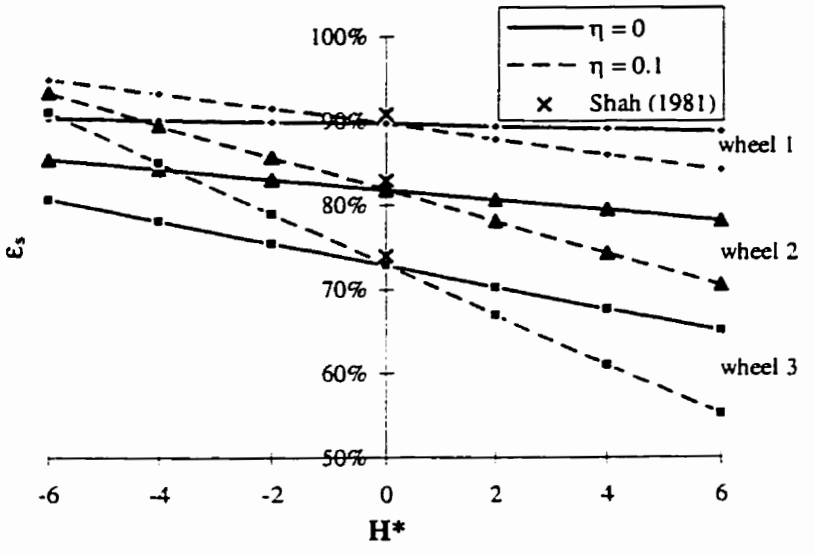

Figure 4.6. *Effect of H* and η on the sensible effectiveness of different energy wheels with $T_{e,i} = 24°C$, $\phi_{e,i} = 50\%$ and $T_{s,i} = 27°C$.*

Figure 4.6 simulation results show that the sensible effectiveness is dependent on both H* and η with ε_s being a linear function of H*. As H* and/or η increase, ε_s

decreases. These results can be explained with equations (4.69) and (4.70) which show that both $NTU_{ht,o}$ and $Cr^*_{ht,o}$ decrease as H^* increases, but only $NTU_{ht,o}$ decreases with η. When $H^* = 0$, $NTU_{ht,o} = NTU_o$ and $Cr^*_{ht,o} = Cr^*_o$ and the conventional correlation for sensible regenerative heat exchangers (i.e. equation (4.7)) is expected to apply. This is found to be the case with the difference between the simulated values and those calculated with the sensible wheel correlation being less than 1%, when $H^* = 0$. Figure 4.6 indicates that large errors will result if the sensible wheel correlation is applied to operating conditions where moisture transfer is significant. This explains the results of Section 2.7 where during cold operating conditions the sensible effectiveness could be predicted reasonably accurately with the correlation for sensible regenerative heat exchangers, but significant errors occurred when the temperature and humidity were high.

Similar to the previous two sections, Figure 4.6 shows that wheel 3 is more sensitive to the operating conditions (i.e., H^*) and η than wheels 1 and 2. The reason for this is simply that decreasing $NTU_{ht,o}$ and $Cr^*_{ht,o}$ has a larger effect on ε_s when $NTU_{ht,o}$ and $Cr^*_{ht,o}$ are small.

The results in Figure 4.6 show a very important characteristic of energy wheels: increasing the moisture transfer decreases ε_s for $H^* > 0$. For most operating conditions of practical importance, H^* is positive, which means that, if H^* is large and high sensible effectivenesses are sought, wheels with larger values of NTU_o and Cr^*_o must be used because the moisture transfer will decrease the heat transfer.

4.3.4 Verification of NTU_o, Cr^*_o and Crm^*_o

The governing dimensionless groups, NTU_o $\left(=\frac{hA_s}{(\dot{m}Cp_a)_{min}}\right)$, Cr^*_o $\left(=\frac{(MCp)_m N}{(\dot{m}Cp_a)_{min}}\right)$ and Crm^*_o $\left(=\frac{M_d N}{\dot{m}_{min}}\right)$, each include several dimensional parameters. The purpose of this section is to verify that these complete dimensionless groups affect the effectiveness regardless of the value of the individual dimensional parameters. Figure 4.7 presents simulation results that show how NTU_o affects ε_s and ε_l when NTU_o is changed numerically by changing the convective heat transfer coefficient (h), the heat and mass transfer surface area (A_s) and the mass flow rate of dry air ($\dot{m}$) from the base parameters shown in Table 4.2.

Table 4.2. *Energy wheel base parameters ($NTU_o = Cr^*_o = Crm^*_o = 10$) used to study the sensitivity of each dimensional parameter.*

h ($W/(m^2 \cdot K)$)	A_s (m^2)	$\dot{m}$ (kg/s)	N (cycles/s)	$(M\ Cp)_m$ ($J/(kg \cdot K)$)	M_d (kg)
40	252	0.5	1/3	15120	15

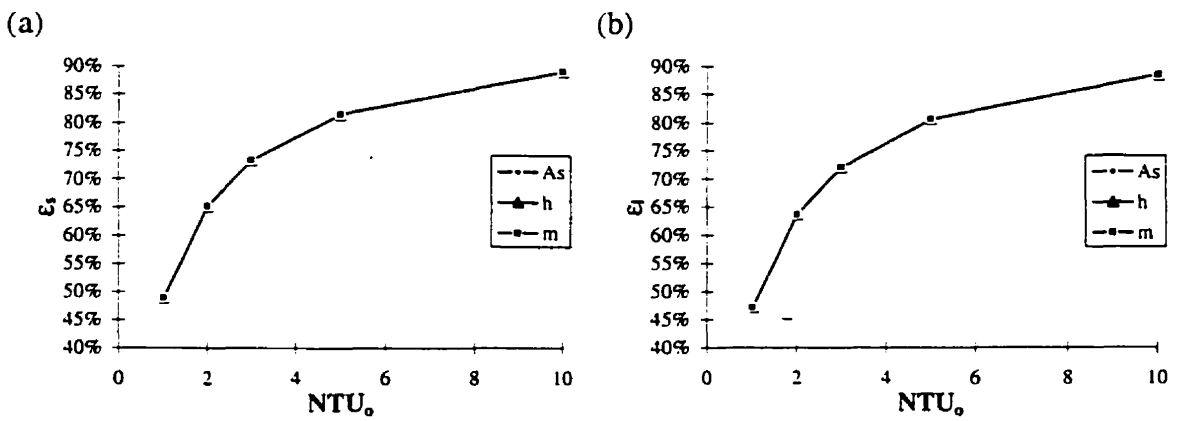

Figure 4.7. *Effect of NTU_o on (a) ε_s and (b) ε_l. NTU_o is changed by changing h, A_s and $\dot{m}$ with $T_{e,i} = 24°C$, $\phi_{e,i} = 50\%$ and $T_{s,i} = 35°C$, $\phi_{s,i} = 60\%$.*

It can be seen in Figure 4.7 that the effectiveness of the energy wheel is the same at any given value of NTU_o regardless of which dimensional parameter is changed to attain the specific value of NTU_o. In Figure 4.7, $Cr^*_o = Crm^*_o = \text{constant}$, therefore when $\dot{m}$ is changed, M_d and M_m are also changed to keep Cr^*_o and Crm^*_o constant. Figure 4.7 shows that the effect of NTU_o on the sensible and latent effectiveness is similar to that for a counter flow heat exchanger.

Figures 4.8 and 4.9 show that Cr^*_o and Crm^*_o affect the effectiveness values in a manner similar to the way Cr^*_o affects the effectiveness of a sensible heat regenerator. Cr^*_o has a larger effect than Crm^*_o. The influence of individual dimensional parameters can clearly be seen to be of secondary importance to the influence of the entire dimensionless group. The greatest difference between the effectiveness calculated with different values of the dimensional parameters, but with the same values of NTU_o, Cr^*_o and Crm^*_o, is 0.3%. This shows that these dimensionless groups are applicable to energy wheels. It is also interesting to note that Cr^*_o and Crm^*_o affect both ε_s and ε_l which shows that the storage of heat and moisture in the energy wheel are coupled. This coupling must be accounted for in the effectiveness correlations.

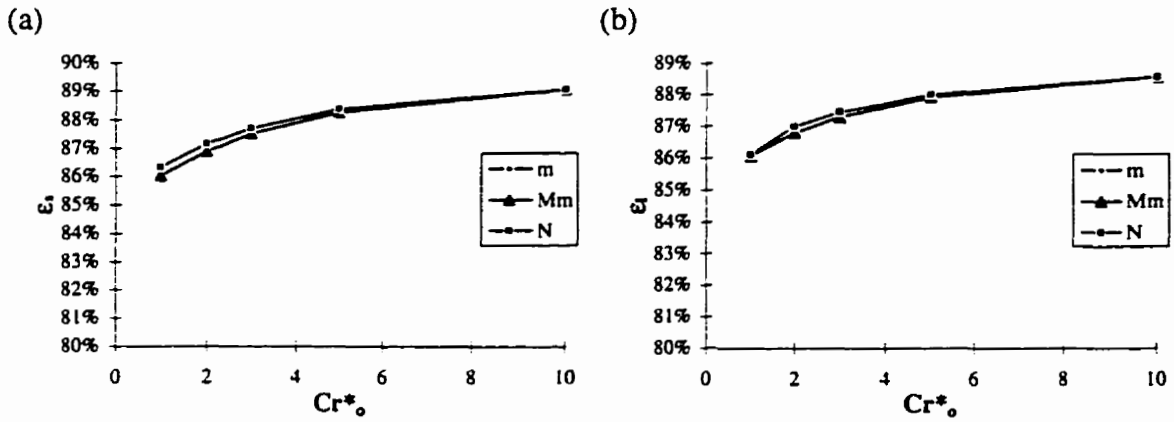

Figure 4.8. Effect of Cr^*_o on (a) ε_s and (b) ε_l. Cr^*_o is changed by changing M_m, N and $\dot{m}$ with $T_{e,i} = 24°C$, $\phi_{e,i} = 50\%$ and $T_{s,i} = 35°C$, $\phi_{s,i} = 60\%$.

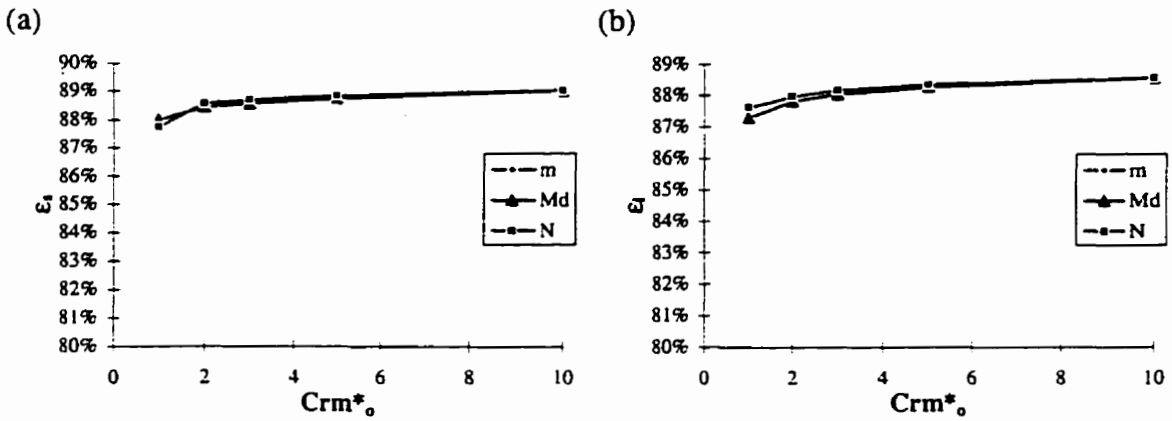

Figure 4.9. Effect of Crm^*_o on (a) ε_s and (b) ε_l. Crm^*_o is changed by changing M_d, N and $\dot{m}$ with $T_{e,i} = 24°C$, $\phi_{e,i} = 50\%$ and $T_{s,i} = 35°C$, $\phi_{s,i} = 60\%$.

4.4 EFFECTIVENESS CORRELATIONS

Although engineering correlations are typically based on measured data, numerical data is sometimes used when a large range of accurate experimental data is unavailable. Correlations based on numerical data have been presented by Lambertson (1958) and Shah (1981) for sensible heat exchangers and by Stiesch et al. (1995) for energy wheels. Similarly, in this section, correlations for sensible, latent and total effectiveness are developed from numerical data. In each case, the dimensionless groups

are used to fit the simulation data with a correlation that has a similar form as the effectiveness correlation for a sensible rotary heat exchanger. An equation of this form is used because the governing equations for energy wheels and sensible regenerators are of the same form and therefore the solutions to the governing equations are expected to be similar. The agreement between the correlations and simulation data is nearly as good as that presented by Shah (1981 and 1988) despite the fact that the number of variables is larger and several simplifications and approximations have been made in determining the dimensionless groups. Although the dimensionless variables developed in Section 4.2 have physical significance as shown in Section 4.3, only the dimensionless components of $NTU_{ht,o}$ and $Cr^*_{ht,o}$ have been chosen for the sensible effectiveness correlation. Correlations of ε_s with $NTU_{ht,o}$ and $Cr^*_{ht,o}$ explicitly formulated proved to be slightly less accurate and for a narrower range of variables than the ones finally presented. Furthermore, ε_s and ε_l can be calculated independently with the selected correlations, eliminating the need for an iterative solution. The correlations presented in this section were determined by minimizing the maximum difference between over 600 simulated effectiveness values and those predicted by the correlation. The coefficients of the correlation were determined using an optimization routine in a commercially available spreadsheet package (Microsoft Excel 5.0).

4.4.1 Latent Effectiveness

The correlation for latent effectiveness is determined from the over 600 simulation data points shown in Figure 4.10 which cover a range of temperatures from -20°C to 40°C and relative humidities near 0% to 90% ($-6 \leq H^* \leq 6$). Simulation data points with

H^* in the range of $-0.3 \le H^* \le 0.2$ have been eliminated because ε_l can be quite large (>100%) or small (<20%) in this range as was shown in Section 3.4. Condensation and frosting effects have also been eliminated. The maximum difference between simulated and correlated effectivenesses is 2% with 98% of the data agreeing within ±1.5%. The correlation for latent effectiveness is:

$$\varepsilon_l = \frac{NTU_o}{1+NTU_o}\left(1-\frac{1}{0.54\left(Cr^*_{mt,o}\right)^{0.86}}\right)\left(1-\frac{1}{\left(NTU_o\right)^{0.51}\left(Cr^*_{mt,o}\right)^{0.54}H^*}\right), \quad (4.73a)$$

where:

$$Cr^*_{mt,o} = \left(Crm^*_o\right)^{0.58} Wm^{0.33}\left(\left.\frac{\partial u}{\partial \phi}\right|_{\phi_{ave}}\right)^{0.2}\left(Cr^*_o\right)^{1.13}\left(\frac{e^{\left(\frac{1482}{T_{ave}}\right)}}{47.9}-1.26\left(\phi_{ave}\right)^{0.5}\right)^{4.66}. \quad (4.73b)$$

Equations (4.73a) and (4.73b) are for a linear sorption curve with: $2 \le NTU_o \le 10$, $3 \le Cr^*_o \le 10$, a full range of Crm^*_o, $-0.3 > H^* > 0.2$, $0.1 \ge Wm \ge 0.5$ and $C^* = 1.0$. For $-0.3 \le H^* \le 0.2$, the moisture transfer can be neglected for most air conditioning energy recovery application because the amount of moisture transferred during these operating conditions is small. It should be noted that for a linear sorption curve the slope of the sorption curve ($\partial u/\partial \phi$) is constant and equal to Wm. Equation (4.73) can also be used for desiccants with Type IM or Type IIIM sorption curves (i.e., $10 \ge C \ge 0.1$) but the uncertainty is expected to increase to about ±5%. The correlation in equation (4.73) is intended to apply for $0 \le \varepsilon_l \le 100\%$.

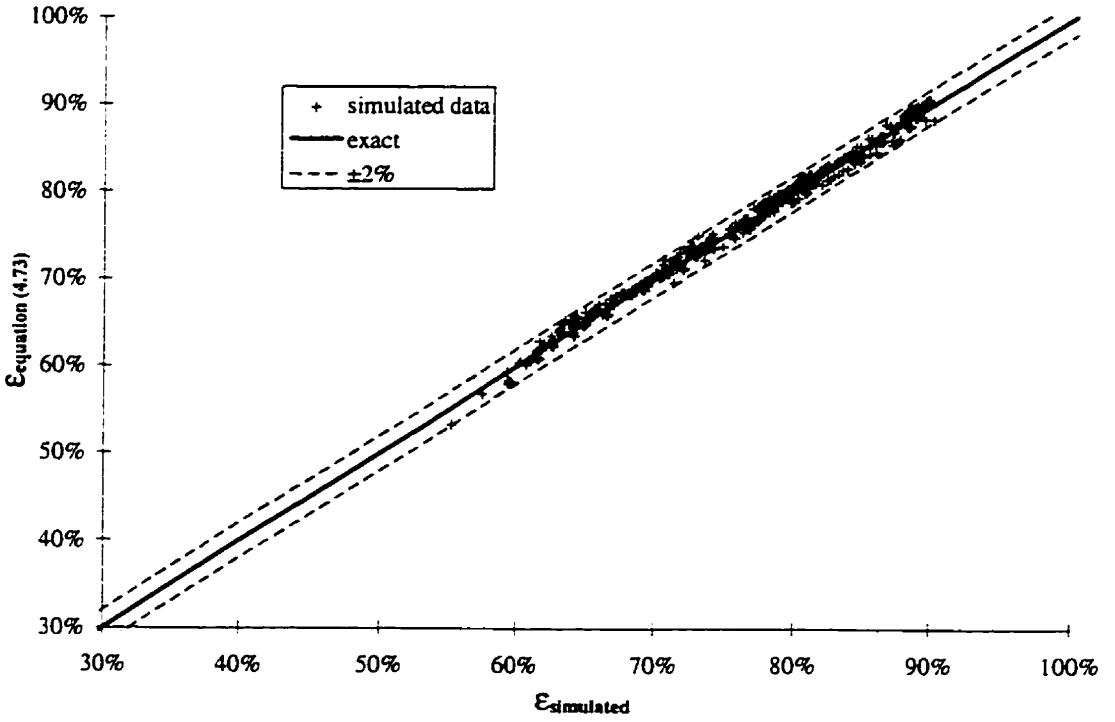

Figure 4.10. *Latent effectiveness calculated with equation (4.73) compared to the simulated latent effectiveness.*

4.4.2 Sensible Effectiveness

The correlation for sensible effectiveness is proposed in the following format,

$$\varepsilon_s = \varepsilon_{s\,(H^*=0)} - \Delta\varepsilon_s \ , \tag{4.74}$$

where $\Delta\varepsilon_s$ is a function of H*, η, NTU_o, Cr^*_o and Crm^*_o and Wm. $\varepsilon_{s\,(H^*=0)}$ is the effectiveness of a sensible wheel (i.e., no moisture transfer) and $\Delta\varepsilon_s$ is a factor which adjusts this effectiveness to account for the effects of moisture transfer. A relation of this type is chosen because $\varepsilon_{s\,(H^*=0)}$ is well known and $\Delta\varepsilon_s$ is a linear function of H* (see Figure 4.6). Figure 4.11 contains $\Delta\varepsilon_s$ for H* = 6, η = 0.1, Wm = 0.2 and $Cr^*_o/Crm^*_o = 5$ with various values of NTU_o and Cr^*_o and shows that $\Delta\varepsilon_s$ can be quite large for low

values of Cr^*_o. For example, with $NTU_o = 10$ and $Cr^*_o = 2$, $\Delta\varepsilon_s = 50\%$. $\Delta\varepsilon_s$ is less than 25% for $Cr^*_o \geq 3$ and therefore the correlations in this thesis use this limit.

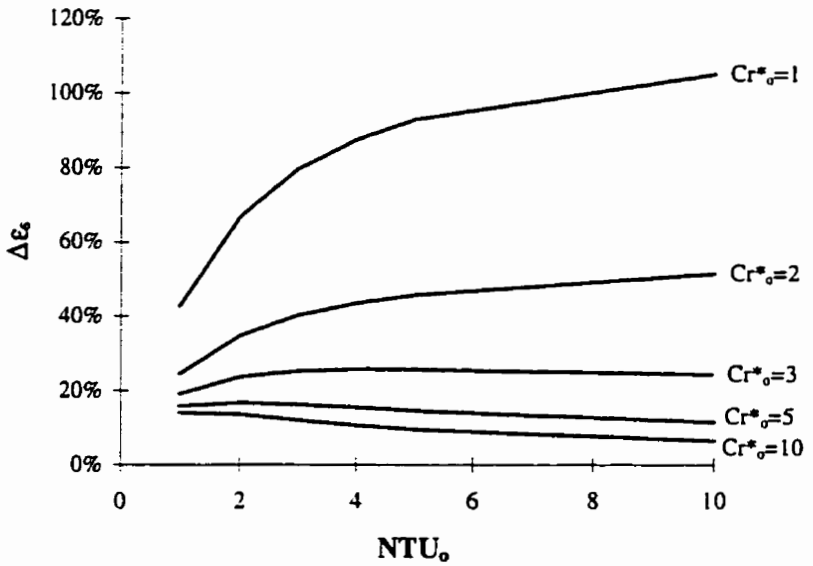

Figure 4.11. *$\Delta\varepsilon_s$ as a function of NTU_o and Cr^*_o for $H^* = 6$, $\eta = 0.1$, $Wm = 0.2$ and $Cr^*_o/Crm^*_o = 5$.*

The final sensible effectiveness correlation is:

$$\varepsilon_s = \frac{NTU_o}{1+NTU_o}\left(1-\frac{1}{7.5\,Cr^*_o}\right)-\left[\frac{0.26\left(\frac{Cr^*_o}{Wm^2 Crm^*_o}\right)^{0.28}}{7.2\left(Cr^*_o\right)^{1.53}+\frac{210}{\left(NTU_o\right)^{2.9}}-5.2}+\frac{0.31\,\eta}{\left(NTU_o\right)^{0.68}}\right]H^* \quad (4.75)$$

Equation (4.75) agrees with the over 600 simulated data points in Figure 4.12 within ±2.5% (98% of data within ±2%) for the following range of parameters: $0 \leq \eta \leq 0.1$, $-6 \leq H^* \leq 6$, $2 \leq NTU_o \leq 10$, $3 \leq Cr^*_o \leq 10$, $1 \leq Cr^*_o/Crm^*_o \leq 5$, $0.1 \leq Wm \leq 0.5$, $C = 1$ and $C^* = 1$. The uncertainty in equation (4.75) increases to ±3% for $0.1 \leq C \leq 1$ and ±5%

for $0.01 \leq C \leq 10$. Even though equation (4.75) predicts the simulated effectiveness well for $\varepsilon_s > 100\%$, it is intended to be used for $0 \leq \varepsilon_s \leq 100\%$.

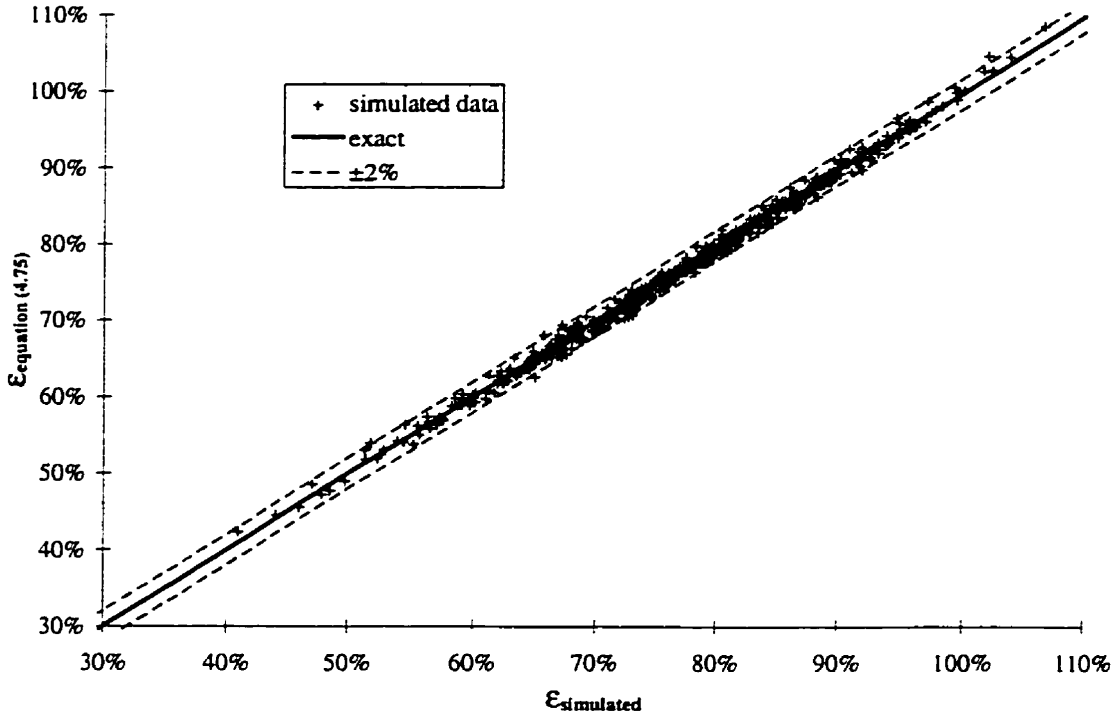

Figure 4.12. *Sensible effectiveness calculated with equation (4.75) compared to the simulated sensible effectiveness.*

Equation (4.75) is for negligible axial heat conduction through the matrix of the energy wheel. Simulation results show that the axial conduction can be accounted for by the method in Shah (1981 and 1988) with little loss in accuracy. The correction for axial thermal conduction is (Shah, 1988),

$$\varepsilon_{s_{(k_m \neq 0)}} = \varepsilon_{s_{(k_m = 0)}} C_\kappa \tag{4.76}$$

where:

$$C_\kappa = \frac{1+NTU_o}{NTU_o}\left[1 - \frac{1}{1+NTU_o \frac{1+\kappa\Phi}{1+\kappa NTU_o}}\right], \tag{4.77}$$

$$\kappa = \frac{A_{m,t}\, k_m}{L(\dot{m}Cp_a)_{min}} \quad \text{, and} \tag{4.78}$$

$$\begin{aligned} \Phi &= \sqrt{\frac{\kappa NTU_o}{1+\kappa NTU_o}}\, \tanh\left(\frac{NTU_o}{\sqrt{\frac{\kappa NTU_o}{1+\kappa NTU_o}}}\right) \\ &\approx \sqrt{\frac{\kappa NTU_o}{1+\kappa NTU_o}} \quad \text{for } NTU_o \geq 3 \end{aligned} \tag{4.79}$$

4.4.3 Total Effectiveness

Using the simulated values for ε_s and ε_l in the relation,

$$\varepsilon_t = \frac{\varepsilon_s + \varepsilon_l H^*}{1 + H^*} \quad , \tag{4.80}$$

gives values for ε_t that are less than 0.4% different from those simulated for the over 600 data points in Figures 4.10 and 4.12 when $-1.5 > H^* > -0.5$. Data points in the range of $-1.5 \leq H^* \leq -0.5$ have been eliminated because ε_t is discontinuous at $H^* = -1$. If the correlated values of ε_s and ε_l (calculated from equation (4.75) and equation (4.73) respectively) are used in equation (4.80), the uncertainty in ε_t is expected to be the same as that quoted for equations (4.73) and (4.75) (i.e., ±2.5%).

4.5 ILLUSTRATIVE EXAMPLE

The illustrative example in this section is for the rating of an energy wheel rather than sizing each component of a wheel. The objective of the rating problem is to verify the thermal and moisture transfer performance of an existing energy wheel as specified by the manufacturer or to determine the off-design performance. Many details of the methodology for the rating and sizing problems are given in Shah (1988) for sensible

rotary heat exchangers. The basic procedure is the same for energy wheels with the main difference being that more property data and more complex equations are required to calculate energy wheel performance. In this example, the somewhat hypothetical energy wheel with the properties listed in Table 4.3, operating in the conditions listed in Table 4.4 will be considered. The value of the dimensionless groups and the effectiveness values at the illustrative hot and cold test conditions are also given in Table 4.4. In each case the effectiveness correlations (i.e., equations (4.73), (4.75), (4.76) and (4.80)) are used to calculate the effectiveness values which include axial conduction through the wheel. In all cases $\eta = 0.05$.

Table 4.3. *Property data of the energy wheel used to illustrate the effectiveness correlations.*

Entire Wheel		
D = 1 m	L = 0.1 m	N = 1/3 cycles/s (20 rpm)
M_m = 14 kg	$\beta = 2667\ m^2/m^3$	porosity = 0.80
Individual Tube (sine duct)		
$D_h = 1.2 \times 10^{-3}$ m	a* = 0.4	Nu = 2.46 (Shah and London, 1978)
Desiccant (silica gel @ 20% by mass)		
Wm = 0.4	C = 1	$\sigma_d = 0.68$
$\rho_d = 350\ kg/m^3$	$Cp_d = 615$ J/(kg·K)	$k_d = 0.06$ W/(m·K)
Support Material (Aluminum)		
$\rho_{Al} = 2702\ kg/m^3$	$Cp_{Al} = 903$ J/(kg·K)	$k_{Al} = 237$ W/(m·K)

Table 4.4. Design operating conditions, dimensionless groups and effectiveness of the energy wheel used to illustrate the effectiveness correlations.

Hot Test	$T_{s,i} = 30°C$	$\phi_{s,i} = 50\%$
$\dot{m}_s = \dot{m}_e = 0.6$ kg/s	$T_{e,i} = 24°C$	$\phi_{e,i} = 50\%$
$H^* = 1.67$	$NTU_o = 4.6$	$Cr^*_o = 6.5$
$Crm^*_o = 1.6$	$C_\lambda = 0.892$	$Cr^*_{mt,o} = 174.3$
$\varepsilon_s = 70.3\%$	$\varepsilon_l = 79.1\%$	$\varepsilon_t = 75.8\%$
Cold Test	$T_{s,i} = 24°C$	$\phi_{s,i} = 50\%$
$\dot{m}_s = \dot{m}_e = 0.6$ kg/s	$T_{e,i} = -10°C$	$\phi_{e,i} = 50\%$
$H^* = 0.63$	$NTU_o = 4.6$	$Cr^*_o = 6.5$
$Crm^*_o = 1.6$	$C_\lambda = 0.892$	$Cr^*_{mt,o} = 1599$
$\varepsilon_s = 71.2\%$	$\varepsilon_l = 80.9\%$	$\varepsilon_t = 74.9\%$

4.5.1 Mass Flow Rate of Air

Figure 4.13 shows the effect of mass flow rate on the sensible, latent and total effectivenesses of the energy wheel for the hot and cold test conditions. The latent and total effectivenesses decrease with increasing mass flow rate (or face velocity) as expected. The sensible effectiveness also decreases with increasing mass flow rate, except at low flow rates where axial heat conduction through the matrix becomes more dominant. Effectiveness values are more sensitive to mass flow rate changes in the hot test than in the cold test as was discovered in Chapter 3. The results in Figure 4.13 are similar to the results in Figure 3.23 which shows that the effectiveness correlations are giving reliable results.

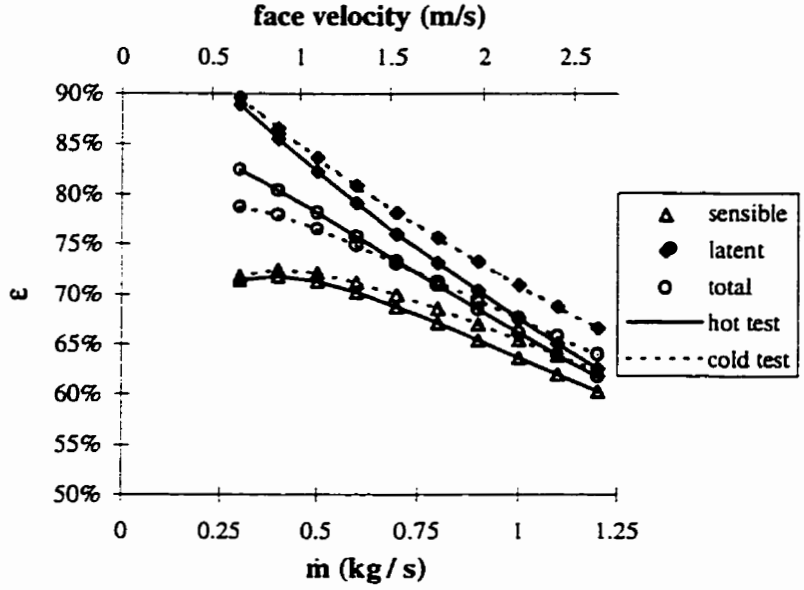

Figure 4.13. Effectiveness versus mass flow rate and face velocity with C = 1.*

4.5.2 Wheel Speed

Changing the wheel speed of the energy wheel will reduce Cr^*_o and Crm^*_o and consequently the effectiveness. This is shown in Figure 4.14 where the effectiveness is plotted as a function of wheel speed. Although the effectiveness correlations were limited to $Cr^*_o \geq 3$, the results in Figure 4.14 appear reasonable for $Cr^*_o \geq 1$. The differences between simulated and calculated effectiveness values for N = 5 rpm are less than 5% which is smaller than the changes in effectiveness that are seen in Figure 4.14. It would appear from this example that using wheel speed to control the rate of heat and moisture transfer for air conditioning applications would likely lead to space temperature and humidity problems. This was seen in the results of Figure 2.12 and adds credibility to the developed effectiveness correlations.

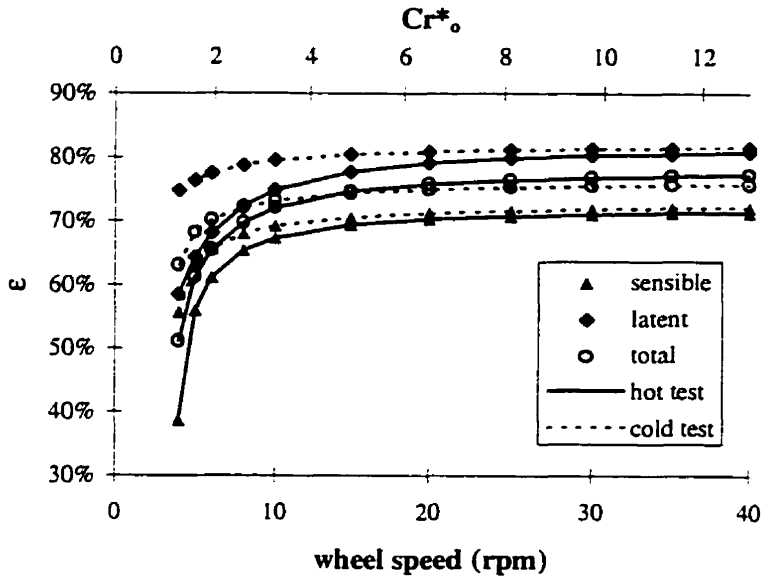

Figure 4.14. Effectiveness versus wheel speed for balanced mass flow rates.

4.5.3 Operating Condition Factor (H*)

The correlations can also be used to show the effect of the operating temperature and humidity on the effectiveness of the energy wheel described in Tables 4.3 and 4.4 (Figure 4.15). The results in Figure 4.15 are for the hot test conditions with various supply inlet relative humidities and they show the sensitivity of effectiveness to the operating conditions (H*). In particular, ε_l is discontinuous at $H^* = 0$ with $\varepsilon_l \rightarrow +\infty$ as $H^* \rightarrow 0^-$, which is similar to the results presented in Figure 3.27. The total effectiveness is also discontinuous with the discontinuity occurring at $H^* = -1$. This corresponds to the case of equal inlet enthalpies to the energy wheel (see Figure 3.11). For $H^* \approx 0$ and $H^* \approx -1$, the moisture transfer and energy transfer rates of the energy wheel are respectively small and therefore these operating conditions are not important for energy saving calculations and optimization of air conditioning designs using energy wheels. Figure 4.15 shows that axial conduction through the aluminum support material of the

energy wheel reduces the effectiveness of the energy wheel by 9% for these operating conditions. This large reduction was also seen in Figure 2.13.

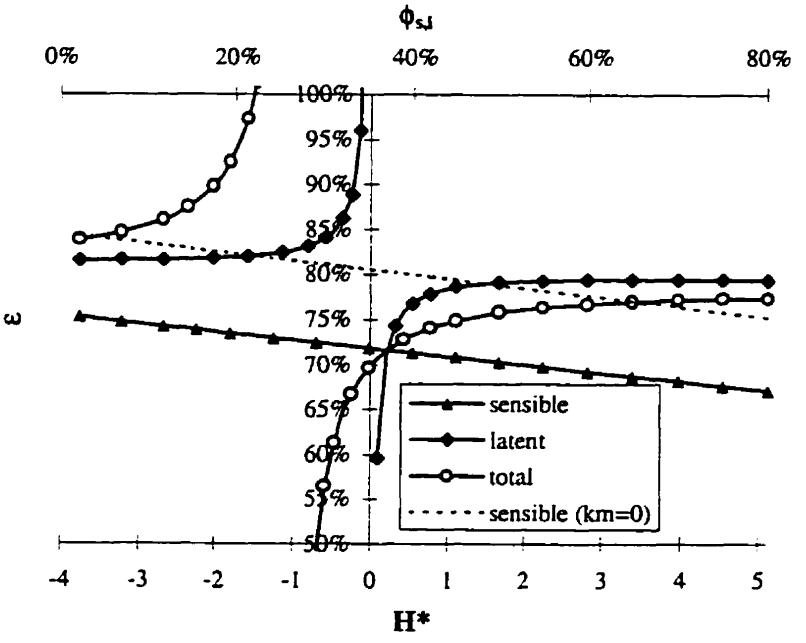

Figure 4.15. Effectiveness versus H for the hot test conditions.*

The brief application of the effectiveness correlations given in this section display their utility. These correlations are much simpler to use than detailed simulations programs which are the current alternative. The correlations are especially important because they can be easily implemented into entire building simulation programs which will allow life cycle cost and energy saving studies. These correlations will also permit HVAC engineers to design and predict savings for energy wheels more accurately.

4.6 SUMMARY

Simulation and correlation results, together with the governing dimensionless groups, presented in this chapter show the importance of operating conditions on the

performance of energy wheels. The operating conditions have the largest effect on the effectiveness when the traditional value of NTU_o and Cr^*_o and the newly defined Crm^*_o (which is similar to Cr^*_o except it applies to moisture storage rather than energy storage) are low. Changes in effectiveness that result from changes in the operating conditions and sorption curve can be explained by the dimensionless groups which are developed in this chapter.

The dimensionless groups and simulation results show that a desiccant with a linear sorption curve will have the best performance over typical operating conditions for energy wheels. Type IM and IIIM sorption curves are also acceptable for energy wheels, but Type IE and Type IIIE sorption curves have poor performance at certain humidities.

The sensible, latent and total effectiveness correlations, developed in this chapter, agree with over 600 simulated values within ±2.5%, ±2% and ±2.5% respectively. The correlations allow the designer to calculate effectiveness from known parameters and are:

$$\varepsilon_s = \frac{NTU_o}{1+NTU_o}\left(1-\frac{1}{7.5\,Cr^*_o}\right)-\left[\frac{0.26\left(\frac{Cr^*_o}{Wm^2 Crm^*_o}\right)^{0.28}}{7.2(Cr^*_o)^{1.53}+\frac{210}{(NTU_o)^{2.9}}-5.2}+\frac{0.31\,\eta}{(NTU_o)^{0.68}}\right]H^*\,, \quad (4.81)$$

$$\varepsilon_l = \frac{NTU_o}{1+NTU_o}\left(1-\frac{1}{0.54(Cr^*_{mt,o})^{0.86}}\right)\left(1-\frac{1}{(NTU_o)^{0.51}(Cr^*_{mt,o})^{0.54}H^*}\right), \text{ and} \quad (4.82)$$

$$\varepsilon_t = \frac{\varepsilon_s+\varepsilon_l H^*}{1+H^*}\;; \quad (4.83)$$

where:

$$NTU_o = \frac{1}{(\dot{m}Cp_a)_{min}}\left[\frac{1}{(hA_s)_s}+\frac{1}{(hA_s)_e}\right]^{-1}, \tag{4.84}$$

$$Cr^*_o = \frac{(MCp)_m N}{(\dot{m}Cp_a)_{min}}, \tag{4.85}$$

$$Crm^*_o = \frac{M_{d,dry} N}{\dot{m}_{min}}, \tag{4.86}$$

$$Cr^*_{mt,o} = (Crm^*_o)^{0.58} Wm^{0.33}\left(\left.\frac{\partial u}{\partial \phi}\right|_{\phi_{ave}}\right)^{0.2} (Cr^*_o)^{1.13}\left(\frac{e^{\left(\frac{1482}{T_{ave}}\right)}}{47.9} - 1.26(\phi_{ave})^{0.5}\right)^{4.66}, \tag{4.87}$$

$$H^* = \frac{\Delta H_l}{\Delta H_s} = \left(\frac{\Delta H_s}{\Delta H_t}\right)^{-1} - 1 = 2500\frac{\Delta W}{\Delta T_g}, \tag{4.88}$$

$$\Delta W = W_{s,i} - W_{e,i}, \text{ and} \tag{4.89}$$

$$\Delta T_g = T_{g_{s,i}} - T_{g_{e,i}}. \tag{4.90}$$

The above correlations apply for the following range of parameters: $0 \le \eta \le 0.1$, $-6 \le H^* \le 6$, $2 \le NTU_o \le 10$, $3 \le Cr^*_o \le 10$, $1 \le Cr^*_o/Crm^*_o \le 5$, $0.1 \le Wm \le 0.5$, $C = 1$ and $C^* = 1$. These effectiveness correlations, although quite complex, are simpler to use than numerical models and will permit manufacturers and HVAC engineers to optimize energy wheel performance and life cycle cost savings for air conditioning applications in different climates for a range of building operating conditions.

CHAPTER 5

CONDENSATION AND FROSTING

One problem that limits the practical application of energy wheels is condensation and frosting. During extreme operating conditions, moisture may continually accumulate in the energy wheel in the form of frost or liquid water. This type of uncontrolled condensation in energy wheels will damage the desiccant coating and result in poorer performance. To improve the understanding of these complex phenomena, condensation and frosting are studied in this chapter. The transition from sorption to moderate condensation/frosting to uncontrolled condensation/frosting is shown numerically. The effectiveness of an energy wheel is also presented during these transitions. The effect of wheel speed and desiccant type on condensation/frosting and energy wheel performance are also presented.

In this chapter, simulation results are presented for both hot and cold outdoor conditions. Water is expected to run off the wheel during the hot and humid outdoor conditions and frost is expected to accumulate in the wheel during the cold outdoor conditions. The specific parameters of the energy wheel are given in Table 5.1 and the test conditions are given in Table 5.2. Other simulation results show that uncontrolled condensation and frosting are unlikely for moderate outdoor temperatures of 30°C and -10°C and are not shown here. Instead, this chapter concentrates on more extreme

outdoor temperatures of 40°C and -20°C. Standard atmospheric pressure (101.325 kPa) is used in all cases. Numerical results are presented for a desiccant with a Type I sorption isotherm (e.g., a molecular sieve desiccant) and a linear sorption isotherm (e.g., a silica gel desiccant). For the properties of the wheel in Table 5.1, η is expected to be about 0.05 as was discussed in Chapter 2. In this chapter, the relative values of effectiveness are more important than the absolute values and therefore $\eta = 0$ is chosen even though this assumption affects the predicted sensible effectiveness by 4% for extreme operating conditions of 40°C and 90% R.H..

Table 5.1. *Energy wheel parameters used in the study of condensation and frosting.*

WHEEL	M = 10.8 kg	L = 0.1 m	D = 0.9 m
speed = 1 to 20 rpm	$D_h = 1.5 \times 10^{-3}$ m	$Re_{D_h} = 152$	porosity = 85%
Nu = 2.48 *	Le = 1	h = 43.5 W/(m²·K) *	h_m = 0.036 m/s *
NTU = 3.4	Cr* = 6.0 @ 20 rpm	U = 1.3 to 1.7 m/s	$\dot{m}$ = 0.5 kg/s
DESICCANT	$\rho_d = 350$ kg/m³	$Cp_d = 615$ J/(kg·K)	mass fraction = 20%
$\sigma_d = 0.66$	Wm = 0.2	C = 0.01 or 1.0	$u = Wm/(1 - C + C/\phi)$

* fully developed

Table 5.2. *Test conditions for the simulation of condensation and frosting.*

	T (°C)	ϕ (%)	T (°C)	ϕ (%)
Supply	-20	50	40	40 - 100
Exhaust	24	10 - 50	24	50

5.1 ONSET OF SATURATION CONDITIONS

It is important to know when the air in an energy wheel becomes saturated because at this time there is a risk of condensation, excessive moisture build up and

degradation of the desiccant coating. A plot of latent effectiveness versus inlet relative humidity can be used to determine when saturation conditions occur in the wheel (Figure 5.1). As the inlet relative humidity increases, ε_l decreases until saturation conditions occur. After the onset of saturation conditions, ε_l increases with increasing relative humidity. Therefore, the minimum point on the ε_l versus ϕ graph represents the onset of saturation conditions. Figure 5.1 shows the latent effectiveness as a function of relative humidity for desiccants with Type I and linear sorption isotherms at different wheel speeds.

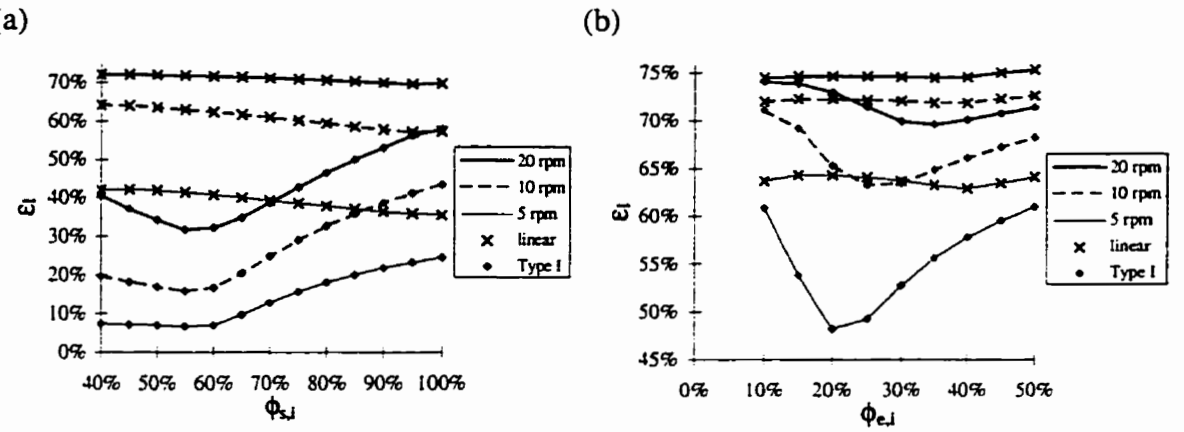

Figure 5.1. *Latent effectiveness as a function of the inlet relative humidity for (a) hot (40°C) and (b) cold (-20°C) test conditions.*

The results in Figure 5.1 show that saturation conditions exist at lower relative humidities for a Type I isotherm than for a linear isotherm. In the hot tests, saturation conditions begin for a Type I isotherm at supply inlet relative humidities of 60% to 65%, whereas saturation conditions exist only at extreme relative humidities of 95% to 100% for a linear isotherm. In the cold test, saturation conditions occur at $\phi_{e,i}$ = 25% to 30% for a Type I isotherm, but do not occur until $\phi_{e,i}$ = 35% to 40% for the linear sorption

curve. These results show that saturation conditions are delayed when a desiccant with a linear sorption curve is used in place of a desiccant with a Type I sorption curve. This indicates that an energy wheel that is coated with silica gel will perform better under more extreme operating conditions than a wheel that is coated with a molecular sieve desiccant.

Figure 5.1 illustrates the effect of the sorption curve on the latent energy transfer of the energy wheel. The latent effectiveness of a wheel coated with a linear sorption curve (e.g., silica gel) is significantly greater and less sensitive to the inlet relative humidity than one coated with a Type I sorption curve. It is possible that the effectiveness of the energy wheel coated with a Type I sorption curve could be increased to that with a linear sorption curve if the wheel speed was increased or the amount of desiccant coating was increased (Klein et al., 1990). However, for comparable wheel configurations and mass fraction of desiccant, the desiccant with a linear sorption curve is a preferable design selection for increased moisture transfer.

The latent effectiveness of the molecular sieve coated energy wheel in Figure 5.1 decreases as the humidity increases during sorption conditions. As discussed in Section 4.3.1, this decrease in ε_l is due to the fact that the amount of moisture that must be stored in the matrix increases more rapidly with humidity than does the moisture storage capacity of the matrix for the Type I sorption curve. However, the latent effectiveness of the silica gel coated energy wheel remains quite constant with humidity during sorption conditions because both the amount of moisture that must be stored in the matrix and the

moisture storage capacity of the matrix increase linearly with the inlet relative humidity for a linear sorption curve. During saturation conditions, the effective moisture storage potential of the desiccant and the moisture transfer rate between the air and the desiccant increases substantially over the case of sorption. Hence, the latent effectiveness begins to increase with humidity. The reason that the latent effectiveness is less sensitive to changes in humidity in the cold tests is that the moisture transfer is significantly smaller in the cold tests than in the hot tests.

The effect of wheel speed is also evident in Figure 5.1. Decreasing the wheel speed decreases the latent effectiveness, but only has a small effect on the onset of saturation conditions.

In Figure 5.2 the inlet conditions where saturation conditions begin are presented on the psychrometric chart to emphasize the fact that a desiccant with a linear sorption curve can be exposed to higher humidity conditions before saturation conditions begin. The process lines in Figure 5.2 connect the inlet conditions for which saturation conditions first begin. All inlet humidities above the lines in Figure 5.2 will result in condensation and/or frosting in the wheel while those below will result in only sorption processes, indicating that the wheel will remain dry. In most cases, saturation conditions begin when a straight line joining the inlet conditions touches the saturation line (Holmberg, 1989 and Klein et al., 1990). The only exception to this rule is in the hot tests when the wheel is coated with a Type I isotherm. In this case, saturation conditions begin before the straight line connecting the inlet conditions touches the saturation line.

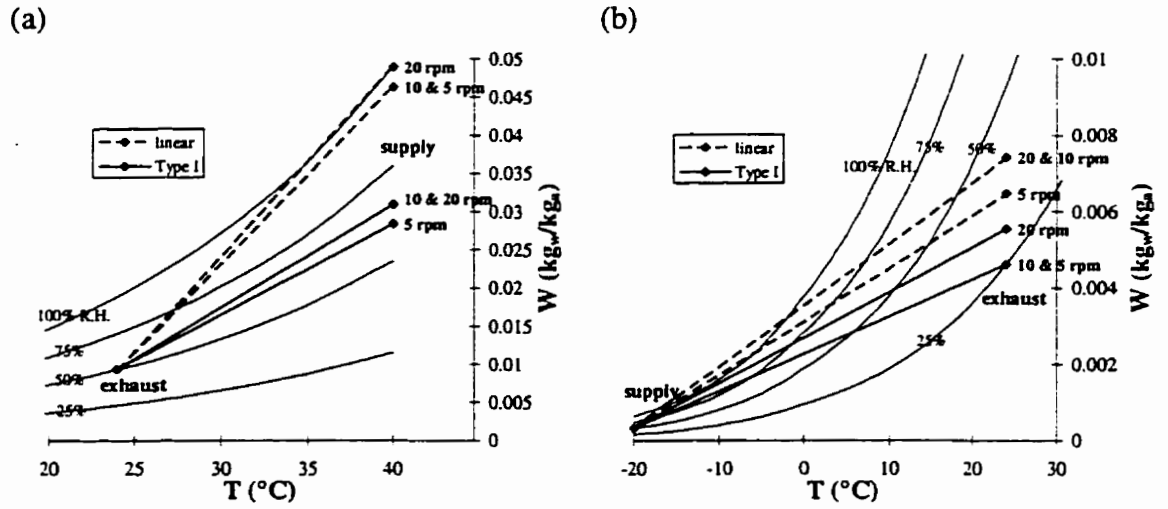

Figure 5.2. *Supply and exhaust inlet conditions for the (a) 40°C and (b) -20°C tests showing the lowest humidity at which saturation conditions occur for different wheel speeds and sorption isotherms.*

5.2 LOCATION OF CONDENSATION/FROSTING

The location of the condensation within the energy wheel coated with a Type I desiccant can be seen in Figure 5.3 for supply air conditions of 40°C and 80% R.H..

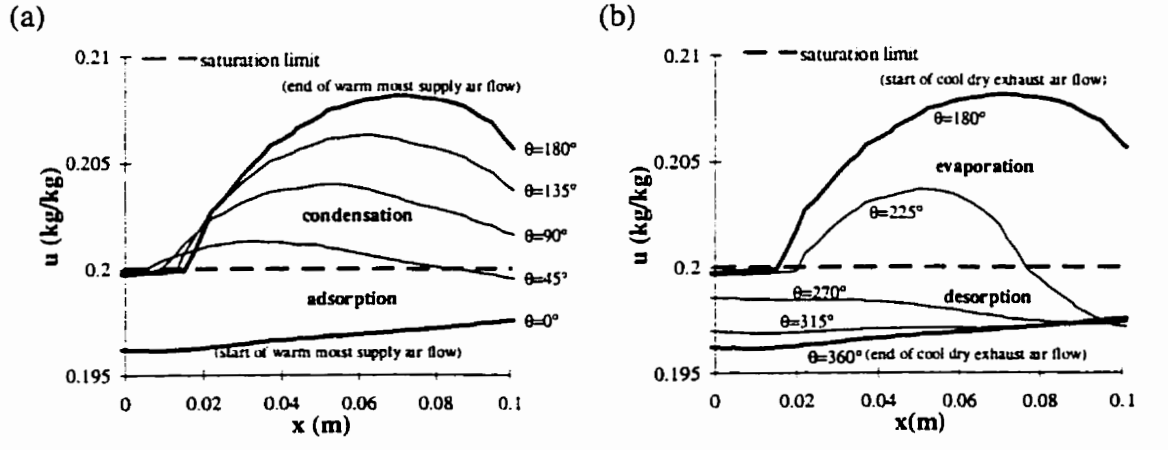

Figure 5.3. *Moisture content profiles in the Type I desiccant coating for (a) supply air flow (40°C & 80% R.H.) and (b) exhaust air flow (24°C & 50% R.H.) through the wheel.*

The results in Figure 5.3 show that saturation and sorption conditions can coexist in the wheel. For a given axial position, sorption and saturation conditions exist at different rotation angles and for a given rotational angle, sorption and saturation conditions exist at different axial positions. Phase change is due to adsorption at a rotational angle (θ) of 0° which is when the tube has just left the cool-dry exhaust side and enters the warm-moist supply side. At this angle, the moisture content of the wheel is the lowest. As the wheel rotates, the moisture content of the desiccant increases and the relative humidity of the air increases. At a rotational angle of 45°, a large part of the wheel experiences condensation. The size of the condensation zone increases slightly as the wheel rotates but the moisture content of the desiccant increases significantly with angle up to 180°. At an angle of 180°, the condensation zone occupies 80% of the energy wheel. Figure 5.3(b) shows the removal of moisture by the cool and dry exhaust air as the wheel rotates from 180° to 360°. Here the transition from saturation to sorption conditions occurs later in the cycle than the transition from sorption to saturation occurs during the hot and humid supply air flow. It can be seen that condensation conditions are present for a longer time or angle of rotation (over 3/4 of the supply flow period) than evaporation conditions (less than 1/2 of the exhaust flow period). The phase change mechanism is clearly changing from adsorption to condensation then to evaporation and finally to desorption conditions during one cycle of the wheel, yet there is no uncontrolled condensation. The moisture that is accumulated on the supply side is removed on the exhaust side in a quasi-steady cyclic process.

The moisture content of the desiccant indicates when the air in an energy wheel reaches saturation. However, inlet-to-outlet process lines on the psychrometric chart show the distribution of temperature and relative humidity of the air in the energy wheel and are presented in Figure 5.4. Saturation conditions are apparent in Figure 5.4.

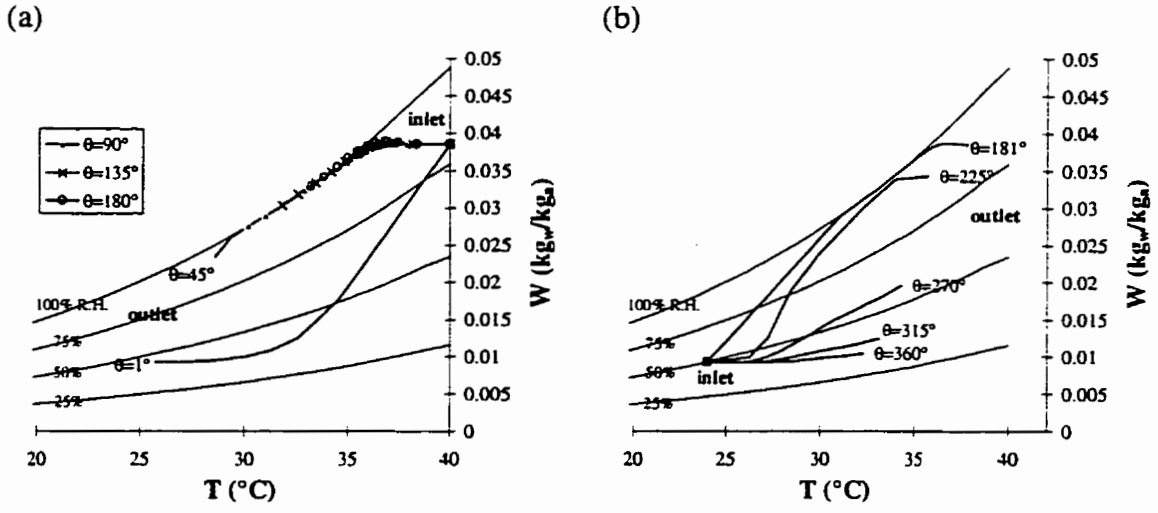

Figure 5.4. *Inlet-to-outlet process lines with (a) supply inlet conditions of 40°C and 80% R.H. and (b) exhaust inlet conditions of 24°C and 50% R.H..*

Figure 5.5 shows the location of frosting for the cold test conditions when the indoor relative humidity is 35% and the desiccant has a Type I sorption isotherm. Here the moisture content profile does not change as much during one revolution of the wheel as in the hot tests. The temperature profiles in the matrix are also included in Figure 5.5 to show where condensation and frosting are expected to occur.

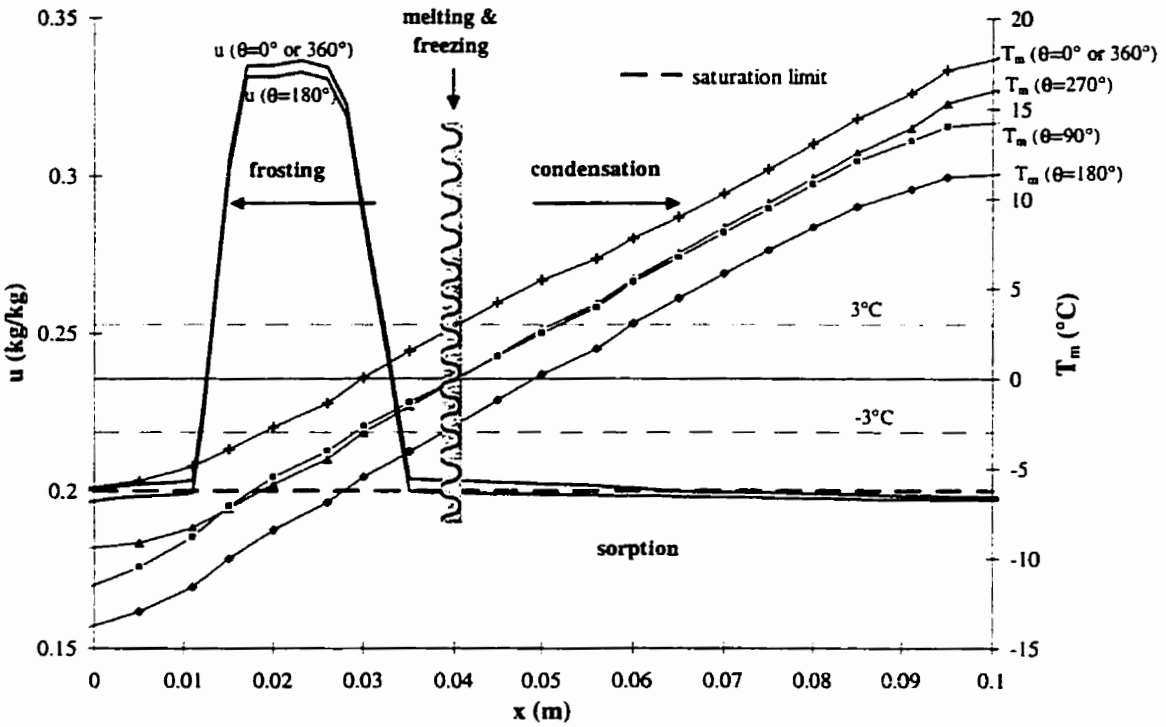

Figure 5.5. *Moisture content and matrix temperature profiles in the desiccant for supply conditions of -20°C & 50% R.H. and exhaust conditions of 24°C & 35% R.H..*

The zone of melting and freezing is sketched in Figure 5.5 as a wavy line because the size of this zone is not exactly known. The size of this zone will depend on the amount of subcooling/superheating that is needed to freeze/melt the water in the matrix. If ±3°C are required, there will be no freezing and melting zone. In frost studies, it has been observed that small droplets of liquid water require up to 15s of subcooling at temperatures of -10°C to -15°C before freezing occurs (Tao et al., 1993a). Also, Simonson et al. (1996) have reported significant subcooling of water during the cycling of moist fiberglass insulation between -20°C and +2°C. Therefore, the amount of water that freezes and melts during the 3s period of the energy wheel is likely very small. At steady state, the wheel will have a zone of frozen water, a zone of liquid water and a very

small zone that periodically changes phase between liquid and solid. For this reason, the latent heat of fusion (which is an order of magnitude smaller than the heat of vaporization) has been neglected in the governing equations in Chapter 2.

From Figure 5.5 it can be seen that the majority of the moisture accumulation in the wheel is in the form of frost. The zone where significant frosting occurs makes up about 25% of the flow length of the energy wheel.

5.3 UNCONTROLLED CONDENSATION/FROSTING

It is important to know at what conditions the air in an energy wheel becomes saturated, but it is more important to know when uncontrolled saturation begins in the energy wheel. Uncontrolled saturation exists when more moisture accumulates in the wheel from the warm-moist air than is removed by the cool-dry air. The net result is that the moisture content of the desiccant continually increases. This will eventually lead to water running off the energy wheel when the temperature is above freezing and excessive frosting and blockage of the wheel when the temperature is below freezing.

In Figure 5.6 (a) the net accumulation in the wheel at the end of the simulation is extrapolated for one hour to see how much moisture is accumulating in the wheel in the hot tests. The rate at which frost growth reduces the flow area for the cold tests can also be estimated from the model. The growth of frost is not included intrinsically in the model because the flow area of the wheel is assumed to be constant. However, based on an average low density frost (~100 kg/m^3 - Tao et al., 1993b) and from moisture content profiles which show that the frost accumulates in about 25% of the tube (Figure 5.5), the

average blockage rate of the wheel can be predicted from the simulation results and is presented in Figure 5.6(b). It should be noted that when there is a net accumulation of moisture in the wheel over time, the quasi-steady conditions stated in Section 2.5 cannot be met. In this case, the simulation was stopped when the typical quasi-steady time for similar test conditions was exceeded. When the quasi-steady conditions are satisfied, the net accumulation in the wheel can be assumed negligible.

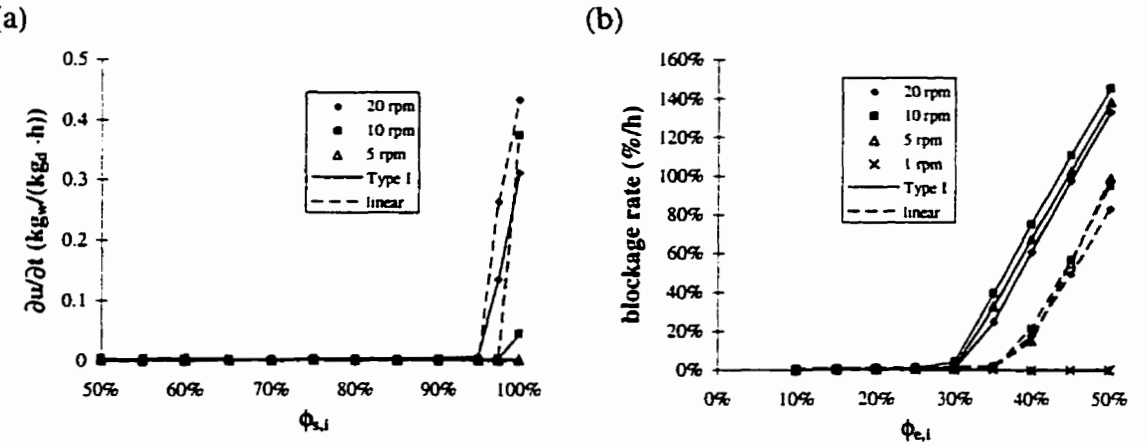

Figure 5.6. *Change in the average moisture content of the desiccant per hour during (a) the hot tests (40°C) and the estimated blockage rate of the wheel due to frost growth during (b) the cold tests (-20°C).*

The results in Figure 5.6 show that reducing the wheel speed, significantly reduces uncontrolled condensation and frosting which is expected from the literature (Stiesch et al., 1995 and Holmberg, 1989). Lower wheel speeds are required to prevent uncontrolled frosting because the sensible effectiveness is higher in the cold tests than in the hot tests for the same wheel speed as shown in Figure 5.7. The difference between a linear and Type I sorption isotherm is not as significant in the hot tests as in the cold tests. Figure 5.6(b) shows that an energy wheel, coated with a desiccant with a linear

sorption curve (e.g., silica gel), has less frosting than one coated with a Type I desiccant (e.g., molecular sieve).

In the hot test, the relative humidity of the supply air must be very high (greater than 95%) before water begins to accumulate in the wheel over time. Because desiccants have large moisture retention capacities and can often hold their equivalent mass in water (i.e. u = 1 kg/kg) before water begins to run off the desiccant, it may take up to an hour of extremely high humidity before water begins to run off the wheel. This implies that short term exposure (i.e. less than one hour) to high relative humidities, as during a rain storm, may not affect an energy wheel adversely. As noted in Section 3.1.2, this water condenses near the hot and humid supply inlet and is expected to be distributed through 1/3 of the energy wheel. The large moisture accumulation shown in Figure 5.6(a) for humidities greater than 95% would likely result in damage to the desiccant coating, however these extreme operating conditions are almost never encountered in practice.

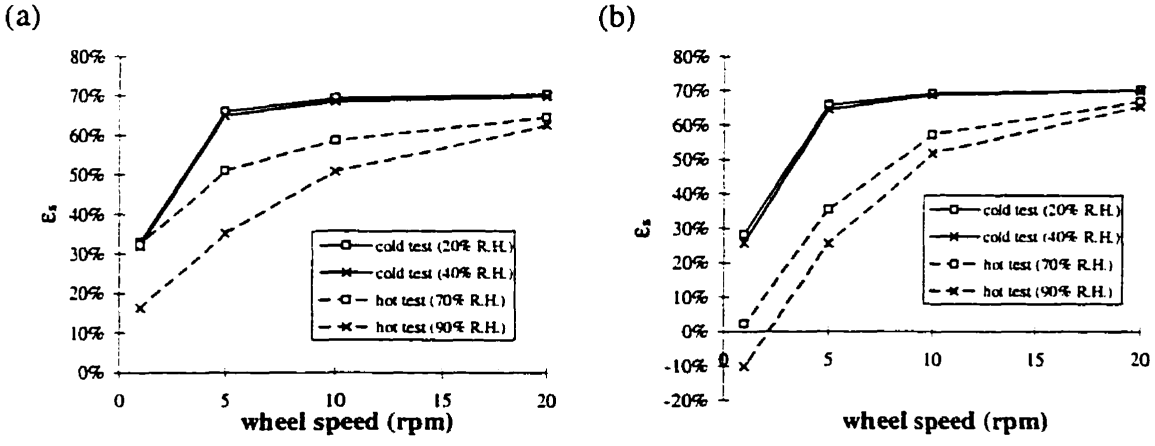

Figure 5.7. Sensible effectiveness versus wheel speed for (a) Type I and (b) linear desiccants.

The cold tests in Figure 5.6 show that the moisture content can continuously increase for relatively moderate indoor relative humidities. Blockage of the wheel occurs for wheel speeds of 5 to 20 rpm when the exhaust relative humidity is greater than 30% and 35% for the Type I and linear desiccant coatings respectively. For a wheel speed of 1 rpm, no blockage is predicted even when the indoor relative humidity is 50%. At indoor conditions of 24°C and 40% R.H. and wheel speeds of 5 to 20 rpm, the blockage rate is 60% per hour when the coating is a Type I desiccant and 20% per hour when the coating is a linear desiccant. During these operating conditions, the energy wheel may require a defrost cycle every hour unless the wheel speed is reduced to 1 rpm or less depending on the rate of frost accumulation and the duration and amount of subcooling. These results show that the energy wheel could be completely blocked with frost after only a few hours of operation. A defrost cycle would be required when frost blockage reaches a certain point, otherwise the exhaust and supply air flow rates would both decrease and the wheel rotation may stop.

Figure 5.7 shows that the sensible effectiveness of the energy wheel decreases with increasing humidity and decreasing wheel speed. The calculated sensible effectivenesses for the cold test conditions with a wheel speed of 1 rpm are comparable to those in the hot tests with a wheel speed of 5 rpm. This explains why the wheel speed needs to be reduced to 1 rpm or less in the cold tests to prevent uncontrolled frosting, while a wheel speed of 5 rpm prevents uncontrolled condensation in the hot tests (see Figure 5.6).

The sensible effectiveness decreases with increasing humidity because of the coupling between heat and moisture transfer. For the test conditions chosen, the heat and moisture transfer are in the same direction and H* is positive (i.e., the air is being cooled and dried or heated and humidified as it passes through the energy wheel). The humidity is transferred from the warm air to the desiccant coated energy wheel releasing the energy of phase change. This will tend to increase the temperature of the matrix and therefore reduce the heat transfer from the warmer air to the cooler matrix. This will clearly increase the temperature of the air leaving the energy wheel and therefore decrease the sensible effectiveness. If the heat and moisture transfer were in opposite directions (H* negative), the sensible effectiveness of the energy wheel would increase as the humidity increases as discussed in Chapter 4. The decrease in sensible effectiveness due to moisture transfer is especially significant at low values of Cr^*_o and high values of H*. Therefore it is not surprising that ε_s is negative in the hot tests at 1 rpm because in this case $Cr^*_o = 0.3$ and $H^* = 5.4$.

Figure 5.7 shows that saturation conditions do not significantly affect the sensible effectiveness. ε_s is nearly equal for the cold tests at 20% R.H. and 40% R.H. even though saturation conditions are present in the latter test but not in the former test.

5.4 ENERGY WHEEL PERFORMANCE

The physical phenomena of adsorption and desorption are different from condensation and evaporation (ablimation and sublimation below 0°C) which means that the performance of energy wheels may depend on the mode of phase change moisture

transfer and the type of desiccant. To study this effect, Figure 5.8 contains the predicted total effectiveness at different inlet humidities with different desiccants for the hot and cold test conditions.

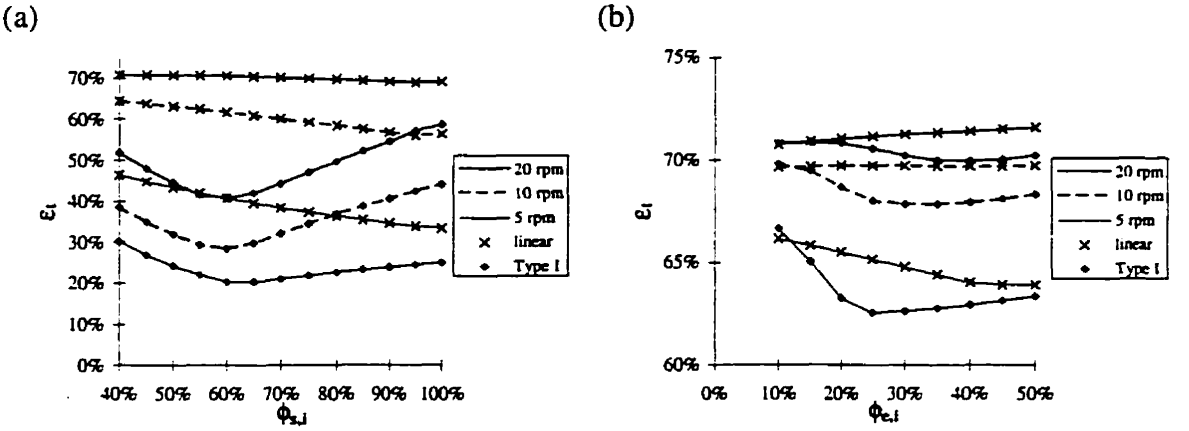

Figure 5.8. *Total effectiveness for supply temperatures of (a) 40°C and (b) -20°C.*

The total effectiveness values in Figure 5.8 are consistently higher for the linear isotherm than for the Type I isotherm. This shows that a desiccant with a linear sorption curve is preferable to a desiccant with an extreme Type I sorption curve. The total effectiveness of an energy wheel that is coated with a linear desiccant is less sensitive to the inlet relative humidity than the total effectiveness of an energy wheel that is coated with a Type I desiccant.

The effectiveness values presented in this chapter (Figures 5.1, 5.7 and 5.8) show that effectiveness depends on the humidity and temperature of the energy wheel. This supports the findings of Chapter 4. In Chapter 4, dimensionless groups and effectiveness correlations for energy wheels operating under conditions that include only phase change by adsorption and desorption were developed. There are no simple correlations in the

literature that will predict energy wheel performance during condensation and frosting conditions. This could be an area of future studies.

5.5 SUMMARY

The numerical results in this chapter show that increasing the inlet relative humidity during adsorption and desorption processes decreases the latent effectiveness of an energy wheel, but increases the latent effectiveness during bulk condensation and evaporation. Typically, the onset of saturation conditions can be determined when a line connecting the inlet conditions on the psychrometric chart touches that saturation line. However, for an energy wheel that is coated with a desiccant that has a Type I sorption isotherm and exposed to hot and humid test conditions, saturation begins well before the straight line intersects the saturation line. Simulation results show that the adverse effects of uncontrolled condensation are expected to be minimal in hot climates, but frosting within energy wheels is expected to be very important in cold climates. Furthermore, because subcooling of water droplets may occur, experimental investigations of frosting within energy wheels should be done to complement these theoretical predictions of when uncontrolled frosting may occur.

Reducing the wheel speed reduces uncontrolled condensation and frosting. For the test conditions in this chapter, uncontrolled condensation can be stopped by reducing the wheel speed to 5 rpm, while lower wheel speeds (1 rpm) are needed to prevent frosting.

A desiccant with a linear sorption curve (e.g., silica gel) appears to be more favorable for energy exchange applications than a desiccant with a Type I sorption curve (e.g., molecular sieve) because the linear sorption curve desiccant has better performance characteristics and smaller amounts of condensation/frosting. It is therefore expected that an energy wheel that is coated with a silica gel desiccant will operate better during more extreme operating conditions than an energy wheel that is coated with a molecular sieve desiccant.

CHAPTER 6

CONCLUSIONS AND FUTURE WORK

As discussed in Chapter 1, there is a significant amount of published research on various types of heat exchangers, but a limited amount on energy wheels. Therefore, the main purpose of this research was to advance the scientific understanding and literature pertaining to energy wheels. These main purposes have been satisfied by the detailed studies presented in this thesis and by their publication (and submission for publication) in scientific journals. The main objectives of this thesis were handled in the following chapters and are:

1. to develop a numerical model for simultaneous heat and moisture transfer in energy wheels (Chapter 2);
2. to validate the numerical model with experimental data and extrapolate this test data to other operating conditions (Chapter 3);
3. to use the validated numerical model to develop effectiveness correlations for energy wheels that have a physical basis (Chapter 4); and
4. to study condensation and frosting conditions in energy wheels (Chapter 5).

Each chapter is relatively independent and contains a summary that discusses the conclusions of the chapter and explains how each of the above listed objectives were met. In this concluding chapter, the final conclusions and contributions of this thesis are presented and areas of future work are recommended.

6.1 CONCLUSIONS

The one-dimensional and transient numerical model of energy wheels, presented in this thesis, is developed from physical principles and includes phase change by sorption, condensation and frosting. Two numerical algorithms are needed - one for mass transfer during sorption conditions and one for mass transfer during saturation conditions. The model is unique because the diffusion of phase change energy is treated in a general manner with some fraction (η) being delivered to the air and the rest being delivered to the matrix. The approach used to determine η is physically logical and more correct than assuming that all the energy of phase change is delivered to the matrix (i.e., $\eta = 0$) which is typical in the literature. Results in this thesis show that assumptions concerning the energy of phase change affect the predicted sensible effectiveness greatly (up to 48%). Sensitivity studies are presented which display the importance of certain assumptions in the numerical model. Notably, controlling the energy transfer rate of energy wheels by controlling wheel speed may be impractical because the sensitivity of each effectiveness to wheel speed differs with each operating condition.

The numerical model is validated with laboratory and field measurements that cover a wide range of mass fluxes, temperatures and humidities. The numerical and experimental effectiveness values agree within the experimental and numerical uncertainties and the trends in the data are the same. The total uncertainty in the numerically simulated effectiveness values, when simulating an existing energy wheel, is a function of both the accuracy of the numerical algorithm and the uncertainty in the measured input property data. For the model presented in this thesis, the uncertainty in

the predicted value of sensible effectiveness is likely less than ±3% and the uncertainty in the predicted value of latent effectiveness is likely less than ±5%. The uncertainty in the predicted total effectiveness lies between the uncertainty in the sensible and latent effectivenesses. The prime cause of these uncertainties is the uncertainty in the input data for the energy wheel because the uncertainty due to the numerical algorithm is less than ±1%.

The validated numerical model is used to extrapolate experimental test data to other operating conditions. Complexities that arise from this extrapolation show that a simple extrapolation of experimental data to other operating conditions is often not possible. A validated numerical model is needed for this.

A major contribution of this thesis is the development of the governing dimensionless groups for simultaneous heat and moisture transfer in energy wheels. These dimensionless groups parallel the dimensionless groups for rotary sensible heat exchangers which can be found in many heat exchanger references. The dimensionless groups for heat and moisture transfer are found to be functions of the operating temperature and humidity of the energy wheel. The physical meaning of the dimensionless groups and the importance of the new operating condition factor (H*) are explained and illustrated. This development is a major break through because it explains why the effectiveness of energy wheels is a function of the operating temperature and humidity as has been observed by several energy wheel manufacturers and researchers.

Furthermore, the analysis shows which parameters are important for understanding and correlating energy wheel performance.

Sensible, latent and total effectiveness correlations, developed in this thesis, agree with over 600 simulated values within ±2.5%, ±2% and ±2.5% respectively. These effectiveness relations are quite complex, but allow a designer to calculate effectiveness from known parameters and are applicable over a large range of conditions. Since the correlations are based on the governing dimensionless groups, a physical meaning is embedded in the correlations which would not be present if they were based on the individual dimensional parameters. These effectiveness correlations are simpler to use than numerical models and will permit future researchers to optimize energy wheel performance and life cycle cost savings for air conditioning applications in different climates and buildings.

Condensation and frosting are included in the validated numerical model of energy wheels. These physical processes are studied numerically in this thesis and the results show that sorption and saturation conditions can coexist in the energy wheel. Uncontrolled condensation is expected to be minimal in hot climates, but frosting is expected to be very important in cold climates. Simulation results confirm that reducing the wheel speed reduces uncontrolled condensation and frosting, but the sensitivity of condensation and frosting to wheel speed is climate dependent. Finally, a desiccant with a linear sorption curve (e.g., silica gel) has smaller amounts of condensation/frosting than a desiccant with a Type I sorption curve (e.g., molecular sieve).

A major finding from this research is that energy wheels coated with a silica gel desiccant are expected to have better performance characteristics than energy wheels coated with a molecular sieve desiccant. Many manufacturers currently produce energy wheels that are coated with molecular sieve desiccants. This design decision needs to be changed if the optimal energy recovery from building exhaust air is to be realized. In addition, the research in this thesis shows that silica gel desiccants may extend the practical operating range of energy wheels because energy wheels coated with silica gel desiccants have less condensation and frosting during extreme operating conditions than energy wheels coated with molecular sieve desiccants.

6.2 FUTURE WORK

The major difference between the energy equations developed in this thesis and those in the literature is the term η which accounts for the distribution of phase change energy between the solid and fluid. A method of estimating the value of η is presented and the value of η for various applications of heat and mass transfer theory is discussed. This complex physical process of phase change within a desiccant coating needs more research to obtain a more accurate estimate of η for different applications and operating conditions. This research would likely involve macroscopic and microscopic experimental and numerical studies. The idea of energy being delivered to both mediums at the interface during phase change is essential in many areas of heat and mass transfer, yet it has been typically neglected in energy wheel analysis. This needs to be resolved in

the literature. The correct value of η and its importance in simultaneous heat and mass transfer problems may be developed and exploited by future research.

Another major area of future research is to apply the correlations developed in this thesis to optimize energy wheels for use in buildings (and vehicles). These correlations should also be extended to include unbalanced flow rates so that the part load performance of energy wheels and yearly energy savings can be calculated. With these correlations and cost data from manufacturers, energy wheels with least life cycle costs can be designed for buildings in different climates with local energy prices. These optimized solutions together with appropriate design methods will be crucial for industry to implement optimal energy wheel designs.

Energy wheel manufacturers and HVAC engineers currently face many questions regarding the design of energy wheels such as the appropriate: wheel thickness, rotational speed and type of desiccant and support material, to name a few. For example, there may be several ways to produce a wheel with a certain effectiveness and the final design may depend on application constraints (e.g., space, carryover, duct size, etc.). The optimal solution is likely a function of the application climate and is further complicated by manufacturing quality control issues such as the consistency of the tube pore size and the desiccant coating thickness. Future research projects should provide guidance to manufacturers and HVAC engineers concerning these design and manufacturing issues.

The performance and control of energy wheels during condensation and frosting conditions needs further research work. Especially important are experimental investigations of frosting within energy wheels to confirm the theoretical predictions of when uncontrolled frosting may occur. Furthermore, there are no available correlations for energy wheel performance during condensation and frosting conditions, indicating a need for further research.

Energy wheels have been used almost exclusively in the HVAC industry for buildings. They have not been widely used in other industries. For example, the transportation industry could benefit from the use of energy wheels. Vehicles require 8 L/(s·person) of outdoor air to maintain acceptable indoor air quality (ANSI/ASHRAE Standard 62-1989). In the case of large passenger buses or coaches, energy wheels have the potential to reduce fuel consumption by nearly 10% during warm and humid weather. This is significant because fuel constitutes 40 to 50% of each bus company's operating expenses. High performance energy wheels could save over 2 million liters of fuel and 1 million dollars for Canadian bus and tour companies each year (Canadian buses travel ~500 million km/year). Greater savings are possible in the US and especially Europe where public transportation is even more common. These savings do not include the savings that are possible in trains, planes, ships and personal vehicles. The potential monetary and fuel savings are significant and clearly indicate an area for future research and innovation. This research on the deployment of energy wheels in vehicles will need to consider two constraints that are not critical in the HVAC industry for buildings. Both

the size and weight of the energy recovery system needs to be small for vehicles and preferably less than the size and weight of existing air conditioning systems.

Finally, for energy wheels to be utilized fully in recovering energy from building exhaust air, manufacturers and engineers need a better understanding of the performance characteristics of energy wheels. Recently, several North American manufacturers of HVAC equipment have developed workable designs for energy wheels which are very effective in transferring heat and moisture. However, these designs are not optimum with respect to performance and life-cycle costs. Indeed, many manufacturers and design engineers do not clearly understand the performance characteristics of energy wheels. They often neglect the fact that each of the three effectiveness values (i.e., sensible, latent and total) change with operating conditions in a unique manner. It is hoped that the research in this thesis will alleviate some of these misunderstanding; however, before appropriate designs for energy wheels will be generally available and applied, manufacturers and design engineers need to be educated regarding the complex performance of energy wheels.

REFERENCES

ANSI/ASHRAE Standard 55-1992, *Thermal environmental conditions for human occupancy*, ASHRAE, Atlanta.

ANSI/ASHRAE Standard 62-1989, *Ventilation for acceptable indoor air quality*, ASHRAE, Atlanta.

ANSI/ASHRAE Standard 84-1991, *Method of testing air-to-air heat exchangers*, ASHRAE, Atlanta.

ANSI/ASME Standard PTC 19.1-1985, *Measurement uncertainty*, ASME, New York.

ANSI/ASME Standard PTC 30-1991, *Air cooled heat exchangers*, ASME, New York.

ASHRAE, 1997, *Fundamentals handbook*, ASHRAE, Atlanta.

ASHRAE, 1992, *Desiccant cooling and dehumidification*, (edited by L. Harriman), ASHRAE, Atlanta.

ASHRAE Standard 90-1975, *Energy conservation in new building design*, ASHRAE, Atlanta.

ASTM, 1994, *Moisture control in buildings*, (edited by H. R. Trechsel), ASTM, Philadelphia.

ASTM Standard E 104-85, Standard practice for maintaining constant relative humidity by means of aqueous solutions, In: *Annual book of ASTM standards*, **11.03** ASTM, Philadelphia.

Bahnke, G. D. and Howard, C. P., 1964, The effect of longitudinal heat conduction on periodic-flow heat exchangers, *Trans. ASME, Journal of Engineering for Power*, **86**, 105-120.

Banks, P. J., 1985a, Prediction of heat and mass regenerator performance using nonlinear analogy method: Part 2–Comparison of methods, *ASME J. Heat Transfer*, **107**, 230-238.

Banks, P. J., 1985b, Prediction of heat and mass regenerator performance using nonlinear analogy method: Part 1–Basis, *ASME J. Heat Transfer*, **107**, 222-229.

Banks, P. J., 1972, Coupled equilibrium heat and single adsorbate transfer in fluid flow through a porous medium–I: Characteristic potentials and specific capacity ratios, *Chemical Engineering Science*, **27**, 1143-1155.

Beck, J. V., Blackwell, B. and St. Clair, C. R. Jr., 1985, *Inverse Heat Conduction: Ill-posed Problems*, Wiley, Toronto.

Brandemuehl, M. J. and Banks, P. J., 1981, Rotary heat exchangers with time varying or nonuniform inlet temperatures, In: *Regenerative and recuperative heat exchangers*, (edited by R. K. Shah and D. E. Metzger), ASME, New York, 59-67.

Carnes, L., 1984, Air-to-air heat recovery systems for research laboratories, *ASHRAE Trans.*, **90**(2A), 327-340.

Carslaw, H. S. and Jaeger, J. C., 1959, *Conduction of heat in solids*, Second Edition, Oxford University Press, New York, 87-89.

Charoensupaya, D. and Worek, W. M., 1988, Parametric study of an open-cycle adiabatic, solid, desiccant cooling system, *Energy*, **13**(9), 739-747.

Christianson, K. L. and Newhouse, K. N., 1985, Analysis of wet-bulb psychrometry, In: *Moisture and humidity: measurement and control in science and industry*, Instrument Society of America, Research Triangle Park, North Carolina, 75-78.

Ciepliski, D. L., 1997, *Testing an air-to-air energy recovery device using performance test standards*, M.Sc. thesis in mechanical engineering, University of Saskatchewan, Canada.

Ciepliski, D. L., Simonson, C. J. and Besant, R. W, 1998, Some recommendations for improvements to ASHRAE standard 84-1991, *ASHRAE Trans.*, **104**(1).

Close, D. J. and Banks, P. J., 1972, Coupled equilibrium heat and single adsorbate transfer in fluid flow through a porous medium–II: Predictions for silica-gel air-drier using characteristic charts, *Chemical Engineering Science*, **27**, 1157-1169.

Coleman, H. W. and Steele, W. G., 1989, *Experimentation and uncertainty analysis for engineers*, Wiley-Interscience, New York.

Collier, R. K., 1988, *Advanced desiccant material assessment: Phase 2*, Gas Research Institute, Report GRI-88-0125, Chicago.

Collier, R. K., Cale, T. S. and Lavan, Z., 1986, *Advanced desiccant materials assessment: Phase 1*, Gas Research Institute, Report GRI-86-0182, Chicago.

Coppage, J. E. and London, A. L., 1953, The periodic-flow regenerator - a summary of design theory, *Trans. ASME*, **75**, 779.

CSA Standard C439-M1988, *Standard methods of test for rating the performance of heat recovery ventilators*, Canadian Standards Association, Rexdale, Ontario, Canada.

de Leeuw, N. H., Watson, G. W. and Parker, S. C., 1995, Atomistic simulation of the effect of dissociative adsorption of water on surface structure and stability of calcium and magnesium oxide, *J. Phys. Chem.*, **99**, 17219-17225.

Downing, C. C. and Bayer, C. W., 1993, Classroom indoor air quality vs. ventilation rate, *ASHRAE Trans.*, **99**(2), 1099-1103.

ENV Standard 308-1996, *Heat Exchangers - Test procedures for establishing performance of air-to-air and flue gases heat recovery devices*, European Committee for Standardization.

Ewing, G. E. and Peters, S. J., 1996, Adsorption of water on NaCl, submitted to *Surface Review and Letters*, November 5.

Gawley, H. N. and Fisher, D. R., 1975, The effectiveness and rating of air-to-air heat exchangers, *ASHRAE Trans.*, **81**(2), 401-409.

Guo, P., Ciepliski, D. L. and Besant, R. W., 1998, A testing and HVAC methodology for air-to-air heat pipe heat exchangers, to be published in *Int. J. HVAC&R Research*, **4**(1), 3-26.

Gregg, S. J. and Sing, K. S. W., 1982, *Adsorption, Surface Area and Porosity*, Second Edition, Academic Press, London.

Harper, D. B., 1957, Seal leakage in the rotary regenerator and its effect on rotary-regenerator design for gas turbines, *Trans. ASME*, **79**, 233-245.

Harper, D. B and Rohsenow, W. M., 1953, Effect of rotary regenerator performance on gas-turbine plant performance, *Trans. ASME*, **75**, 759-765.

Heiselberg, P., 1996, Room air and contaminant distribution in mixing ventilation. *ASHRAE Trans.*, **102**(2), 332-339.

Holmberg, R. B., 1989, Prediction of condensation and frosting limits in rotary wheels for heat recovery in buildings, *ASHRAE Trans.*, **95**(1), 64-69.

Holmberg, R. B., 1979, Combined heat and mass transfer in regenerators with hygroscopic materials, *Trans. ASME, Journal of Heat Transfer*, **101**, 205-210.

Incropera, F. P. and Dewitt, D. P., 1996, *Fundamentals of Heat and Mass Transfer*, Fourth Edition, Wiley, Toronto.

Irwin, D. R., Simonson, C. J., Saw, K. Y. and Besant, R. W., 1998, Contaminant and heat removal effectiveness and air-to-air heat/energy recovery for a contaminated air space, accepted for publication in *ASHRAE Trans.*, **104**(2).

ISO Standard 5167-1, 1991, *Measurement of air flow by pressure differential devices - Part 1: orifice plates and venturi tubes inserted in circular conduits running full*, International Standards Organization, Geneva.

Janssen, J. E., 1994, The V in ASHRAE: an historical perspective, *ASHRAE Journal*, **36**(8), 126-132.

Johnson, A. B., Besant, R. W. and Schoenau, G. J., 1995, Design of multi-coil run-around heat exchanger systems for ventilation air heating and cooling, *ASHRAE Trans.*, **101**(2), 967-978.

Johnson, A. B., Simonson, C. J. and Besant, R. W., 1998, Uncertainty analysis in the testing of air-to-air heat/energy exchangers installed in buildings, *ASHRAE Trans.*, **104**(1).

Kays, W. M. and London, A. L., 1984, *Compact Heat Exchangers*, Third Edition, McGraw-Hill, New York.

Klauss, A. K., Tull, R. H., Roots, L. M. and Pfafflin, J. R., 1970, History of the changing concepts in ventilation requirements, *ASHRAE Journal*, **12**(6), 51-55.

Klein, H., Klein, S. A. and Mitchell, J. W., 1990, Analysis of regenerative enthalpy exchangers, *Int. J. Heat Mass Transfer*, **33**, 735-744.

Lafarie, J.-P., 1985, Relative humidity measurement: a review of two state-of-the-art sensors, In: *Moisture and humidity: measurement and control in science and industry*, Instrument Society of America, Research Triangle Park, North Carolina, 975-889.

Lambertson, T. J., 1958, Performance factors of a periodic-flow heat exchanger, *Trans. ASME*, **80**(1), 586-592.

Lebrun, J. J., 1996, Some HVAC&R research pitfalls, *Int. J HVAC&R Research*, **2**(3), 171-172.

Leersum, J. G. and Banks, P. J., 1977, Equilibrium heat and mass transfer in regenerators in which condensation occurs, *Int. J. Heat Mass Transfer*, **20**, 927-934.

London, A. L., Sampsell, D. F. and McGowan, J. G., 1964, The transient response of gas turbine plant heat exchangers - Additional solutions for regenerators of the periodic-flow and direct-transfer types, *Trans. ASME, Journal of Engineering for Power*, **86**, 127-135.

Maclaine-cross, I. L., 1974, *A theory of combined heat and mass transfer in regenerators*, Ph.D. thesis in mechanical engineering, Monash University, Australia.

Maclaine-cross, I. L. and Banks, P. J., 1972, Coupled heat and mass transfer in regenerators–Prediction using an analogy with heat transfer, *Int. J. Heat Mass Transfer*, **15**, 1225-1242.

McFarland, J. K., Jeter, S. M. and Abdel-Khalik, S. I., 1996, Effect of a heat pipe on dehumidification of a controlled air space, *ASHRAE Trans.*, **102**(1), 132-139.

Meckler, M., 1995, Desiccant outdoor air preconditioners maximize heat recovery ventilation potentials, *ASHRAE Trans.*, **101**(2), 992-1000.

Moffat, R. J., 1988, Describing the uncertainties in experimental results, *Exp. Thermal Fluids Sci.*, **1**, 3-17.

Mondt, J. R., 1964, Vehicular gas turbine periodic-flow heat exchanger solid and fluid temperature distributions, *Trans. ASME, Journal of Engineering for Power*, **86**, 121-126.

Nimmo, B. G., Collier, R. K. Jr. and Rengarajan, R., 1993, DEAC: Desiccant enhancement of cooling-based dehumidification, *ASHRAE Trans.*, **99**(1), 842-848.

Ochoa-Tapia, J. A. and Whitaker, S., 1997, Heat transfer at the boundary between a porous medium and a homogeneous fluid, *Int. J. Heat Mass Transfer*, **40**, 2691-2707.

Patankar, S. V., 1980, *Numerical heat transfer and fluid flow*, Hemisphere, New York.

Pesaran, A. A. and Mills, A. F., 1992, Moisture transport in silica gel packed beds - I. Theoretical study, In: *Desiccant cooling and dehumidification*, (edited by L. Harriman), ASHRAE, Atlanta, 98-109.

Rengarajan, K. and Nimmo, B. G., 1993, Desiccant enhanced air conditioning (DEAC): An approach to improved comfort, In: *Heat pump and refrigeration systems design, analysis and applications*, AES-**29**, ASME, New York, 129-138.

Rengarajan, K., Shirey, D. B. III and Raustad, R. A., 1996, Cost-effective HVAC technologies to meet ASHRAE Standard 62-1989 in hot and humid climates, *ASHRAE Trans.*, **102**(1), 166-182.

Ruth, D. W., Fisher, D. R. and Gawley, H. N., 1975, Investigation of frosting in rotary air-to-air heat exchangers, *ASHRAE Trans.*, **81**(2), 410-417.

Ruthven, D. M., 1984, *Principles of adsorption and adsorption processes*, Wiley, Toronto.

Sauer, H. J. and Howell, R. H., 1981, Promise and potential of air-to-air energy recovery systems, *ASHRAE Trans.*, **87**(1), 167-182.

Schaefer, J. A., Diblasio, R. and Bernacki, E. J., 1996, The effectiveness of a molecular sieve heat wheel in maintaining good air quality in a major research facility, In: *Proceedings of IAQ 96 - Paths to better building environments*, (edited by K. Y. Teichman), ASHRAE, Atlanta, 223-225.

Shah, R. K., 1988, Counter flow rotary regenerator thermal design procedures, In: *Heat transfer equipment design*, (edited by R. K. Shah, E. K. Subbarao and R. A. Mashelkar), Hemisphere, New York, 267-296.

Shah, R. K., 1981, Thermal Design Theory for Regenerators, In: *Heat Exchangers: Thermal-Hydraulic Fundamentals and Design*, (edited by S. Kakaç, A. E. Bergles and F. Mayinger), Hemisphere, New York, 721-763.

Shah, R. K. and London, A. L., 1978, *Advances in Heat Transfer: Laminar flow forced convection in ducts: A source book for compact heat exchanger analytical data*, (edited by T. F. Irvine, Jr. and J. P. Hartnett), Academic Press, New York.

Shirey, D. B. III and Rengarajan K., 1996, Impact of ASHRAE Standard 62-1989 on small Florida offices, *ASHRAE Trans.*, **102**(1), 153-165.

Simonson, C. J., Tao, Y-X. and Besant, R. W., 1996, Simultaneous heat and moisture transfer in fiberglass insulation with transient boundary conditions, *ASHRAE Trans.*, **102**(1), 315-327.

Simonson, C. J. and Besant, R. W., 1997a, Heat and moisture transfer in desiccant coated rotary energy exchangers: Part I - Numerical model, *Int. J. HVAC&R Research*, **3**(4), 325-350.

Simonson, C. J. and Besant, R. W., 1997b, Heat and moisture transfer in desiccant coated rotary energy exchangers: Part II - Validation and sensitivity studies, *Int. J. HVAC&R Research*, **3**(4), 351-368.

Simonson, C. J., Besant, R. W. and Wilson, G. W., 1997, Condensation and frosting in energy wheels, In: *Proceedings ASME 32nd National Heat Transfer Conference*, HTD **339**(1), *Current developments in numerical simulation of heat and mass transfer*, (edited by K. Vafai and J. L. S. Chen), ASME, New York, 161-169.

Simonson, C. J. and Besant, R. W., 1998a, Energy wheel effectiveness. Part I – Development of dimensionless groups, submitted for publication in *Int. J. Heat Mass Transfer*, April.

Simonson, C. J. and Besant, R. W., 1998b, Energy wheel effectiveness. Part II – Correlations, submitted for publication in *Int. J. Heat Mass Transfer*, April.

Simonson, C. J. and Besant, R. W., 1998c, Heat and moisture transfer in energy wheels during sorption, condensation and frosting conditions, accepted for publication in *ASME J. Heat Transfer*.

Simonson, C. J., Ciepliski, D. L. and Besant, R. W., 1998a, Determining the performance of energy wheels: Part I - Experimental and numerical methods, submitted for publication in *ASHRAE Trans.*, April.

Simonson, C. J., Ciepliski, D. L. and Besant, R. W., 1998b, Determining the performance of energy wheels: Part II - Experimental data and numerical validation, submitted for publication in *ASHRAE Trans.*, April.

Stiesch, G., Klein, S. A. and Mitchell, J. W., 1995, Performance of rotary heat and mass exchangers, *Int. J HVAC&R Research*, **1**(4), 308-323.

Sundell, J., 1996, What we know, and what don't know about sick building syndrome, *ASHRAE Journal*, **38**(6), 51-57.

Sunden, B. and Karlsson, I., 1991, Enhancement of heat transfer in rotary heat exchangers by streamwise-corrugated flow channels, *Exp. Thermal Fluids Sci.*, **4**, 305-316.

Tamblyn, R. T., 1994, Supplying 100% outside air with less energy and providing individual occupant temperature control with less initial cost, In: *Proceedings of IAQ 94 - Engineering Indoor Environments*, (edited by E. L. Besch), ASHRAE, Atlanta, 15-22.

Tao, Y.-X., Besant, R. W. and Mao, Y., 1993a, Characteristics of frost growth on a flat plate during the early growth period, *ASHRAE Trans.*, **99**(1), 739-745.

Tao, Y.-X., Besant, R. W. and Rezkallah, K. S., 1993b, A mathematical model for predicting the densification of frost on a flat plate, *Int. J. Heat Mass Transfer*, **36**, 353-363.

Thiel, P. A. and Madey, T. F., 1987, The interaction of water with solid surfaces: fundamental aspects, *Surf. Sci. Rep.*, **7**, 211-385.

Tredgold, T., 1836, *The principles of warming and ventilation-public buildings*, M. Taylor, London.

Uddin, M. A. K. M. and Bell, K. J., 1988, Effect of uncertainties on the design and operation of systems of heat exchangers, In: *Heat transfer equipment design*, (edited by R. K. Shah, E. K. Subbarao and R. A. Mashelkar), Hemisphere, New York, 39-47.

Van den Bulck, E., Klein, S. A. and Mitchell, J. W., 1988, Second law analysis of solid desiccant rotary dehumidifiers, *ASME J. Solar Energy Eng.*, **110**, 2-9.

Wang, C. C., Chen, P. Y. and Jang, J. Y., 1996, Heat transfer and friction characteristics of convex-louver fin-and-tube heat exchangers, *Exp. Heat Transfer*, **9**, 61-78.

Woods, J. E., 1988, Air quality, In: *Encyclopedia of architecture: design, engineering and construction*, **1**, John Wiley & Sons, New York, 137-149.

Wyon, D. P., 1996, Indoor environmental effects on productivity, In: *Proceedings of IAQ 96 - Paths to better building environments*, (edited by K. Y. Teichman), ASHRAE, Atlanta, 5-15.

Zheng, W. and Worek, W. M., 1993, Numerical simulation of combined heat and mass transfer processes in a rotary dehumidifier, *Numerical Heat Transfer*, **23**(A), 211-232.

Zheng, W., Worek, W. M. and Novosel, D., 1993, Control and optimization of rotational speeds for rotary dehumidifiers, *ASHRAE Trans.*, **99**(1), 825-833.

APPENDIX A

INTERFACE BOUNDARY CONDITION BETWEEN THE AIR AND MATRIX

The major difference between the energy equations developed in this thesis and those in the literature is the term η which arises from the interface boundary condition between the air and matrix. η accounts for the distribution of phase change energy between the solid and fluid. A method of estimating the value of η is presented in this appendix and the value of η for various applications of heat and mass transfer theory is discussed.

η is used in the energy equations because the bulk mean properties are used rather than the local two or three dimensional fields. The energy released by phase change at the interface between the air and matrix cannot be assumed to be completely transferred to the air or the matrix. At this interface, some of this energy will be conducted into the matrix and some will be convected into the air. The main question is: what fraction of the phase change energy is transferred directly to the air or directly to the matrix? This may be similar to the problem of two solids in contact with a uniform heat source along the contact plane as shown in Figure A.1.

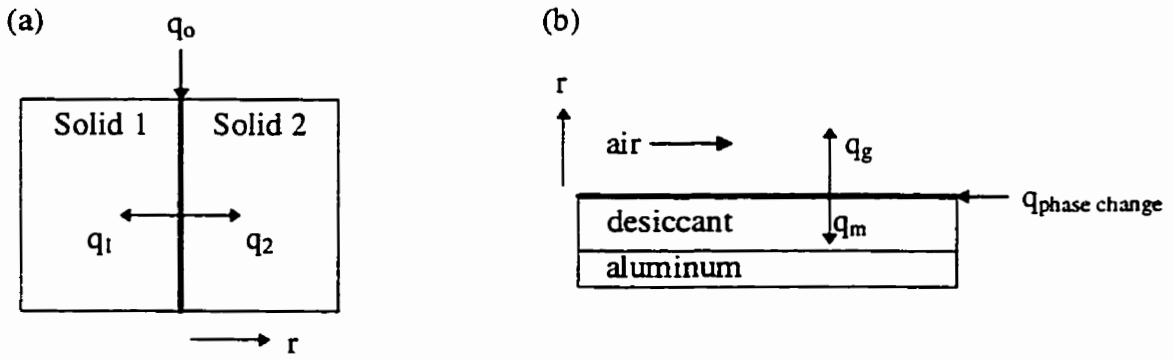

Figure A.1. *Schematic representation of heat generation at the interface between (a) two solids and (b) a solid and a moving fluid.*

The analytical solution for temperatures in two infinite solids with initial temperature of zero and a constant heat flux (due to a heat source initiated at time t = 0) at the interface are (Carslaw and Jaeger, 1959),

$$T_1 = \frac{2q_o\sqrt{\alpha_1\alpha_2 t}}{k_1\sqrt{\alpha_2}+k_2\sqrt{\alpha_1}}\,\text{ierfc}\left(\frac{r}{2\sqrt{\alpha_1 t}}\right), \text{ and} \tag{A.1}$$

$$T_2 = \frac{2q_o\sqrt{\alpha_1\alpha_2 t}}{k_1\sqrt{\alpha_2}+k_2\sqrt{\alpha_1}}\,\text{ierfc}\left(\frac{r}{2\sqrt{\alpha_2 t}}\right), \tag{A.2}$$

where:
$$\text{ierfc}(r) = \int_r^\infty \text{erfc}(\xi)\ d\xi = \frac{1}{\sqrt{\pi}}e^{-r^2} - r\,\text{erfc}(r)\ , \text{and} \tag{A.3}$$

$$\text{erfc}(r) = \frac{2}{\sqrt{\pi}}\int_r^\infty e^{-\xi^2}\,d\xi\ . \tag{A.4}$$

From the temperature profile, the fraction of the heat source that is transferred to the air can be determined as,

$$\eta = \frac{q_g}{q_{\text{phase change}}} = \frac{-k_g\left.\frac{\partial T_g}{\partial r}\right|_{r=0}}{q_{\text{phase change}}} = \frac{k_g/\sqrt{\alpha_g}}{k_g/\sqrt{\alpha_g}+k_d/\sqrt{\alpha_d}}\ , \tag{A.5}$$

where, for convection, k_g and α_g are defined as,

$$k_g = h\, D_h \quad \text{and} \quad \alpha_g = \frac{k_g}{\rho_g Cp_g} \,. \tag{A.6}$$

For steady-state heat transfer, η could be calculated as,

$$\eta = \frac{\text{Conductance air}}{\text{Conductance air} \;+\; \text{Conductance matrix}} = \frac{h}{h + k_d / t_d} \,, \tag{A.7}$$

where t_d is the thickness of the desiccant. Using equation (A.5), $\eta = 0.073$ and using equation (A.7), $\eta = 0.035$. Equation (A.5) is more appropriate because equation (A.7) does not include thermal storage effects and because air flowing cyclically from hot moist air to cold dry air through the wheel subjects both the air and the matrix to step-change transient heat sources. If the properties of the entire matrix (i.e. aluminum and desiccant) are used to calculate η instead of the desiccant properties, the value of η will decrease to 3%.

A non-smooth or rough interface between the desiccant and air may, for molecular sieve coatings, tend to decrease the value of η from the 7% calculated with equation (A.5) because some of the water vapor will be deposited in the matrix depressions that are less exposed to air flow. However, the majority of the phase change is expected to occur in the most exposed parts of the desiccant because moisture is desorbed and adsorbed cyclically during energy wheel operation. In addition, the relative humidity of the air is seldom less than 10% during energy exchange applications which means that the water molecules deep within the desiccant will not likely by desorbed

during normal operation. This means that η is likely more important for energy wheels with thin desiccant coatings than for desiccant dryers which have thicker coatings and use lower relative humidities for regeneration. The scanning electron microscope photographs in Ruthven (1984) show that molecular sieve coatings have some roughness but no fin-like structures. Fin-like structures may have the opposite effect if most of the water molecules are adsorbed on the fins, causing η to increase beyond 0.07. Considering the above discussion, a value of $\eta = 0.05$ is chosen for the molecular sieve coating in this thesis. Further research on this boundary condition will be necessary to further quantify the correct value of η. It should be noted that when $\eta = 1$, all the energy of phase change is convected into the air and when $\eta = 0$, all the energy of phase change is conducted into the matrix. For $0 < \eta < 1$ some of the energy of phase change is convected into the air and the rest is conducted into the matrix. The inclusion of η as a parameter in the model allows the model to be general for any physically possible interface flux conditions and matrix properties.

The above continuum processes need a molecular explanation. The desiccant coating on the metal film of an energy wheel is a porous media into which both dry air and water vapor molecules can penetrate and diffuse energy. Water molecules deposited within and on the porous structure lose their kinetic energy, releasing the heat of sorption but interacting with both the desiccant structure surface and the adjacent air molecules. Thiel and Madey (1987) have reviewed water vapor adsorption on selected surfaces which are both rough and smooth. They show that surface morphologies affect the molecular structure of adsorbed water and rough surfaces can cause chemical

dissociation. Another study showed that the chemical reactions of water on the metal oxide MgO takes place entirely on defect sights while smooth surfaces of MgO are inert (de Leeuw et al., 1995). Ewing and Peters (1996) have reviewed the adsorption of water on the alkali halide NaCl (i.e., salt) surfaces. They point out that chemical reactions and Na^+ and Cl^- ion migration occur on salt crystal surface defects well below the deliquescence point (75% R.H. at 25°C) where the mass of water adsorbed into a salt solution is without limit. Changes in the surface morphology have been observed at humidities as low as 20%.

Solid desiccants, such as silica gel and molecular sieve, are composed of oxygen and hydrogen compounds of the semi conductor silicon which have a strong affinity for water molecules. The can adsorb 20% or more times their own dry mass in water vapor by adsorbing multiple layers of water on a very porous microstructure. Clogging of this microstructure can be a problem during the manufacture of an energy wheel or when the supply or exhaust air is highly contaminated. These adsorbents tend to be stable chemically but they can be damaged by prolonged exposure to liquid water and very large temperature differences at high values of relative humidity. These complex physical and chemical processes within the desiccant coating need more research to obtain a more accurate estimate of η. This research would likely involve microscopic experimental and numerical studies.

The general approach to considering the energy release at the interface as being delivered partly to the air and desiccant is more general than the assumptions currently in

the literature for desiccant drying and energy transfer wheels. This theory has a physical basis and can be used to explain why there is a range of assumptions concerning this issue in the scientific literature. The various assumptions are:

- condensation theory: the energy of phase change is delivered to the condensate (i.e., $\eta = 0$);
- solidification theory: energy of phase change is delivered to both the solid and liquid as calculated by an energy balance at the interface (i.e., η is variable);
- chemical reaction at an interface theory: similar to solidification theory; and
- phase change in porous media: energy of phase change is divided between the different components such that local thermal equilibrium is maintained.

In the case of film condensation of water vapor, equation (A.5) predicts a very small value of η (less than 0.01) because the thermal conductivity and density of water vapor are orders of magnitude smaller than the thermal conductivity and density of liquid water. Therefore, this theory can be used to explain why the assumption of $\eta = 0$ is acceptable for most condensation problems. This does not mean that $\eta = 0$ can be applied to all simultaneous heat and mass transfer problems. If transient dropwise condensation occurs on a rough surface with liquid droplets forming on top of the roughness elements, the droplets will interact and transfer heat with the air as well as the rough solid surface, in which case $\eta \neq 0$.

During solidification, the energy released cannot be simply assumed to be delivered to the solid (or liquid melt). The amount that is delivered to the solid or liquid must be calculated with heat conduction theory which parallels the ideas presented in this thesis. Similar statements are applicable for a chemical reaction at an interface.

In the case of porous media, which uses the assumption of local thermal equilibrium, the fraction of the energy of phase change that is delivered to the fluid is such that local thermal equilibrium is maintained. The theory presented here for transient one dimensional heat and mass transfer is more general than this and, in fact, could be used to modify porous media theory when there is significant phase change. Furthermore, at the interface between a porous medium and a homogenous fluid, an excess heat exchange term or jump condition, that determines how heat flux is distributed between different phases, is necessary (Ochoa-Tapia and Whitaker, 1997). It is important to note that when the local 2 or 3 dimensional temperature and moisture concentrations are solved on both sides of the interface, there is no need to include the parameter η because it will be included intrinsically in the energy balance at the interface. However, when the bulk mean properties are used for transient fluid flow with heat and mass transfer in a duct or tube it is of fundamental importance to accurately define how the energy source terms are distributed between the fluid and solid.

In conclusion, the idea of energy being delivered to both mediums at the interface during phase change is not entirely new; indeed, it is essential for many similar areas of study as noted above. This needs to be resolved in the literature and therefore this issue has been raised even though there is clearly the need for further research. The correct value of η and its importance in simultaneous heat and mass transfer problems may be developed and exploited by future research.

APPENDIX B

TEMPERATURE DEPENDENCE OF SORPTION ISOTHERM

A Type I sorption isotherm can be described by the following relation,

$$\frac{u}{Wm} = \frac{bP_v}{1+bP_v} = \frac{C_I\phi}{1+C_I\phi} \quad , \tag{B.1}$$

where the constants b and C_I are related by,

$$C_I = bP_{sat} \quad . \tag{B.2}$$

The constant Wm describes the number of surface sites available for sorption and is independent of temperature. The temperature dependence of constant b is governed by the vant Hoff equation (when the heat of sorption is constant and equal to the heat of vaporization (Ruthven, 1984)) which is,

$$b(T) = b_{ref} e^{\frac{h_{fg}}{R_v T}} \quad , \tag{B.3}$$

where b_{ref} is the value of the constant b at some reference temperature. Similarly the temperature dependence of the constant C_I is,

$$C_I(T) = C_{I,ref} e^{\frac{h_{fg}}{R_v T}} P_{sat}(T) \quad , \tag{B.4}$$

where, from the Clapeyron equation,

$$P_{sat}(T) = P_{ref}\, e^{\frac{h_{fg}}{R_v T_{ref}}}\, e^{\frac{-h_{fg}}{R_v T}} = \text{constant}\left(e^{\frac{-h_{fg}}{R_v T}} \right) . \tag{B.5}$$

Substituting equation (B.5) into (B.4) gives the result that the constant C_I is independent of temperature when the heat of sorption is constant and equal to the heat of vaporization.

The saturation pressure equation used in this thesis is an empirical equation which should be nearly the same as the Clapeyron equation. Therefore, it is expected that the constant C_I will be nearly temperature independent when the empirical equation is used to calculated $P_{sat}(T)$. This is in agreement with the results of Section 2.7.2.

When the heat of sorption is a function of the moisture content of the desiccant, the Clausius-Clapeyron equation can be used to determine the temperature dependence of the constant C_I. The Clausius-Clapeyron equation in the differential form is,

$$h_{ad} = R_v T^2 \left.\frac{d(\ln P_v)}{dT}\right|_u \quad . \tag{B.6}$$

Integrating equation (B.6) from T_1 to T_2 with the temperature dependence of h_{ad} defined as,

$$h_{ad} = h^*(a - mT) \quad , \tag{B.7}$$

gives the following,

$$\frac{P_{v,2}}{P_{v,1}} = e^{\frac{-h^*a}{R_v}\left(\frac{T_1 - T_2}{T_1 T_2}\right)} \left(\frac{T_2}{T_1}\right)^{\frac{-h^*m}{R_v}} \quad . \tag{B.8}$$

Substituting the inverse of equation (B.1) into equation (B.8) and rearranging allows the calculation of constant C_I at temperature T_2 knowing the value of C_I at temperature T_1. The relation is,

$$C_{I@T_2} = C_{I@T_1} \frac{P_{sat,2}}{P_{sat,1}} \left(\frac{T_2}{T_1} \right)^{\frac{h^* m}{R_v}} e^{\frac{h^* a}{R_v}\left(\frac{T_1 - T_2}{T_1 T_2} \right)}, \qquad \text{(B.9)}$$

where temperatures are in units of K.

APPENDIX C

DISCRETIZED GOVERNING EQUATIONS AND NUMERICAL CODE

The discretization of the governing equations is performed based on the control volume shown in Figure C.1.

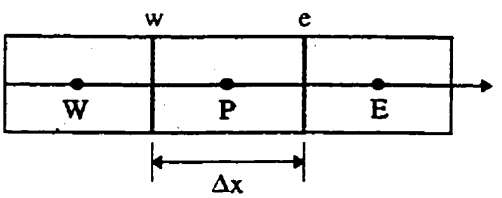

Figure C.1. *Control volume used to discretize the governing equations.*

The discretized energy equation for air on the supply side (U (+)) is:

$$a_P T_{g,P} = a_W T_{g,W} + a_m T_{m,P} + b \ , \tag{C.1}$$

where:

$$a_P = a_p^o + a_W + a_m \ , \tag{C.2}$$

$$a_p^o = \frac{A_g (\rho_g Cp_g)_P \Delta x}{\Delta t} \ , \tag{C.3}$$

$$a_W = A_g (U \rho_g Cp_g)_w \ , \tag{C.4}$$

$$a_m = (h \frac{A'_s}{L})_P \Delta x \ , \text{ and} \tag{C.5}$$

$$b = a_P^o T_{g,P}^o + \eta (\dot{m}' h_{ad})_P \Delta x \ . \tag{C.6}$$

The discretized energy equation for air on the exhaust side (U (-)) is the same as on the supply side (U(+)) except that the west node (subscript W) is replaced with the east node (subscript E), the east face (subscript e) and west face (subscript w) are interchanged and U retains its positive sign.

The discretized energy equation for the matrix is:

$$a_P T_{m.P} = a_E T_{m.E} + a_W T_{m.W} + a_g T_{g.P} + b \ . \tag{C.7}$$

where:

$$a_P = a_p^o + a_E + a_W + a_g \ , \tag{C.8}$$

$$a_P^o = \frac{A_m (\rho_m Cp_m)_P \Delta x}{\Delta t} \ , \tag{C.9}$$

$$a_E = a_W = \frac{k_{Al} A_{Al}}{\Delta x} \ , \tag{C.10}$$

$$a_g = (h \frac{A'_s}{L})_P \Delta x + \dot{m}'_P Cp_w \Delta x \ , \text{ and} \tag{C.11}$$

$$b = a_P^o T_{m.P}^o + (1-\eta)(\dot{m}' h_{ad})_P \Delta x \ . \tag{C.12}$$

The discretized conservation of mass equation for dry air (when U is positive) is:

$$a_e U_e = a_w U_w + b, \tag{C.13}$$

where:

$$a_e = \rho_{a.e} \ , \tag{C.14}$$

$$a_w = \rho_{a.w} \ , \text{ and} \tag{C.15}$$

$$b = \frac{(\rho_a^o - \rho_a)_P \Delta x}{\Delta t} \ . \tag{C.16}$$

When U is negative the equation is the same except the east and west faces are interchanged and U = -U (i.e. U is positive).

The discretized conservation of mass equation for water vapor during sorption processes is (when U is positive):

$$a_P \rho_{v,P} = a_W \rho_{v,W} + b \ , \tag{C.17}$$

where:

$$a_P = a_p^\circ + A_g U_e + (h_m \frac{A'_s}{L})_P \Delta x \ , \tag{C.18}$$

$$a_p^\circ = \frac{A_g \Delta x}{\Delta t} \ , \tag{C.19}$$

$$a_W = A_g U_w \ , \text{and} \tag{C.20}$$

$$b = a_P^\circ \rho_{v,P}^\circ + (h_m \frac{A'_s}{L} \rho_{v,m})_P \Delta x \ . \tag{C.21}$$

When U is negative the equation is the same except the east node replaces the west node, the east and west faces are interchanged and U(+) is used (i.e. U = -U).

During saturation conditions, the discretized conservation equation for water vapor in the air is used to solve $\dot{m}'_p$ because $\rho_{v,P}$ is known (saturation density). The discretized equation in this case is,

$$\dot{m}'_p = \left(a_W \rho_{v,W} - a_P \rho_{v,P} + b\right) / \Delta x \ , \tag{C.22}$$

where:

$$a_W = A_g U_w \ , \tag{C.23}$$

$$a_P = a_p^\circ + A_g U_e \ , \tag{C.24}$$

$$a_p^\circ = \frac{A_g \Delta x}{\Delta t} \ , \text{and} \tag{C.25}$$

$$b = a_P^\circ \rho_{v,P}^\circ \ . \tag{C.26}$$

The discretized conservation of mass for water in the matrix is:

$$a_P u_P = b \ , \tag{C.27}$$

where:

$$a_P = a_P^\circ \ , \tag{C.28}$$

$$a_P^\circ = \frac{\rho_{d,dry} A_d}{\Delta t} \ , \text{ and} \tag{C.29}$$

$$b = a_P^\circ u_P^\circ + \dot{m}_P' \ . \tag{C.30}$$

The numerical code was written using FORTRAN Visual Workbench version 1.00 (Copyright © 1993 Microsoft Corporation) and is given below.

```
      program ENERGYWHEEL
*** Numerical code to simulate simultaneous heat and moisture transfer in energy wheels written during
*** my Ph.D. studies at the University of Saskatchewan in Saskatoon, SK, Canada (Jan. 95 - May 98).
*** Copyright © 1997 Carey J. Simonson

*** Include files
      include 'geometry.inc'
      include 'param.inc'
      include 'variable.inc'
      include 'coeff.inc'

      open (unit=1,status='OLD',file='input.dat')
      open (unit=2,status='UNKNOWN',file='output.dat')
      open (unit=7,status='UNKNOWN',file='contin.dat')

*** Beginning of program
      CALL Geometry
      CALL InputData
      CALL HConvective
      CALL Initialize
      CALL OpenFiles
      CALL Parameters

      do while (.not. steadystate)
        avecount=avecount+count
        count=0
        dt=dto
        time=time+dt
*** Determine whether it is a hot or cold cycle
        if(mod(time,pt).le.phot+dt/10..and.mod(time,pt).gt.dt/10.)then
          hcycle=.true.
        else
```

```
        hcycle=.false.
      end if
*** Account for the No Flow section in the laboratory tests
      if (test .eq. 'y' .or. test .eq. 'Y') CALL NoFlow
      converge=.false.
      do while (.not. converge .and. count .lt. 50)
        count=count+1
*** Solve the Governing equations
        CALL EnergyMatrix
        CALL MassAirWater
        CALL MassAir
        CALL MassMatrix
        CALL EnergyAir
        CALL Thermodynamics
        CALL OtherEquations
        CALL CheckConverge
      enddo
      CALL Effectiveness
      CALL Output
*** Check for steady state after each cycle
      if(mod(time,pt).lt.dt/10. .or. mod(time,pt).gt.pt-dt/10.) then
        CALL CheckSteadyState
      end if
    enddo

    stop
    end
```

SUBROUTINE Geometry

```
*** This subroutine reads in the geometric parameters from a data file and calculates the geometric
*** properties of the wheel.

    include 'geometry.inc'
    double precision maxerror,pi,hbr,pDh
    integer nintegrate
    character entireline*75

    read(1,*) entireline
    write(2,*) entireline
    read(1,*) n,dto
    write(2,*) n,dto
    dt=dto
    read(1,*) entireline
    write(2,*) entireline
    read(1,*) L,d
    write(2,*) L,d
    read(1,*) entireline
    write(2,*) entireline
    Cpal=903.
    ral=2702.
    read(1,*) Cpdo,rdo
    write(2,*) Cpdo,rdo
    read(1,*) entireline
```

```
      write(2,*) entireline
      read(1,*) kal
      write(2,*) kal
      dx=L/n
      write(2,*) 'The grid size is: ',dx
      do i=0,n+1
        xp(i)=dx*i-dx/2
      enddo
      read(1,*) entireline
      write(2,*) entireline
      read(1,*) tal,td,Dh,Dho,hbr
      write(2,*) tal,td,Dh,Dho,hbr
      h=Dh
      Dh=Dh
      base=h/hbr
      maxerror=1.e-3  !error in mm
      p=pDh+maxerror*2.
*** Calculate the Matrix Properties
      do while (abs(pDh-p).ge. maxerror)
        pDh=2.*base*h/Dh
        pi=3.141592654
        nintegrate=1.6074*h*sqrt((1.+12.5664/base)/maxerror)+1
        p=0.
        do i=0,nintegrate
          p=p+sqrt(1.+(pi*h/base*cos(2.*pi*i/nintegrate))**2)
        enddo
        p=p-sqrt(1.+(pi*h/base)**2)/2.-sqrt(1.+(pi*h/base)**2)/2.
        p=p*base/nintegrate+base
        h=h/pDh*p
        base=h/hbr
      enddo
      p=p/1000.   !convert to m
      pDh=pDh/1000.
      h=h/1000.
      base=base/1000.
      Dh=Dh/1000.
      Dho=Dho/1000.
      td=td/1000.
      tal=tal/1000.
      Ad=td*p
      Aal=tal*p
      Am=Aal+Ad
      A=0.5*base*h
      Atot=pi/4.*d**2
      Atube=A+Aal+Ad
      num=Atot/Atube
      f=rdo*td/(ral*tal+rdo*td)
      Mmt=num*(Ad*rdo+Aal*ral)*L
      sal=Aal/Am
      sd=Ad/Am
      rmo=sd*rdo+sal*ral
      Cpmo=(sd*rdo*Cpdo+sal*ral*Cpal)/rmo
      Dh=4*A/p
*** Output the Geometric Results
```

```
      write(2,*)
      write(2,*) 'GEOMETRY OF THE WHEEL'
      write(2,*) 'Note: the matrix area and thickness are for 1/2 plane'
      write(2,'(a,1p,2e15.7,0p)')' flow area , matrix area ',A,Am
      write(2,'(a,1p,2e15.7,0p)')' Aluminum , desiccant thick ',tal,td
      write(2,'(a,1p,1e15.7,0p,f15.2)')' perimeter , # of tubes ',p,num
      write(2,'(a,4f14.6)')' por  sd  Dh  A/V',A/Atube,Ad/Am,Dh,p/Atube
      write(2,'(a,4f14.7)')' h  b Mmt f',h*1000.,base*1000.,Mmt,f
      write(2,*)

      return
      end
```

```
      SUBROUTINE InputData
*** This subroutine reads input from a data file to initialize the variables and obtain the required
*** information to solve the problem.

      include 'geometry.inc'
      include 'param.inc'
      include 'variable.inc'
      character entireline*75

      read(1,*) entireline
      write(2,*) entireline
      read(1,*) dry,continue
      write(2,*) dry,' ',continue
      read(1,*) entireline
      write(2,*) entireline
      read(1,*) neta
      write(2,*) neta
      read(1,*) entireline
      write(2,*) entireline
      read(1,*) trapez,test
      write(2,*) trapez,' ',test
      read(1,*) entireline
      write(2,*) entireline
      read(1,*) store,sorp,entry,aveentry
      write(2,*) store,' ',sorp,' ',entry,' ',aveentry
      read(1,*) entireline
      write(2,*) entireline
      read(1,*) tss,ptime,hpran,cpran
      write(2,*) tss,ptime,hpran,cpran
      tss=tss*60.  !Convert to seconds
      read(1,*) entireline
      write(2,*) entireline
      read(1,*) tolconv,tolss,tolssp,rlxo
      write(2,*) tolconv,tolss,tolssp,rlxo
      rlx=rlxo
*** Properties
      Cpa=1007.
      Cpv=1872.
      Cpl=4179.
      Cps=2040.
```

```
hfg=2445000.
hsg=2835000.
rl=997.
rs=920.
Rac=287.1
Rvc=461.8
read(1,*) entireline
write(2,*) entireline
read(1,*) C,Wm,Tsub
write(2,*) C,Wm,Tsub
read(1,*) entireline
write(2,*) entireline
read(1,*) Thot,rhhot,Qhot,Pghot
if (dry .eq. 'y' .or. dry .eq. 'Y') rhhot=0.
write(2,'(4f15.5)') Thot,rhhot,Qhot,Pghot
Thot=Thot+273.15
CALL SaturationPressure(Thot)
if (rhhot .lt. .1) then !input is W (kgw/kga)
   Whot=rhhot
   Pvhot=Whot*Pghot/(Whot+Rac/Rvc)
   rhhot=Pvhot/Psat*100.
   write(2,*) 'Hot side relative humidity:',rhhot
else
   Pvhot=Psat*rhhot/100.
end if
rvhots=Psat/(Rvc*Thot)
rvhot=Pvhot/(Rvc*Thot)
Pahot=Pghot-Pvhot
rahot=Pahot/(Rac*Thot)
rghot=rvhot+rahot
Whot=rvhot/rahot
Hhot=(Cpa*(Thot-273.15)+Whot*(hfg+Cpv*(Thot-273.15)))/1000.
read(1,*) entireline
write(2,*) entireline
read(1,*) Tcold,rhcold,Qcold,Pgcold
if (dry .eq. 'y' .or. dry .eq. 'Y') rhcold=0.
write(2,'(4f15.5)') Tcold,rhcold,Qcold,Pgcold
Tcold=Tcold+273.15
CALL SaturationPressure(Tcold)
if (rhcold .lt. .1) then !input is W (kgw/kga)
   Wcold=rhcold
   Pvcold=Wcold*Pgcold/(Wcold+Rac/Rvc)
   rhcold=Pvcold/Psat*100.
   write(2,*) 'Cold side relative humidity:',rhcold
else
   Pvcold=Psat*rhcold/100.
end if
rvcolds=Psat/(Rvc*Tcold)
rvcold=Pvcold/(Rvc*Tcold)
Pacold=Pgcold-Pvcold
racold=Pacold/(Rac*Tcold)
rgcold=rvcold+racold
Wcold=rvcold/racold
Hcold=(Cpa*(Tcold-273.15)+Wcold*(hfg+Cpv*(Tcold-273.15)))/1000.
```

```
*     if (Qcold .ge. 25.) then  !Q is in cfm
*       mhot=Qhot*.472/1000.*rghot
*       mhota=Qhot*.472/1000.*rahot
*       mcold=Qcold*.472/1000.*rgcold
*       mcolda=Qcold*.472/1000.*racold
*       write(2,'(a,2f9.5)')' Air mass flow rate(h,c):  ',mhota,mcolda
*       write(2,'(a,2f9.5)')' Total mass flow rate(h,c):',mhot,mcold
*     else  !Q is mass flow rate of AIR in kg/s
        mhota=(Dh/Dho)**2.*Qhot
        mcolda=(Dh/Dho)**2.*Qcold
*       mhota=Qhot
        Qhot=mhota/rahot/.472*1000.
        mhot=mhota/rahot*rghot
*       mcolda=Qcold
        Qcold=mcolda/racold/.472*1000.
        mcold=mcolda/racold*rgcold
        write(2,'(a,2f9.5)')' Dry Air mass flow (h,c):',mhota,mcolda
        write(2,'(a,2f9.5)')' Total mass flow rate(h,c):',mhot,mcold
***   Q is TOTAL mass flow rate
*       mhot=Qhot
*       Qhot=mhot/rghot/.472*1000.
*       mhota=mhot/rghot*rahot
*       mcold=Qcold
*       Qcold=mcold/rgcold/.472*1000.
*       mcolda=mcold/rgcold*racold
*       write(2,'(a,2f9.5)')' Air mass flow rate(h,c): ',mhota,mcolda
        write(2,'(a,2f9.2)')' Volume flow rate(h,c) (cfm):',Qhot,Qcold
*     end if
      write(*,'(a,3f12.6)')' HOT (T , W , H)  ',Thot-273.15,Whot,Hhot
      write(2,'(a,3f12.6)')' HOT (T , W , H)  ',Thot-273.15,Whot,Hhot
      write(*,'(a,3f12.6)')' COLD (T , W , H) ',Tcold-273.15,Wcold,Hcold
      write(2,'(a,3f12.6)')' COLD (T , W , H) ',Tcold-273.15,Wcold,Hcold
      read(1,*) entireline
      write(2,*) entireline
      read(1,*) nlouvtot
      write(2,*) nlouvtot
      nlouvtot=nlouvtot+1
      dlouv=L/nlouvtot
      read(1,*) entireline
      write(2,*) entireline
      read(1,*) rpm,anghot,angcold
      write(2,*) rpm,anghot,angcold
      rpmo=rpm
      pt=1./(rpm/60.)
      phot=pt*anghot/360.
      pcold=pt*angcold/360.
      Uhot=mhota/(rahot*A*num*anghot/360.)
      Ucold=mcolda/(racold*A*num*angcold/360.)
      Uhoto=uhot
      Ucoldo=Ucold
      write(2,'(a,2f9.4)')' Hot & Cold face velocities(m/s):',Uhot,Ucold
      read(1,*) entireline
      write(2,*) entireline
      read(1,*) Crdes,Crmdes,NTUdes
```

```
      write(2,*) Crdes,Crmdes,NTUdes

      return
      end
```

```
      SUBROUTINE SaturationPressure(Ta)
*** This subroutine calculates the saturation water vapor pressure at a given air temperature (Ta) using
*** equations (5 & 6) on p.6.2 of ASHRAE Fundamentals (1997).

      include 'param.inc'
      double precision Ta,c1,c2,c3,c4,c5,c6,c7,c8,c9,c10,c11,c12,c13

      c1=-5.6745359e3
      c2=6.3925247
      c3=-9.677843e-3
      c4=6.22115701e-7
      c5=2.0747825e-9
      c6=-9.484024e-13
      c7=4.1635019

      c8=-5.8002206e3
      c9=1.3914993
      c10=-4.8640239e-2
      c11=4.1764768e-5
      c12=-1.4452093e-8
      c13=6.5459673

      if (Ta.lt.273.15) then
        Psat=exp(c1/Ta+c2+c3*Ta+c4*Ta**2+c5*Ta**3+c6*Ta**4+c7*log(Ta))
      else
        Psat=exp(c8/Ta+c9+c10*Ta+c11*Ta**2+c12*Ta**3+c13*log(Ta))
      end if

      return
      end
```

```
      SUBROUTINE HConvective
*** This subroutine calculates the convective heat and mass transfer coefficients.

      include 'geometry.inc'
      include 'param.inc'
      double precision kgh,Cpgh,kgc,Cpgc,astar,h1,h2,h3
      integer nlouv

*** Exponential profile parameters (needed only when not upwinding!)
      ka=0.0263
      kv=0.0196
      kgh=(rahot*ka+rvhot*kv)/(rghot)
      Cpgh=(rahot*Cpa+rvhot*Cpv)/(rghot)
      Peh=rghot*Uhot*dx/(kgh/Cpgh)       !grid Peclet number
      kgc=(racold*ka+rvcold*kv)/(rgcold)
      Cpgc=(racold*Cpa+rvcold*Cpv)/(rgcold)
```

```
      Pec=rgcold*Ucold*dx/(kgc/Cpgc)     !grid Peclet number
      write(2,*)
      write(2,*)'The grid Peclet # (hot,cold):',Peh,Pec
      write(2,'(a,f9.4,1p,e14.4,0p)')' Alpha , Beta (hot):',
     2 1-2*(exp(Peh/2)-1)/(exp(Peh)-1),Peh*exp(Peh/2)/(exp(Peh)-1)
      Peh=rghot*Cpgh*Uhot*dh/kgh         !fluid Peclet number
      Pec=rgcold*Cpgc*Ucold*dh/kgc       !fluid Peclet number
*** Calculate the convective Nusselt Number
      astar=h/base
*** Note that this equation is applicable for h/base <=2
      if (astar .gt. 2.) then
         write(2,*) 'WARNING! OUTSIDE RANGE (a* is greater than 2)'
      end if
      Nu=sqrt((3.6912+33.0533*astar**2)/(1.+2.8391*astar**2))
      hfd=Nu*(kgh+kgc)/2./Dh
*** h/(hm*(rho*Cp)mixture)=1 for analogy between heat and mass transfer i.e. (Lewis Relation) see
*** p.5.11 ASHRAE Fundamentals (1997)
      hmfdh=hfd/(rghot*Cpgh)
      hmfdc=hfd/(rgcold*Cpgc)
      if (dry .eq. 'y' .or. dry .eq. 'Y') then
         hmfdh=1.e-40
         hmfdc=1.e-40
      end if
*** Calculate the local (and mean) heat and mass transfer coefficients. If i=0 on hot side or if i=n+1 on
*** cold side then the expression for h & hm will be undefined because x* cannot be less than zero.
*** h=hfd*(h1+h2/(x*)^.5)^2/h3; x*=x/(Dh*Pe) (Curve fit from Shah & London (1978), p.243.)
      h1=1.5715
      h2=0.09822
      h3=3.111
      hht=0.
      hmht=0.
      hct=0.
      hmct=0.
      nlouv=0
      do i=1,n
         if (nlouv .lt. nlouvtot-1) then
            if (xp(i) .gt. (nlouv+1)*dlouv) nlouv=nlouv+1
         end if
         if((xp(i)-nlouv*dlouv)/(dh*Peh) .lt. 0.25) then
            hh(i)=hfd/h3*(h1+h2/sqrt((xp(i)-nlouv*dlouv)/(dh*Peh)))**2
            hmh(i)=hh(i)/hfd*hmfdh
         else
            hh(i)=hfd
            hmh(i)=hmfdh
         end if
         if (hh(i) .lt. hfd .or. hmh(i) .lt. hmfdh) then
            hh(i)=hfd
            hmh(i)=hmfdh
         end if
         hht=hht+hh(i)/n
         hmht=hmht+hmh(i)/n
      end do
      hh(0)=hh(1)
      hmh(0)=hmh(1)
```

```
 hh(n+1)=hh(n)
 hmh(n+1)=hmh(n)
 nlouv=0
 do i=n,1,-1
    if (nlouv .lt. nlouvtot-1) then
       if (L-xp(i) .gt. (nlouv+1)*dlouv) nlouv=nlouv+1
    end if
    if((L-xp(i)-nlouv*dlouv)/(dh*Pec) .lt. 0.25) then
     hc(i)=hfd/h3*(h1+h2/sqrt((L-xp(i)-nlouv*dlouv)/(dh*Pec)))**2
     hmc(i)=hc(i)/hfd*hmfdc
    else
       hc(i)=hfd
       hmc(i)=hmfdc
    end if
    if (hc(i) .lt. hfd .or. hmc (i) .lt. hmfdc) then
       hc(i)=hfd
       hmc(i)=hmfdc
    end if
    hct=hct+hc(i)/n
    hmct=hmct+hmc(i)/n
 enddo
 hc(0)=hc(1)
 hmc(0)=hmc(1)
 hc(n+1)=hc(n)
 hmc(n+1)=hmc(n)
 if (entry .eq. 'y' .or. entry .eq. 'Y') then
    if (aveentry .eq. 'y' .or. aveentry .eq. 'Y') then !Ave. entry
       do i=0,n+1
          hh(i)=hht
          hmh(i)=hmht
          hc(i)=hct
          hmc(i)=hmct
       end do
    end if
 else  !Neglect the entry region
    do i=0,n+1
       hh(i)=hfd
       hmh(i)=hmfdh
       hc(i)=hfd
       hmc(i)=hmfdc
    enddo
    hht=hfd
    hmht=hmfdh
    hct=hfd
    hmct=hmfdc
 end if
 write(2,'(a,f12.6,1p,e15.6,0p,f9.4)')' Nu  Dh  h/base',Nu,Dh,astar
 write(2,*) 'The mean heat and mass transfer coefficients are:'
 write(2,'(a,3f12.5)')' HEAT (fd,hottot,coldtot):',hfd,hht,hct
 write(2,'(a,4f12.7)')' MASS (fdh,tot)(h,c):',hmfdh,hmfdc,hmht,hmct
 write(2,'(a,4f9.3)')' Re , Peh (h,c)',Peh/.707,Pec/.707,Peh,Pec
 write(2,'(a,2f10.6)')' Entry Length (h,c)',0.05*Dh*Peh,0.05*Dh*Pec

 return
```

```
      end
```

```
      SUBROUTINE Initialize
*** This subroutine initializes the variables.

      include 'geometry.inc'
      include 'param.inc'
      include 'variable.inc'

*** Initialize variables
      do i=0,n+1
        do j=0,2
          T(i,j)=Thot
          Te(i)=Thot
          Tm(i,j)=Thot
          rv(i,j)=rvhot
          ra(i,j)=rahot
          rve(i)=rvhot
          rae(i)=rahot
          U(i,j)=uhot
*           uw(i,j)=Wm*C*rhhot/100./(1+C*rhhot/100.)  ! Type I sorption curve
          uw(i,j)=Wm/(1.-C+C/(rhhot/100.))  ! General sorption curve
          Cpw(i,j)=Cpl
        enddo
        sat(i)=.false.
        Pv(i)=Pvhot
        Pa(i)=Pahot
        rh(i)=rhhot
        s(i)=1.
        rw(i)=rl
        had(i)=hfg
        rm(i)=rmo
        Cpm(i)=Cpmo
        if (uw(i,1) .le. 0.) then
          rvm(i)=0.
        else
          CALL SaturationPressure(Tm(i,1))
          if (uw(i,1) .lt. Wm) then
*             rvm(i)=Psat/(Rvc*Tm(i,1))*uw(i,1)/(C*(Wm-uw(i,1)))  ! Type I sorption curve
            rvm(i)=Psat/(Rvc*Tm(i,1))*C/(Wm/uw(i,1)-1.+C)  ! General sorption curve
          else
            rvm(i)=Psat/(Rvc*Tm(i,1))
          end if
        end if
      enddo
      Pg=Pghot
*** Initialize with the continuation file
      if (continue .eq. 'y') then
        do i=0,n+1
          read(7,*)T(i,0),Tm(i,0),rv(i,0),ra(i,0),uw(i,0),rvm(i)
          do j=1,2
            T(i,j)=T(i,0)
            Tm(i,j)=Tm(i,0)
```

```
            rv(i,j)=rv(i,0)
            ra(i,j)=ra(i,0)
            ra(i,j)=uw(i,0)
          enddo
        enddo
      end if

      count=0
      avecount=0.
      hcount=0
      ccount=0
      time=0.
      Thout=0.
      Tcout=0.
      Whout=0.
      Wcout=0.
      Hout=0.
      Hcout=0.
      converge=.false.
      steadystate=.false.
      scount=0

      return
      end
```

SUBROUTINE OpenFiles

*** This subroutine opens the output files and writes the heading information.

```
      include 'geometry.inc'
      include 'param.inc'
      include 'variable.inc'

      open (unit=3,status='UNKNOWN',file='ntu.dat')
      open (unit=4,status='UNKNOWN',file='twh.dat')
      open (unit=5,status='UNKNOWN',file='eff.dat')
      open (unit=6,status='UNKNOWN',file='converge.dat')
      open (unit=8,status='UNKNOWN',file='contout.dat')
      close (unit=8)
      open (unit=9,status='UNKNOWN',file='xdist.dat')
      open (unit=10,status='UNKNOWN',file='tdist.dat')
      open (unit=11,status='UNKNOWN',file='propsens.dat')
      open (unit=12,status='UNKNOWN',file='proplat.dat')

*** Headings
      write(3,*) ' Cr*    Crm*   Ntu    es     em     et'
      write(4,'(a,2f13.6)')'T(hot,in&cold,in)=',Thot-273.15,Tcold-273.15
      write(4,'(a,1p,2e18.6,0p)')'W(hot,in&cold,in)=',Whot,Wcold
      write(4,'(a,2f13.6)')'H(hot,in&cold,in)=',Hhot,Hcold
      write(4,*) ' time(min.)  Th,out   Tc,out   Wh,out    Wc,out     Hh,out   Hc,out'
      write(5,*)'t(min) Cr*  Crm* Ntu   esh    esc    emh    emc    eth    etc'
      write(6,*)'time(min.)  senserror  masserror energyerror de/dt(max)'

      return
```

```
      end
```

SUBROUTINE Parameters

```
*** This subroutine calculates the parameters for correlating the effectiveness.  The parameters are:
*** cold and hot capacitance rates, C*, Cr*, Crm* and Ntu.

      include 'geometry.inc'
      include 'param.inc'
      double precision Crratio,Crmratio,NTUratio,Hstar,CrstarmtS

10    mcolda=Ucold*racold*A
      mhota=Uhot*rahot*A
      mmina=min(mcolda,mhota)
      mmaxa=max(mcolda,mhota)
*** Dimensionless groups for Sensible effectiveness
      Ccolds=Ucold*racold*Cpa*A
      Chots=Uhot*rahot*Cpa*A
      Cmins=min(Ccolds,Chots)
      Cmaxs=max(Ccolds,Chots)
      Crs=rmo*Am*L*Cpmo/pt*2. ! 2 times to include both hot and cold sides
      Crstars=Crs/Cmins       ! otherwise divide by ph or pc rather than pt
      Cstars=Cmins/Cmaxs
      ntus=1./Cmins/(1./(hht*p*L*anghot/180.)+1./(hct*p*L*angcold/180.))

*** Dimensionless groups for Moisture effectiveness
      if (dry .ne. 'y' .and. dry .ne. 'Y') then
        Ccoldm=Ucold*racold*A
        Chotm=Uhot*rahot*A
        Cminm=min(Ccoldm,Chotm)
        Cmaxm=max(Ccoldm,Chotm)
        Crm=rdo*Ad*L/pt*2.  ! 2 times to include both hot and cold sides
        Crstarm=Crm/Cminm   ! otherwise divide by ph or pc rather than pt
        Cstarm=Cminm/Cmaxm
        ntum=ntus
      end if

*** Dimensionless groups for Total effectiveness
      Ccoldt=Ucold*racold*Cpa*A
      Chott=Uhot*rahot*Cpa*A
      Cmint=min(Ccoldt,Chott)
      Cmaxt=max(Ccoldt,Chott)
      Crt=rmo*Am*L*Cpmo/pt*2. ! 2 times to include both hot and cold sides
      Crstart=Crt/Cmint       ! otherwise divide by ph or pc rather than pt
      Cstart=Cmint/Cmaxt
      ntut=ntus

***  THESE lines are ONLY to allow simple simulation of various Ntu and Cr*
      if (Crdes.ne.0. .and. Crmdes.ne.0. .and. NTUdes.ne.0.) then
***  Increase the matrix density to get a round Cr* value
        Crratio=Crdes/Crstars
        if (dry .ne. 'y' .or. dry .ne. 'Y') then
          Crmratio=Crmdes/Crstarm
        else
```

```
        Crmratio=0.
      end if
      rdo=rdo*Crmratio
      ral=(rmo*Cpmo*Crratio-sd*rdo*Cpdo)/(sal*Cpal)
      rmo=sd*rdo+sal*ral
      Cpmo=(sd*rdo*Cpdo+sal*ral*Cpal)/rmo
*** Increase the heat transfer area to get a round Ntu value
      NTUratio=NTUdes/ntus
      p=p*NTUratio
      NTUdes=0. !Needed so that Cr* & Ntu are not changed again
      goto 10  !Recalculate Cr* & Ntu
    end if

    write(2,*) 'FOR Sensible effectiveness'
    write(2,*) '   Chot     Ccold     C*     Cr*     Ntu '
    write(2,100) Chots,Ccolds,Cstars,Crstars,ntus
    write(2,*) 'FOR Moisture effectiveness'
    write(2,*) '   Chot     Ccold     C*     Cr*     Ntu '
    write(2,100) Chotm,Ccoldm,Cstarm,Crstarm,ntum
    write(2,*) 'FOR Total effectiveness'
    write(2,*) '   Chot     Ccold     C*     Cr*     Ntu '
    write(2,100) Chott,Ccoldt,Cstart,Crstart,ntut

*** Output the dimensionless property data to: file# 11 ("propsens.dat") & file# 12 ("proplat.dat")
    Hstar=2500.*(Whot-Wcold)/(Thot-Tcold)
    CrstarmtS=Crstarm
    write(11,*) '   neta    Hstar  C*ht   Cr*ht,S  NTUht,o,S'
    write(12,*)' C*mt    Cr*mt   Cr*mt,S NTUmt,o,S   Th      Tc    rhh   rhc    Wm    C'
    write(11,110) neta,Hstar,Cstars,Crstars,ntus
    write(12,120) Cstarm,Crstarm,CrstarmtS,ntum,Thot,Tcold,rhhot/100.,rhcold/100.,Wm,C

100  format(1x,1p,e10.4,2x,e10.4,0p,f7.3,f9.4,f9.4)
110  format(1x,3f8.4,2f10.4)
120  format(1x,f6.4,3f10.4,2f10.3,2f7.4,f6.4,f8.3)

    return
    end
```

SUBROUTINE NoFlow

*** This subroutine solves the Governing Equations during the period of no flow in the lab. experiments.

```
    include 'geometry.inc'
    include 'param.inc'
    include 'variable.inc'
    include 'coeff.inc'
    double precision nft,hho(0:210),hco(0:210),hmho(0:210),hmco(0:210)

    if ((hcycle.and.hcount.eq.0).or.(.not.hcycle.and.ccount.eq.0))then
      if (hcycle) then  !HOT SIDE
        hcount=1
        ccount=0
      else  !COLD SIDE
        ccount=1
```

```
          hcount=0
        end if
        nft=0.
*** Reduce convective transfer coefficients and save old ones
        do i=0,n+1
          hho(i)=hh(i)
          hmho(i)=hmh(i)
          hco(i)=hc(i)
          hmco(i)=hmc(i)
          hh(i)=hfd/Nu
          hc(i)=hfd/Nu
          hmh(i)=hmfdh/Nu
          hmc(i)=hmfdc/Nu
        end do
*** Set the fluid velocity to zero
        do i=0,n+1
          do j=0,2
            U(i,j)=0.
          enddo
        enddo

        pause=.true.
        do while (nft .lt. pt/4.-dt/10.)
          nft=nft+dt
          time=time+dt
          converge=.false.
          count=0
          do while (.not. converge  .and. count .lt. 500)
            count=count+1
            CALL EnergyMatrix
            CALL MassAirWater
*             CALL MassAir      !Because U(i,j)=0.
            CALL MassMatrix
            CALL EnergyAir
            CALL Thermodynamics
            CALL OtherEquations
            CALL CheckConverge
          enddo
        enddo
        pause=.false.
*** Restore the old convective transfer coefficients
        do i=0,n+1
          hh(i)=hho(i)
          hmh(i)=hmho(i)
          hc(i)=hco(i)
          hmc(i)=hmco(i)
        end do
      end if

      return
      end
```

```
      SUBROUTINE EnergyMatrix
*** This subroutine calculates the matrix temperature using the energy equation for the matrix.

      include 'geometry.inc'
      include 'param.inc'
      include 'variable.inc'
      include 'coeff.inc'
      double precision alpha(0:210),beta(0:210)

*** West boundary
      ap(0)=1.
      ae(0)=1.
*** East boundary
      ap(n+1)=1.
      aw(n+1)=1.
      ae(n+1)=0.
      b(n+1)=0.
      ac(n+1)=0.
      if (hcycle) then  !HOT SIDE
         do i=1,n
            ac(i)=hh(i)*p*dx+m(i)*Cpw(i,1)*dx
         enddo
      else  !COLD SIDE
         do i=1,n
            ac(i)=hc(i)*p*dx+m(i)*Cpw(i,1)*dx
         enddo
      end if
*** Internal nodes
      do i=1,n
         ae(i)=kal*Aal/dx
         aw(i)=kal*Aal/dx
         anot(i)=rm(i)*Cpm(i)*Am*dx/dt
         ap(i)=ae(i)+aw(i)+anot(i)+ac(i)
         b(i)=anot(i)*Tm(i,0)+(1.-neta)*m(i)*had(i)*dx+ac(i)*T(i,1)
      enddo
*** Solve alpha and beta from West to East (0 to n+1)
      alpha(0)=ae(0)/ap(0)
      beta(0)=0.
      do i=1,n+1
         alpha(i)=ae(i)/(ap(i)-aw(i)*alpha(i-1))
         beta(i)=(b(i)+aw(i)*beta(i-1))/(ap(i)-aw(i)*alpha(i-1))
      enddo
*** Solve Tm from East to West (n+1 to 0)
      Tm(n+1,1)=beta(n+1)
      do i=n,0,-1
         Tm(i,1)=alpha(i)*Tm(i+1,1)+beta(i)
      enddo

      return
      end
```

```
      SUBROUTINE MassAirWater
*** This subroutine calculates (using the mass balance of water in the air) the density of the water vapor
*** during sorption conditions and the rate of phase change during saturation conditions.

      include 'geometry.inc'
      include 'param.inc'
      include 'variable.inc'
      include 'coeff.inc'

      if (hcycle) then  !HOT SIDE
*** West Boundary
        rv(0,1)=rvhot
        if (pause) rv(0,1)=rv(1,1)
*** Internal Nodes
        do i=1,n
          ae(i)=0.
          aw(i)=U(i-1,1)*A
          if (store .eq. 'n' .or. store .eq. 'N') then
            anot(i)=0.  !neglect storage in air
          else
            anot(i)=A*dx/dt  !include storage in air
          end if
          ap(i)=anot(i)+U(i,1)*A+hmh(i)*p*dx
          if (.not. sat(i)) then
            b(i)=anot(i)*rv(i,0)+hmh(i)*p*rvm(i)*dx
            rv(i,1)=(aw(i)*rv(i-1,1)+b(i))/ap(i)
          else
            b(i)=anot(i)*rv(i,0)
            ap(i)=anot(i)+U(i,1)*A
            m(i)=(aw(i)*rv(i-1,1)-ap(i)*rv(i,1)+b(i))/dx
          end if
        enddo
*** East Boundary (Outflow)
        rv(n+1,1)=rv(n,1)
      else  !COLD SIDE
*** East Boundary
        rv(n+1,1)=rvcold
        if (pause) rv(n+1,1)=rv(n,1)
*** Internal Nodes
        do i=n,1,-1
          ae(i)=U(i+1,1)*A
          aw(i)=0.
          if (store .eq. 'n' .or. store .eq. 'N') then
            anot(i)=0.  !neglect storage in air
          else
            anot(i)=A*dx/dt  !include storage in air
          end if
          ap(i)=anot(i)+U(i,1)*A+hmc(i)*p*dx
          if (.not. sat(i)) then
            b(i)=anot(i)*rv(i,0)+hmc(i)*p*rvm(i)*dx
            rv(i,1)=(ae(i)*rv(i+1,1)+b(i))/ap(i)
          else
            b(i)=anot(i)*rv(i,0)
```

```
            ap(i)=anot(i)+U(i,1)*A
            m(i)=(ae(i)*rv(i+1,1)-ap(i)*rv(i,1)+b(i))/dx
          end if
        enddo
*** West Boundary (Outflow)
        rv(0,1)=rv(1,1)
      end if

      return
      end
```

SUBROUTINE MassAir

*** This subroutine calculates the air velocity at the downstream face using the mass balance of air.

```
      include 'geometry.inc'
      include 'param.inc'
      include 'variable.inc'
      include 'coeff.inc'

      if (hcycle) then  !HOT SIDE
*** West Boundary
        U(0,1)=Uhot
*** Internal Nodes
        do i=1,n
          ae(i)=0.
          aw(i)=rae(i-1)
          ap(i)=rae(i)
          if (store .eq. 'n' .or. store .eq. 'N') then
            b(i)=0.  !neglect storage in air
          else
            b(i)=(ra(i,0)-ra(i,1))*dx/dt  !include storage in air
          end if
          U(i,1)=(aw(i)*U(i-1,1)+b(i))/ap(i)
        enddo
*** East Boundary (Outflow)
        U(n+1,1)=U(n,1)
      else  !COLD SIDE
*** East Boundary
        U(n+1,1)=Ucold
*** Internal Nodes
        do i=n,1,-1
          ae(i)=rae(i)
          aw(i)=0.
          ap(i)=rae(i-1)
          if (store .eq. 'n' .or. store .eq. 'N') then
            b(i)=0.  !neglect storage in air
          else
            b(i)=(ra(i,0)-ra(i,1))*dx/dt  !include storage in air
          end if
          U(i,1)=(ae(i)*U(i+1,1)+b(i))/ap(i)
        enddo
*** West Boundary (Outflow)
        U(0,1)=U(1,1)
```

```
    end if

    return
    end
```

SUBROUTINE MassMatrix

```
*** This subroutine calculates the mass fraction of water in the desiccant using the mass balance of
*** water on the matrix.

    include 'geometry.inc'
    include 'param.inc'
    include 'variable.inc'
    include 'coeff.inc'

    do i=1,n
      anot(i)=rdo*Ad/dt
      b(i)=anot(i)*uw(i,0)+m(i)
      ap(i)=anot(i)
      uw(i,1)=b(i)/ap(i)  !Note: May need to restrict uw>=0
    enddo
    uw(0,1)=uw(1,1)
    uw(n+1,1)=uw(n,1)

    return
    end
```

SUBROUTINE EnergyAir

```
*** This subroutine calculates the air temperature using the energy equation for the air.

    include 'geometry.inc'
    include 'param.inc'
    include 'variable.inc'
    include 'coeff.inc'

    if (hcycle) then  !HOT SIDE
*** West Boundary
      T(0,1)=Thot
      if (pause) T(0,1)=T(1,1)
*** Internal Nodes
      do i=1,n
        aw(i)=U(i-1,1)*rge(i-1)*Cpge(i-1)*A
        ae(i)=0.
        if (store .eq. 'n' .or. store .eq. 'N') then
          anot(i)=0.  !neglect storage in air
        else
          anot(i)=rg(i)*Cpg(i)*A*dx/dt
        end if
        ac(i)=hh(i)*p*dx
        b(i)=anot(i)*T(i,0)+neta*m(i)*had(i)*dx
        ap(i)=anot(i)+aw(i)+ac(i)
        T(i,1)=(aw(i)*T(i-1,1)+ac(i)*Tm(i,1)+b(i))/ap(i)
```

```
      enddo
*** East Boundary (Outflow)
      T(n+1,1)=T(n,1)
   else  !COLD SIDE
*** East Boundary
      T(n+1,1)=Tcold
      if (pause) T(n+1,1)=T(n,1)
*** Internal Nodes
      do i=n,1,-1
        aw(i)=0.
        ae(i)=U(i+1,1)*rge(i)*Cpge(i)*A
        if (store .eq. 'n' .or. store .eq. 'N') then
          anot(i)=0.  !neglect storage in air
        else
          anot(i)=rg(i)*Cpg(i)*A*dx/dt
        end if
        ac(i)=hc(i)*p*dx
        b(i)=anot(i)*T(i,0)+neta*m(i)*had(i)*dx
        ap(i)=anot(i)+ae(i)+ac(i)
        T(i,1)=(ae(i)*T(i+1,1)+ac(i)*Tm(i,1)+b(i))/ap(i)
      enddo
*** West Boundary (Outflow)
      T(0,1)=T(1,1)
   end if

   return
   end
```

SUBROUTINE Thermodynamics

```
*** This subroutine calculates the partial pressure of dry air and water vapor and the density of dry air
*** and total gas phase using ideal gas relations.  The saturation pressure, relative humidity, heat of
*** adsorption and humidity ratio(W) are also calculated.

   include 'geometry.inc'
   include 'param.inc'
   include 'variable.inc'

   if (hcycle) then  !HOT SIDE
     Pg=Pghot
   else  !COLD SIDE
     Pg=Pgcold
   end if
   do i=0,n+1
     Pv(i)=rv(i,1)*Rvc*T(i,1)
     call SaturationPressure(T(i,1))
     rh(i)=Pv(i)/Psat*100.
     if (sat(i)) then
       rh(i)=100.
       Pv(i)=Psat
       rv(i,1)=Pv(i)/(Rvc*T(i,1))
     end if
     Pa(i)=Pg-Pv(i)
     ra(i,1)=Pa(i)/(Rac*T(i,1))
```

```
      if (hcycle) then
        rve(i)=rv(i,1)     !Upwind
        Te(i)=T(i,1)       !Upwind
      else
        rve(i)=rv(i+1,1)   !Upwind
        Te(i)=T(i+1,1)     !Upwind
      end if
      if(Te(i).ne.0.) rae(i)=(Pg-(rve(i)*Rvc*Te(i)))/(Rac*Te(i))
      rg(i)=ra(i,1)+rv(i,1)
      rge(i)=rve(i)+rae(i)

*       s(i)=0. !All Solid
      s(i)=1.  !All Liquid
      had(i)=s(i)*hfg+(1.-s(i))*hsg
      W(i,1)=rv(i,1)/ra(i,1)
      if(rae(i).ne.0.) We(i)=rve(i)/rae(i)
    enddo

    return
    end
```

SUBROUTINE OtherEquations

```
*** This subroutine calculates the necessary volume average properties for the gas phase and the matrix.
*** It also calculates the water vapor density on the matrix surface and the rate of vapor phase change.

    include 'geometry.inc'
    include 'param.inc'
    include 'variable.inc'

    do i=0,n+1
      rw(i)=s(i)*rl+(1.-s(i))*rs
      Cpw(i,1)=(s(i)*rl*Cpl+(1.-s(i))*rs*Cps)/rw(i)
      Cpg(i)=(ra(i,1)*Cpa+rv(i,1)*Cpv)/rg(i)
      Cpge(i)=(rae(i)*Cpa+rve(i)*Cpv)/rge(i)
      rd(i)=rdo*(uw(i,1)+1.)
      Cpd(i)=rdo*(uw(i,1)*Cpw(i,1)+Cpdo)/rd(i)
      rm(i)=sd*rd(i)+sal*ral
      Cpm(i)=(sd*rd(i)*Cpd(i)+sal*ral*Cpal)/rm(i)
      CALL SaturationPressure(Tm(i,1))
*** Inverse Sorption Curve
      if (uw(i,1) .le. Wm) then
*       rvm(i)=Psat/(Rvc*Tm(i,1))*uw(i,1)/(Wm*C-uw(i,1)*C)   ! Type I sorption curve
        rvm(i)=Psat/(Rvc*Tm(i,1))*C/(Wm/uw(i,1)-1.+C)   ! General sorption curve
      else
        rvm(i)=Psat/(Rvc*Tm(i,1))
      endif
enddo
    if (hcycle) then  !HOT SIDE
      do i=0,n+1
        if (.not.sat(i)) m(i)=hmh(i)*p*(rv(i,1)-rvm(i))
      enddo
    else  !COLD SIDE
      do i=0,n+1
```

```
        if (.not.sat(i)) m(i)=hmc(i)*p*(rv(i,1)-rvm(i))
      enddo
    end if

    return
    end
```

SUBROUTINE CheckConverge

*** This subroutine checks if a converged solution has been reached for the given time.

```
    include 'geometry.inc'
    include 'param.inc'
    include 'variable.inc'
    double precision Tchange,Tmchange,rvchange,uwchange,mchange,mprev(0:210),mmax,mmin

    Tchange=0.
    Tmchange=0.
    rvchange=0.
    uwchange=0.
    mchange=0.
    mmax=-1.
    mmin=1.
    do i=0,n+1
      Tchange=abs(T(i,1)-T(i,2))/(n+2)+Tchange
      Tmchange=abs(Tm(i,1)-Tm(i,2))/(n+2)+Tmchange
      rvchange=abs(rv(i,1)-rv(i,2))/(n+2)+rvchange
      uwchange=abs(uw(i,1)-uw(i,2))/(n+2)+uwchange
      mchange=abs(m(i)-mprev(i))/(n+2)+mchange
      if (m(i) .gt. mmax .and. i.ne.0 .and. i.ne.n+1) mmax=m(i)
      if (m(i) .lt. mmin .and. i.ne.0 .and. i.ne.n+1) mmin=m(i)
    enddo
    if (Thot-Tcold .ne. 0.) then
      Tchange=Tchange/abs(Thot-Tcold)
      Tmchange=Tmchange/abs(Thot-Tcold)
    end if
    if (rvhot-rvcold .ne. 0.) rvchange=rvchange/abs(rvhot-rvcold)
    if (uwhot-uwcold .ne. 0.) uwchange=uwchange/abs(uwhot-uwcold)
    if (mmax-mmin.ne.0..and..not.pause) mchange=mchange/abs(mmax-mmin)
    if (count .eq. 90) then
      dt=dto/2.   !WON'T be time accurate for this Cycle
      write(*,'(a,f9.5)')' Not time accurate for time = ',time/60.
      write(2,'(a,f9.5)')' Not time accurate for time = ',time/60.
    end if
100  format(1x,1p,6e9.1,0p)

    if(Tchange .lt. tolconv .and. Tmchange .lt. tolconv .and. rvchange .lt. tolconv .and.
   2 uwchange .lt. tolconv .and. mchange .lt. tolconv) then
      converge=.true.
      do i=1,n
        if(rh(i).gt.100. .and. .not.sat(i)) then
*           converge=.false.  ! Implicit switching between Sorption and Saturation
          sat(i)=.true.
        else if(rh(i).lt.100. .and. sat(i)) then
```

```
*             converge=.false.  ! Implicit switching  between Sorption and Saturation
            sat(i)=.false.
          else if (sat(i)) then
            if(hcycle) then
              if(m(i) .lt. hmh(i)*p*(rv(i,1)-rvm(i))) then
*               converge=.false.  ! Implicit switching  between Sorption and Saturation
                sat(i)=.false.
              end if
            else
              if(m(i) .lt. hmc(i)*p*(rv(i,1)-rvm(i))) then
*               converge=.false.  ! Implicit switching  between Sorption and Saturation
                sat(i)=.false.
              end if
            end if
          end if
        enddo
      end if
      if (count .ge. 100) then
        write(6,'(a,f9.5)') ' Did not converge @ ',time/60.
        converge=.true.
      end if
      if (converge) then
        do i=0,n+1
          T(i,0)=T(i,1)
          Tm(i,0)=Tm(i,1)
          rv(i,0)=rv(i,1)
          ra(i,0)=ra(i,1)
          uw(i,0)=uw(i,1)
          Cpw(i,0)=Cpw(i,1)
          W(i,0)=W(i,1)
        enddo
      else
        do i=0,n+1
          T(i,1)=T(i,2)+rlx*(T(i,1)-T(i,2))
          T(i,2)=T(i,1)
          Tm(i,1)=Tm(i,2)+rlx*(Tm(i,1)-Tm(i,2))
          Tm(i,2)=Tm(i,1)
          rv(i,1)=rv(i,2)+rlx*(rv(i,1)-rv(i,2))
          rv(i,2)=rv(i,1)
          uw(i,1)=uw(i,2)+rlx*(uw(i,1)-uw(i,2))
          uw(i,2)=uw(i,1)
          U(i,1)=U(i,2)+rlx*(U(i,1)-U(i,2))
          U(i,2)=U(i,1)
          m(i)=mprev(i)+rlx*(m(i)-mprev(i))
          mprev(i)=m(i)
        enddo
      end if

      return
      end
```

SUBROUTINE Effectiveness

*** This subroutine calculates the average hot and cold outlet temperatures, humidity ratios and

```
*** enthalpies.  It also calculates the sensible, moisture and total effectivenesses.

      include 'geometry.inc'
      include 'param.inc'
      include 'variable.inc'
      double precision Tthot,Wthot,Hthot,Ttcold,Wtcold,Htcold,maout

*** Calculate the average outlet conditions
      if(hcycle) then
         maout=rae(n)*U(n,1)*A
         Eshout=Eshout+maout*(Cpa+We(n)*Cpv)
         Tthot=maout*(Cpa+We(n)*Cpv)*(Te(n)-273.15)
         Wthot=maout*We(n)
         mahout=mahout+maout
         Hthot=maout*(Cpa*(Te(n)-273.15)+We(n)*(hfg+Cpv*(Te(n)-273.15)))/1000.
         Thout=Thout+Tthot
         Whout=Whout+Wthot
         Hhout=Hhout+Hthot
      else
         maout=rae(0)*U(1,1)*A
         Escout=Escout+maout*(Cpa+We(0)*Cpv)
         Ttcold=maout*(Cpa+We(0)*Cpv)*(Te(0)-273.15)
         Wtcold=maout*We(0)
         macout=macout+maout
         Htcold=maout*(Cpa*(Te(0)-273.15)+We(0)*(hfg+Cpv*(Te(0)-273.15)))/1000.
         Tcout=Tcout+Ttcold
         Wcout=Wcout+Wtcold
         Hcout=Hcout+Htcold
      end if
*** Calculate the effectiveness at the end of each complete cycle
      if(mod(time,pt).lt.dt/10. .or. mod(time,pt).gt.pt-dt/10.) then
         Thout=Thout/Eshout
         Whout=Whout/mahout
         Hhout=Hhout/mahout
         Tcout=Tcout/Escout
         Wcout=Wcout/macout
         Hcout=Hcout/macout
         esh=mhota*((Thot-273.15)-Thout)/(mmina*(Thot-Tcold))
         esc=mcolda*(Tcout-(Tcold-273.15))/(mmina*(Thot-Tcold))
         emh=mhota*(Whot-Whout)/(mmina*(Whot-Wcold))
         emc=mcolda*(Wcout-Wcold)/(mmina*(Whot-Wcold))
         eth=mhota*(Hhot-Hhout)/(mmina*(Hhot-Hcold))
         etc=mcolda*(Hcout-Hcold)/(mmina*(Hhot-Hcold))
         es(0)=es(1)
         es(1)=(esh+esc)/2.
         em(0)=em(1)
         em(1)=(emh+emc)/2.
         et(0)=et(1)
         et(1)=(eth+etc)/2.
      end if

      return
      end
```

```
      SUBROUTINE CheckSteadyState
*** This subroutine checks the energy and mass balances and the periodicity of the wheel to see if the
*** solution has reached quasi-steady state.

      include 'geometry.inc'
      include 'param.inc'
      include 'variable.inc'
      double precision Eerr,Merr,edmax,Eshin,Escin,Eserr,Hstar

      if (test .eq. 'y' .or. test .eq. 'Y') then
         mahout=mahout/(phot/dt)*2.
         macout=macout/(pcold/dt)*2.
         Eshout=Eshout*Thout/(phot/dt)*2.
         Escout=Escout*Tcout/(pcold/dt)*2.
      else
         mahout=mahout/(phot/dt)
         macout=macout/(pcold/dt)
         Eshout=Eshout*Thout/(phot/dt)
         Escout=Escout*Tcout/(pcold/dt)
      end if
      Eshin=mhota*(Cpa+Whot*Cpv)*(Thot-273.15)
      Escin=mcolda*(Cpa+Wcold*Cpv)*(Tcold-273.15)
      Eerr=abs((mhota*Hhot-mahout*Hhout)-(macout*Hcout-mcolda*Hcold))
      Eerr=abs(Eerr/(mmina*(Hhot-Hcold)))
      Merr=abs((mhota*Whot-mahout*Whout)-(macout*Wcout-mcolda*Wcold))
      Merr=abs(Merr/(mmina*(Whot-Wcold)))
      edmax=max(abs(es(1)-es(0)),abs(em(1)-em(0)),abs(et(1)-et(0)))/pt
      Eserr=abs((Eshin-Eshout)-(Escout-Escin))
      Eserr=abs(Eserr/(Cmins*(Thot-Tcold)))
      if(Eerr.lt.tolss .and. Merr.lt.tolss .and. edmax.lt.tolssp) then
         scount=scount+1
         if (scount .eq. 2) then
            steadystate=.true.
         end if
      else if (edmax .lt. 1.e-6) then
         scount=scount+1
         if (scount .eq. 2) then
            steadystate=.true.
         end if
      else if (time .ge. tss-2.*pt-dt) then
         scount=scount+1
         if (scount .eq. 2) then
            steadystate=.true.
         end if
      end if
      if (.not. steadystate) then
         Thout=0.
         Tcout=0.
         Whout=0.
         Wcout=0.
         Hhout=0.
         Hcout=0.
         Eshout=0.
```

```
      Escout=0.
      mahout=0.
      macout=0.
    end if

    avecount=avecount/(pt/dt)
    write(2,100) count,avecount
    avecount=0.
    write(6,110) time/60.,Eserr,Merr,Eerr,edmax,abs(esh-esc)
*** Output the final results and write to the continuation file
    if (steadystate) then
      Hstar=2500.*(Whot-Wcold)/(Thot-Tcold)
      write(3,130)Hstar,Crstars,Crstarm,ntus,es(1),em(1),et(1)
      if(time.ge.tss-pt-dt)write(3,*)'PROG STOP time = ',time/60.
      if(edmax .lt. 1.e-6)write(3,*)'PROG STOP(de) time = ',time/60.
      open (unit=8,status='OLD',file='contout.dat')
      do i=0,n+1
        write(8,*)T(i,1),Tm(i,1),rv(i,1),ra(i,1),uw(i,1),rvm(i)
      end do
      close (unit=8)
    end if

100  format(1x,'last count= ',i4,'   Ave. Count = ',f8.3)
110  format(1x,f7.3,3x,1p,5e12.3,0p)
120  format(1x,'DE%(es,mass,energy)',3f9.4,' de/dt(%)',1p,e9.2,0p,f9.4)
130  format(1x,f8.3,f6.2,f8.2,f8.2,3f9.5)

    return
    end
```

**** This is the file '**geometry.inc**'

```
    integer n
    double precision L,d,dx,dt,xp(0:210),tal,td,p,h,base,Dh,Dho,Nu,
   2 hfd,hmfdh,hmfdc,hc(0:210),hh(0:210),hmc(0:210),hmh(0:210),hht,
   3 hct,hmht,hmct,f,ral,rdo,rmo,Mmt,kal,Cpal,Cpdo,Cpmo,A,Aal,Ad,Am,
   4 Atube,Atot,sd,sal,num,Crdes,Crmdes,NTUdes,dto
    logical steadystate,converge,hcycle

    common /common1/ n,L,d,dx,dt,xp,tal,td,p,h,base,Dh,Dho,Nu,
   2 hfd,hmfdh,hmfdc,hc,hh,hmc,hmh,hht,hct,hmht,hmct,
   3 f,ral,rdo,rmo,Mmt,kal,Cpal,Cpdo,Cpmo,A,Aal,Ad,Am,Atube,Atot,
   4 sd,sal,num,Crdes,Crmdes,NTUdes,steadystate,converge,hcycle,dto
```

---

* This is the file '**param.inc**'

```
    double precision tolconv,rlx,rlxo,Cpa,Cpv,Cpl,Cps,avecount,
   2   Rac,Rvc,Thot,rhhot,mhot,Pghot,Tcold,rhcold,mcold,Pgcold,
   3   rpm,pt,anghot,angcold,phot,pcold,rvhot,rvhots,rvcold,rvcolds,
   4   Pvhot,C,Wm,Pvcold,Psat,rahot,racold,rghot,rgcold,Uhot,Ucold
   5   ,Pahot,Pacold,rl,rs,ptime,tss,tolss,tolssp,Ucoldo,Uhoto,Peh,
   6   Pec,rpmo,ntut,Crstart,Ccoldt,Chott,Cmint,Cmaxt,Crt,Cstart,Pe,
```

```
     7   Whot,Wcold,Hhot,Hcold,Qhot,Qcold,ka,kv,mhota,mcolda,mmina,
     8   mmaxa,hfg,hsg,dlouv,uwhot,uwcold,hpran,cpran,Tsub,
     9   ntus,Crstars,Ccolds,Chots,Cmins,Cmaxs,Crs,Cstars,
     1   ntum,Crstarm,Ccoldm,Chotm,Cminm,Cmaxm,Crm,Cstarm,neta
      integer count,hcount,ccount,nlouvtot,scount
      character*1 dry,continue,trapez,test,store,sorp,entry,aveentry
      logical pause

      common /common2/ tolconv,rlx,rlxo,Cpa,Cpv,Cpl,Cps,Rac,Rvc,Thot,
     2   rhhot,mhot,Pghot,Tcold,rhcold,mcold,Pgcold,rpm,pt,anghot,
     3   angcold,Phot,Pcold,rvhot,rvhots,rvcold,rvcolds,Pvhot,C,
     4   Wm,Pvcold,Psat,rahot,racold,rghot,rgcold,Uhot,Ucold,Pahot,
     5   Pacold,rl,rs,ptime,tss,tolss,tolssp,Ucoldo,Uhoto,count,
     6   avecount,rpmo,ntut,Crstart,Ccoldt,Chott,Cmint,Cmaxt,Crt,Cstart
     7   ,Pe,Peh,Pec,Whot,Wcold,Hhot,Hcold,trapez,Qhot,Qcold,uwhot,
     9   uwcold,ka,kv,dry,continue,test,mhota,mcolda,hpran,cpran,Tsub,
     1   mmina,mmaxa,hfg,hsg,dlouv,hcount,ccount,nlouvtot,scount,
     2   ntus,Crstars,Ccolds,Chots,Cmins,Cmaxs,Crs,Cstars,
     3   ntum,Crstarm,Ccoldm,Chotm,Cminm,Cmaxm,Crm,Cstarm,neta,
     4   store,sorp,entry,aveentry,pause
```

---

* This is the file '**variable.inc**'

```
      double precision T(0:210,0:2),Tm(0:210,0:2),rv(0:210,0:2),
     2   ra(0:210,0:2),rg(0:210),U(0:210,0:2),rw(0:210),
     3   Pv(0:210),Pa(0:210),Pg,rh(0:210),rvm(0:210),Cpw(0:210,0:2),
     4   Thout,Tcout,time,esh,esc,emh,emc,eth,etc,es(0:2),em(0:2),
     5   et(0:2),m(0:210),sattime(0:210),had(0:210),s(0:210),
     6   Whout,Wcout,W(0:210,0:2),We(0:210),Hhout,Hcout,Hout,
     7   Cpg(0:210),rm(0:210),rd(0:210),Cpm(0:210),Cpd(0:210),
     8   uw(0:210,0:2),rae(0:210),rve(0:210),Te(0:210),rge(0:210),
     9   resena,resenm,resma,resmw,resmm,Cpge(0:210),Eshout,Escout,
     1   mahout,macout
      logical sat(0:210)
      integer satcount(0:210)

      common /common3/ T,Tm,rv,ra,rg,U,Pv,Pa,Pg,sat,satcount,sattime,
     2   rh,rvm,Thout,Tcout,time,esh,esc,emh,emc,eth,etc,es,em,et,
     3   m,Whout,Wcout,W,We,had,s,
     4   Hhout,Hcout,Hout,Cpg,rm,rd,Cpm,Cpd,Cpw,rw,
     5   uw,resena,resenm,resma,resmw,resmm,rae,rve,Te,rge,Cpge,
     6   Eshout,Escout,mahout,macout
```

*** This is the file '**coeff.inc**'

```
      double precision ap(0:210),aw(0:210),ae(0:210),b(0:210),ac(0:210),anot(0:210)

      common /common4/ ap,aw,ae,b,ac,anot
```

IMAGE EVALUATION TEST TARGET (QA-3)

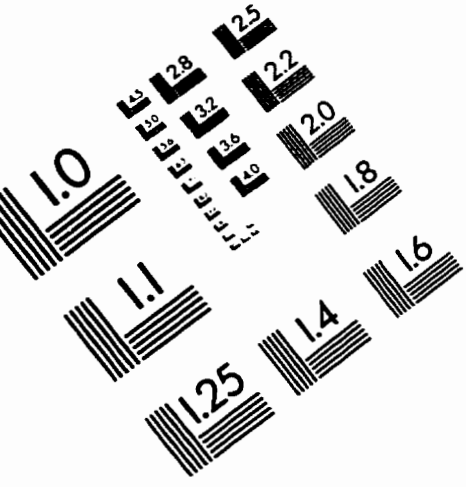

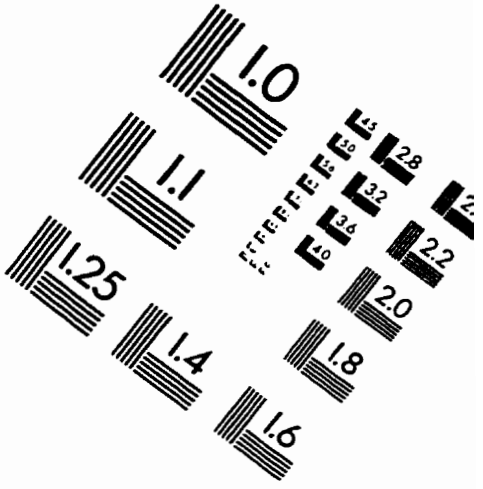

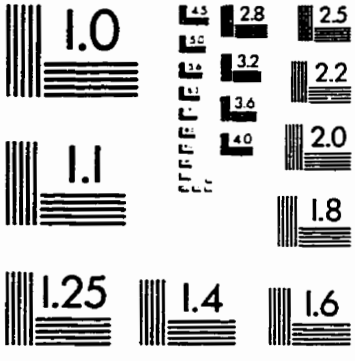

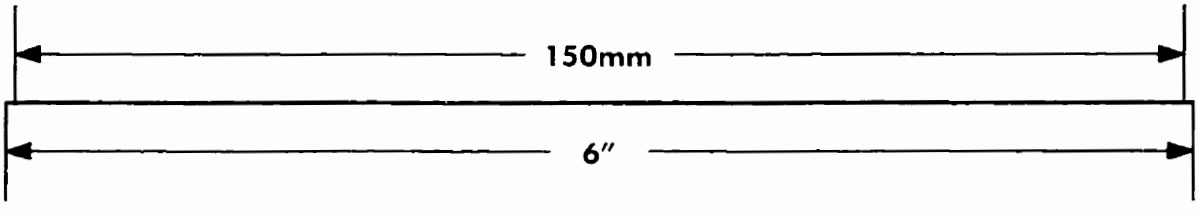

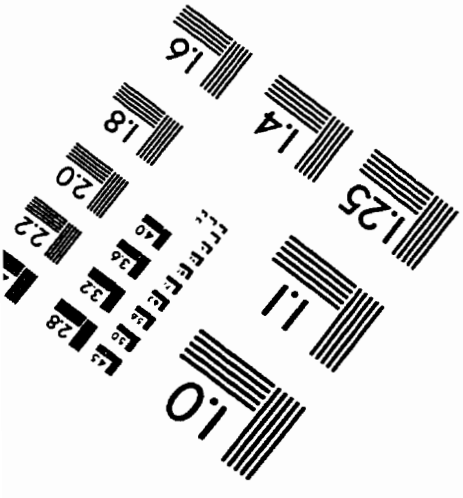

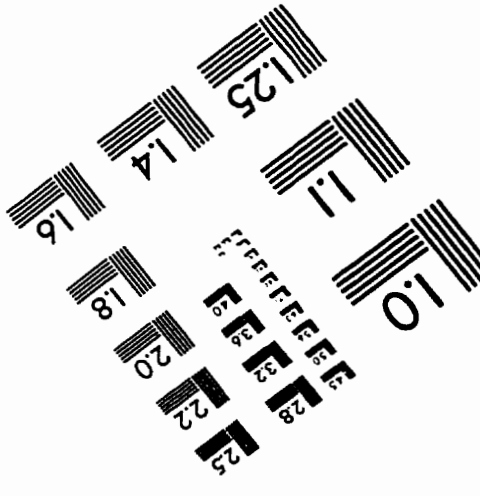

APPLIED IMAGE, Inc
1653 East Main Street
Rochester, NY 14609 USA
Phone: 716/482-0300
Fax: 716/288-5989